Bioskiving: Tendon-derived Scaffolds for Biomedical Applications

A dissertation submitted by

Kyle A. Alberti, B.S.

in partial fulfillment of the requirements for the degree of

Doctor of Philosophy

in

Biomedical Engineering

Tufts University

August 2015

Advisor: Prof. Qiaobing Xu

Abstract: The work contained herein is the development of a method to directly utilize the intricate and proven structures contained within tendon for biomedical applications ─ a technique called Bioskiving. The hypothesize is that this sectioning-based technique will allow for maintenance of these structures while creating thin sheets that are flexible and can be formed into desired shapes. This fabrication process is applied to tendon, in order to capitalize on the mechanical and biological properties of the hierarchical and well-ordered collagen structures found within. This work progresses through the development of the processing technique and creation of scaffolds, which involves: decellularization, sectioning, and stacking and rolling to create two- and three-dimensional scaffolds. The mechanical properties of the material are then characterized, and tuned using crosslinking to achieve a 20-fold increase in mechanical strength and transverse isotropy. The biological properties of the material are also characterized, including the degradation *in vitro* and *in vivo*, and the interaction of the material with platelets. Lastly, one potential application of constructs comprised of the material is explored, peripheral nerve repair. The material's potential for nerve repair is evaluated in vitro using Schwann cells and chick dorsal root ganglia explants, and *in vivo* using a rat sciatic nerve defect model. The tendon-derived material proves to be a suitable substrate for promoting peripheral nerve repair, and is biocompatible and biodegradable. The mechanical properties can be tuned and the geometry of structures created be altered, allowing others to find use for it in a number of biomedical applications.

i

Acknowledgements

My first thanks must go to my advisor, Qiaobing Xu, for your continued support, inspiration, and experience in so many different fields. I have learned so much from you over the past four years, and have been able to achieve things I would've never thought possible. Only with your guidance have I been able to reach where I am today. I'd also like to thank the members of the Xu Lab who have provided continuous feedback and support to keep me on the right track. I must also thank Milva Ricci, Carmen Preda, Martin Hunter, and Keleigh Sanford, who have all made sure everything has stayed running smoothly throughout my time here.

Thank you to the collaborators that have assisted with various parts of this thesis: Lorenzo Tozzi, for help and expertise with all things blood; Amy Hopkins for teaching me how to work with DRG; Prof. Zhigang Suo, Jeong-Yun Sun, and Widusha Illeperuma from Harvard University, for your knowledge and lessons about material properties; and to the members of the Marra Lab at UPMC for showing me the sciatic nerve repair surgery.

To my mother, stepfather, sisters, and particularly, my grandmother: thank you for your support over all of these years and for always loving and believing in me. You have always been there for me, and I know, always will. Finally, lots of love and thanks to Laura; you have motivated me to succeed, keeping me ever looking forward and working harder. You have made writing this dissertation a far better process than I would've ever expected.

Table of Contents

iv

List of Publications

1. **Alberti, K. A.,** & Xu, Q. Degradation and Biocompatibility of Tendon-derived Sections In Vivo. *Submitted.*

2. Mostafalu, P., Akbari, M., **Alberti, K.A.**, Xu, Q., Khademhosseini, A., & Sonkusale, S., Thread based microfluidics, sensors, and electronics for medical and life sciences. *Submitted*.

3. Domigan L.J., Andersson M., **Alberti K.A.**, Chesler M., Xu A., Johansson J., Rising A., & Kaplan D. "Carbonic anhydrase generates a pH gradient in Bombyx mori silk glands. *Submitted.*

4. **Alberti, K. A.**, Wang, J. & Xu, Q. In Vivo Peripheral Nerve Repair Using Tendon-derived Nerve Guidance Conduits. *Submitted.*

5. **Alberti, K. A.**, Sun, J. Y., Illeperuma, W., Suo Z. & Xu, Q. Laminar Tendon Composites with Enhanced Mechanical Properties. *J. Mater. Sci.* **50,** 2616-2625 (2015).

6. **Alberti, K. A.**, Hopkins, A., Tang-Schomer, M., Kaplan, D., Xu, Q. The Behavior of Neuronal Cells on Tendon-Derived Collagen Sheets as Potential Substrates for Nerve Regeneration, *Biomaterials*, **35,** 3551-3557 (2014).

7. Kuang, Y., Shi, J., Li, J., Yuan D., **Alberti, K. A.**,Xu Q. & Xu, B. Pericellular Hydrogel/Nanonets Inhibit Cancer Cells. *Angew. Chem. Int. Ed.,* **53,** 8104-8107 (2014).

8. Wang, M., **Alberti, K. A.**, Varone, A., Pouli, D., Georgakoudi, I. & Xu, Q. Enhanced Intracellular siRNA Delivery Using Bioreducible Lipid-like Nanoparticles. *Adv. Healthc. Mater.* **3,** 1398-1403 (2014).

9. Wang, M., **Alberti, K. A.**, Sun S., Arellano C. L. & Xu, Q. Combinatorially-designed Lipid-like Nanoparticles for Intracellular Delivery of Cytotoxic Protein for Cancer Therapy, *Angew. Chem.* **126,** 2937-42 (2014).

10. **Alberti, K. A.** & Xu, Q. Slicing, Stacking and Rolling: Fabrication of Nanostructured Collagen Constructs from Tendon Sections. *Adv. Healthc. Mater*, **2,** 817-21 (2013).

11. Sun S., Wang, M., **Alberti, K. A.**, Choy, A. & Xu, Q. DOPE Facilitates Quaternized Lipidoids (QLDs) for in vitro DNA Delivery. *Nanomed.* **9,** 849-54 (2013).

12. Wang, M., Sun S., **Alberti, K. A.** & Xu, Q. A Combinatorial Library of Unsaturated Lipidoids for Efficient Intracellular Gene Delivery. *ACS Synth. Biol.* **1,** 403-407 (2012).

13. **Alberti, K.A.** & Xu, Q. Bioinspired Fabrication of Nanostructures from Tissue Slices. In: Jabbari, E., Khademhosseini, A., Kim, D. H., Ghaemmaghami, A., eds. *Handbook of Biomimetics and Bioinspiration: Biomimetic Bioinspired Materials, Mechanics, and Dynamics.* (World Scientific Publishing Co., 2014).

Patent:
    Alberti, K.A.; Xu, Q. "MULTILAYERED COLLAGEN TUBULAR SCAFFOLD". PCT/US2012/064388.

List of Tables

List of Figures

x

Abbreviations

ANOVA – Analysis of variance
BSA – Bovine serum albumin
COMP – Cartilage oligomeric matrix protein
DAPI – 4',6-diamidino-2-phenylindole
DC – Distal conduit
DHT – Dehydrothermal crosslinking
diH2O – Deionized water
DN – Distal nerve
DRG – Dorsal root ganglia
DTBP – Dimethyl 3,3'-dithiobispropionimidate
ECM – Extracellular matrix
EDC – 1-ethyl-3-(3-dimethylaminopropyl)carbodiimide hydrochloride
EDTA – Ethylenediaminetetraacetic acid
FTIR – Fourier transform infrared spectroscopy
GA – Glutaraldehyde
GAG – Glycosaminoglycan
H&E – Hematoxylin and eosin
HMDS – Hexamethyldisilazane
HPF – High powered field
HRP – Horse radish peroxidase
HUVEC – Human umbilical vascular endothelial cell
MC – Middle conduit
MES – 2-(N-morpholino)ethanesulfonic acid
NC –Non-crosslinked
NCM – Non-collagenous matrix
NF160 – Neurofilament 160
NGC – Nerve guidance conduit
NHS – N-hydroxysulfosuccinimide
OCT – Optimal cutting temperature compound
PBS – Phosphate buffered saline
PBST – Phosphate buffered saline with Tween 20
PC – Proximal conduit
PDL – Poly-D-Lysine
PDMS – Poly(dimethylsiloxane)
PLGA – Poly(lactic-co-glycolic acid)
PN – Proximal nerve
PNS – Peripheral nervous system
PRP – Platelet rich plasma
PTFE – Polytetrafluoroethylene
RFU – Relative fluorescence units
RGD – Arginylglycylaspartic acid
SDS – Sodium dodecyl sulfate

SEM – Scanning electron microscopy
SFI – Sciatic functional index
SIS – Small intestine submucosa
SLRP – Small leucine-rich proteoglycans
SMC – Smooth muscle cells
TCPS – Tissue culture polystyrene
TNBS – 2,4,6-Trinitrobenzenesulfonic acid
TSE – transmissible spongiform encephalopathies
UTS – Ultimate tensile strength
UV – Ultraviolet
vWF – von Willebrand factor

Chapter 1.

Introduction and Background

1.1 INTRODUCTION

Numerous complex, well-defined structures and patterns have developed in nature, many of which we interact with daily without a second thought. Many of these are at the micro or nanoscale, yet have a dramatic impact on the way materials function. Everything from the elaborate fractal patterns in snowflakes, to the Fibonacci spirals in Romanesco broccoli, to the silicate shells of diatoms, contains a hidden world of detail and beauty that has inspired scientists and engineers for centuries. These ordered and multiscale structures have withstood the test of time and can serve as a template for bioinspiration[1].

Such biomimicry can be found in numerous innovative applications: adhesive materials mimicking the hairs found on gecko feet[2], artificial micropropulsion devices based off of cellular flagellae[3], using the natural material directly as a template for inorganic structures[4,5], and even synthetic materials designed to mimic the native extracellular matrix (ECM) for tissue engineering[6,7].

Despite these advancements, direct utilization of the natural material, and the micro and nanostructures contained within, would avoid the need to replicate and reproduce what nature has already provided us with.

1.1.1 Purpose and organization

The overall motivation of the work that comprises this dissertation is to develop a method to directly utilize the intricate and proven structures contained within tendon for biomedical applications. We hypothesize that a sectioning-based technique will allow for maintenance of these structures while creating thin sheets that are flexible and can be formed into desired shapes. This fabrication process will be applied to tendon, in order to capitalize on the mechanical and biological properties of the hierarchical and well-ordered collagen structures found within. This work will progress through the development of the processing technique and creation of scaffolds, to mechanical characterization of the material, followed by biological characterization. The utility of the material will then be demonstrated by applying it to a particular biomedical engineering challenge.

Chapter 2 covers the fabrication technique, including tendon decellularization, sectioning, processing, and construction of two- and three-dimensional structures. In Chapter 3, the tensile mechanical properties and burst pressure of the material are measured, and the fabrication technique expanded to allow for a variety of material properties. The mechanism of failure that the material undergoes in tension is determined, and finally the permeability of the material to several biologically-relevant compounds is measured.

In Chapter 4, the degradation of the tendon-derived material is measured *in vitro* using collagenase following various crosslinking treatments, and related to the mechanical properties and surface structure. The hemocompatibility is then assessed, and the surface of the material modified to alter interaction with platelets. The *in vivo* degradation and biocompatibility of the material in a non-crosslinked state and a crosslinked state are then determined in relation to encapsulation, cell number and macrophage presence.

Chapter 5 takes the tendon-derived material and applies it for peripheral nerve regeneration. *In vitro* studies assaying adhesion, proliferation, and alignment are conducted using Schwann cells, as well as chick dorsal root ganglia (DRG) explants to determine the influence of the tendon substrate at multiple levels of complexity. Finally, a tubular conduit is used to regenerate a peripheral nerve over a critically-sized defect in a rat sciatic nerve model.

Chapter 6 contains conclusions surrounding the work presented here, and presents future work that the sectioning technique, as well as the tendon-derived material, could be applied towards. The remainder of the current chapter will serve to provide background for the field, and the application investigated herein.

1.2 BACKGROUND

1.2.1 Biomaterials

In the past decade, tissue engineering and regenerative medicine have made significant strides to improve medical treatments and expand the frontiers of science. One area of research that has made these developments possible is in the field of biomaterials, where advancements in composition, structure, and treatment methods have revolutionized both implanted biomedical devices and allowed for tissue engineered organs[8,9].

The overarching descriptor of biomaterials includes ceramics, natural materials, and synthetic materials. Synthetic biomaterials, produced via polymerization, such as: poly(lactic-co-glycolic) acid (PLGA), polyethylene glycol and polycaprolactone, demonstrate great adaptability in terms of tunability, and potential for modification. Yet, they are limited in that they don't generally contain any inherent bioactivity, nor do they have cell attachment sites (e.g. RGD[10]). Although these sites can be functionally added[11],

it is difficult to recapitulate the degree of complexity found in natural extracellular matrices[7].

A wide assortment of natural materials that do contain these structures can be derived from a variety of sources. Several such materials include: collagen and elastin isolated from tendon[12], ligaments and skin[13]; silk, derived from spiders and the cocoons of silk worms[14,15]; and chitin, often from the shells of crustaceans like shrimp and crabs[16]. Many of these natural biomaterials have also been derived from genetically engineered sources, including recombinant collagen[17], silk and elastin proteins[18,19]. The list of biomaterials is nearly endless, as are their potential applications. One abundant and commonly used source of natural biomaterials is directly from decellularized ECM.

Decellularized ECM are the structures that remain when a piece of tissue, or whole organ, has been processed to remove all cellular components (Figure 1.1). This remaining ECM is comprised of a number of types of proteins, carbohydrates, and minerals, including structural proteins (e.g. collagen and laminin), growth factors, and cell adhesion molecules, whose type and number will vary depending on the source organ and decellularization process used[20,21]. *In vivo*, the ECM provides structural support, along with biochemical cues to the cells in a given tissue, and the composition will reflect this. For example, tendon is primarily comprised of fibrillar Type I collagen (70-90%), along with various proteoglycan molecules, as it is designed to transmit tensile stress from muscle to bone[22,23]. Bone, however, generally undergoes compressive stresses, and as such is comprised of 50-70% inorganic mineral matrix, primarily hydroxyapatite, with the remaining organic matrix largely consisting of Type I collagen[24].
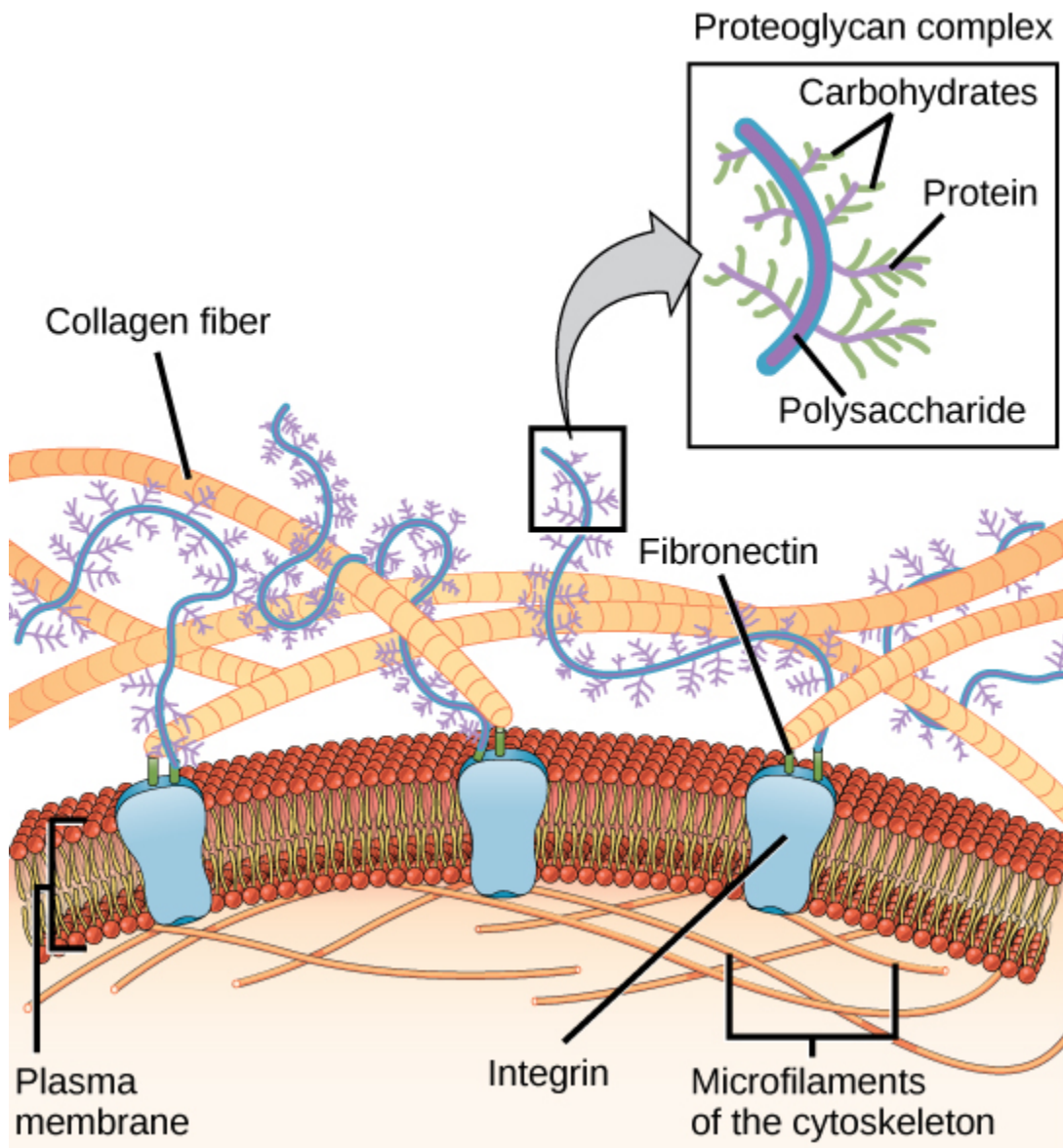
Figure 1.1 Illustration showing the various components commonly found in mammalian extracellular matrix. Reproduced from OpenStax College CNX via CC BY 3.0.

Decellularized ECM has been used for a wide variety of applications including both as a source for biomaterials following processing, and directly as a scaffold for tissue engineering. There are a number of benefits to using decellularized tissue for these applications over synthetic materials including: i) the presence of biologically active

molecules, ii) the preservation of natural structures with physical cues, iii) its renewable nature, and iv) overall ultrastructure in the case of decellularized whole organs. The complex biological cues found in the decellularized tissue are representative of the specific source tissue, and can range from biologically active sites found directly on the proteins that predominantly make up the matrix[25], to growth factors and cell adhesion molecules[26,27], acting as a template for future growth. These benefits are particularly evident when decellularizing a whole organ, which additionally maintains the physiological geometries.

1.2.2 Tissue processing

The method that is used to decellularize a tissue is crucial, as it can have a large impact on the number and type of remaining growth factors, as well as the physical 3D structure of the ECM. It is for this reason that a variety of application and tissue specific methods have been developed to remove the cellular components from both whole organs and smaller pieces of tissues. Decellularization techniques fall into three general categories: physical, chemical, and enzymatic methods, summarized in Table 1.1. Often a combination of techniques is used.

Physical methods include mechanical agitation, mechanical force, and freezing. Mechanical agitation and force can result in cell lysis; however they also often result in damage to the ultrastructure of the ECM which may be desirable to keep intact[28]. Freezing, often applied in several freeze-thaw cycles, causes ice crystals to form, rupturing cell membranes[29]. This technique may disrupt some ultrastructure but has been demonstrated to retain the mechanical properties of the material[30]. Freezing has been implemented on its own to decellularize nerve grafts for peripheral nerve repair[31], and in conjugation with other methods to decellularize adipose tissue for stem cell differentiation[32]. Many decellularization protocols use physical methods in conjunction

with other chemical or enzymatic methods to ensure adequate distribution of the decellularization agents, or to minimize exogenous agents needed to remove cells.

Method	Action	References
Physical		
Mechanical agitation & force	Cell lysis, can result in damaged ECM ultrastructure	28
Freezing	Ice crystal formation ruptures cells	29
Chemical		
Hyper/hypotonic	Osmotic shock causing cell lysis	33,34
pH-based	Solubilize cytoplasmic components, nucleic acids; can damage proteoglycans and ECM	29,35,36
Ionic detergents *(e.g. SDS)*	Solubilize cellular membranes; can denature proteins	37,38
Non-ionic detergents *(e.g. Triton-X100)*	Disrupt lipid, DNA components	38,39
Other solvents *(e.g. alcohol, acetone)*	Action depends on solvent, often results in cell lysis	28,40
Enzymatic		
Trypsin	Cleaves peptide bonds	41
Nucleases	Cleave phosphodiester bonds	42
Dispases	Cleaves fibronectin, some collagen	43

Table 1.1: An overview of tissue decellularization methods.

A vast array of chemical decellularization agents have been utilized that fall into several categories: hyper/hypotonic solutions, pH-based treatments, detergents, and other solvents. Hypertonic and hypotonic solutions can be used to lyse cells, however cellular

remnants often remain and require subsequent decellularization steps[33,34]. Acids and bases, when used to decellularize achieve adequate decellularization as they solubilize cytoplasmic components and nucleic acids but have the unfortunate side effect of also damaging proteoglycans or other ECM components[29,35,36]. Collagen in particular can be damaged by acidic decellularization solutions.

Detergents, particularly ionic detergents like sodium dodecyl sulfate (SDS) and sodium deoxycholate are commonly used as they are very effective at solubilizing and removing both cellular and nuclear components, but can also disrupt ECM structure[37,38]. Non-ionic detergents (Triton X-100) on the other hand primarily only disrupt lipid and DNA components, while leaving protein structures intact[38,39]. Zwitterionic detergents, such as CHAPS and Sulfobetaine-10, exhibit properties of ionic and non-ionic detergents, allowing them to remove most cellular components, but with less ECM disruption than ionic detergents alone[33]. Detergent decellularization is by far the most widely used process, with notable examples including: recellularization and transplantation of liver grafts[44], decellularization of porcine[45] and human valves[46], and bone-ligament-bone grafts[47].

Solvents such as alcohols and acetone have also been used which result in the lysis of cells, however they can impact the properties of the ECM through crosslinking of collagen and other proteins[28,40]. For many of these methods, chelating agents such as ethylenediaminetetraacetic acid (EDTA) are often added in order to further dissociate cells from the ECM; however, they are not often used on their own.

Lastly, enzymatic methods such as trypsin, nucleases or dispases can be used to decellularize ECM, but given the function of these compounds care must be taken not to over-decellularize and disrupt the ECM. Enzymatic methods have been shown to disrupt the ECM, remove glycosaminoglycan (GAGs) and reduce mechanical properties in decellularized heart valves however these effects may not be as pronounced as with detergent-based decellularization[48,49].

Many of these decellularization methods are applied to small pieces of tissue in order to allow greater penetration and cell removal, however whole organs have also been decellularized[28]. This process primarily involves perfusion through the native vasculature, both antegrade and retrograde, which results in efficient decellularization of the tissue and drastic changes can be seen following processing of these tissues (Figure 1.2). The benefit of a scaffold created in such a way is maintenance of the native three-dimensional architecture in contrast to the deconstruction and reconstruction required for smaller pieces or mechanically disrupted tissues. Decellularization of whole organs has been demonstrated on rat lungs using a low concentration of SDS, and subsequently recellularized and implanted *in vivo*, successfully providing gas exchange[50,51]. Whole rat hearts have been decellularized, also using low concentration SDS solutions, and reseeded, and achieving functional contraction that allowed pumping[52]. Whole liver decellularization, recellularization with host cells and transplantation has also been achieved, yielding tissue with liver-specific functions *in vitro* and surviving implantation *in vivo*[53].
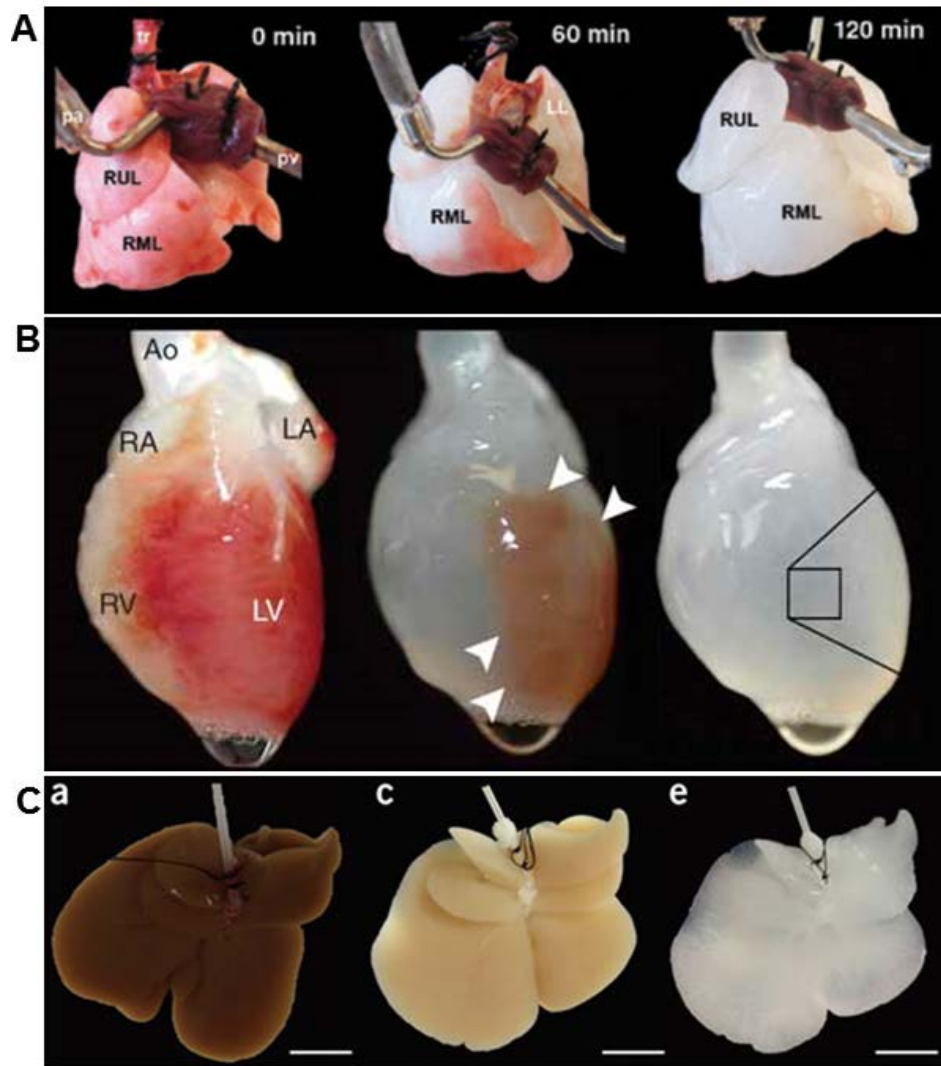
Figure 1.2: Whole organ decellularization of **A)** rat lung, **B)** rat heart, **C)** liver. Adapted and reprinted from references: [54], [52], [53] respectively with permission from Nature Publishing Group.

This process has also been successfully translated to humans with tissue engineered airways[8] using decellularized human trachea seeded with epithelial cells and chondrocytes. Tissue engineered blood vessels from patient specific cells on a polymer scaffold[55] and with no scaffold[56,57] at all have also been transplanted, as have bladders created on collagen and collagen-PLGA scaffolds[9]. As promising as this progress is, they

are less complex than heart, lung, and liver, and do not require large vasculature. This work demonstrates the immense potential for tissue engineering using decellularized matrices; however, progress in humans has not advanced as far.

1.2.3 Repurposing ECM

Direct use of decellularized ECM for partial or whole organ engineering of that same tissue is a common use of such material; however several novel methods have recently been developed to repurpose these structures. With the current explosion in availability and diversity of 3D printers and related equipment, available in the last decade, bioprinting has been increasingly used for the creation of scaffolds for tissue engineering. Many directly utilize synthetic materials for the scaffolds, while others will use decellularized ECM or other natural polymers as their substrate for printing. Natural polymer scaffolds are usually extruded and deposited as hydrogels in layer-by-layer techniques (Figure 1.3A-C), or via inkjet printing, as more traditional additive manufacturing techniques (e.g. sintering, lithography) would not work or would damage the material. 3D printing of polymers like collagen, gelatin, chitosan, hyaluronic acid, and silk fibroin has all been successfully demonstrated for the creation of various scaffolds[58–62].

These techniques are limited in that construction of large tissues would require integration of vasculature, but they have great potential for creating a diverse selection of tissues in patient-specific shapes[63]. 3D bioprinting has also been used directly with cells, allowing the construction of scaffold-free tissues[64], as well as to allow printing proteins or other biomolecules on their own[65].

Other processes that do use synthetic materials, including 3D printing, have taken to modifying the synthetic materials directly with ECM molecules to achieve the benefits of ECM while retaining the extensive tunability of the synthetic polymers. Incorporation

of the ECM is achieved in several ways; one of simplest techniques is direct coating on the synthetic material using decellularized and processed ECM[66,67]; for example, coating a polypropylene mesh with collagen[68]. Direct modification has been shown with bulk ECM and also with specific proteins (e.g. fibronectin, laminin) and smaller peptides[6]. This functionalization can also be achieved through chemical conjugation which allows for more precise adhesion and spatial patterning dependent on the polymer structure[69].
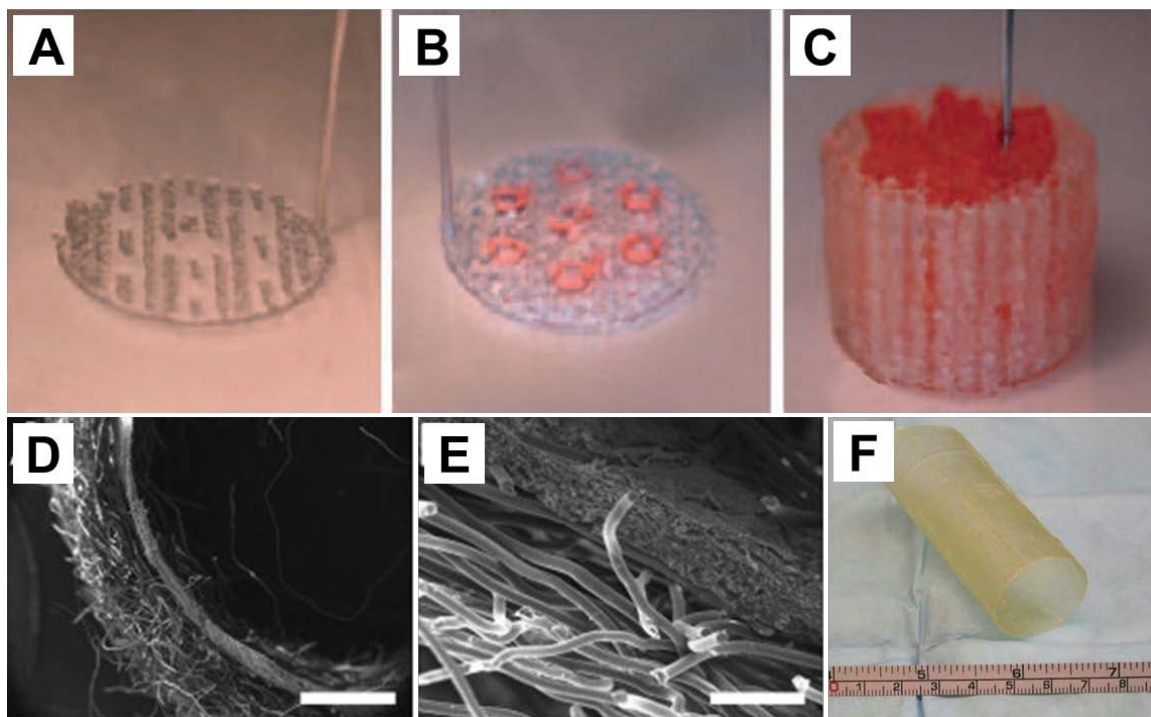
Figure 1.3: A-C) 3D bioprinted structures comprising cells in gelatin/alginate/fibrinogen and gelatin/alginate/chitosan hydrogels. **D,E)** Composite scaffold of polyglycolic acid and acellular collagen matrix, scale bars are 2 mm (D) and 500 μm (E). **F)** Photograph of ECM scaffold composed of decellularized bladder matrix, used for esophageal repair in conjunction with muscle tissue. Reprinted from references [70], [71], [72] with permission from SAGE Publications and Elsevier.

ECM can also be directly deposited by cells cultured on the material, followed by decellularization and reuse of the scaffold[73,74], however this is time consuming and the type of ECM deposited is limited. An alternative to surface modification of the polymers

is the creation of a hybrid scaffold in the opposite way by impregnating ECM scaffolds with synthetic polymers dissolved in solvents, followed by evaporation, to create an interpenetrating polymer network[75] (Figure 1.3D,E).

Other biomedical applications make direct use of the ECM, but they utilize it for repair or construction of another tissue. For example, ovine forestomach, following decellularization, has been repurposed for chronic wound healing[76,77], effectively utilizing the native architecture and biological components contained within. Similarly, acellular dermis has been used for repair of ventricular aneurysm[78] and abdominal wall defects[79], while acellular bladder has been used for esophageal repair (Figure 1.3F), achieving structural and functional restoration in dogs[72], and facial tissue reconstruction in rabbits[80].

One of the most widely used ECM sources, small intestine submucosa (SIS), has been adapted to repair vocal folds[81], rotator cuffs[82], vascular grafts[83], peripheral nerve regeneration[84], tracheal reconstruction[85], bone defects[86], and more. The wide adoption of SIS towards this variety of applications is likely due to its physical properties which provide mechanical integrity, and its biological properties (e.g. retained proteoglycans and growth factors) which allow it to promote angiogenesis along with tissue growth and differentiation[87].

Despite being from other tissues or even other species, ECM contains structural and functional proteins, along with appropriate three dimensional spatial patterning, that can act as a scaffold for new cellular and tissue growth[88]. Bioprinting, synthetic polymer modification, and alternative tissue use further show the utility that ECM can provide as it is able to be repurposed for many applications. This also demonstrates that decellularized ECM doesn't have to take a direct route following processing to reconstruct the homologous physiological tissues that it was derived from, as it can be processed and reincorporated to utilize its many benefits.

1.2.4 Tendon and collagen

Collagen comprises a large portion of proteins in the body of mammalian species, making up approximately 20-30% of proteins by weight. The majority of these proteins can be found in locations such as the skin and tendons and provides a variety of functions such as mechanical strength in tendon, ligaments and cartilage, sites of cellular attachment in ECM and protection in the form of scar tissue[89]. There are a number of types of collagen found throughout the body that have a variety of structures and functions, however many of are far less-common and only found in site specific areas providing an explicit function[90]. Fibrillar collagens in particular make up about 90% of the total-body collagen[91]. Their synthesis in vivo includes multiple modification steps, including hydroxylation of amino acid, and isomerization intracellularly which allows for formation of collagen's characteristic triple helical structure, as well as cleavage of propeptide molecules, and presence of specific proteoglycans extracellularly which allow for alignment and formation of collagen fibrils[92].

Tendon is one tissue in which this collagen formation process is crucial. Present in tendon is a hierarchical arrangement of type I collagen (Figure 1.4), where the collagen molecules described above bundle to form micro and sub fibrils through lateral assembly[93], which in turn assembly to form fibrils that exhibit the characteristic 67nm banding pattern of collagen, due to their staggered molecular packing. These fibrils are then brought together into intermediate assemblies and ensheathed by fibroblasts to form collagen fibers which again are assembled into the major fascicles that make up the tendon[94].

Within these structures also exists several non-collagenous components. Nerves and blood vessels are interspersed and function in their normal physiological roles, but there are also a variety of glycoproteins that exist both interfibrillarly and interfascicularly and are important to the structure-function relationship within tendon[95].

Interfibrillar proteoglycans including the small leucine-rich proteoglycans (SLRPs) (decorin, aggregcan) critical in assembly of the collagen fibrils, as well larger proteoglycans like collagen oligomeric matrix protein (COMP), lubricin, tenascin-C, and tenomodulin and some elastin[95–97]. These proteoglycans will affect the mechanical properties of the tendon by modulating hydration, binding multiple collagen fibrils together (e.g. COMP), or allowing greater movement (e.g. lubricin)[98]. In tendon, the bulk of GAGs bound to the proteoglycans are primarily dermatan sulphate and chondroitin sulphate, along with keratan sulphate[99,100].

Similar proteoglycans are present in the interfasicular regions with a greater amount of elastin, as well as type III and VI collagens and are believe to contribute to tendon elasticity during initial loading[101]. This composition does however vary between species, tendon anatomical location, and age.
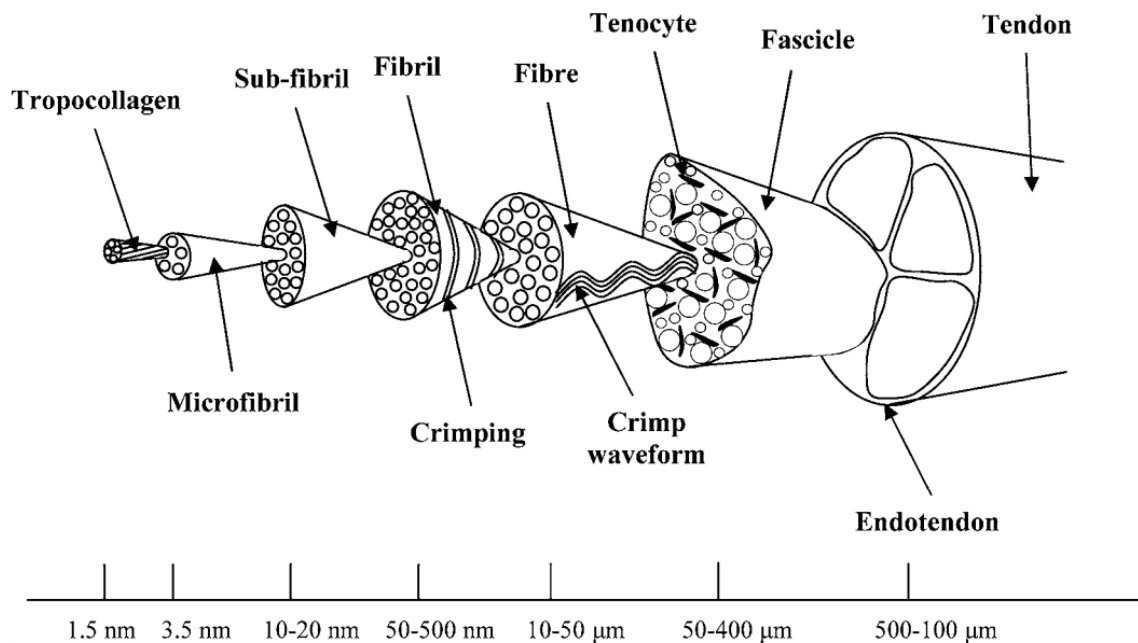
Figure 1.4: Illustration of the hierarchical structure of collagen within tendon. Reprinted from Screen et al. [22] with permission from Springer Science and Business Media.

1.2.5 Collagen as a biomaterial

In most biomaterial applications where collagen is used, it is isolated from animal sources like skin and tendon, fish scales[13], or marine sponges[102], with the primary methods of extraction involve solubilization with neutral salts, acids, or pepsin solutions. These various extraction methods will isolate different portions of the collagen, and must be tuned depending on the source tissue[103]. This extraction process can take upwards of 10 days and often results in in impure collagen with varying amino acid sequences[102].

These treatments are required however, as fibrillar collagen is generally insoluble in water and the collagen must be separated from other ECM components[103,104]. One major result of this extensive processing is dissociation of the fiber and fibrillar structure of the collagen, including intermolecular bonds and any alignment that was originally observed in the structure[105]. This solubilized collagen is then commonly reconstituted out of solution and then used for a number of biomedical applications.

As a material for tissue engineering, it can be cast into scaffolds, often hydrogels, sponges, or compressed layers, and has been used for wound healing[89] and *in vitro* and *in vivo* growth of many tissue including teeth[106,107], bone[108], cartilage[109,110], cornea[111] and more[112]. Alternatively, it can be used as a delivery vehicle, either through direct conjugation or through encapsulation. This has been demonstrated in the aforementioned formats and when developed into films and microparticles[113], for the delivery of antibiotics[114], small molecules[115], proteins[116], DNA/RNA[117,118] and even chemotherapeutics[119,120]. It is exactly this vast adaptability that has made collagen such a commonly used biomolecule, hundreds of iterations.

Many of these applications involve efforts to reintroduce a fiber/fibrillar structure, along with some sense of alignment. One of the common methods used to accomplish this in many materials through electrospinning, which can be challenging due to collagen's water-insoluble nature, and subsequently requires volatile organic solvents like

hexafluoroisopropanol[121]. Some reports have shown this process is able to reintroduce lateral packing resulting in 67nm banding[121], however others have shown that fluorinated solvents completely remove secondary folding of the protein and electrospinning can only restore a maximum of 42% of the structural folding[122]. In addition to this, reintroduction of higher levels of organization (i.e. fiber, fascicle) has not been achieved. It is likely these challenges, along with low mechanical strength[123,124] that electrospun collagen has not found widespread application as a standalone scaffold material compared to other collagen gel methods.

Other methods of introducing alignment have included: magnetic alignment, where collagen gels are neutralized and allowed to gel in a strong magnetic field (7-13T) alone[125,126], or in a low magnetic field alongside magnetic beads[127], resulting in varying degrees of fiber alignment. This technique has been used to create multilayer aligned scaffolds resembling corneal stroma[125], as well as tubular rods for neuronal growth[128]. Extrusion-based methods have included cone extrusion[129] and ink jet[130] and micromechanical-based[131] technologies to produce alignment, as has using traditional photolithography techniques[132,133], and gel-casting/freeze drying[134]. Lastly, compressive loading or extension resulting in axial strain during gelation have also been shown to induce fibril alignment[135,136], however the degree of alignment does not appear to be as substantial as the other methods discussed here.

Chapter 2.

Fabrication of 2D and 3D Scaffolds from Decellularized Tendon Using a Combination of Sectioning, Stacking, and Rolling

2.1 INTRODUCTION

The creation of thin sections of tissue using a microtome dates back to the late 1700's, by George Adams Jr. and later by Alexander Cummings[137], following the earlier development of light microscopy. Since then, microtomes have been crucial piece of equipment for routine histology. More recently, their use has expanded into the material development and fabrication realm. For example, Xu et al. used an ultramicrotome to create metallic nanostructures from a thin film of metal that had been deposited on a topographically contoured substrate, a process termed Nanoskiving[138,139]. The objective of this technique was to replace traditional fabrication techniques that were constraining due to factors such as cost, requirements for a clean room, and limited material selections.

Techniques such as Nanoskiving demonstrate the utility and versatility of sectioning as a method of fabrication. With this in mind, we set out to develop a method of creating a biomaterial fabrication technique from nature-derived materials. A number of materials in nature have exquisitely defined and arranged structures within them, such

as the lamellae in bone osteons[140], the fibers in silk [141], the ornate silica frustules of diatoms[142], or the hierarchical arrangement of collagen fibers and fibrils in tendon[93,143].

The collagen found in tendon, as well as many other tissues such as skin, has been used for numerous biomedical applications, due to its excellent biocompatibility and biodegradability. Conventional processing techniques, however, result in the breakdown of the collagen fiber structure, a unique feature that can be utilized. A sectioning-based fabrication technique, called Bioskiving, was developed to address this.
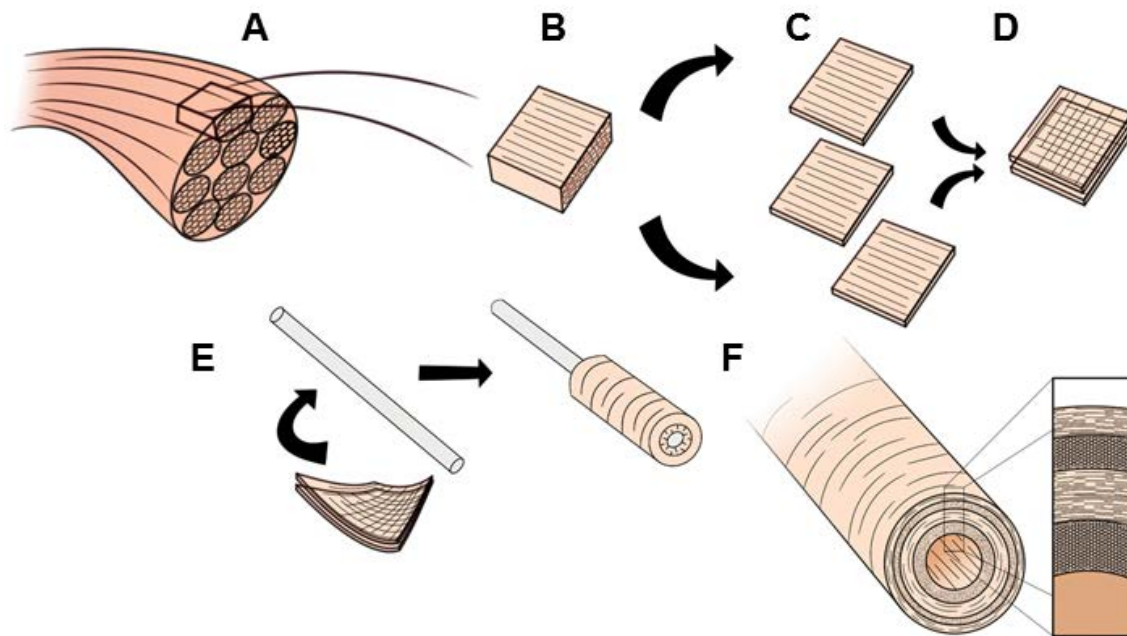
Figure 2.1: Schematic illustrating the Bioskiving technique: **A)** a block is removed from the tendon, **B)** the block is decellularized, **C)** sectioned using a cryomicrotome, **D)** and the sections either stacked, **E)** or rolled around a rod, **F)** creating multi-layer structures[144].

2.2 FABRICATION OF CONSTRUCTS

The basic Bioskiving process[144] involves taking a piece of a tendon, such as the bovine Achilles tendon, which is particularly large and robust, and cutting a block from it with a razor blade (Figure2.1A). The block is then decellularized (Figure 2.1B), sectioned using a microtome (Figure 2.1C) and then either stacked (Figure 2.1D) or rolled around a

tubular rod (Figure 2.1E). This allows for the creation of flat scaffolds with 'plys' of tendon that can be oriented in any transverse direction, or tubular conduits (Figure 2.1F). This process allows for the creation of individual sheets, stacked sections, tubular conduits (Figure 2.2), or a number of other shapes where the fiber orientation and structure are maintained (Figure 2.3A,B). Other tendons can also be used; however small tendons limit the size (e.g. rat tail) and other tendons may not have as well aligned collagen fiber, like those in the bovine neck tendon (Figure 2.3)
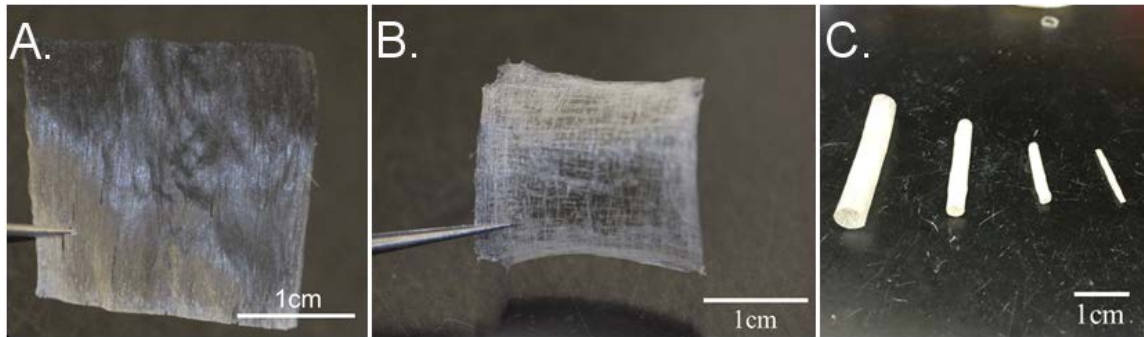
Figure 2.2: Samples of some of the types of structures that can be created using Bioskiving. **A)** 50µm sheet of tendon. **B)** A stack of 10, 50µm sections with each layer rotated 90°. **C)** Tubular conduits with varying lengths, diameters and wall thicknesses.
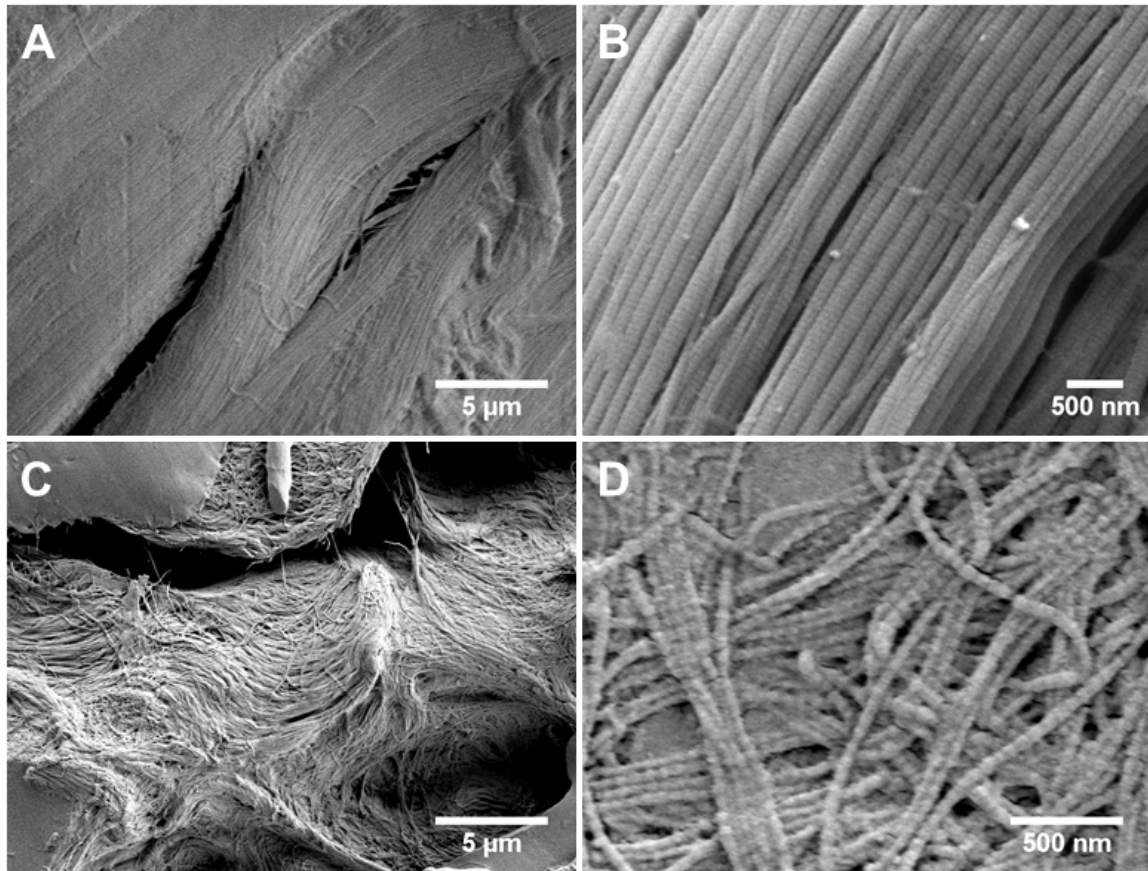
Figure 2.3: Electron micrographs of **(A,B)** bovine Achilles and **(B,C)** bovine neck tendon illustrating the high degree of alignment and organization in the Achilles tendon compared to the neck tendon.

2.2.1 Decellularization

A critical step of this process is the decellularization of the tendon, as inadequate decellularization greatly increases the chance of eliciting an immune response if it were to be implanted[88]. Numerous methods have been developed for the decellularization of biological extracellular matrix (ECM), and fall into several categories: Chemical agents, enzymatic agents, and physical agents[28], or a combination of the three. Each method has advantages and drawbacks, depending on the tissue that is being decellularized.
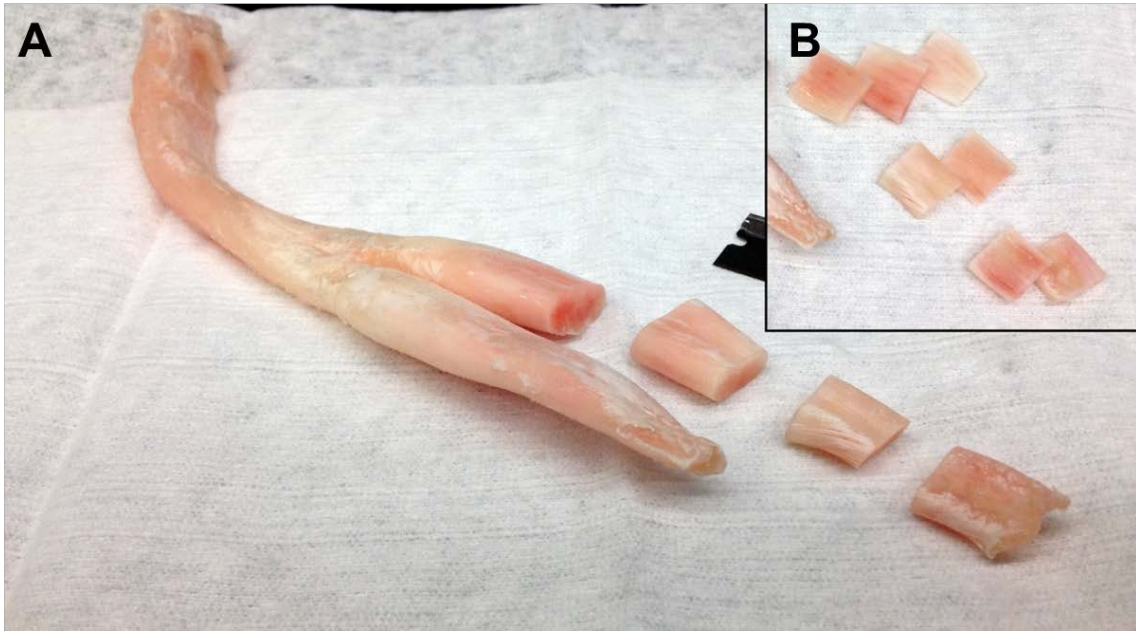
Figure 2.4: Photograph of a frozen bovine Achilles tendon that has been cut into **A)** 2cm lengths and **B)** again into 2cm x 2cm x 2mm squares.

For Bioskiving, a combination of the detergent SDS, and the chelating agent, EDTA are used. This combination has been shown by Cartmell et al. to completely decellularize rat tendons, resulting in better properties than other decellularization reagents such as Triton X-100 or tri(n-butyl)phosphate[145]. The procedure for decellularization used here first involves cutting the tendon into sections roughly 2cm in length, along the axis of the tendon using a standard razor blade (Figure 2.4A). Any pieces containing noticeable defects or vasculature should be discarded. The 2cm pieces can then be sliced parallel to the fiber orientation, into 2mm thick pieces. The resulting blocks should be roughly 2cm x 2cm x 2mm (Figure 2.4B), and can be decellularized as-is, or trimmed smaller for a desired application. This process is most easily done on tendons that have been frozen to -20°C.
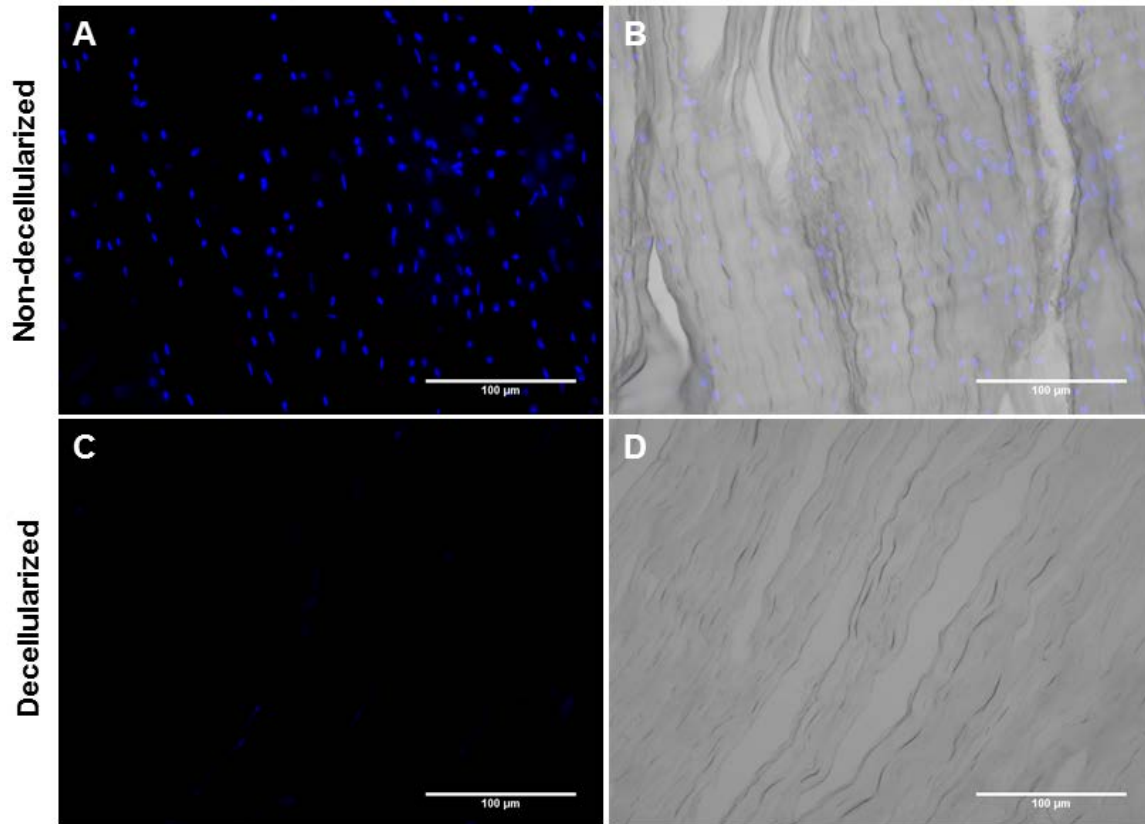
Figure 2.5: Fluorescence and light micrographs of tendon sections that have not been decellularized **(A, B)** and that have been decellularized **(C, D)**. Blue is DAPI staining for nuclei.

The tendon pieces are then placed into a 50ml conical tube with a decellularization solution containing 1% SDS, 1mM Tris-HCl, 0.1mM EDTA. Four to six pieces can be placed into each tube. These conical tubes are then placed onto a rotating shaker at 4°C for 48 h, with the decellularization solution being changed after 24 h. After which, the samples are thoroughly rinsed in running deionized water (diH2O) and returned to the shaker at 4°C in diH2O for an additional 24 h. The pieces should now be decellularized and can be frozen at -20°C until they are to be sectioned. Complete decellularization can be verified by taking sections of the tendon and then staining for nuclei using 4',6-diamidino-2-phenylindole (DAPI), or hematoxylin and eosin (H&E). An example of DAPI-stained tendon sections before and after decellularization can be seen

in Figure 2.5. Following decellularization, no intact nuclei and only slight residual DNA is observable. Additional testing for complete removal of cellular components may include a DNA quantification assay such as PicoGreen.

A critical qualifier of this fabrication technique is that it maintains the native collagen structure, including the collagen triple helix. These structures can be observed using scanning electron microscopy as the staggered packing of the collagen molecules within the triple helix results in a banding pattern with gaps of ~67nm (Figure 2.6A). This also allows for quantification of the fiber diameter, which in bovine Achilles tendon has collagen fibrils around 220nm (Figure 2.6A) and fibers around 10μm in diameter (Figure 2.6B).
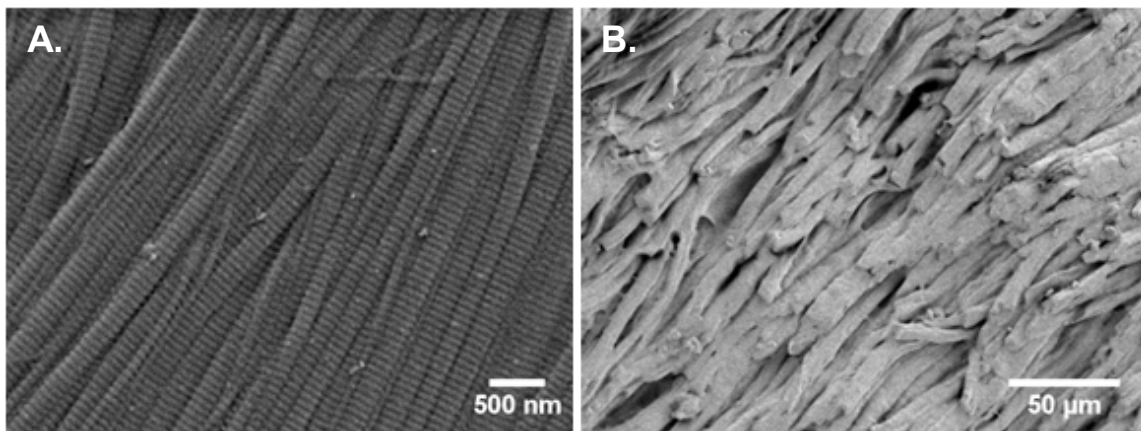
Figure 2.6: Collagen fibers in decellularized bovine Achilles tendon. **A)** Collagen nanofibrils ~220nm in diameter and **B)** fibers ~10μm in diameter.

2.2.2 Sectioning

Once decellularized and frozen, the block can then be sectioned using a cryomicrotome. Conventional sample preparation for a cryomicrotome usually involves sucrose soaking cryoprotection steps and embedding in an optimal cutting temperature compound (OCT). However, these are usually to preserve cell morphology and delicate

structures for observation. The dense, robust collagen fibers in the decellularized tendon sample can be mounted directly to the sample block holder using OCT. Once this is frozen, the sample holder can be placed in the chuck for sectioning (Figure 2.7). The collagen fibers should be oriented parallel to the blade (left to right in Figure 2.7B), as it is easier to get long sections of fibers, whereas orienting it perpendicular (fibers up and down) often results in short, transected fibers. The face of the block should also be oriented normal to the blade in order to create the maximum size slices from a block. This can be accomplished through adjusting the angle of the block holder chuck.
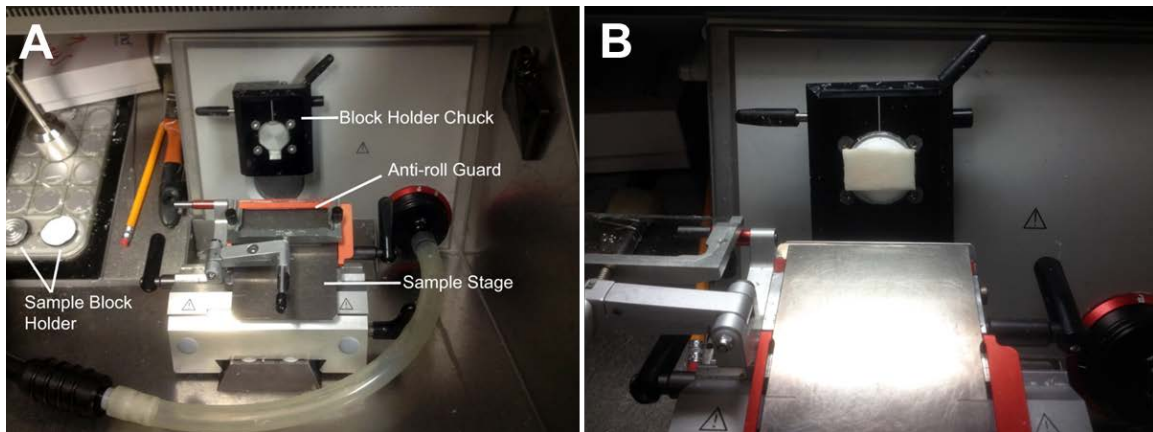
Figure 2.7: A) Diagram showing various pieces of equipment in a cryomicrotome used for Bioskiving. **B)** Image of a decellularized tendon sample oriented parallel to the microtome blade.
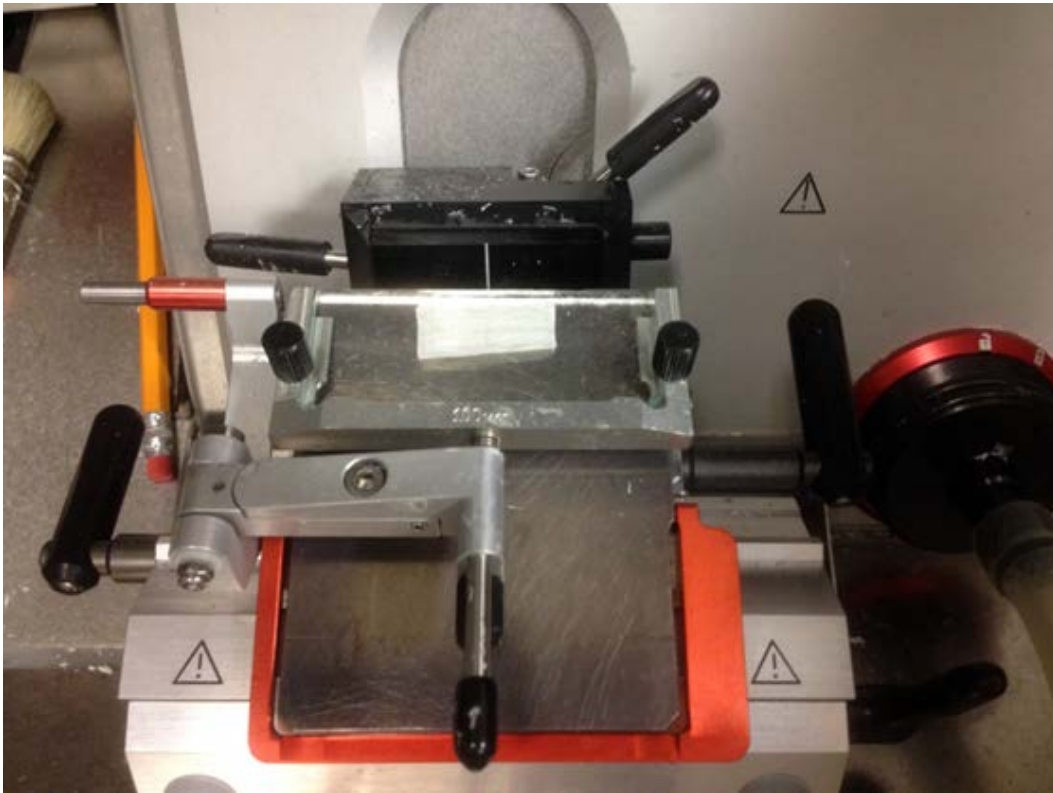
Figure 2.8: Photograph of a 50µm tendon section underneath the anti-roll guard following sectioning.

With this preliminary setup accomplished, the tendon block can now be sectioned. Several sections should first be made in order to assure the sections comprise the entire block. Once that is done, the anti-roll guard can be lowered. Sections can now be produced as shown in Figure 2.8. It is possible to produce sections from 5-100µm thick using this technique. Thicker sections (~300µm) can be produced however the cross-sectional area must be reduced as at this thickness, the blade will bind in the sample if the area is too great. The thicker the section is, the more continuous the sheet will be following drying. During the drying process the collagen fibers contract and can produce gaps that run parallel to the fibers. A thickness of 50µm appears to be optimal for creating continuous sheets that remain pliable for later fabrication steps.

Two common problems that occur with routine histology and with this technique are the section either rolling up, and curling on itself, despite the anti-roll plate, or the section compressing as it comes off the sample. If the section is curling, the chamber temperature should be made warmer; if the section is compressing the temperature should be reduced. The ideal cutting temperatures is around -18°C for the chamber and the cutting head; however this can vary depending on the ambient conditions of the room you are working in, such as temperature and humidity.

2.2.3 Stacking and rolling

Once a section is produced, the section can easily be handled using cold forceps that have been left in the chamber (Figure 2.9A). If the forceps are not cold the sections will melt and stick to the forceps making handing a challenge. The sections can be placed onto a room temperature polytetrafluoroethylene (PTFE) block (Figure 2.9B). Individual sections can be placed onto the block, or the sections can be stacked on top of each other with any desired fiber orientation. The sections will rapidly melt as they contact the surface, and subsequent sections placed on top of each other will melt together.
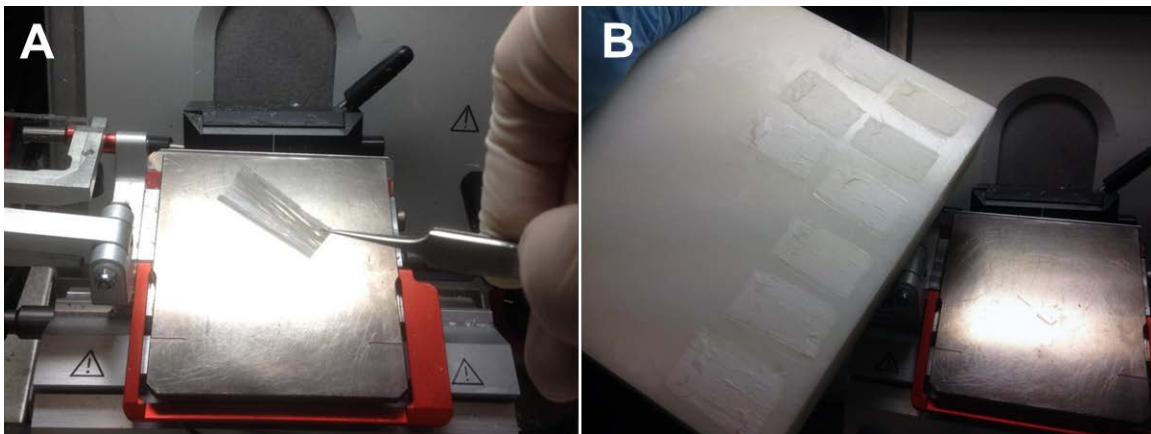
Figure 2.9: A) Tendon sections being removed with forceps and **B)** placed on to a room temperature PTFE block.
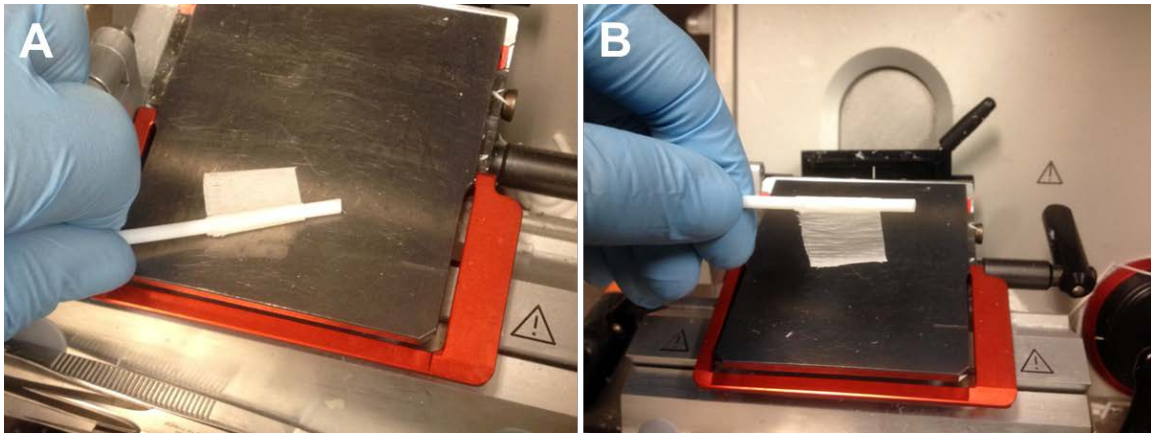
Figure 2.10: A) A tendon section is picked up using a room temperature PTFE rod. **B)** A tendon section is rolled around the PTFE rod with the collagen fibers oriented parallel to the rod.

Alternatively, tubular conduits can be created using a room temperature PTFE rod to pick up the sections (Figure 2.10A). The section will melt to the PTFE rod, which can then be rotated to continue wrapping the section around the rod (Figure 2.10B). This procedure can be repeated a number of times, again with any fiber orientation. The size of the initial sample block will affect the size of the section and subsequently how many times the section will wrap around the rod which should also be taken into consideration. By using different sized rods, the length, diameter and wall thickness can be varied (Figure 2.2C). Overlapping multiple sheets progressively can be used to create tubes that are longer than the initial sample size. Later crosslinking can make these structures quite robust. Using a laminating technique like this it is possible to create more complex structures such as tubes with bifurcations and conical shapes (Figure 2.11).
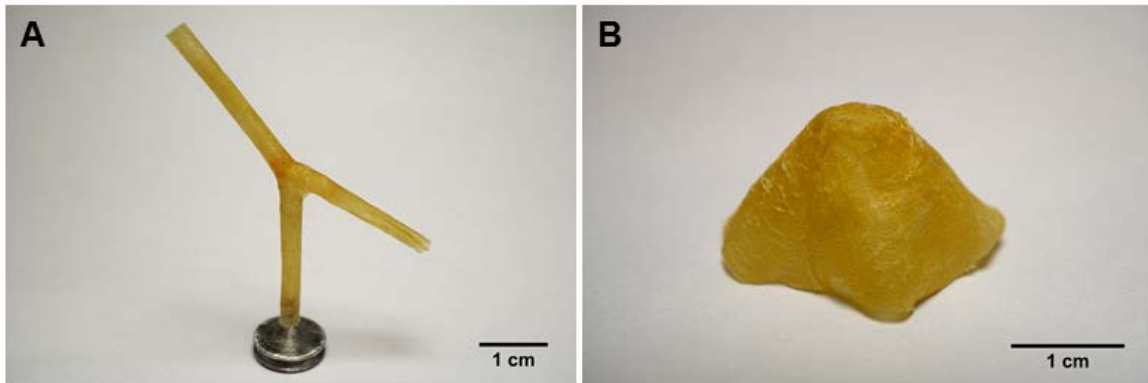
Figure 2.11: Complex structures fabricated using the Bioskiving technique: **A)** tube with bifurcation, **B)** conical structure, both crosslinked with glutaraldehyde.

Sections should be allowed to dry on the PTFE overnight, after which they are easily removable. The sections can be rinsed in diH2O several times to remove any residual OCT; tubular conduits should be left on the template rod during rinsing. Once the sections are rinsed they are allowed to dry again and can then be crosslinked.

Scanning electron microscope (SEM) analysis of the structures created here reveals that the fiber orientation is preserved following drying. Figure 2.12A shows a cross section of the interface between two stacked sheets of tendon. In the bottom of the image, the collagen fibrils run left to right, while the top of the images shows the ends of the fibrils coming out of the page. Similar structures will be present in the cross-section of the tubular conduits (Figure 2.2B).
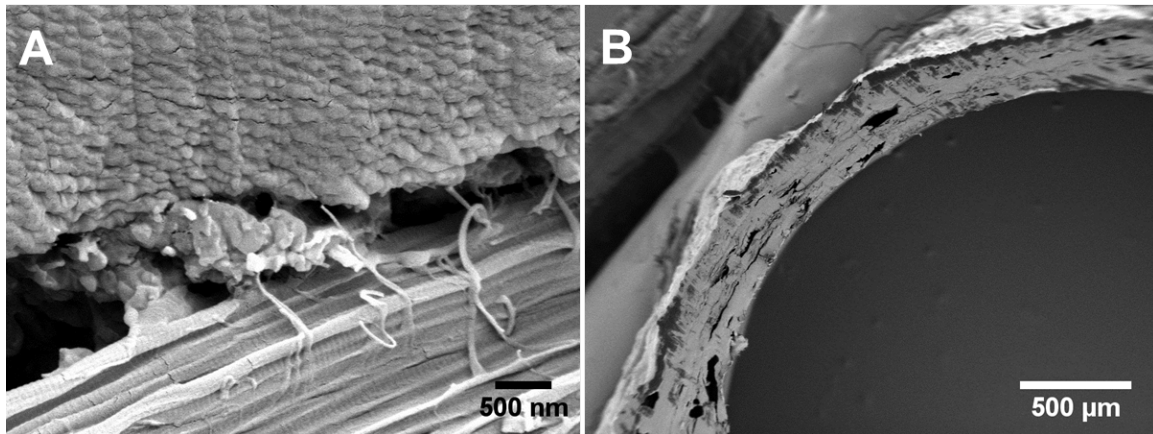
Figure 2.12: Electron micrographs that show: **A)** the intersection between two stacked sheets with collagen fibrils oriented 90° to each other and **B)** cross-section of a tubular conduit showing the multiple layers.

2.2.4 Crosslinking

The tendon sections will adhere to each other when dry; when rehydrated there is still some adhesion between the sheets, however they can be manually separated without too much force. The adhesion between the rehydrated sections may be a result of one of two things: 1) the reformation of some of the interfibrillar bonds that were interrupted in the sectioning process; 2) new crosslinks forming as a result of the drying process, similar to the crosslinks formed in dehydrothermal crosslinking. One way to ensure the adhesion as well as to tune the mechanical properties of the material is through crosslinking. There are three primary ways in which collagen can be crosslinked: chemical, enzymatic and physical methods.

Chemically creating crosslinks can be accomplished using glutaraldehyde (GA), carbodiimides, riboflavin, and dimethyl 3,3'-dithiobispropionimidate (DTBP), among other methods. Glutaraldehyde crosslinking occurs through the reaction of the aldehyde groups of the GA with the amine groups in the tendon[146,147] (simplified illustration in Figure 2.13A). GA has been used extensively in the biomedical field for crosslinking and

preparing decellularized extracellular matrices for implantation in several FDA approved products[148–150], however it is known to be cytotoxic[148,151]. It has been shown that this cytotoxicity can be reduced through treatment of the material with glutamic acid and prevented through the addition of insulin-like growth factor 1, *in vitro*[152]. Carbodiimide crosslinking uses 1-ethyl-3-(3-dimethylaminopropyl)carbodiimide hydrochloride (EDC), usually in conjunction with N-hydroxysulfosuccinimide (sulfo-NHS), creates a zero-order crosslink between amine and lysine groups found in the collagen. Unlike GA, EDC/NHS has been shown to not by cytotoxic once the crosslinking byproducts have been removed (i.e. urea derivatives)[153]. However, EDC/NHS is unable to for intramolecular crosslinks as it cannot form bonds between functional groups which are greater than 1nm apart[154], whereas GA can from crosslinks at greater distances[148], resulting in greater mechanical properties[155]. Greater details on additional chemical crosslinkers can be found in the appropriate literature[156–160].

Enzymatic and physical methods are less common than crosslinking via chemical methods; however they can still be accomplished. Physical crosslinking is accomplished through application of ultraviolet (UV) light irradiation, which bonds free radicals on aromatic amino acids[161,162], or dehydrothermal (DHT) treatment, which permanently affects the axial molecular packing of the collagen fibers[163]. Enzymatic crosslinking is done through use of transglutaminase[164,165].
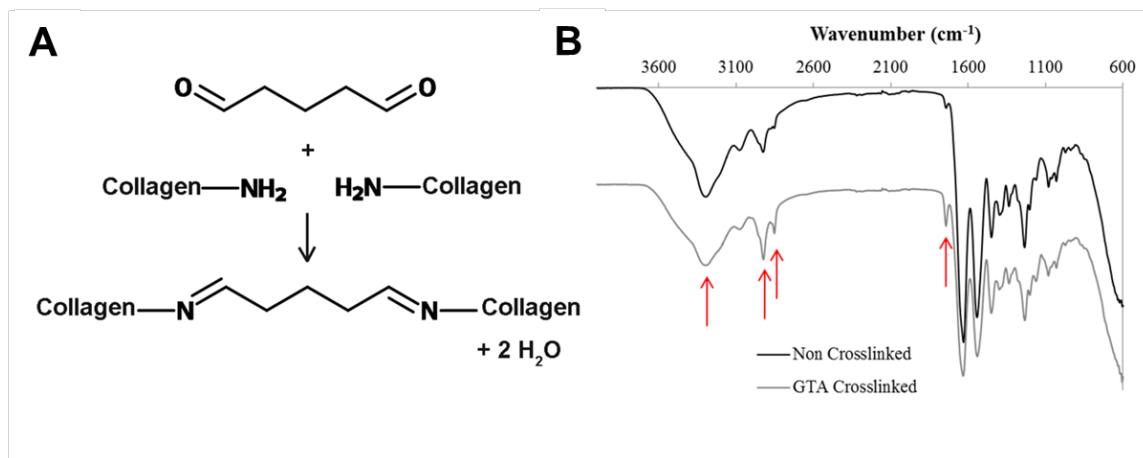
Figure 2.13: A) Illustration of a simplified mechanism of one type of GA crosslinking in collagen, **B)** FTIR spectrum of non-crosslinked and glutaraldehyde crosslinked tendon samples. Arrows from left to right in both plots are 3260cm-1 (secondary amine), 2915cm-1 and 2850cm-1 (methylene bridge), and 1700cm-1 (imine). From non-crosslinked to crosslinked the ratio of secondary amines to imine and methylene decreases showing the crosslinking of the secondary amines with glutaraldehyde.[166]

In this work, GA is primarily used, as preliminary results indicated GA-crosslinked tendon sections had good mechanical properties, possibly due to the fact that GA would better crosslink two adjacent sheets to each other due to its longer crosslinking ability compared to EDC/NHS.

The ability of GA to crosslink the Bioskiving samples was thoroughly investigated through mechanical analysis of samples crosslinked with different concentrations of GA for a constant time[166]. To confirm that GA-mediated crosslinks were actually forming, crosslinked and non-crosslinked tendon (NC) sections were observed via fourier transform infrared spectroscopy (FTIR) (Figure 2.13B). Non-crosslinked tendon samples displayed peaks at wavenumbers characteristic of tendon[167] (ex. amide peaks at 1630-1635cm-1) and once crosslinked, the expected peaks developed[168,169]. These include a decrease in the ratio of secondary amines at 3260cm-1 to imines at 1700cm-1 (1:0.48 [NC] compared to 1:0.51[GA]), and secondary amines and

methylene bridges at 2915cm-1 and 2850cm-1(1:0.58 [NC] compared to 1:0.87[GA]). These changes can be associated with the formation of a carbon-nitrogen double bond between the GA and an amine of the collagen molecules, and the addition of the methylene bridge of the GA, for the changes to amine to imine and amine to methylene bridges, respectively. Additionally, when the collagen blocks are crosslinked prior to being sectioned and stacked, the sections will not adhere to each other during the drying process. This may be due to the GA crosslinking residues that would have otherwise reformed crosslinks in the drying process.

2.3 SUMMARY

The sectioning-based fabrication technique, Bioskiving, was developed to utilize the intricate micro and nanostructures found in many natural biomaterials that often go unutilized — such as the nanotopography of the collagen fibers found in tendon, lost during solubilization. Bioskiving involves decellularizing a block of tendon, sectioning it using a microtome, and then stacking or rolling these sections into 2 or 3 dimensional scaffolds. Structures constructed from Bioskiving tendon sections would likely find use in biomedical applications including tissue engineering and regenerative medicine.

2.4 MATERIALS AND METHODS

2.4.1 Decellularization and sectioning

Frozen bovine Achilles tendon is cut into blocks ~20x20x2mm and placed into a decellularization solution containing 1% w/v sodium dodecyl sulfate (SDS) (Sigma, St. Louis, MO), 1mM Tris HCl, 0.1mM EDTA (Tris-EDTA pH 7.4, Sigma) in phosphate buffered saline (PBS), on a shaker at 4°C for 48h with the solution being changed after

24h. Following that, the blocks are rinsed in deionized water (diH2O) and placed back onto the shaker in diH2O for an additional 24h to remove residual SDS.

The decellularized 20x20x2mm blocks are frozen at-20°C and adhered to the sample holder in a cryomicrotome (CM1950, Leica Microsystems, Buffalo Grove, IL) with optimal cutting temperature (OCT) compound (Tissue-Tek® O.C.T. Compound, Sakura Finetek) Once frozen to the sample holder, the blocks are sectioned at 50μm thick with the blade oriented parallel to the fibers and cutting between the fibers (rather than cutting the ends off the fibers).

2.4.2 Stacking and rolling

The 50μm sections are stacked on a room temperature polytetrafluoroethylene (PTFE) block with fibers orientated in one of four orientations: 1) Parallel (0°) stacks had ten sections, all with the fibers oriented in parallel to each other. 2) Perpendicular (90°) stacks had ten sections with fiber direction alternating by 90° in adjacent stacks. This would result in stacks with 5 sheets in two directions orthogonal to each other. 3) A 45° rotation between 12 sections, resulting in four fiber orientations each with 3 sections. 4) A 30° rotation between 12 sections, resulting in 6 fiber orientations each with 2 sections. Note: the 90° and 0° stacks created for the 'stacking angle test' comprised 12 sheets each to keep them consistent with the 30° and 45° stacked sections. The stacked sections are then air dried overnight, rinsed three times with diH2O and left to dry overnight again on a PTFE block.

Tubular conduits were created by rolling individual 50μm sections around PTFE rods, or PTFE-coated wires of various diameters (500μm, 1.58mm, 3.175mm, 6.35mm) (McMaster-Carr, Robbinsville, NJ). An initial section was wrapped around the room temperature rod by touching one edge with the rod, allowing it to melt, and then rotating the rod causing the rest of the section to adhere and melt. An initial section was placed on

the rod with fibers oriented parallel to the axis of the rod; subsequent sections were either alternated by 90° creating axial and circumferential orientations, or 45° creating axial, circumferential and helical orientations. The sections were allowed to dry on the rod, rehydrated and gently rinsed in three changes of diH2O and again allowed to dry. Care was taken to keep the rods standing vertical until they were completely dry, as if they touch anything the tendon will stick and become deformed.

2.4.3 Crosslinking

Sections were crosslinked in glutaraldehyde (GA) by immersing the samples in the indicated concentration (0.1%, 0.5%, 1%, 2.5%) of glutaraldehyde (pH 7.4) for twenty minutes, followed by three rinses of diH2O and allowed to dry overnight.

2.4.4 SEM procedure

Samples were air dried overnight, further dehydrated in graded ethanol (70%, 2x 80%, 3x 90%, 3x 95%, 3x 100%) and finally dried with hexamethyldisilazane (Sigma). The samples were then sputter-coated with Pt:Pd 80:20 using a Cressington 208HR Sputter-coater (Cressington Scientific, Watford, Hertfordshire, UK) to a thickness of 3nm and imaged using a Zeiss Ultra-55 Scanning Electron Microscope (Zeiss, Oberkochen, Germany). Fiber and fibril size were measured by taking images of 3 locations on 4 different samples and measuring the fiber size using ImageJ (NIH).

2.4.5 Verification of cell removal

Sections were decellularize and sectioned using the previously described procedures, placed onto Superfrost Plus slides and dried overnight. They were then rinsed three times with diH2O and allowed to dry again. One drop of Fluoroshield mounting media with DAPI (Sigma) was placed onto a section, followed by a coverslip. The

sections were imaged using a fluorescence microscope (Leica) with appropriate excitation/emission filters for DAPI, and brightfield.

2.4.6 FTIR analysis

Analysis was conducted using an ATR-FTIR spectrophotometer (FT-IR 6000, Jasco, Easton, MD). Three samples each of 10-layer stacked sections, rinsed but non-crosslinked and 5% glutaraldehyde crosslinked samples were analyzed. The samples were scanned from 600cm^{-1} to 4000cm^{-1}.

Chapter 3.

Characterization of the Physical Properties of Scaffolds Created from Tendon-derived Sections

3.1 INTRODUCTION

Many biomedical applications that utilize scaffolds or structures for implantation require a material that can undergo substantial loading while also being biocompatible. For example, rotator cuff patches designed to repair the torn tendon require strengths of at least 230N[170] in order to provide mechanical augmentation and prevent suture pull through of the tendon, a common problem of current repair patches[171,172]. Tendon and ligament repair patches and devices must be able to withstand physiological loads upwards of 2000N in a tissue that has little to no self-repair capability[14,173] such as the anterior cruciate ligament. Similarly, blood vessel prostheses require high burst pressures capable of resisting natural physiological forces and specific moduli to match the native tissue's compliance. Currently there are a number of material options that support these high burst pressures, however, many are comprised of synthetic materials that are not biodegradable[34,174].

3.2 CHARACTERIZATION OF TENDON-DERIVED CONSTRUCTS

3.2.1 Tensile properties

As many potential biomedical applications would benefit from increased mechanical properties, methods of improving the mechanical strength, such as crosslinking, were investigated. Uniaxial tensile testing was performed in order to determine the effect of the GA crosslinking on the mechanical properties. The representative stress-strain curves and ultimate tensile strength and moduli values of samples crosslinked with varying GA concentrations are shown in Figure 3.1A-C and summarized in Table 3.1. These values indicate that crosslinking results in an increase in ultimate tensile strength (UTS), 20 times greater than non-crosslinked samples and a modulus nearly 50 times higher.

Sample Crosslinking Condition	Ultimate Tensile Strength (MPa)	Elastic Modulus (MPa)
0% - Non-crosslinked	0.63 ± 0.07	3.11 ± 1.35
0.1% Crosslinked	4.55 ± 0.34	48.17 ± 3.58
0.5% Crosslinked	11.25 ± 1.35	95.86 ± 16.1
1% Crosslinked	13.32 ±0.643	129.08±10.44
2.5% Crosslinked	13.59±1.35	145.54 ±18.72

Table 3.1: Ultimate tensile strength and elastic modulus values for samples crosslinked with various concentrations of glutaraldehyde[9].

Native tendon has much greater mechanical strength than this due to its hierarchical structure and fibril-fascicle-tendon structure that prevents the failure of the non-continuous uniform fibers from early failure. One hypothesis to explain the difference is that the sectioning process disrupts this macro-fascicular strengthening as discussed previously[175], and the decellularization may disrupt the proteoglycans that make up the non-collagenous matrix (NCM), and the crosslinks between the collagen fibrils and the NCM. This allows fracture between the fibers and the matrix, resulting in the failure.

Crosslinking with GA should re-introduce inter-collagen crosslinks between the collagen fibers, and possibly between proteoglycans and the collagen, if primary amine sites are available. A macroscopic view of the non-crosslinked sample failure can be seen in Figure 3.1D,E where large portions of the tendon-sections pull apart with a number of locations appearing to have multiple failure points along the direction of applied force. As expected, crosslinking with GA increases the mechanical strength, proportional to the amount of crosslinker, until the samples are saturated and maximally crosslinked. Figure 3.1F,G shows the macroscopic failure of maximally crosslinked samples, where the failure appears to be a complete transverse fracture across the width of the sample.

To confirm this observation at the micro-scale, the sections were imaged before and after failure with a scanning electron microscope. Prior to testing, the morphologies of both non-crosslinked (Figure 3.2A) and crosslinked (Figure 3.2B) appear to be identical, being primarily comprised of large sections of continuous, highly aligned collagen fibers. However, after testing, the failure point of the non-crosslinked sections (Figure 3.2C) appears to be relatively smooth, as if fibers pulled out from between each other, while the failure point of the crosslinked sections is jagged, like the fibers failed (Figure 3.2D).
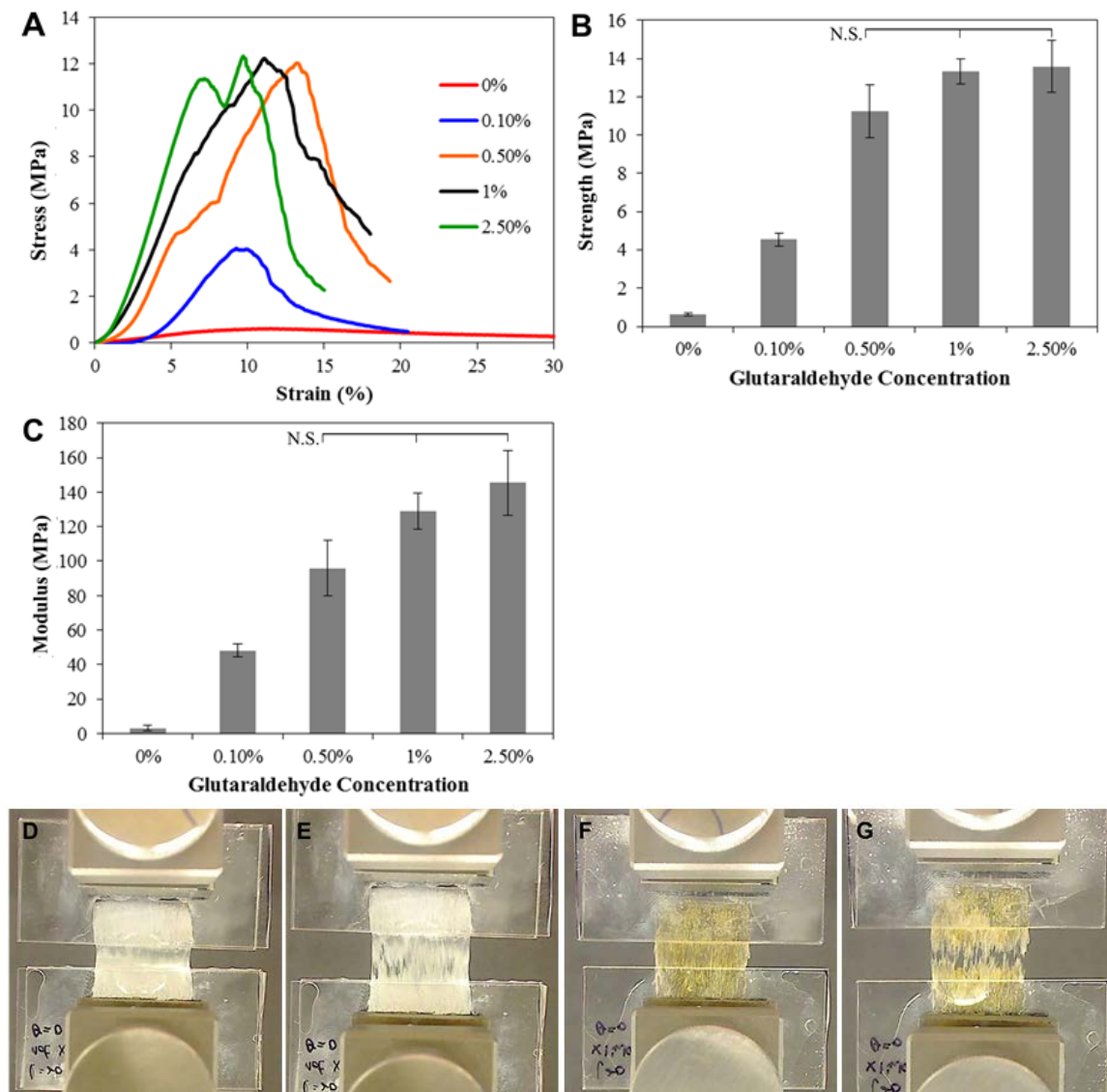
Figure 3.1: A) Representative stress strain curves of 10-layer (50μm thick each) stacked samples that have been crosslinked with various concentrations of glutaraldehyde (0.1,0.5, 1. 2.5%) for 20 min., or not crosslinked (0%). **B, C)** Graphs illustrating the ultimate tensile strength and elastic modulus, respectively, of crosslinked samples. **D)** photographs showing uniaxial tensile testing of noncrosslinked samples prior to testing and **E)** at failure. **F)** photographs showing uniaxial tensile testing of 2.5% glutaraldehyde-crosslinked samples prior to testing and **G)** at failure. Stress and modulus that are not statistically different are marked N.S.; all other comparisons p>0.05, (n=4) for all samples.[166]
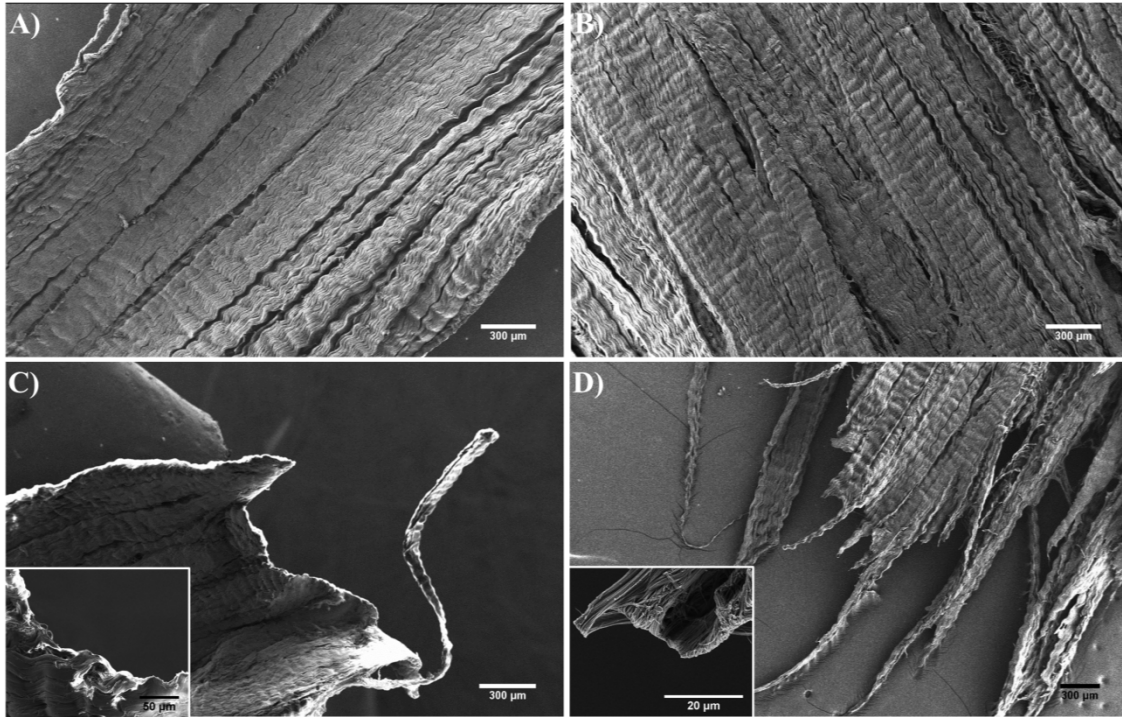
Figure 3.2: A,B) Scanning electron micrographs of a section of non-crosslinked and glutaraldehyde crosslinked tendon-stacks prior to testing, respectively. **C,D)** Scanning electron micrographs of a section of non-crosslinked and glutaraldehyde-crosslinked (2.5%, 30min) tendon-stacks prior to testing, and the failure-point following rupture under tension . All samples consist of 10 layers with a thickness of 50μm for each layer. All layers have their fiber orientation aligned in the same direction and were tested with the force applied in that direction.

This difference is a result of changes in the failure mechanism before and after crosslinking. In the non-crosslinked samples, there is little remaining crosslinking between fibers and matrix, which allows sliding of the collagen fibrils between each other as the fibrils are relatively short (5-20 mm[176,177]). This can be compared to the shear-lag model for failure of short-fibered composites developed by Cox[178], where stress is transferred from the matrix to the fibers by interfacial shear stress. However, with the reduction in the crosslinking between the NCM and the fibrils, the fibrils slip past each other slowly at much lower stresses, resulting in the ends of various fibers creating a relatively smooth edge. This is not observed in native tendon, as the tendon fascicles are believed to extend the length of the tendon[179] and could be considered 'continuous',

however due to their short length, collagen fibrils do not[176,180]. In the crosslinked samples, the interfacial shear stresses are much greater. At the point where the interfacial shear stresses exceed the tensile strength of the fibrils in the material, the mode of failure changes. The new failure method is rapid fracture of collagen fibrils at various points, resulting in the jagged appearance observed in Figure 3.2D. The inset figures for both samples make the failure more clear, where there are curled fibrils at the end of one 'bundle' of collagen fibrils on the non-crosslinked sample (Figure 3.2C inset), and a distinct edge at the edge of the end of a bundle of collagen fibrils in the crosslinked sample where the fracture propagated (Figure 3.2D inset).

The stacked sections show improved mechanical properties following crosslinking, however that is only when force is applied in the direction of the fibers. When force is applied in another direction, such as 45° or 90° to the fibers as shown in Figure 3.3A,B the ultimate tensile strength (Figure 3.3C) is greatly reduced as is the modulus (Figure 3.3D). The resulting ultimate tensile strength and elastic moduli values are summarized in Table 3.2.

Sample Orientation	Ultimate Tensile Strength (MPa)	Elastic Modulus (MPa)
0° rotation	10.84 ± 1.25	158.29 ± 21.11
45° rotation	3.90 ± 0.47	41.72 ± 8.83
90° rotation	1.17 ± 0.21	15.48 ± 5.28

Table 3.2: Ultimate tensile strength and elastic modulus values for samples with aligned fibers tested at the indicated angle to their fiber orientation

A 0° rotation yields the highest UTS with 10.84 ± 1.25MPa, while force applied at 45° and 0° resulted in UTS of 3.90 ± 0.47MPa and 1.17 ± 0.21 MPa. Similar results were seen with the moduli, where the samples tested at 0° had a modulus of 158.29 ± 21.11 MPa, 45° a modulus of 41.72 ± 8.83 MPa and 90° a modulus of 15.48 ± 5.28 MPa.

This is as expected as the force is no longer being applied to the fibers themselves, but rather the strength is dependent on the matrix. A similar phenomenon is

seen in many anisotropic materials, and one method to produce improved isotropic strength is to create laminar composite where the fiber orientation is rotated in adjacent sheets. Perhaps the most common example of this is the multilayer construction of plywood; however this technique is also used widely in the construction of other organic or metallic-fiber based materials[181]. Similar arrangements of varying fiber orientations can also be found in nature, such as the twisting arrangement of collagen fibril lamellae found in the remarkably tough scales of the Arapaima fish[182].
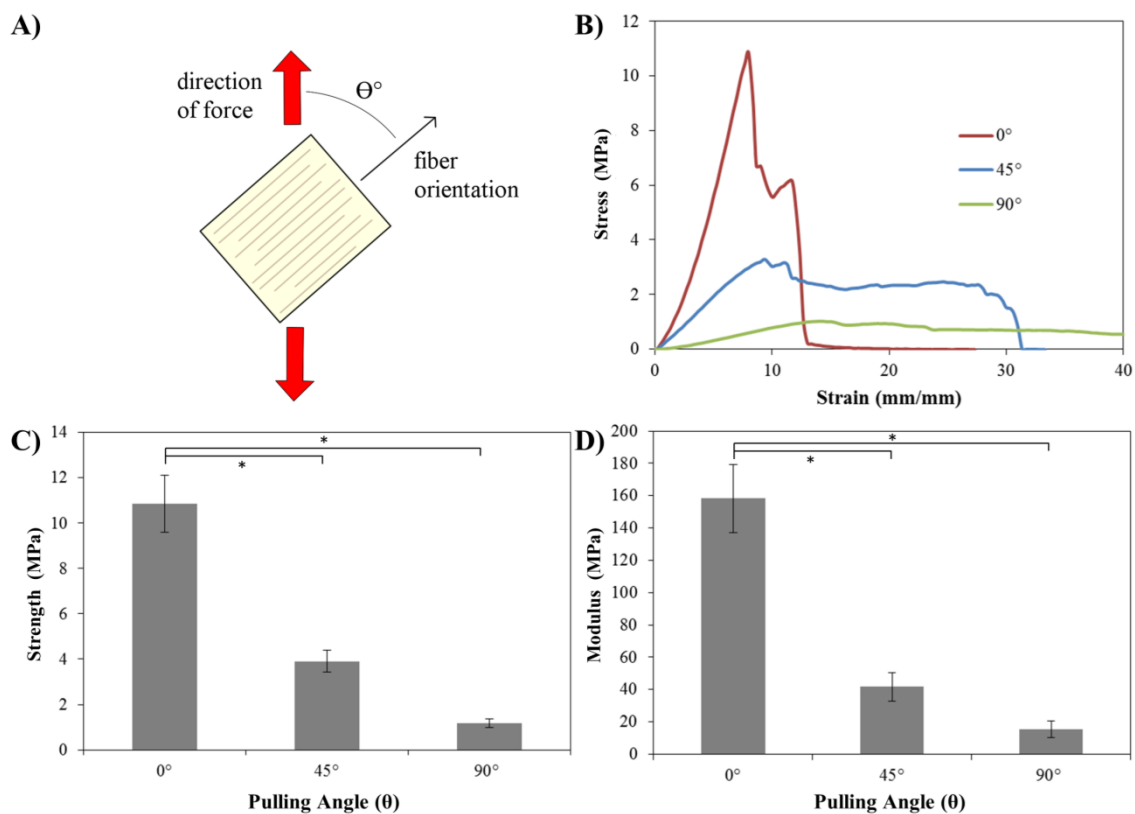
Figure 3.3: A) Schematic illustrating the nature of the uniaxial tensile test, where force is applied vertically (red arrows) and the tendon section samples are tested with fiber alignment in various directions. The samples were tested at angles (θ) of 0, 45 and 90°. All samples were 10 layers of 50µm each, crosslinked with glutaraldehyde in excess (5% for 30min). **B)** Representative stress-strain curves for samples tested at the various orientations. **C)** Graph illustrating the ultimate tensile strength of the samples tested in uniaxial tension at 0, 45 and 90°. **D)** Graph showing the elastic modulus as determined by linear regression of the samples tested at 0, 45 and 90°. Statistical differences marked with * ($p < 0.05$), (n=4) for all samples.

This laminar composite technique was also used with the tendon derived sheets, alternating the ply orientation by either: 0°, 30°, 45° or 90° (Figure 3.4A) in an effort to create a transversely isotropic material. Following stacking of the sections, the mechanical strength of each material was evaluated under uniaxial tension. While the material's strength was only evaluated in the primary direction, each direction of fiber orientation should have the same properties. The samples with no fiber rotation were expected to have the greatest mechanical strength as they contain 12 layers in the primary direction whereas the other sections have either 3 sections in each orientation (30° rotation), 4 sections (45° rotation) or 6 sections (90° rotation). The ultimate tensile strength and moduli values calculated for the various samples are summarized in Table 3.3.

Stacking Angle	Ultimate Tensile Strength (MPa)	Elastic Modulus (MPa)
0° rotation	10.84 ± 1.25	158.29 ± 21.11
30° rotation	6.34 ± 0.93	81.71 ± 13.1
45° rotation	8.25 ± 0.78	108.77 ± 10.6
90° rotation	4.71 ± 0.59	74.03 ± 16.21

Table 3.3: Ultimate tensile strength and moduli values for samples stacked at various angles

Interestingly, even with fewer sections completely in the direction of applied force, the 45° rotated samples were not statistically weaker than the 0° sections (Figure 3.4C) nor was the material any less elastic (Figure 3.4D). However, the 90° rotated sections were significantly weaker, despite a greater number of sections. Therefore, a 45° rotation of fiber orientation should be the optimal strategy for fabricating transversely isotropic materials from tendon-derived sections.
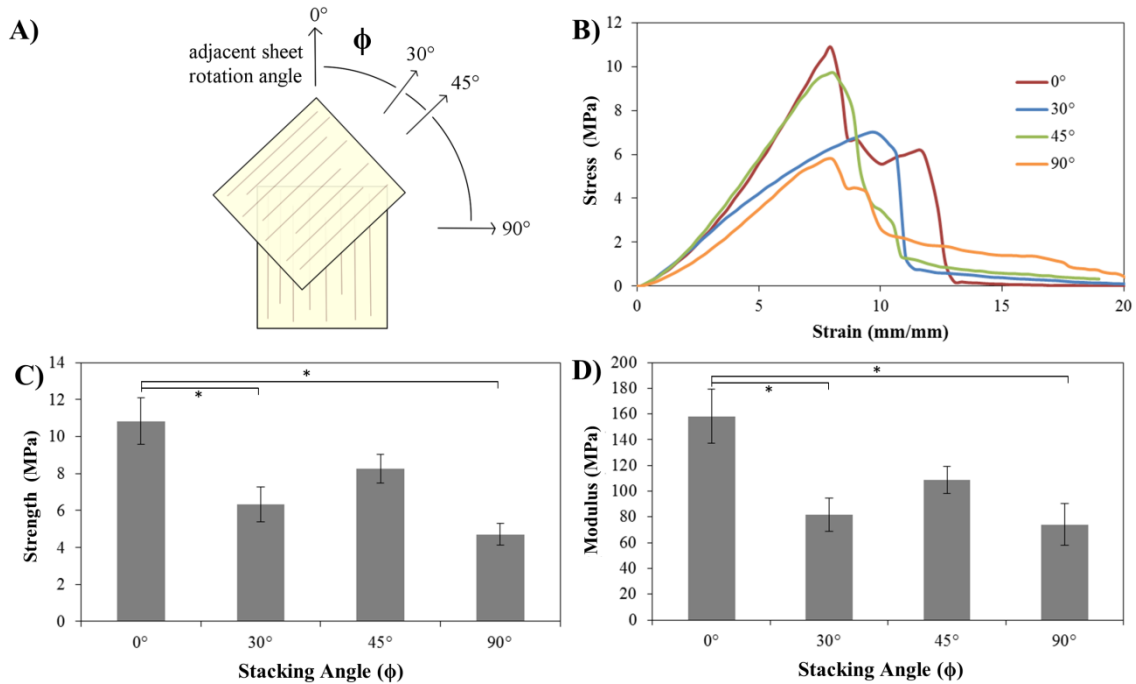
Figure 3.4: A) Schematic illustrating the stacking process. A single 50μm-thick section is placed at the 0° orientation and subsequent sections are stacked on top, rotated by either 0° (all aligned), 30°, 45° or 90° for a total of 12 layers. Each sample consisted of only one rotation angle and were subsequently crosslinked with glutaraldehyde (5%, 30min). The load during testing was applied in the direction of the first sheet. **B)** Representative stress-strain curves for samples tested at with the various rotation angles under uniaxial tension. **C)** Graph illustrating the ultimate tensile strength of the samples tested. **D)** Graph showing the elastic modulus as determined by linear regression of the samples tested at varying rotation angles. Statistical differences marked with * ($p > 0.05$), (n=4) for all samples.

One could also imagine that increasing the section thickness would provide this mechanical strength without the need for crosslinking; however, these thin sections are useful as substrates for cell-seeding and can be easily manipulated into complex geometries. Additionally, thick sections would still have the problem of anisotropic mechanical properties, and the fabrication of a laminar composite would be limited, as individual laminate thicknesses must remain small compared to other material dimensions[181,183].

3.2.2 Burst pressure

Many applications such as tissue engineered blood vessels require robust geometries in three-dimensions in addition to flat, two-dimensional structures. One example is a tubular structure comprised of multiple layers of fibers with varying orientations. These tubes may consist of sections that are oriented 90° to each other, where interior and exterior sections can be oriented to guide cell growth in the desired directions, while intermediate layers will provide strength and prevent suture pull-out. Alternatively, design cues can be taken from biology, where a the adventitia in blood vessels has circumferentially arranged collagen fibers, while the media has multiple layers helically in alternating, opposing directions[184]. Similarly, compliance should be considered for tubular structures as compliance mismatching in vessel replacement can lead to anastomotic intimal hyperplasia[185,186].
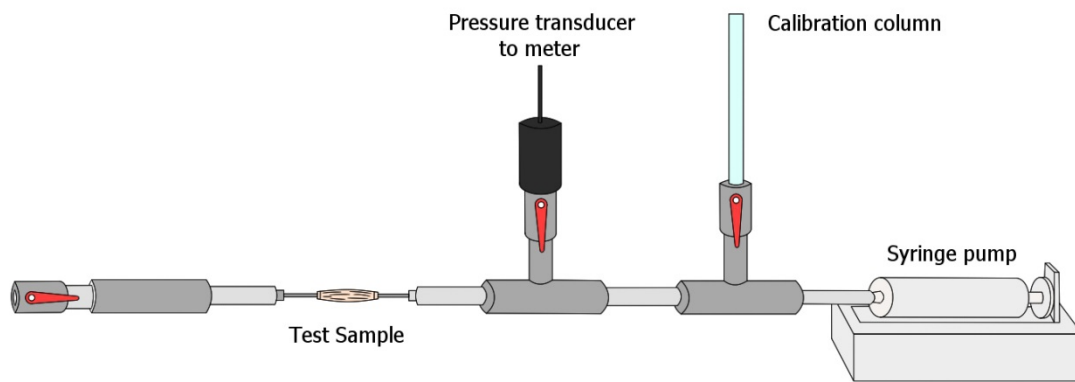
Figure 3.5: Schematic of the burst pressure device. A syringe pump increases pressure in a test sample as pressure is measured by a pressure transducer in parallel.

To test the properties of the tubular constructs, a burst pressure testing apparatus was developed that consisted of a series of rigid piping with an in-line mounted pressure transducer (Figure 3.5). At one end of the piping two luer-lock stubs are mounted where a tube can be mounted. The system can then be pressurized at a

constant rate using a syringe pump while the other end is closed with a valve. As the pressure in the tube increases the transducer will produce a digital readout on the meter, while a digital camera records the diameter of the tube as it expands.

The burst pressure of tubes in GA-crosslinked and non-crosslinked states was tested; all samples comprised 5 tendon sections that each wrapped around the template rod twice. Each sample was tested at a flow rate of 10ml/min until failure. Figure 3.6 shows representative images of failure, from which the diameter was calculated. The average maximum pressures and compliance are reported in Table 3.4.
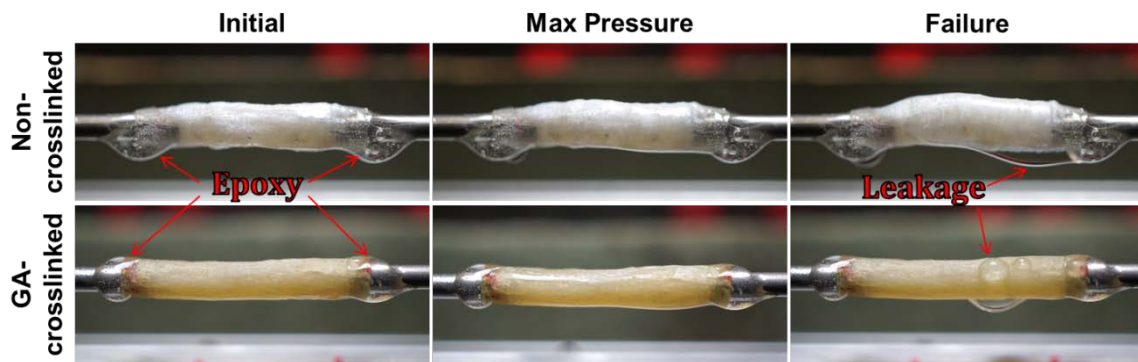
Figure 3.6: Sample burst pressure images showing tubular conduits prior to testing, at the maximum recorded pressure, and post failure. Epoxy used to seal tubes and leakage through sample is indicated.

The GA-crosslinked tubular conduits have a greater burst pressure, while the non-crosslinked conduits have the greatest degree of elasticity. For comparison, human external iliac artery are reported to have compliance of 8.0% per µmHg the compliance of and proximal human saphenous veins a compliance of 5.0% per µmHg [187]. Ideal burst pressures for vessel replacements would be 2000mmHg or greater (native saphenous veins burst = 1680mmHg[188]), however in most cases, as burst pressure increases compliance will decline. Following crosslinking, the conduits are able to achieve suitable pressures; however, their compliance is significantly lower than necessary.

	Burst Pressure (mmHg ± Standard Error)	Burst Diameter (Percent Increase ± Standard Error)
Non-crosslinked	236.34 ± 4.137	29.25±4.63
GA-crosslinked	2094.45 ± 168.59	6.63±1.56

Table 3.4: Burst pressure and compliance values for tubular conduits

3.2.3 Tendon-section permeability

Permeability of a construct material to various biological components may be of concern for a number of potential applications such as the development of a nerve guidance conduit, or an entirely tissue engineered construct in order to reduce the distance of necrotic core formation. Ideally, a material would be highly permeable to dissolved gasses such as oxygen, and small molecules required for cellular function, like glucose. Permeability of these compounds would not only mean that nutrients could get into the scaffold, but also that waste products could exit the scaffold. Permeability of larger molecules such as proteins through a scaffold may be desirable depending on the application. In the example of a nerve guidance conduit, entrapment of growth factors and cytokines released from the damaged nerve stump would be considered a positive. For a tissue engineered construct, delivery of growth factors would require permeability of the scaffold to proteins.

In order to elucidate the permeability characteristics of decellularized tendon sections, the diffusion of three biological relevant molecules was assayed. Oxygen (O_2), glucose, and bovine serum albumin (BSA) were selected as they represent three classes of compounds with different sizes that could be relevant to this material. The effective diameters of O_2, glucose and BSA are 31.99Da, 180Da, and 66.5kDa, respectively. The diffusion of each of these compounds was measured using a custom-made two chambered setup that was constantly stirred and kept at 37°C. A membrane comprised of

10 sections, each 50μm thick, was placed between the two chambers and one chamber loaded with the compound of interest, the donor chamber, and the other chamber acting as the receptor chamber. The effect of the orientation of the fibers and the presence of GA crosslinking on the effective diffusion coefficients was measured. Diffusion coefficients for each compound in each condition were calculated using an equation derived from Fick's law:

$$D't = \ln\left(\left(\frac{C_D - C_R}{C_D - C_{R0}}\right)\left(\frac{1}{-\beta}\right)\right) \text{ where } \beta = \frac{A}{z}\left(\frac{1}{V_R}\right)$$

Where: t = time, C_D and C_R = concentration in the diffusion and receptor chambers, respectively and R_0 at time zero; A = area of the membrane, z = membrane thickness V_R = volume of receptor chamber[189].

The following facts were assumed: 1) the solutions in each chamber were well-mixed; 2) no consumption of our compound of interest occurred (e.g. bacteria); 3) concentration across our samples was linear and at steady state[189]. Table 3.5 shows the calculated effective diffusion coefficients.

The effective diffusion coefficients for oxygen are within a reasonable range, slightly higher than published values (2.43x10^{-6} to 6.61x10^{-6} cm^2/sec) for similar extracellular matrix scaffolds such as decellularized small intestine submucosa[189]. Crosslinking appears to have a large effect on the diffusion of oxygen, despite the molecule having such a small size. Interestingly, the orientation of the fibers does not affect the diffusion coefficient in non-crosslinked samples however it does in the GA-treated samples. This is likely a result of packing density of the collagen fibers/fibrils; when all of the fibers are aligned parallel, peaks and valleys of collagen in adjacent sections can fit together; however, other physical factors such as water content or charge interactions may also influence the diffusion rates. Samples with perpendicularly oriented fibers may have less cohesive packing between sheets resulting in pores or voids the

oxygen can travel through. Fiber orientation likely doesn't have an effect on the non-crosslinked samples as all of the fibers will be loosely packed already.

Sample Orientation	O$_2$ Diffusion Coefficient (cm^2/sec $\pm$ *standard error*)	Glucose Diffusion Coefficient (cm^2/sec $\pm$ *standard error*)	BSA Diffusion Coefficient (cm^2/sec $\pm$ *standard error*)
Parallel fibers (NC)	1.84×10^{-4} $\pm\ 6.11\times10^{-5}$	3.13×10^{-6} $\pm\ 3.82\times10^{-7}$	1.12×10^{-7} $\pm\ 2.84\times10^{-8}$
Perpendicular fibers (NC)	1.86×10^{-4} $\pm\ 5.39\times10^{-5}$	4.82×10^{-6} $\pm\ 2.11\times10^{-6}$	2.48×10^{-7} $\pm\ 4.03\times10^{-8}$
Parallel fibers (GA)	$2.44\mathrm{x}10^{-5}$ $\pm\ 7.75\times10^{-6}$	1.87×10^{-6} $\pm\ 1.43\times10^{-7}$	7.57×10^{-7} $\pm\ 3.00\times10^{-9}$
Perpendicular fibers (GA)	1.06×10^{-4} $\pm\ 3.58\times10^{-5}$	2.90×10^{-6} $\pm\ 1.01\times10^{-7}$	8.54×10^{-8} $\pm\ 5.04\times10^{-9}$

Table 3.5: Effective diffusion coefficients for oxygen (O$_2$), glucose, and bovine serum albumin (BSA) through tendon sections. (NC – non-crosslinked, GA – glutaraldehyde crosslinked).

Similar trends can be seen in the diffusion of BSA, glucose, oxygen, and where greater diffusion is seen through the perpendicular fibers compared to the parallel fibers, and greater diffusion in non-crosslinked samples compared to GA-crosslinked samples. The difference in diffusion rate between oxygen and glucose and between glucose and BSA was approximately two orders of magnitude, which is reasonable due to the increasing size of each molecule. Additionally, the diffusion of BSA may have been reduced due to the possible adhesion of BSA onto the collagen fibers.

Overall, the permeability characteristics of these three biologically relevant molecules can be used to make educated decisions when designing tissue engineered scaffolds from this material, or other biomedical applications. The fiber orientation and degree of crosslinking for such applications are likely to be chosen based on the

mechanical properties; however these data will help allow predictions of how cells might survive, whether they will receive externally delivered growth factors, and the sorts of microenvironments that might develop with culture or growth.

3.3 SUMMARY

Two- and three-dimensional scaffolds created from tendon via Bioskiving, are unique in that they maintain the native conformation of collagen in tendon. The properties of this material were measured, and tuned through crosslinking, and made transversely isotropic through selective orientation of the fiber direction in adjacent sheets during fabrication. These methods were used to fabricate a robust material with differing methods of failure once crosslinked. Tubular constructs were also made, with burst pressures in the range required for biomedical applications like blood vessel replacement. Structures constructed from Bioskiving tendon sections have applications involving cell growth, and as such, the diffusion of three biologically relevant molecules through the material was measured.

3.4 METHODS AND MATERIALS

3.4.1 Crosslink density mechanical testing

Sections (50μm thick) were stacked as described in Chapter 2.4.2, in 10 layers with all fiber directions oriented parallel to each other. The sections were then crosslinked for 20 min at glutaraldehyde concentrations of 0.1%, 0.5%, 1% and 2.5%, (pH 7.4 in PBS) or not crosslinked. Each sample was then glued between two acrylic plates using super glue, rehydrated, and tested under uniaxial tension at a strain rate of 2mm/min on a mechanical testing apparatus (Instron, Norwood, MA) with a 1000N load cell until failure.

3.4.2 Pulling angle mechanical testing

Sections (50μm thick) were stacked as described in Chapter 2.4.2 in 10 layers with all fiber directions oriented parallel to each other. The sections were then crosslinked with 5% glutaraldehyde for 30min. Each stack was then tested in one of three orientations: fibers in line with the direction of the force ($\theta = 0°$), fibers oriented at an angle to the applied force ($\theta = 45°$), or with fibers perpendicular to the direction of applied force ($\theta = 90°$).

3.4.3 Stacking angle mechanical testing

Sections (50μm thick) were stacked as described in Chapter 2.4.2 in 12 layers during fabrication with alternating fiber orientations. Following the first section, each subsequent section was rotated either: 0°, 30°, 45°, or 90°. This pattern was repeated until all 12 sections had been placed with the degree of rotation remaining constant within a single sample.

3.4.4 Burst pressure device fabrication

Designs for a burst pressure device were modified from Gray et al.[190] All parts were purchased from McMaster-Carr unless otherwise noted. PVC tubing (1/4" ID, 3/8" OD, 1/16" Wall Thickness) was mounted to 1" solid aluminum T-slotted framing using 3/8" loop clamps. Nylon Luer-lock couplings were used to mount 16G stainless steel dispensing needles to hold the tubular conduits. Miniature 1/4" ball valves were used to regulate flow from a single syringe pump (NE-1000, New Era Pump Systems Inc., Farmingdale, NY). Pressure was measured using a gage pressure transducer with a 0-100Psi range (PX26-100GV, Omega, Stamford, CT) coupled to a voltage meter (DP25B-S, Omega). Samples were secured to the dispensing needles using Loctite general epoxy.

Sample diameter was recorded using a Sony α6000 camera with a SEL30M35 30mm F3.5 macro lens (Sony).

3.4.5 Burst pressure measurement

Tubular samples (non-crosslinked and 2.5% 20min GA crosslinked) were mounted to the dispensing needles using epoxy. The epoxy was allowed to cure for 1h and the samples rehydrated using diH2O. The syringe pump was set to a flow rate of 10ml/min, the system cleared of air, and the exit flow shut off. The samples were tested until failure while being imaged.

3.4.6 Burst compliance measurement

Frames of the initial and final diameter were extracted from video recordings of the tested tubes. The diameter was calculated using ImageJ between still images from before testing and at failure.

3.4.7 Permeability testing

Permeability of the tendon samples was measured by placing a sample (0°, 90° fiber orientations, non-crosslinked and 2.5% 20min GA-crosslinked) between two chambers each with a volume of 15ml. The chambers were kept at 37°C, filled with PBS and constantly stirred with bar magnets on a magnetic stir plate. The solute being measured was placed in a 'donor' chamber and the measurement samples taken from an 'acceptor' chamber. Effective diffusivity (D') was then calculated using the following formula:

$$D't = \ln\left(\left(\frac{C_D - C_R}{C_D - C_{R0}}\right)\left(\frac{1}{-\beta}\right)\right) \text{ where } \beta = \frac{A}{z}\left(\frac{1}{V_R}\right)$$

Where: t = time, C_D and C_R = concentration in the diffusion and receptor chambers, respectively and R_0 at time zero; A = area of the membrane, z = membrane thickness V_R = volume of receptor chamber[189].

3.4.8 Permeability measurements

Oxygen diffusion was measured using a PreSens Oxygen Microsensor Probe (PreSens, Regensburg, Germany). The probe was calibrated using a 100% humidified chamber and a 1% w/v sodium sulfite solution. The acceptor chamber of the diffusion device was bubbled with N_2 gas for 20min or until the oxygen probe measured 0% oxygen saturation. At the start of the test the donor chamber was bubbled with atmospheric air. Oxygen saturation was recorded electronically every 30s for 300min.

Glucose permeability was measured using a 5mg/ml solution in the donor chamber and measured using a Glucose (HK) Assay Kit (Sigma) following the manufactures instructions, with all volumes scaled by 1/10. Samples were taken every 30min for 8h. BSA permeability was assessed using a 10mg/ml solution and samples taken at 0, 1, 4, 8, 24, 32, and 48 h, and BSA concentration measured using a Pierce BCA Protein Assay Kit (Life Technologies, Grand Island, NY).

3.4.9 Mechanical and statistical analysis

Ultimate tensile strength (UTS) was determined as the maximum stress of each sample's stress-strain curve. The elastic modulus was calculated via linear regression of the slope of the stress-strain curve. All values reported as mean ± standard error and a sample size of n=4 was used for all conditions. Differences in UTS and modulus were analyzed by analysis of variance (ANOVA) with post hoc Tukey's testing using IBM SPSS software (IBM, Armonk, NY).

Chapter 4.

Biocompatibility and *in Vivo* Response

4.1 INTRODUCTION

The behavior of a material in the body following implantation can be crucial to determining whether a tissue engineered construct will be successful, both in terms of how the material breaks down, and how the body reacts to the material's presence in the first place. These two points are one of the reasons why natural polymers are often used for biomedical and tissue engineering applications.

The biodegradation of a material is important when considering its use. For many tissue engineering applications, the breakdown of the scaffold and regrowth of host tissue is the ideal case, and ideally the degradation rate of the material will be tuned to match the regrowth[15]. Even more traditional biomedical-oriented applications, such as joint replacement where a non-degradable metallic scaffold is implanted, could be of benefit from a degradable scaffold. For example, a scaffold that promoted bone or cartilage regrowth and provided suitable mechanical properties could prevent the need for revisionary surgeries common to joint replacements[191].

Collagen is typically degraded *in vivo* through proteolytic activity, particularly via MMP-1 (collagenase) activity[192]. The degradation and clearance of implanted ECM materials typically occurs very rapidly following implantation[193], thus many collagen-based biomaterials are crosslinked prior to use. Crosslinking has been shown to reduce

the degradation of collagen[194,195], as well as to reduce any potential immune response that the collagen may elicit through masking of potential antigenic markers[196].

Prevention of premature degradation is important for the tendon-derived scaffolds as one of the major features of the fabrication technique is maintenance of the highly aligned collagen fibrils and fibers which have the potential to guide cellular growth. If degradation were to occur too rapidly, prior to adequate cell growth and infiltration, these structures would not be able to provide their nanotopographical growth guidance cues.

4.2 TENDON-DERIVED SECTION DEGRADATION *IN VITRO*

Due to these concerns, the degradation characteristics of the tendon-derived material were assayed. An initial analysis into the degradation rate was conducted on decellularized tendon sections after various degrees of crosslinking, via degradation with bacterial collagenase. One concern regarding bacterial collagenase is that *Clostridium histolyticum* collagenase has been shown to cleave collagen into several small fragments[197], whereas mammalian collagenase cleaves it into only two[198]. However, degradation *in vitro* using bacterial collagenase has been shown to correlate well with *in vivo* degradation, despite the differences in the cleavage mechanism[199]. Therefore, *in vitro* analysis can be used as a preliminary mechanism for determining degradative behavior[200].

4.2.1 Collagenase degradation

Samples for *in vitro* degradation were created by stacking 10, 50μm sheets with a 90° rotation in fiber orientation. These sheets were then crosslinked using either 2.5% GA for 1h, 2.5% GA for 20min, 0.625% GA for 20min, or left untreated. The samples were then dried overnight in a vacuum desiccator, and trimmed into rectangular strips roughly 15mm x 5mm weighing ~10mg, with the exact weight being recorded before

being placed into a solution containing 10U collagenase/mg of sample. Removal, rinsing and subsequent drying showed the amount of mass lost after various times of incubation (Figure 4.1).

As expected, glutaraldehyde reduces the degradability of the collagen sections. Variations in the crosslinking density and type of crosslinker used also have an impact on how much weight is lost per sample, with highly crosslinked (2.5% GA for 1h) only losing 1.9% after 96h, moderate crosslinking (2.5% GA for 20min) losing 2.1%, and low crosslinked (0.625% GA for 20min) samples losing 4.3% of their initial weight, while non-crosslinked samples lost 33.5% of their initial weight. The collagenase in solution was not replenished during the degradation experiments, which may have led to reduced activity over time; however, the continued degradation of the non-crosslinked sample indicates that some enzymatic activity remained.
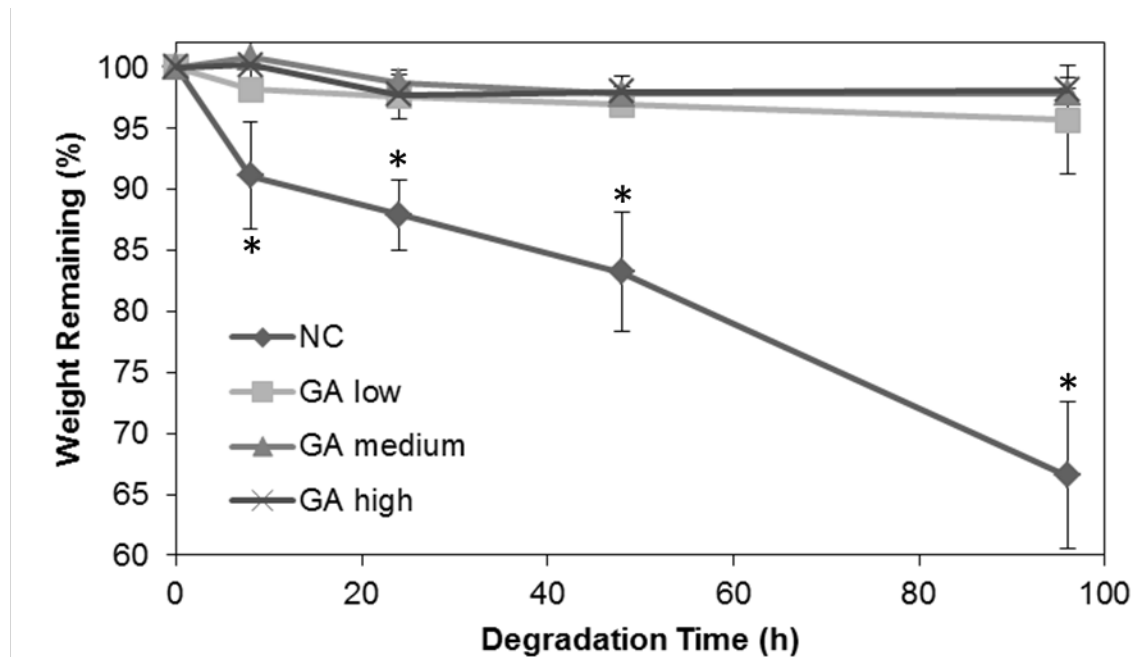
Figure 4.1: Mass remaining in Bioskiving scaffolds following bacterial collagenase degradation. (n=4) * = P-value < 0.05.

4.2.2 Mechanical properties

Loss of mass indicates that there are sections of collagen that are being removed from the sample, however crosslinked samples may have collagen fibrils that are cleaved yet remain attached to the scaffold via crosslinks. This would not affect the weight; however it could have a substantial impact on the mechanical properties. Mechanical analysis showed this to be a likely scenario as the ultimate tensile strength of GA-crosslinked samples was significantly reduced following extended periods of collagenase degradation (Figure 4.2). The ultimate tensile strength of maximally crosslinked GA scaffolds reduced by nearly half of the initial value following 96 h of degradation, whereas the already low mechanical properties of the non-crosslinked samples reduced further, much more rapidly. Interestingly, a significant difference in tensile strength was observed for all GA-crosslinked samples despite only a minimal change in sample weight. Maintenance of mechanical properties following degradation would be an important factor to consider, specifically for load-bearing applications like tendon or ligament repair.
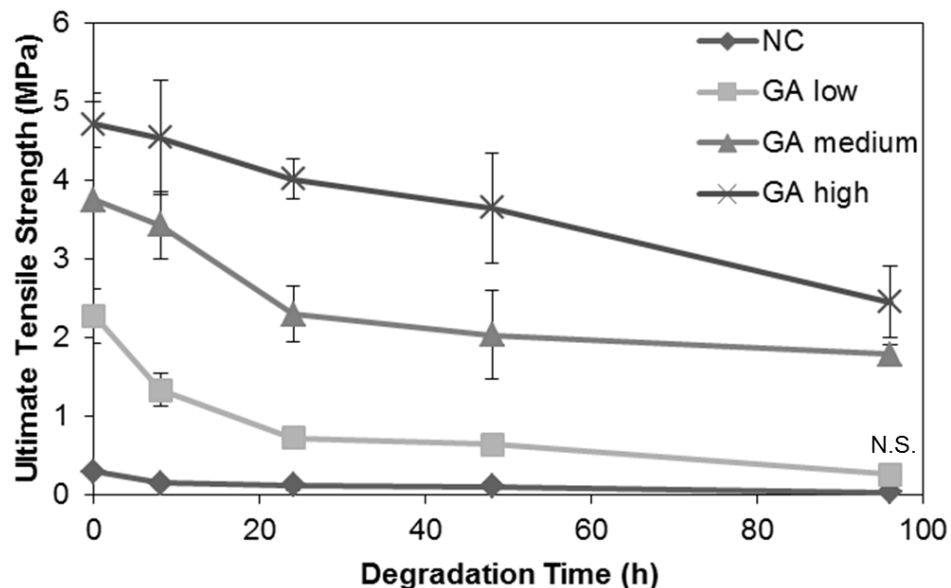
Figure 4.2: Ultimate tensile strength of Bioskiving scaffolds following bacterial collagenase degradation. (n=4) All values statistically significant (P-value < 0.05) except GA low vs NC at 96h indicated N.S.

4.2.3 Fiber morphology

As growth guidance cues are an important aspect of this material, maintenance of fiber morphology will be important to consider. SEM analysis of samples can indicate the status of the fibers following collagenase degradation. Figure 4.3 shows the morphology of samples prior to crosslinking, and after 24 and 96 h of crosslinking.

Fiber structure can clearly be seen in the non-crosslinked samples, and the maximally crosslinked samples (i.e. 2.5% GA for 1 h). After 24 h, most of the surface structure in the non-crosslinked samples is gone while after 96 h, the surface is largely flat with little to no definition. The GA-crosslinked samples however retain well-defined fiber structures for 24 h, along with some fiber structure after 96 h. The fibers in the GA-crosslinked samples after 96 h have been degraded to some degree, appearing similar to the fibers in the non-crosslinked 24 h samples. Some peaks and valleys are still observable, as are more macroscopic aligned topographies. The remaining ability of these features to guide cell growth, however, would have to be evaluated independently.

The rapid loss of the collagen fiber structure in the non-crosslinked samples compared to the GA-crosslinked samples verifies the results of the previous experiments. All three experiments indicate that a scaffold designed to influence cell growth for prolonged periods of time may require some degree of crosslinking to retain this ability. The results presented here indicate that loss of fiber structure occurs rapidly; however, *in vivo* it is likely that numerous cells will interact with these features prior to their degradation. These cells themselves may become aligned, which could further act as a template for cell alignment, providing topographical cues beyond the life of the scaffold. For example, this type of secondary alignment guidance has been demonstrated with neurons following morphologies based on a Schwann cell template[201].
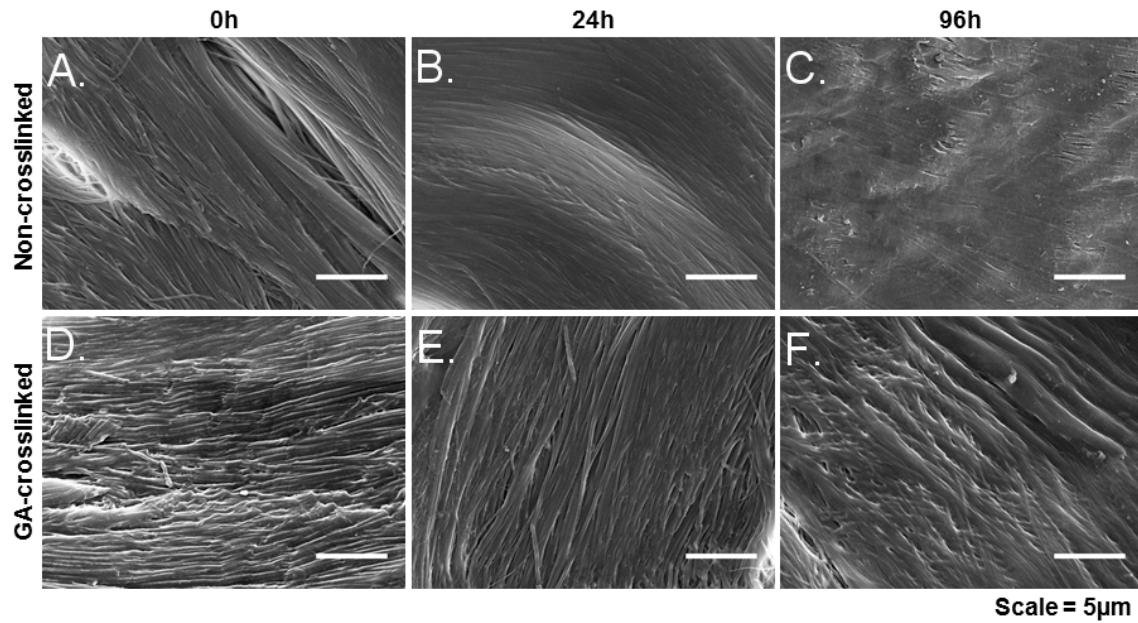
Figure 4.3: Scanning electron micrographs of: **A)** non-crosslinked samples prior to collagenase degradation, **B)** after 24 h, **C)** after 96 h and **D)** GA-crosslinked samples prior to degradation, **E)** after 24 h, **F)** after 96 h.

4.3 HEMOCOMPATIBILITY OF THE TENDON-DERIVED SECTIONS

Collagen has been used in numerous biomedical applications; however one of its limitations is its propensity to induce blood clotting, one of collagen's physiological roles. Blood vessel walls comprise a large percentage of collagen fibers; if there is damage to the endothelial layer lining the lumen of a blood vessel, the collagen is exposed to platelets and other plasma proteins which induce platelet aggregation, activation and formation of thrombi. This could be particularly detrimental for a tissue engineering application where platelets are likely to encounter the material (e.g. a vascular graft or tissue engineered blood vessel).

Platelets are believed to interact with collagen through several receptors: integrin α2β1, specific for certain amino acid residues in the α1 chain of collagen[202], glycoprotein VI[203], which likely interacts via glycine-proline-hydroxyproline motifs[204], and

glycoprotein Ib and integrin αIIbβ3, which interact with collagen indirectly through von Willebrand factor (vWF)[205,206]. Integrin α2β1 is directly involved in platelet adherence to collagen, while glycoprotein VI activates platelets. Glycoprotein Ib and integrin αIIbβ3 on the other hand are important for vWF-mediated adhesion in high shear situations such as those found in small diameter arteries and arterioles[205].

4.3.1 Heparin conjugation

The multiplicity of ways through which platelets bind to collagen and activate presents a large challenge to finding a method of making collagen hemocompatible. One method that has been reported for collagen is through the covalent conjugation of heparin[207,208], a process that has reported both decreased adhesion and activation[209], and contradictorily, increased adhesion[210]. Commonly, EDC/NHS is used to crosslink the carboxylic acid groups of the heparin to the free primary amine groups in the tendon.
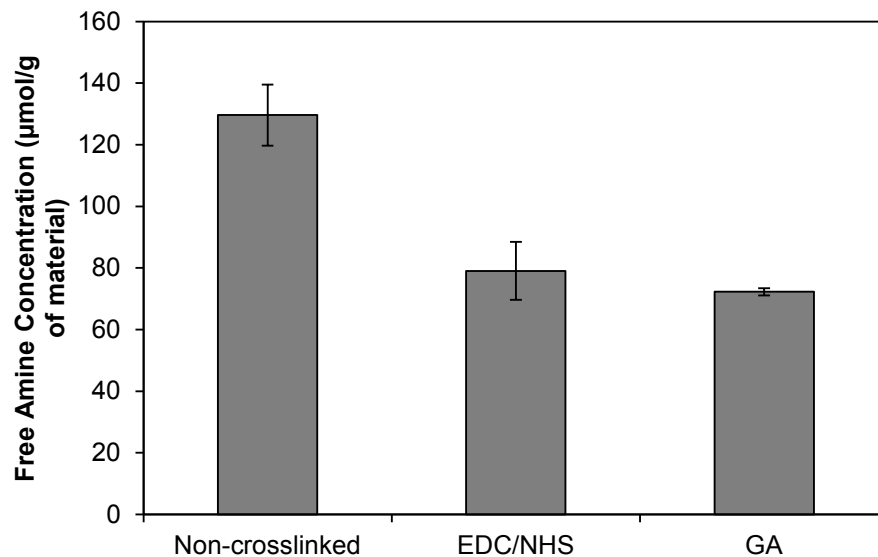
Figure 4.4: Free primary amine content in non-crosslinked and crosslinked Bioskiving samples as measured using trinitrobenzene sulfonate.

In order to determine the potential heparin binding to the tendon sections, the free primary amine content of the material needed to be measured. To do this, the number of free primary amine was measured using trinitrobenzene sulfonate (TNBS). The results (Figure 4.4) indicate that non-crosslinked tendon contains 129.6μmol free primary amine/g of material, while samples that were crosslinked with EDC/NHS or GA in excess contain 79.0 and 72.3μmol/g of material, respectively.

Collagen has a theoretical value of 151μmol free amine/g[207], close to the 129.6umol/g calculated here. The difference is likely due to the fact that tendon is not 100% collagen. Based on these values, the tendon used here is approximately 86.1% collagen, nearly the reported fat-free dry weight content of tendon (86%)[172,211]. Using the difference between the non-crosslinked and EDC/NHS-crosslinked sections, the number of EDC-crosslinkable amine sites can be calculated: 50.6μmol/g. With this value, and previously reported optimal heparin/EDC/NHS crosslinking ratios (1:0.4:0.24 Hep-COOH:EDC:NHS)[207], heparin can be immobilized to the surface of the tendon. Successful heparin conjugation was verified with using toluidine blue[212], which adheres and stacks in contact with polysaccharides, like heparin, producing a colorimetric change from blue to purple[213] (Figure 4.5). The heparin-conjugated samples had an increase in purple color, however samples that did not contain heparin also had some purple staining, which makes direct quantification challenging. This is likely due to the toluidine blue binding to endogenous GAGs present in the tendon[38].
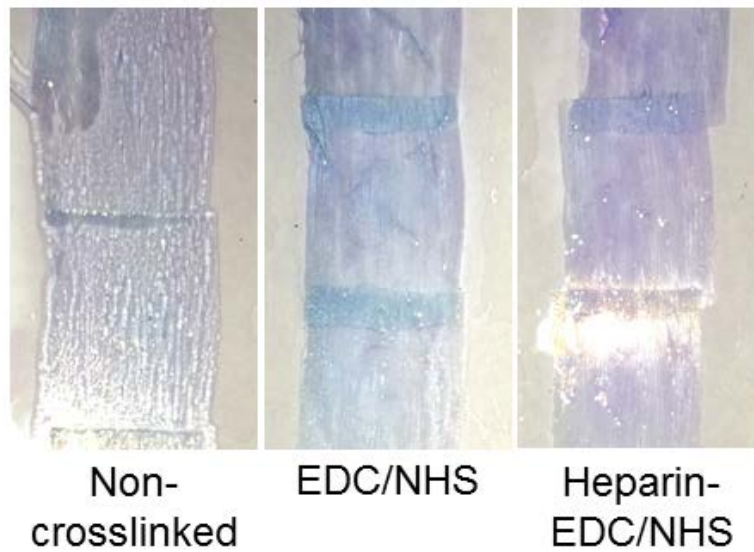
Figure 4.5: Toluidine blue-stained tendon sections, crosslinked with EDC/NHS with or without heparin. Purple indicates binding.

4.3.2 Platelet adhesion and activation

Following the conjugation of heparin to single sections of the tendon-derived collagen, the adherence and activation of platelets was tested statically by applying platelet rich plasma (PRP) containing freshly-isolated human platelets to samples in a 24 well plate. SEM analysis of the samples (Figure 4.6) revealed differences between the samples. On non-crosslinked and EDC/NHS crosslinked tendon samples platelets appeared to have a spread, branching morphology, characteristic of activated platelets. The total number of platelets also appeared to be slightly less on the crosslinked samples, however this was not quantified. On the heparin conjugated samples, a much larger number of platelets appeared to be adherent, however they appeared rounded, indicating an inactivated state. This is likely due to the different pathways through which platelets adhere to a surface and how they are activated, and that heparin acts as an anticoagulant through thrombin[214] inhibition. In fact, the larger number of platelets adherent on the

heparin-conjugated sample may be due to plasma vWF binding to the heparin and mediating the adhesion[215,216].
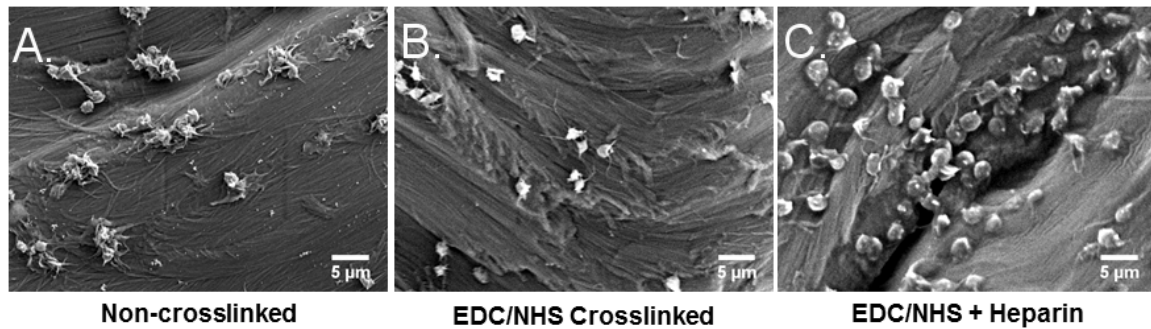
Figure 4.6: Representative electron micrographs of platelets following a static test on **A)** non-crosslinked tendon sections, **B)** EDC/NHS-crosslinked sections, C) heparin-conjugated tendon sections.

The preceding results were from static administration of platelets, which may not accurately reproduce flow and shear stresses observed *in vivo*. To better reproduce these conditions, a microfluidic flow chamber capable of being placed over a tendon section on a glass slide was fabricated (Figure 4.7). A syringe pump connected to the chamber allowed for adjusting flow rates to approximate shear stresses platelets may experience *in vivo* ($\sim$2.3dyn/cm^2 at 1ml/min). All sample analysis was conducted with the collagen fibers oriented parallel to the direction of flow, as flow parallel to submicron fibers has been shown to reduce thrombogenicity on its own[217].
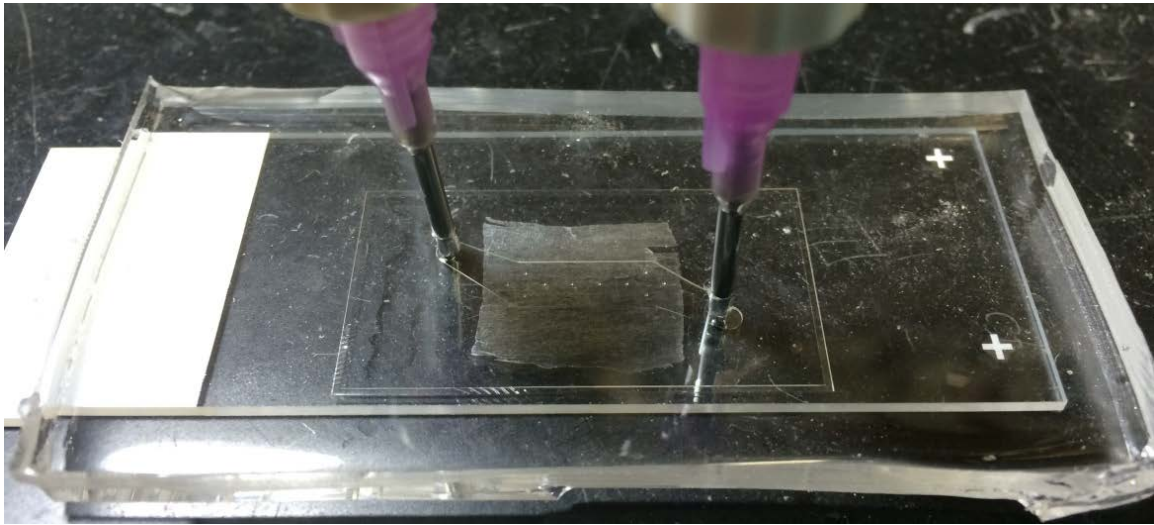
Figure 4.7: Microfluidic flow chamber used to flow platelets over a tendon section at physiologically relevant flow rates.

Samples treated using the same conditions as in static flow were placed into the chamber and platelets (1×10^5 platelets/ml) flowed through the chamber for 10min. The resulting SEM images (Figure 4.8) show that a larger number of activated platelets adherent to the non-crosslinked samples. Additionally, in many locations, large aggregates of platelets were observed, as were fibrin clots (Figure 4.9A) which were only observed on the non-crosslinked samples. EDC/NHS crosslinked samples had also a substantial number of platelets adherent on the surface which were activated to some degree. Heparin-conjugated samples however had relatively few adherent platelets, and those that were attached did not appear to be activated. Interestingly, in multiple locations on all three samples there appeared to be protein aggregates adherent on the tendon (Figure 4.8B). These features were not consistently distributed throughout the surface of the samples, however in several instances platelets appeared to have adhered specifically to these proteins, as shown in Figure 4.8B which was a platelet adherent on an EDC/NHS

crosslinked section. It is possible that these protein aggregates are vWF bound to the surface, interacting with platelets[218].
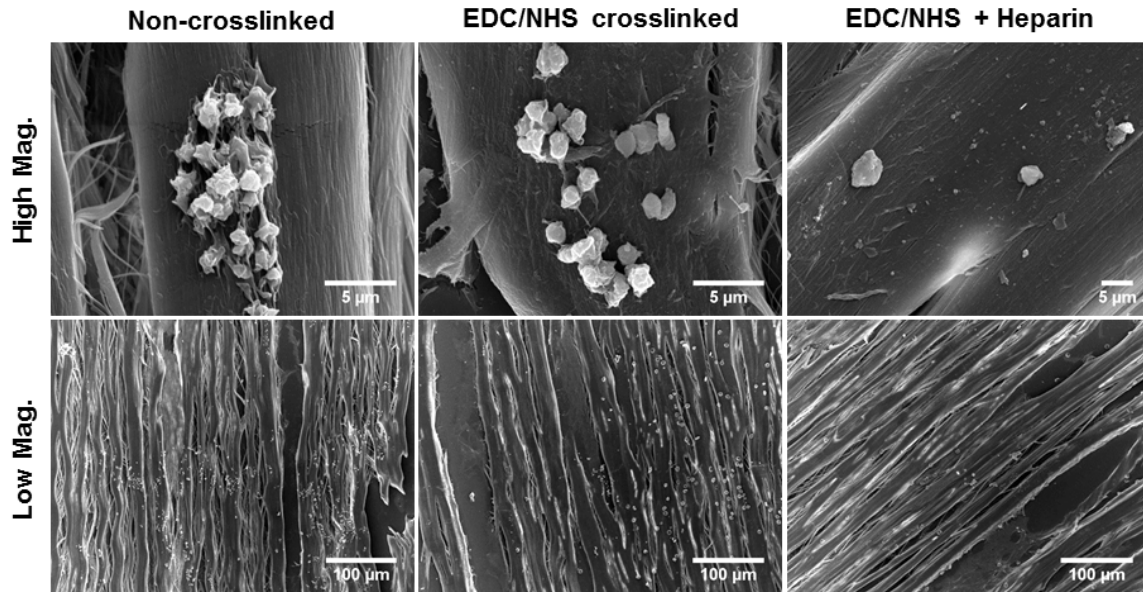
Figure 4.8: Representative electron micrographs of platelets following a dynamic test on non-crosslinked tendon sections, EDC/NHS-crosslinked sections, heparin-conjugated tendon sections at high and low magnification.

Overall, these results confirm that tendon-derived sections are thrombogenic, as collagen is known to be. However, covalent conjugation of heparin to the surface, through EDC/NHS crosslinking has the ability to reduce platelet adherence on the surface and to reduce the activation of those that do adhere when under physiologically-relevant conditions. The difference between the results of the heparinized samples in the dynamic experiments and the static experiments is likely due to how the platelets interacted with the heparinized surface. In the static experiments the platelets likely settled and were bound to the surface of the tendon, whereas in the dynamic experiments the platelets would have had to roll along the surface and undergone a shape change[219]. Furthermore, heparinized surfaces have been shown to increase the rolling velocity of platelets[220],

which likely affects their interaction time with other factors such as vWF, in the dynamic case.
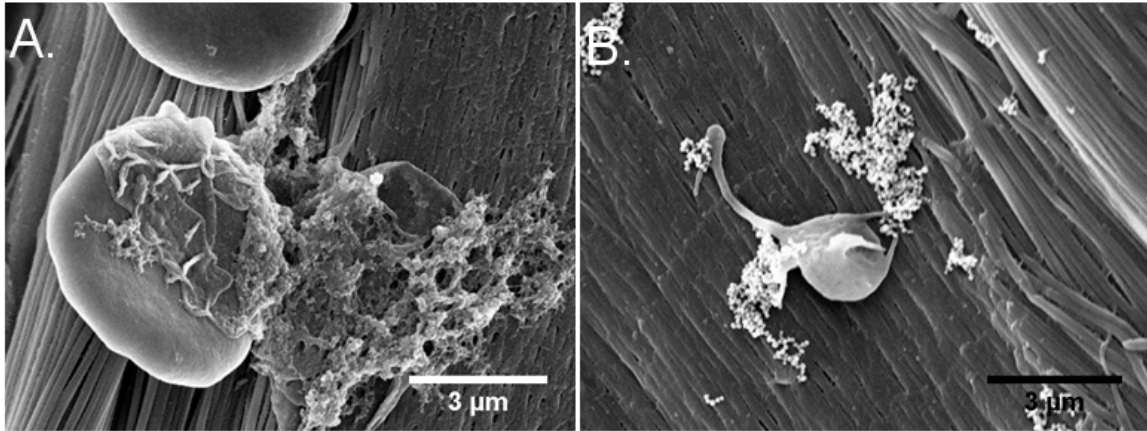
Figure 4.9: Electron micrographs of: **A)** a red blood cell trapped in a fibrin clot adherent to a non-crosslinked tendon section following dynamic flow. **B)** Protein aggregates, possibly vWF, interacting with a platelet on an EDC/NHS crosslinked tendon section.

Alternative methods of reducing the thrombogenicity of the tendon-derived material also exist, such as the endothelialization of the luminal surface[221]. Preliminary experiments show that human vascular endothelial cells (hUVEC) grow well and display a continuous, polygonal cobblestone-like morphology (Figure 4.10A), desired in endothelialization[222]. HUVECS could also be combined with other cell types, such as smooth muscle cells (SMC) (Figure 4.10B), to create a more biologically-relevant graft.
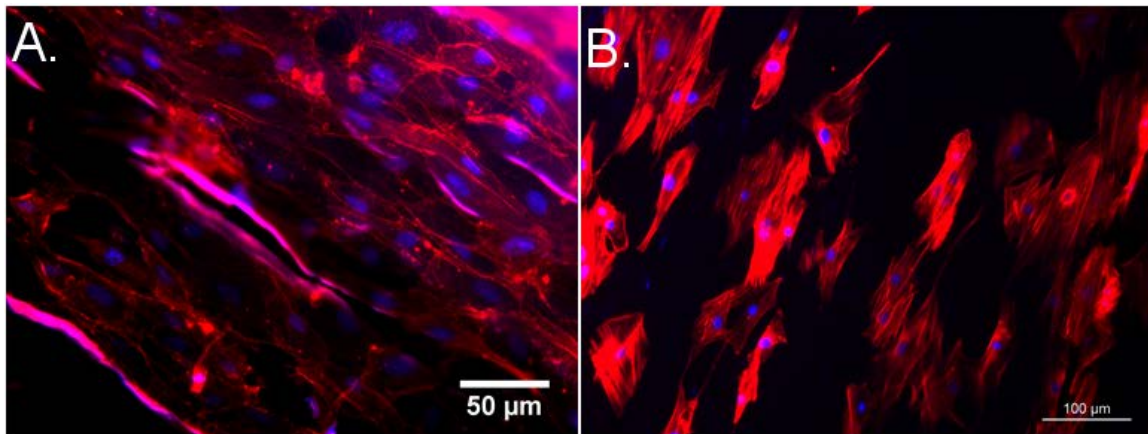
Figure 4.10: A) Human vascular endothelial cells, and **B)** rat vascular smooth muscle cells cultured on tendon sections after 5 and 3 days in culture, respectively. Red is phalloidin-rhodamine staining and blue DAPI staining of cell nuclei.

4.4 BIOCOMPATIBILITY AND FOREIGN BODY REACTION IN RATS

Knowing the way a material degrades *in vitro* can be beneficial for screening a variety of samples for the optimal conditions; however, there are a number of other ways the body could respond to an implant in addition to degradation, such as a foreign body reaction. A foreign body reaction is a graded response to an implanted material that the body does not recognize, or recognizes as detrimental. The reaction involves protein adsorption and encapsulation, macrophage recruitment, and potentially macrophage fusion to form foreign body giant cells[223]. These cells will attempt to phagocytize the foreign object, however if it is too large, the cells will isolate it via fibrotic encapsulation. This will ultimately affect the degradation rate, biocompatibility of the material, and could lead to outright failure of an implant.

4.4.1 Subcutaneous implantation

To assess the biological response to tendon-derived collagen sections, we implanted non-crosslinked and GA-crosslinked tendon sections, along with a known biocompatible control (PLGA) subcutaneously into the back of male Sprague-Dawley rats following ASTM Designation: F1408 – 97. Samples were implanted for 1, 3, or 9 weeks, with 6 samples per condition per time point. At the time of sacrifice, condition of the implant and surrounding tissue was noted, and both the implant and tissue excised. The excised sample was fixed in 4% paraformaldehyde, sectioned using a cryomicrotome, and stained with Masson's trichrome stain.

Figure 4.11 shows representative images of the explanted tissues. One week following implantation, a well-defined square shape can be observed. No significant local redness indicating inflammation was observed, however the vasculature surrounding the implant did appear to be larger. This is likely vascular dilation and initial cell infiltration associated with the acute and chronic inflammatory phase that occurs 1-2 weeks following implantation[224]. Again at week 3, no local tissue redness appears and the surrounding vasculature appears to have largely subsided. The edges of the implants are beginning to round over, possibly either from degradation or integration into the surrounding tissue. By week 9, significant degradation had occurred in the non-crosslinked and PLGA samples. Three out of six non-crosslinked implants were no longer observable, and those that remained appeared to have little integrity remaining. Four of six PLGA samples had formed into a round shape, ECM contracture, a result of myofibroblast contracture[225,226]. Little change was observed in the GA-crosslinked sample between weeks 1, 3, and 9. Macroscopic evaluation of the implants at time of excision suggests that non-crosslinked tendon degrades rapidly, while GA-crosslinked exhibit little to no degradation in the same time frame.
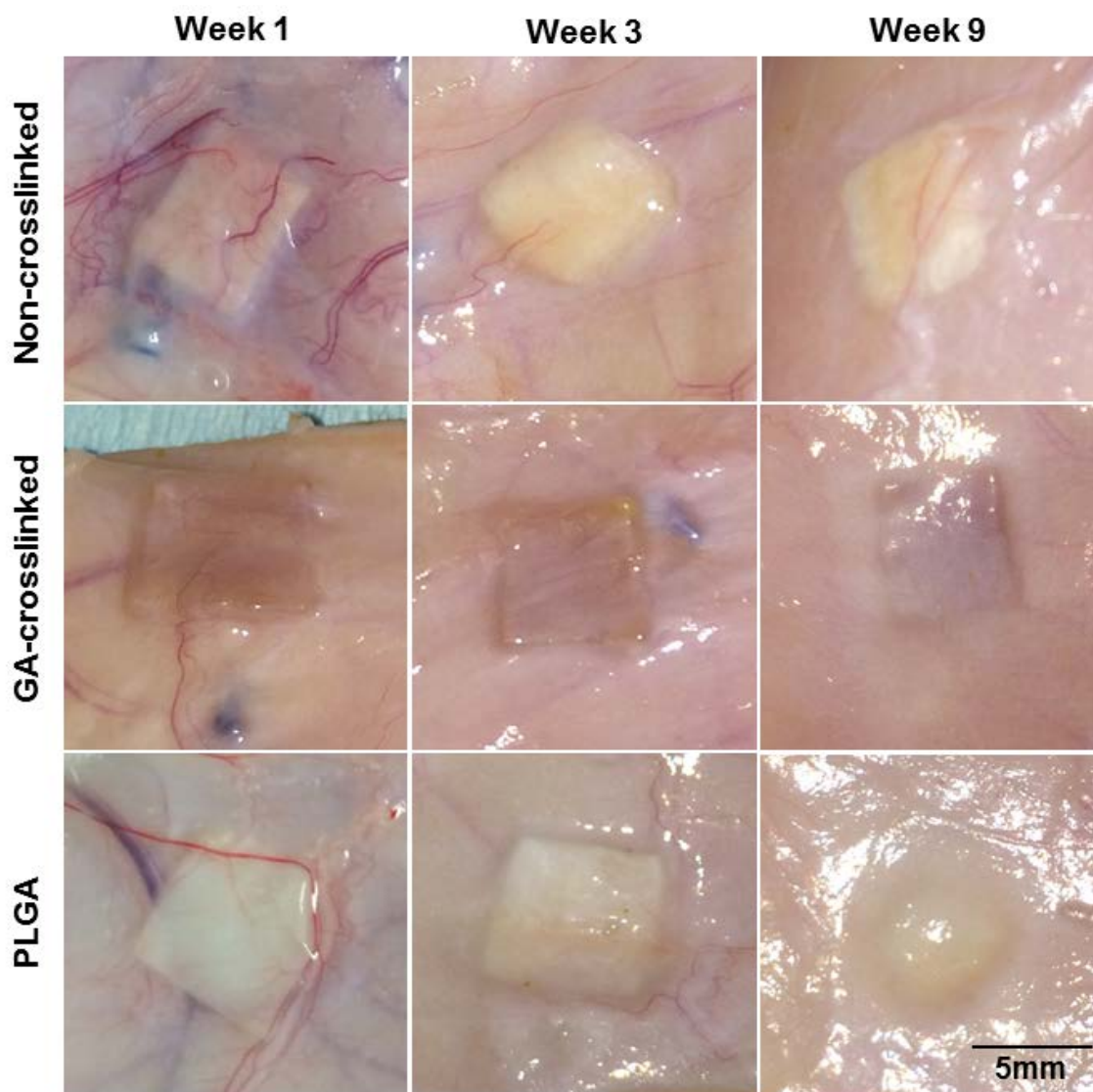
Figure 4.11: Representative photographs of subcutaneously implanted samples (Non-crosslinked tendon, GA-crosslinked tendon, and PLGA) after 1, 3, or 9 weeks of implantation. Note: not all week 9 non-crosslinked samples were visible. 5mm Scale bar relevant for all images

4.4.2 Histological evaluation

Histological evaluation of the implants at each time point (Low magnification - Figure 4.12, High magnification – Figure 4.13, 4.14) shows similar results. At week 1, the non-crosslinked samples have swollen from their initial dry thickness (200μm) to 600-700μm (Figure 4.12A). This is likely due to hydration but also due to cell infiltration into and between the ends of the layers (Figure 4.13A), and between the outermost layers. There is also a large number of cells directly surrounding the material along with some loosely packed collagenous tissue. Small neovasculature (Figure 4.15A) can be seen developing around the perimeter of the implant.
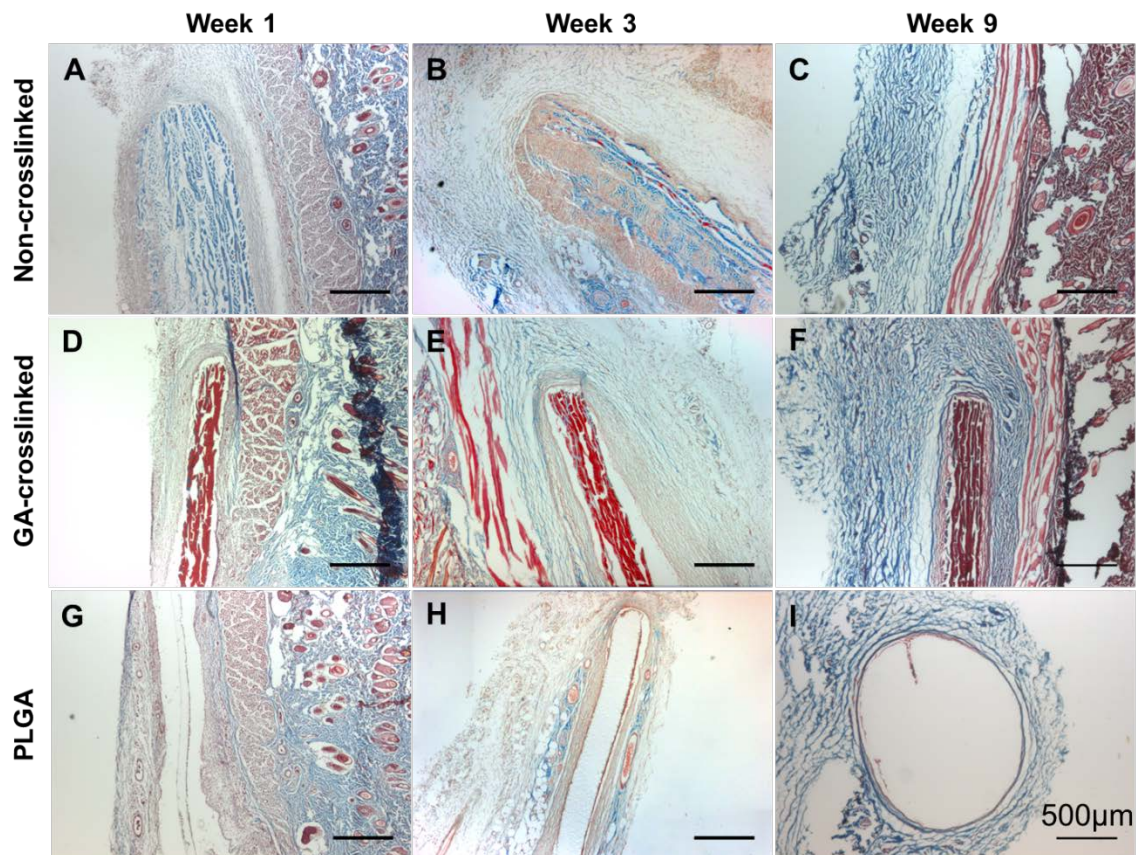
Figure 4.12: Low magnification images of Masson's trichrome stained sections of implanted: non-crosslinked decellularized tendon sections **(A-C)**, GA-crosslinked decellularized tendon sections **(D-F)**, and PLGA **(G-I)**. All scale bars are 500μm.

By week 3, the cellular response has dramatically changed. The tendon sample has been inundated with a large number of cells (Figure 4.12B), likely granulation tissue containing host fibroblasts and macrophages as part of an inflammatory response. There are fewer cells surrounding the tissue but many more in the sample that have grown in between the fibers of the individual sheets and cells can be seen growing or moving along the collagen fibers that are running in the plane of the image, indicating that these cells are likely still being influenced and oriented by the nanotopography (Figure 4.13B). Additionally, larger more developed vasculature can be seen growing near the implant. Individual sheets have largely been degraded, but some change in fiber orientation can still be observed between adjacent sections (Figure 4.16) and the collagenous network surrounding the cellular infiltration is largely dispersed.

At week 9, the majority of the noncrosslinked samples were no longer clearly visible in the histological images (Figure 4.12C). The samples that had been visible at explant in Figure 4.11C had some dense areas of collagen present in the hypodermis (Figure 4.15B); however surprisingly in these areas there is no longer a large cellular response (Figure 4.13C). It is possible that in these cases, the tendon sections were completely degraded and in the process, new collagen put down using the tendon as a template, resulting in the visible structures — Oliver *et al.* observed a 60% degradation of collagen scaffolds within 20 weeks of implantation, accompanied by a an equal amount of collagen regeneration, using ^{3}H-labelled collagen samples[227].

The GA-crosslinked samples at week 1 underwent little hydration, resulting in minimal separation between collagen fibers and sheets, and reduced cell infiltration (Figure 4.12D). The thickness of the cell layer surrounding the GA sample was greater and denser, and a well-defined layer 1-2 cells thick directly surrounding the implant (Figure 4.13D), which was absent in the non-crosslinked samples. This lack of cell infiltration may be desirable for applications like nerve guidance conduits where you would not want fibroblast infiltration into the lumen of the conduit. Interestingly, the GA-

crosslinked sections stain red, rather than blue as is expected with a Masson's trichrome stain. This is likely due to the large increase in density of the fibrils due to the crosslinking, as Analine Blue and Biebrich scarlet-acid fuchsin, used in Masson's trichrome staining, rely on differential penetration into tissue based on the molecule size.
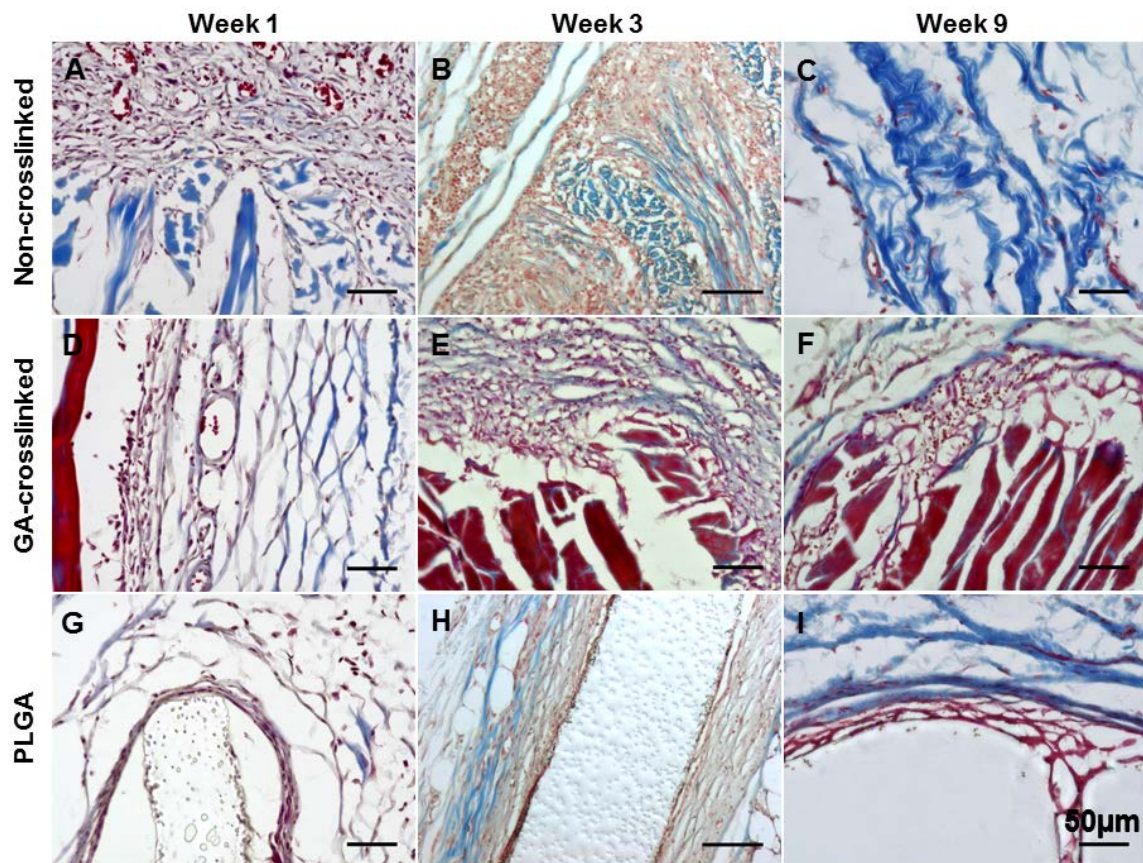
Figure 4.13: High magnification images of Masson's trichrome stained sections of implanted: non-crosslinked decellularized tendon sections **(A-C)**, GA-crosslinked decellularized tendon sections **(D-F)**, and PLGA **(G-I)**. All scale bars are 50μm.

At week 3, a large cellular response is also seen in the GA-crosslinked samples, along with some vascular development nearby (Figure 4.13E). However, the cells here are largely confined to the perimeter of the sample, and are unable to penetrate in between the individual sections, or within the fibers of the collagen. By week 9, the immediate area surrounding the implant remains highly cellular (Figure 4.12F), and it appears that cells begin to penetrate between sheets of the construct (Figure 4.13F).

Several sections contained locations with a high degree of cellular infiltration, where areas in immediate contact with cells stain blue as collagen is expected to (Figure 4.17). This is a result of the degradation of the material, reducing the density and allowing for typical staining.

PLGA samples were used as known biocompatible and biodegradable control. At week 1, the PLGA samples had a dense cellular layer around it (Figure 4.12G) and a 1-2 cell thick layer (Figure 4.13G) similar to the GA-crosslinked samples. At week 3, an increase can be seen in cell density; however no cell infiltration is seen. At week 9 the cellularity is decreased and confined to directly around the implant. Vasculature, some particularly large (Figure 4.12H), can be seen at all stages following explant.
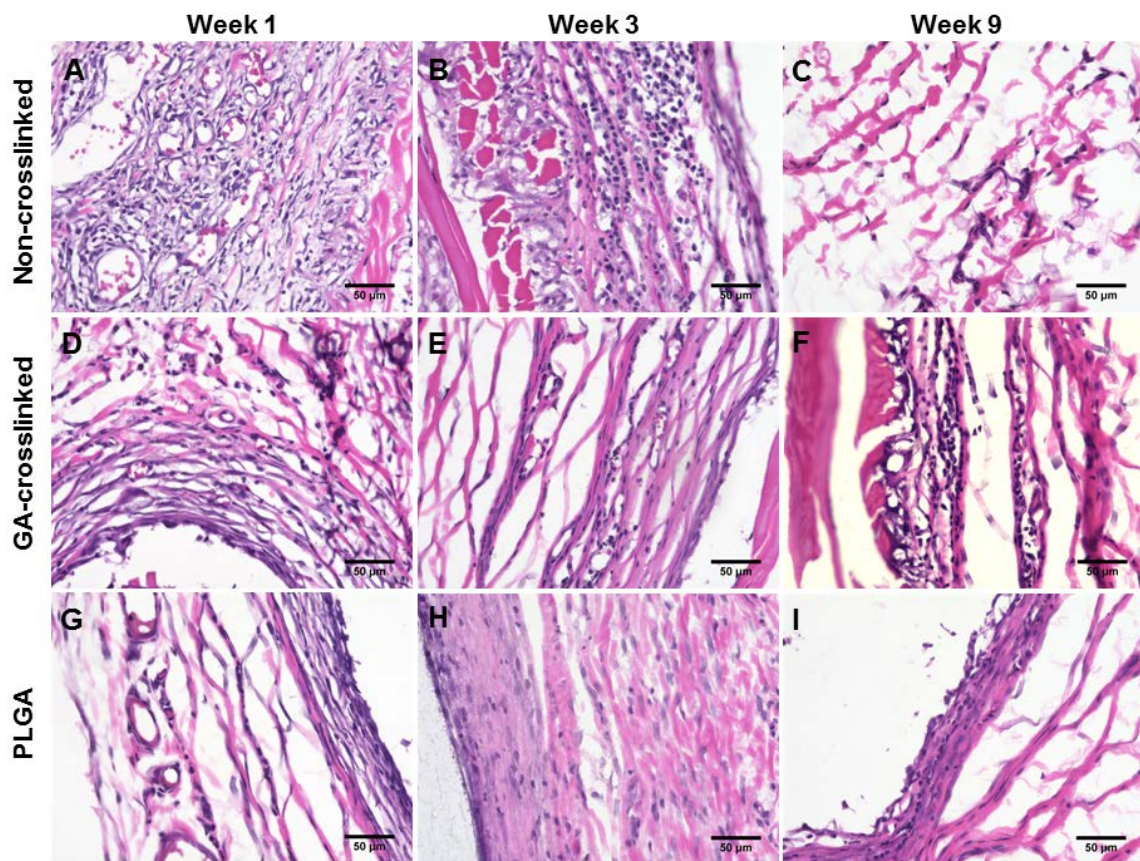
Figure 4.14: Photomicrographs of H&E stained sections explanted from non-crosslinked **(A-C)**, GA-crosslinked **(D-F)**, and PLGA **(G-I)** implants at weeks 1, 3, and 9. Scale = 50μm.

Overall, a comparison between the three conditions indicates that the non-crosslinked collagen is very well accepted by the body and rapidly degraded. There appears to be an inflammatory response, likely M2 macrophages associated with constructive remodeling, rather than rejection; a similar phenomenon is seen with decellularized dermis and small intestine[77,228]. Cells quickly infiltrate and degrade the material, and if in direct contact with the tendon may be guided by the material for at least 3 weeks. By week 9, the non-crosslinked sample has been degraded to the point where it is difficult to identify histologically, and no longer elicits a cellular response. At this point, the material would provide little to no mechanical strength or nanotopographical guidance cues. The GA-crosslinked implant and the PLGA implant appear to elicit similar reactions characterized by inflammation with dense cellular tissue at weeks 1 and 3, neither of which penetrates significantly into the material. At week 9, the cellular response and inflammation have largely subsided and are isolated to the area directly surrounding the implant, as the materials enter a state of biological tolerance following the inflammatory response.
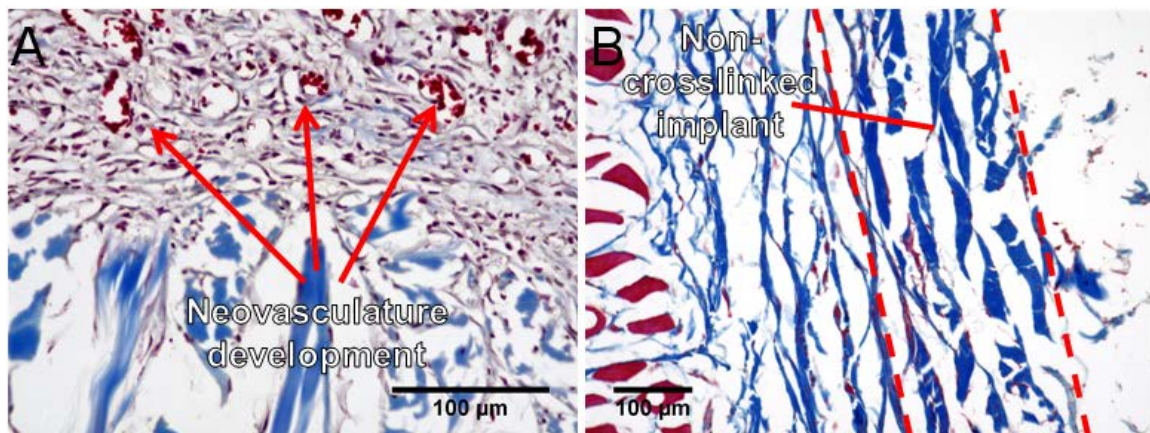
Figure 4.15: Histological sections showing **A)** neovasculature development at week 1 near a non-crosslinked implant and **B)** the likely remnants of non-crosslinked implant following explant at week 9.

Additionally, the GA-crosslinked samples did not present with any overt signs of toxicity or necrosis to the surrounding tissue. The high level of cellularity surrounding the implant at week 3 may indicate that the GA breakdown byproducts are not too detrimental as to prohibit cell growth in in immediate area; however they may have an effect on the cell type which remains to be analyzed. These data indicate that the non-crosslinked tendon samples are biocompatible and biodegradable, as they undergo integration followed by resorption. The GA-crosslinked samples elicit a similar response to PLGA. These implants appear to elicit some degree of a foreign body response. Primary evidence of this is the one- to two-cell layer that surrounds the latter samples, indicating a foreign body reaction[223].
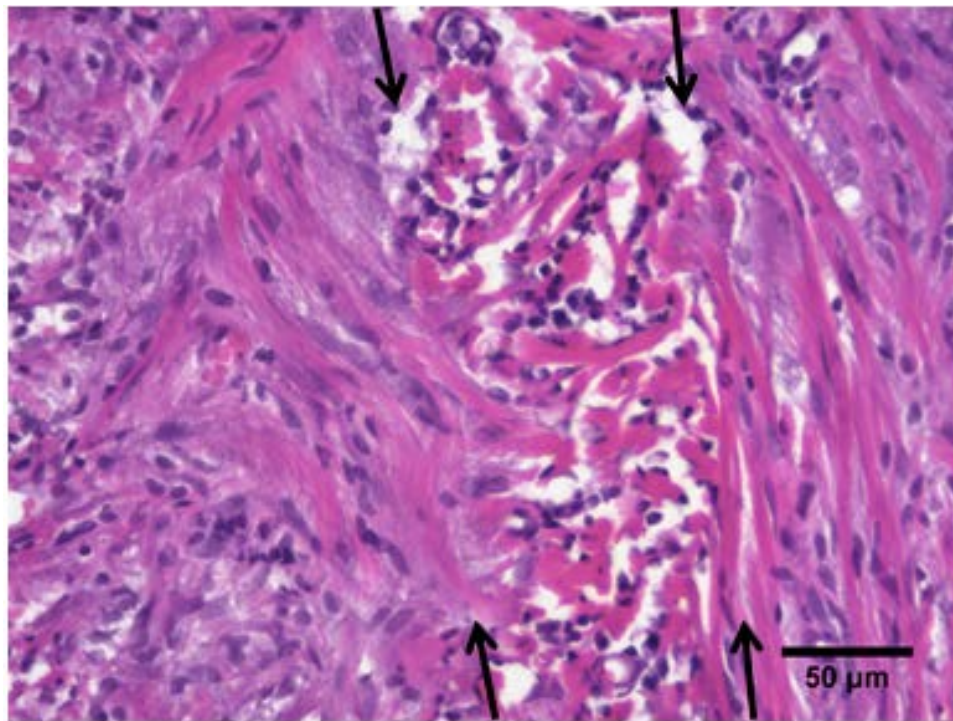
Figure 4.16: Photomicrograph of an H&E stained non-crosslinked sample at Week 3 post-implantation. A change in collagen fiber orientation is still visible (as marked by the arrows) despite significant cell infiltration.

These results are consistent with previous reports of acellular dermal scaffolds exhibiting a lack of long term inflammation when implanted subcutaneously; and GA crosslinked scaffolds exhibiting a slight response[229–232]. The reported amount of degradation in decellularized ECM scaffolds also varies greatly, with complete degradation occurring in scaffolds without crosslinking in 50 days and 0-15% degradation in glutaraldehyde crosslinked [227,232], some absorption after 20 weeks for Permacol scaffolds[233], and 28 days for Alloderm[234].
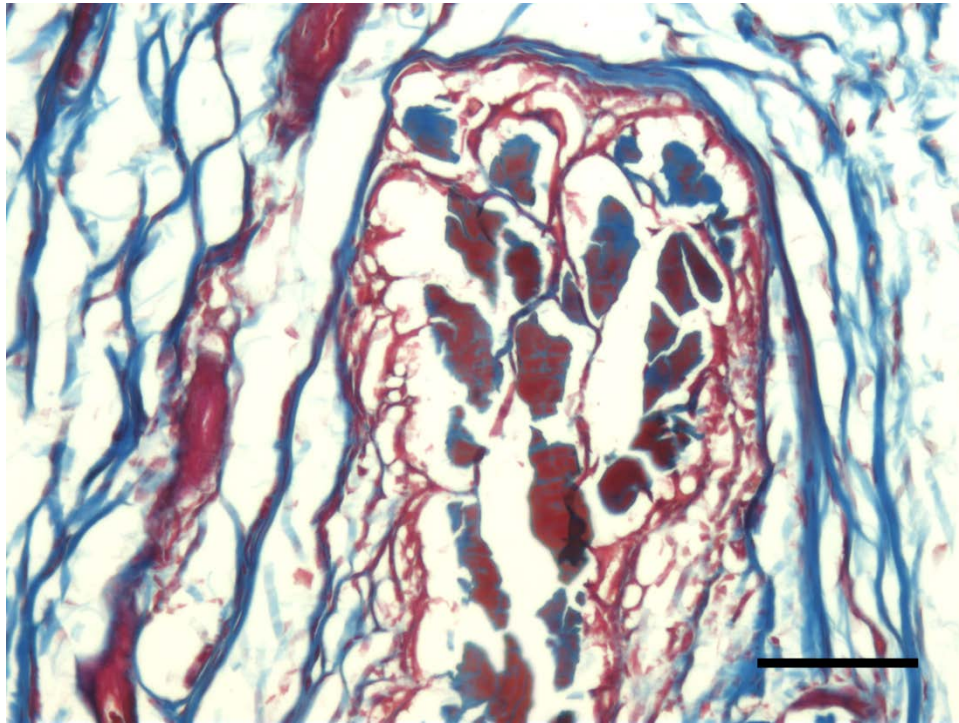
Figure 4.17: Photomicrograph of a Masson's trichrome stained GA-crosslinked implant at week 9 showing degradation and change in staining color. Scale = 50μm.

4.4.3 Implant encapsulation

As a quantitative assessment of these results the thickness of the inflammatory capsule surrounding each implant was measured. The inflammatory capsule was defined as the area between the implant and the area that returns to normal, extracellular matrix,

and contains granulation tissue primarily comprised of blood vessels, fibroblasts and immune cells. Figure 4.18 shows the thickness of each capsule. Initially there was a high degree of cell growth and encapsulation at week 1 for all samples. Over time the degree of encapsulation decreased for all samples, disappearing for the non-crosslinked samples as they were nearly completely degraded.

With many implants you would expect the capsule thickness to increase over time and change composition as the granulation tissue is replaced with fibrotic tissue (collagen), particularly for non-biodegradable samples, as the body attempts to wall off the implant. That is not observed here as the inflammatory capsule appears to resolve itself over time. This is most likely due to the xenogeneic collagen eliciting some immune response that then abates as acute and chronic inflammatory responses subside. This phenomenon has been observed previously with xenogeneic collagen, including bovine dermal collagen[235,236].
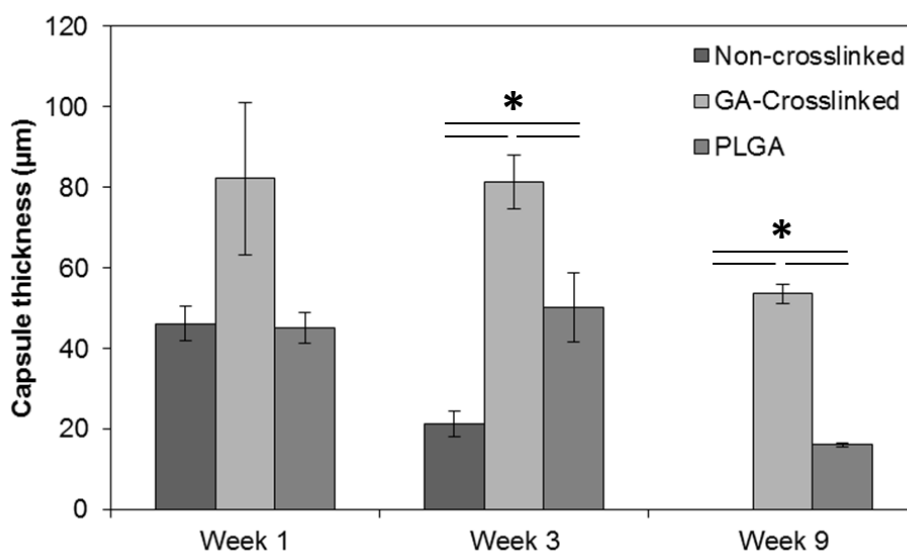
Figure 4.18: Inflammatory capsule thickness of non-crosslinked, GA-crosslinked and PLGA samples at 1, 3, and 9 weeks post implantation. * = $p < 0.05$

4.4.4 Cell number

The number of cells surrounding each implant was also quantified to elucidate the biological response. Four random locations around each implant were imaged on H&E stained sections, and the number of cells in the area from the implant to the edge of one field of view at 400x magnification (350μm) counted. Analysis of cell number correlates with the phenomena described in the histological images.

Initially there are a large number of cells surrounding the non-crosslinked implant. This number then decreases as the cells infiltrate the scaffold, and finally decreases further as the samples near complete degradation. A similar trend is seen with the GA-crosslinked samples; however, the decline in cell number is not as precipitous as the implant is not completely degraded but the inflammatory response has decreased by this point. Interestingly, the number of cells around the PLGA sample is initially the lowest yet remains relatively constant over the 9 weeks of implantation. This is likely due to a reduced degree of antigen-induced inflammation initially, but a constant number of cells present to surround and degrade the material.
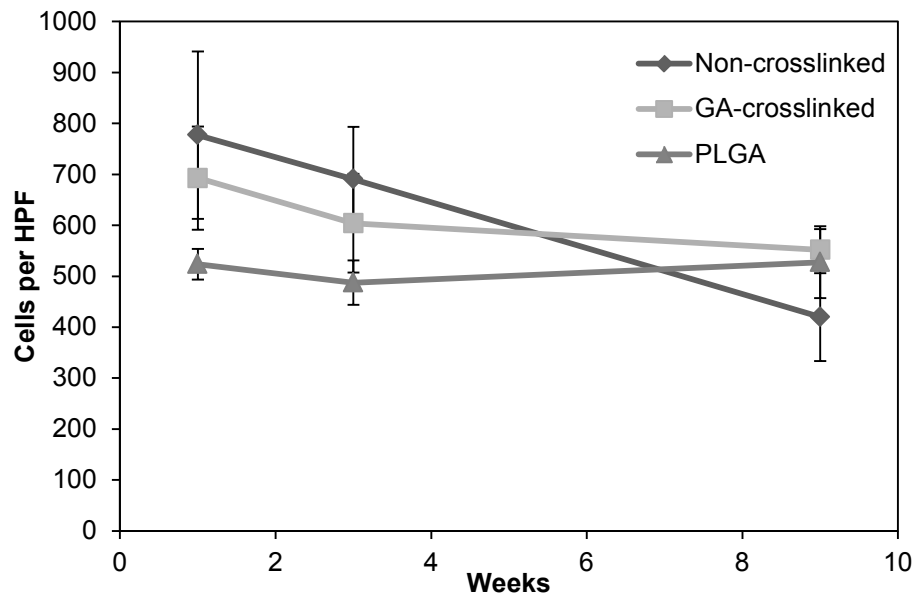
Figure 4.19: Average cells per high powered field (HPF) (400x) extending from the edge of the implant out 0-350μm away. No statistical difference was observed between samples at 1 week, 3 weeks or 9 weeks.

4.4.5 Sample morphology

As one of the anticipated applications for this material is the guidance of cellular growth, the degradation of the material would clearly impact its potential to achieve this. The non-crosslinked samples appear to degrade most rapidly, yet there still appears to be some guidance of the cells at week 3, indicating there is likely still some structure. Therefore, the morphological features of the collagen fibrils at each time point of excision were assessed.

A piece of each sample that had not been sectioned was separated from the surrounding tissue capsule through tweezing and blunt dissection to remove any fibrous outer layers. These samples were dehydrated in graded ethanol followed by hexamethyldisilazane (HMDS), sputter coated with Pt-Pd and imaged using SEM. As these samples were not post-fixed with osmium tetroxide, it is likely many of the cellular components that would have been adherent to the surface were removed and not imaged. Figure 4.20 shows the electron micrographs of the explants prior to implantation and at each time point following excision.

In the non-crosslinked samples you can see a high degree of alignment in the collagen fibers prior to implantation, while at week 1 many of the fibers are disrupted, but still identifiable, with some areas containing disarrayed collagen fibrils. At week 3 little to no fiber architecture can be seen and the entire surface appears to be a tangled network of fibers. Following week 9, the samples that were able to be identified and separated, displayed no fiber structure or alignment or fibril structure. At week 9 however, bundles of collagen fibers containing aligned fibrils can be seen again, however the overall fiber architecture is disorganized and a likely a result of resorption and redeposition of host collagen.

In contrast, highly aligned collagen fibers and fibrils can be seen prior to implantation and at weeks 1 and 3 within the GA-crosslinked sample. At week 9, some of

the fiber morphology is lost but a large number of collagen fibers are still identifiable. The PLGA samples show development of pores in the surface at week 1 and 3 and large surface degradation by week 9.
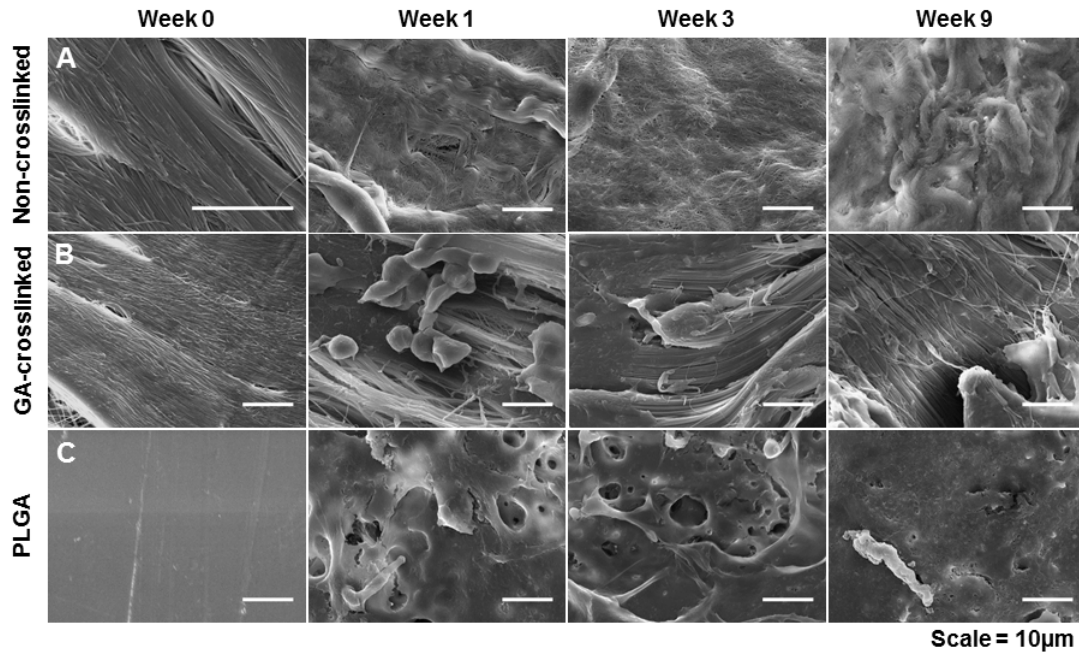
Figure 4.20: Electron micrographs of the surface of implants prior to implantation and at weeks 1, 3, and 9 following excision of **A)** Non-crosslinked, **B)** GA-crosslinked, and **C)** PLGA.

4.5 SUMMARY

This work demonstrates the biological properties of the material and gives researchers' insight into the potential biological responses and the ability to predict the behavior in different potential applications. One consideration in evaluating the material is that applications may require a specific degradation rate to correspond to variations in tissue regeneration and host response. *In vitro* degradation experiments show the rate can be tuned through crosslinking, extending the lifetime of the material. A second factor that must be accounted for is collagen's propensity to induce thrombosis. Modifications can be made to the material through covalent heparin conjugation that will reduce this

property as demonstrated through platelet adhesion and activation experiments. Lastly the *in vivo* response of the material was tested, as material that induced a large foreign body reaction and significant fibrotic encapsulation would have a detrimental impact on tissue engineering applications. These experiments demonstrated that the tendon material derived through Bioskiving is biocompatible, biodegradable and can be crosslinked to maintain surface features for extended periods of time *in vivo*. Although implantation does result in some inflammation and granulation tissue development, these issues resolve themselves following the chronic inflammatory response. Additionally, it may be possible to take advantage of the large number of blood vessels that develop in the granulation tissue to supply nutrients for future tissue engineering applications.

4.6 MATERIALS AND METHODS

4.6.1 Tendon-derived section degradation *in vitro*

4.6.1.1 Scaffold fabrication

Tendon sections were fabricated as described in Chapter 2 and 3, comprised of 10 layers of decellularized tendon oriented 90° in adjacent layers. These sections were crosslinked in GA at concentrations of 0.625% and 2.5% for 20min and 2.5% for 1h, as previously described. Non-crosslinked and GA-crosslinked samples were then dried overnight in a vacuum desiccator. The square samples were then cut into equal rectangular strips weighing 10-12mg and roughly 20x5mm in size.

4.6.1.2 Collagenase degradation

Samples were accurately weighed and the weights recorded. Each sample was placed into a 24 well plate and 0.5ml 0.1M Tris-HCl with 0.005M $CaCl_2$ (pH 7.4) added to hydrate the samples for 20min. To this 0.5ml of a collagenase solutions containing

2mg/ml collagenase (Clostridium histolyticum (125CDU/mg), Sigma) in the same Tris-HCl buffer. This resulted in a final concentration of 1mg/ml collagenase or roughly 10-12CDU/mg of sample. These plates were placed into a humidified incubator at 37°C and 5% CO_2 on a shaker at 80rpm. The samples were digested for 8, 24, 48 or 96h before being removed from the incubator, rinsed 3 times in diH2O and dried for 24h in a vacuum desiccator. The samples were then reweighed and percent mass remaining calculated.

4.6.1.3 Mechanical testing

Each sample was rehydrated in PBS and tested under uniaxial tension at a rate of 5%/min on a mechanical testing apparatus (Instron, Norwood, MA) with a 1000N load cell until failure. Ultimate tensile strength was calculated from the load vs extension data based on initial sample geometries.

4.6.1.4 SEM analysis

A small piece was trimmed from the end of each tendon sample and dehydrated using graded ethanol followed by HMDS. The samples were then placed on stub mounts and sputter coated with 3nm Pt:Pd 80:20 using a Cressington 208HR Sputter-coater (Cressington Scientific, Watford, Hertfordshire, UK) to a thickness of 3nm and imaged using a Zeiss Ultra-55 Scanning Electron Microscope (Zeiss, Oberkochen, Germany).

4.6.1.5 Statistics

Ultimate tensile strength (UTS) was determined as the maximum stress of each sample's stress-strain curve. All values reported as mean ± standard error and a sample size of n=4 was used for all conditions. Differences in UTS and modulus were analyzed

by analysis of variance (ANOVA) with post hoc Tukey's testing using IBM SPSS software (IBM, Armonk, NY).

4.6.2 Hemocompatibility of the tendon-derived sections

4.6.2.1 Sample preparation and heparin conjugation

Tendon sections were decellularized as previously described and sectioned at 20μm thick and placed onto Superfrost Plus slides (Fisher Scientific, Waltham, MA). The sections were allowed to dry, rinsed 3 times with diH2O. The samples were then crosslinked with EDC/NHS or a heparin containing solution. EDC/NHS crosslinked samples were crosslinked as previously described. Heparin concentrations were calculated based on the free amine content calculated in 3.3.1, assuming 18.75mol COOH/mol heparin[207], 50μmol EDC-crosslinkable NH_2/g collagen, and an average molecular weight of 18,000 Da for heparin sodium salt isolated from porcine mucosa as reported by the manufacturer (Sigma). A 20-fold molar excess of Heprain-COOH to Collagen-NH_2 was used and 1:0.4:0.24 molar ratio of Heparin-COOH:EDC: NHS. Each tendon sample cut from the same block weighed ~10mg dry. Heparin, EDC, and NHS were combined in 1ml MES buffer and stirred for 15min covered from light to activate, prior to being added to a tendon section. The samples were reacted for 3h at room temperature covered rom light, rinsed in 0.1M sodium phosphate dibasic for 1h and rinsed 3 times with diH2O before being placed into the diffusion chamber for testing.

4.6.2.2 Amine content (TNBS) assay

Primary amine content in the tendon-derived samples was measured using a TNBS (2, 4, 6-trinitrobenzenesulfonic acid) assay. Tendon samples were dehydrated overnight and a 2mg placed into a vial to which 1ml of 4% sodium bicarbonate and 1ml

of 0.5% TNBS in diH2O was added. This solution was heated to 40°C for 2h, after which 3ml of 6M hydrochloric acid was added and the solution heated to 60°C for 90min. This was diluted with 5ml of diH2O and the absorbance measured at 345nm. A standard curve was created using glycine and the primary amine content determined.

4.6.2.4 Flow chamber fabrication

Photolithography-etched silicon wafers were generously provided by Dr. Lorenzo Tozzi and used as a mold to create the flow chambers out of polydimethylsiloxane (PDMS) (Sylgard 184, Dow Corning, Midland, MI). The central portion of each chamber was 8mm wide and 200μm in height. PDMS prepolymer was mixed well at a 10:1 ratio with the curing agent, cast onto the mold, placed under vacuum to clear bubbles, and cured in a 100°C vacuum oven for 2h. After, the PDMS was removed and could then be secured to the tendon-containing slides using clips.

4.6.2.5 Activation and adhesion experiment

Whole blood was centrifuged at 250g for 15min at room temperature to obtain platelet rich plasma. CMFDA (Invitrogen) was added to a final concentration of 5μm and allowed to incubate for 1h at 37°C.

For static experiments, blood was prepared by centrifugation at 1200 rpm for 10 min at room temperature to obtain platelet rich plasma (PRP). Prostaglandin I2 (PGI2) and CMFDA (Invitrogen) was added to a final concentration of 5μm and allowed to incubate for 45min at 37°C. The PRP was then centrifuged at 3000rpm for 15min and the plasma resuspended in a Tyrode's/BSA solution. The platelets were counted using fluorescence activated cell sorting and the concentration adjusted to $1x10^5$ cells/ml. For dynamic experiments the red blood cells were washed 5 times in PBS at 1200rpm for 10 min and re-added to the PRP before being resuspended.

Each chamber (2 non-crosslinked, 2 EDC/NHS crosslinked, 2 Heparin crosslinked) were placed in an incubator and attached to a multichannel syringe pump. The labelled blood was flown through the chamber at 1ml/min for 15min. After which, 10ml PBS was flown through the chamber to remove any non-adherent platelets. The samples were then visualized under a fluorescence microscope. After imaging, the samples were fixed with 2.5% GA for 1h, washed 3 times in 0.1M phosphate buffer, and fixed in 1% osmium tetroxide in 0.1M phosphate buffer for 1h. The samples were then dehydrated in graded ethanol (50% 2x5min, 70% 2x5min, 80% 3x5min, 90% 3x10min, 95% 3x10min and 100% 3x10min), before being incubated in HMDS for 3min.

4.6.2.6 SEM analysis

Dehydrated samples were placed on stub mounts and sputter coated with 3nm Pt:Pd 80:20 using a Cressington 208HR Sputter-coater (Cressington Scientific, Watford, Hertfordshire, UK) to a thickness of 3nm and imaged using a Zeiss Ultra-55 Scanning Electron Microscope (Zeiss, Oberkochen, Germany). Representative images of the surface and adherent platelets were taken.

4.6.3 Biocompatibility and foreign body response

4.6.3.1 Sample fabrication

Tendon samples were decellularized and sectioned as previously described. Non-crosslinked sections were created from 10, 50μm thick sections with each section oriented 90° to each other. GA-crosslinked samples were crosslinked in 2.5% GA for 1h. Poly(lactic-co-glycolide) (75:25, MW:76,000-115,000) (PLGA) samples were fabricated by dissolving the PLGA in acetone at 100mg/ml on a shaker overnight. Once dissolved it was cast in a glass petri dish and placed into a fume hood for 3 days to evaporate. It was

then placed into a vacuum oven at room temperature overnight to remove any residual solvent. The resulting film was 0.2mm thick.

Each sample (non-crosslinked, GA-crosslinked, PLGA) was cut into 5 x 5mm squares and immersed in ethanol for 1h followed by 1h under the UV light in a tissue culture hood to sterilize them. The samples were then placed into autoclaved glass vials until implantation.

4.6.3.2 Subcutaneous implantation surgical procedure and explant

The research protocol was approved and in compliance with Tufts University's Institutional Animal Care and Use Committee (IACUC, protocol # M2013-58) in accordance with the Office of Laboratory Animal Welfare (OLAW) at the National Institutes of Health (NIH). Two samples were implanted into the back above the left and right hind flank of each animal. The implantation procedure was as follows: Each animal was weighed and anesthetized via 2-3% isoflurane inhalation and appropriate analgesics provided. The surgical area was shaved and cleaned and a surgical drape is placed onto the animal with a hole cut to expose the surgery site. Two, 1 cm incisions were made through the skin on the upper back above the right and left hind legs. One implant was placed into each wound site and the skin closed with 4-0 vicryl sutures in a running subcuticular manner. The animals were allowed to recover and wound healing monitored daily until completely healed. There were no complications with any of the surgeries.

At 1, 3, or 9 weeks the animals were sacrificed and the implant and surrounding tissue excised, noting tissue condition and any inflammation. The samples were placed into freshly prepared paraformaldehyde for 1h, and then rinsed in PBS.

4.6.3.3 Histology and staining

Excised samples and surrounding tissue were placed in a 30% sucrose solution for 2 days. They were then cut in half and one half placed in OCT for 1h at room temperature. These blocks were then snap frozen on dry ice and stored at -20°C until sectioning. The blocks were sectioned at 6μm thick and the sections placed on Superfrost Plus slides. The slides were dried at room temperature overnight and then frozen until staining. The sections were stained with hematoxylin and eosin, or Masson's trichrome stain using the manufacturer's protocol (HT15, Sigma). The slides were then mounted with DPX mounting media (Sigma) and cover slipped. Images of the sections were taken with 4x and 40x objectives using a Keyence BZX fluorescence microscope.

4.6.3.4 Capsule thickness and cell density measurement

Tissue capsule thickness was measured by imaging four random locations around the outside of the implant. The capsule was defined as the area between the implant and the surrounding material until it returned to normal ECM structure appearance. At each of these locations, four measurements were taken using ImageJ. The average capsule thickness was calculated for each of the sections and implants.

Cell number was measured by counting the total number of cells in a 250 x 250μm area extending out from the implant. The total number of cells was measured at four locations per sample and averages calculated for each implant and implant material.

4.6.3.5 SEM analysis

The sections that were not used for sectioning were imaged using a scanning electron microscope. The implant was removed from excised tissue using forceps and blunt dissection. In samples that were highly integrated with the tissue care was taken to avoid disrupting the structure as much as possible. The samples were dehydrated using

graded ethanol followed by HMDS, placed on stub mounts, and sputter coated with 3nm Pt:Pd 80:20 using a Cressington 208HR Sputter-coater (Cressington Scientific, Watford, Hertfordshire, UK) to a thickness of 3nm and imaged using a Zeiss Ultra-55 Scanning Electron Microscope (Zeiss, Oberkochen, Germany). Representative images of the surface were taken.

4.6.3.6 Statistics

Differences in capsule thickness and cell number were analyzed for statistical significance by performing a two-way Student's t-test assuming an equal variance with an α-value of 0.05. A p-value <0.05 was determined to be statistically significant.

Chapter 5.

Tendon-derived Conduits for Nerve Regeneration

5.1 INTRODUCTION

5.1.1 Peripheral nerve injuries

Peripheral nervous system (PNS) injuries result in a decreased quality of life due to factors such as neuropathic pain and oftentimes reduced mobility[237]. Complete nerve transections are a major problem, and on average there are 200,000 incidences every year that require surgical intervention in the United States alone[238]. Peripheral nerve damage is often the result of traumatic injury, such as motor vehicle crashes, burns, explosive injuries, and can be a complication of some surgical procedures. These injuries will often result in a significant loss of nervous tissue, or may elicit a pathophysiological response in the damaged nerve including axonal loss, and demyelination[239]. Early treatment of the damage has been shown to be optimal for achieving functional restoration, however this is not always possible due to compounding issues such as significant damage to the surrounding tissues[240].

In order to fully understand the challenges presented by nerve injury a basic understanding of the structure and function of nerves, as well as the regenerative process that occurs is important. Peripheral nerves in general can be divided into three main categories, those that contain: motor neurons, sensory neurons or a mixture of neurons.

As their name suggests, motor neurons are efferent neurons that signal from the spine to muscles to elicit contraction, while sensory neurons transmit impulses relaying sensory information to the central nervous system[241]. Both sensory and motor neurons contain additional subclassifications and can be linked in more complex circuits within the body but that is beyond the scope of this discussion. What is important to note is that there is a difference in function, as support cells (e.g. Schwann cells), can retain a preferential specialization associated with one type or the other[242]. Similarly, some experiments have shown preferential regeneration or differences in increased speed or distance for motor vs sensory regeneration[242–247]. Explanations for the differences seen include the support cells, as well as differences in location of the cell body origin along the spine[242,248]. However, other studies have suggested equal regeneration of motor and sensory neurons under equal conditions[249]. Clinically this is of importance as motor vs sensory graft use for repair of mixed nerves has been shown to elicit preferential regeneration towards the graft type[250], and selection of auto- or allograft donor location must be considered.

Independent of nerve type, the general regenerative process of the axons is similar. Following injury, the nerve undergoes Wallerian degeneration where axoplasmic microtubules and neurofilaments undergo proteolytic breakdown. In the days following injury axons in the distal stump are broken down, macrophages infiltrate the damaged area, and Schwann cells alter their morphology and proliferate. The Schwann cells will reorganize to form longitudinal bands of Bungner, and nerve fibers proximal to the injury will sprout daughter axons. These axons will regenerate along the Schwann cells, and in the process, separate into many small fascicles. Axons that successfully reach their target will mature in response to growth factors at the target and while those that did not will be withdrawn or form neuromas[150,251,252]. This regenerative process is illustrated in Figure 5.1 in the case of a nerve guidance conduit used for repair.
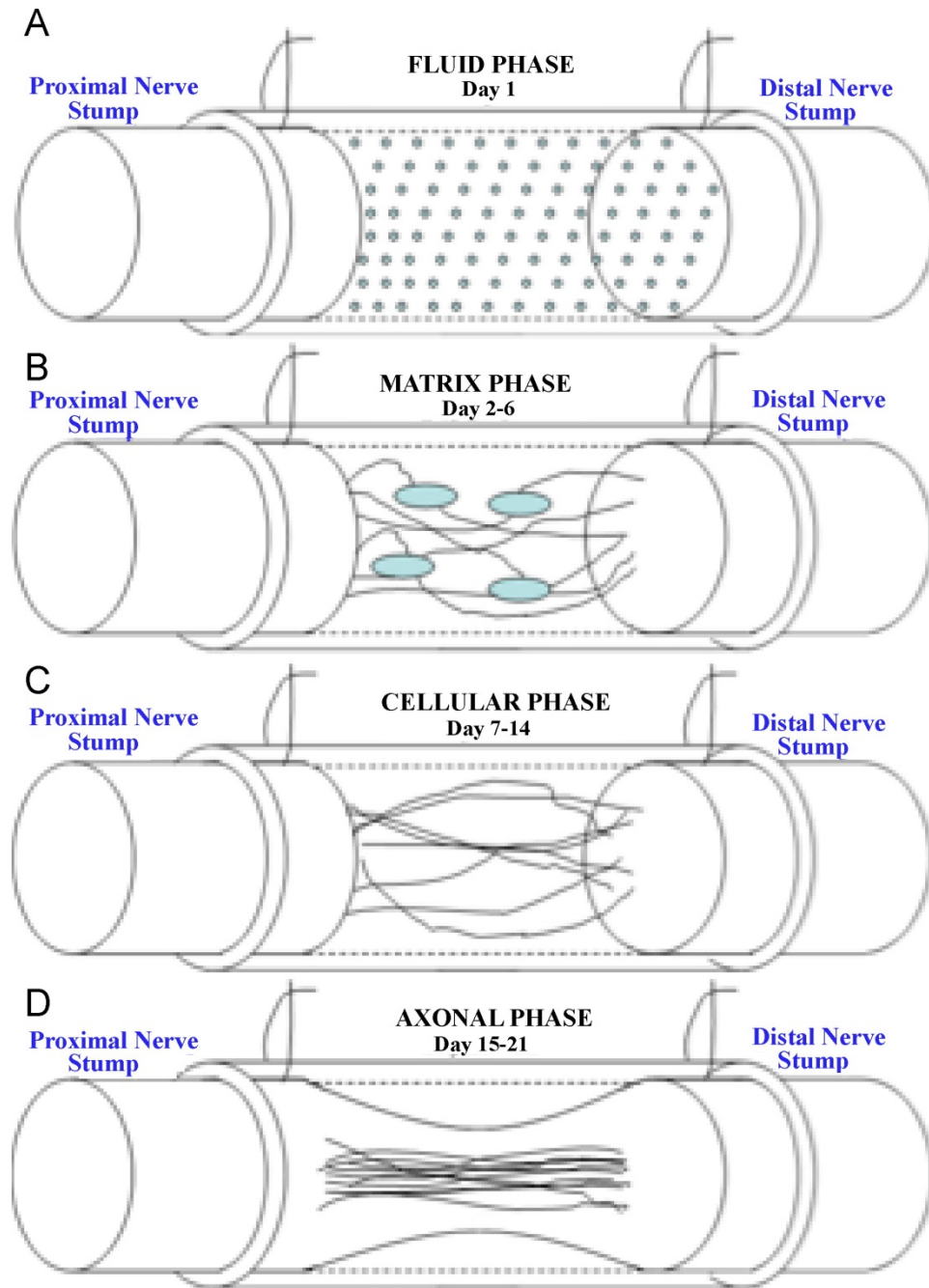
Figure 5.1: Illustration of the phases of nerve regeneration in a nerve guidance conduit. Reprinted from reference [150], with permission from Elsevier.

5.1.2 Peripheral nerve repair

Presently, the options for clinical repair of peripheral nerves are limited. When the damage is small, the two ends of the nerve stump can often be sutured together end-to-end in order to induce repair. However, this is only possible when the damaged nerve segment is less than several millimeters, as tension in the injured portion of nerve has been shown to increase scaring and impair regeneration[253–255]. When this is not possible there are a number of other options available, including the gold standard of replacing the damaged portion with a nerve autograft. A limitation of this approach is a loss of function at the donor site, while the repaired portion of nerve still may not achieve complete functional restoration. Alternatively, allografts (from both cadaveric and living-related donors), which can be stored for several days following harvest, can be used; however they suffer from related issues like donor compatibility which requires immunosuppression[256].

Over the past decade a number of alternative options have emerged for peripheral nerve repair including nerve guidance conduits (NGC). The goal of a NGC is to provide a pathway along which two ends of a sutured nerve stumps can regrow towards each other. This regrowth involves several stages (Figure 5.2) including fluid infiltration, formation of a fibrin matrix and migration of a variety of cell types including Schwann cells[150]. These events can be influenced greatly by the properties of the NGC, such as permeability, stiffness, and degradation rate [257].

A number of nerve guidance conduits are currently available on market including those comprised of synthetic polymers such as PLGA, and polycaprolactone[150], as well as natural materials such as animal extracted collagen[258,259] and silk [257,260,261] . Collagen NGC include the Neuroflex™ and NeuroMatrix™ from Collagen Matrix Inc and NeuraGen® from Integra Life Sciences, as well as collagen nerve wraps from each of these companies, NeuroMend™ and NeuroWrap™, respectively. Similarly, AxoGen Inc.

makes a NGC from decellularized porcine small intestine submucosa (SIS), called AxoGuard®. These conduits have shown positive results pre-clinically[262], however, clinically they still have limited success when repairing defects greater than 3cm[150,263,264], leaving room for improvement.
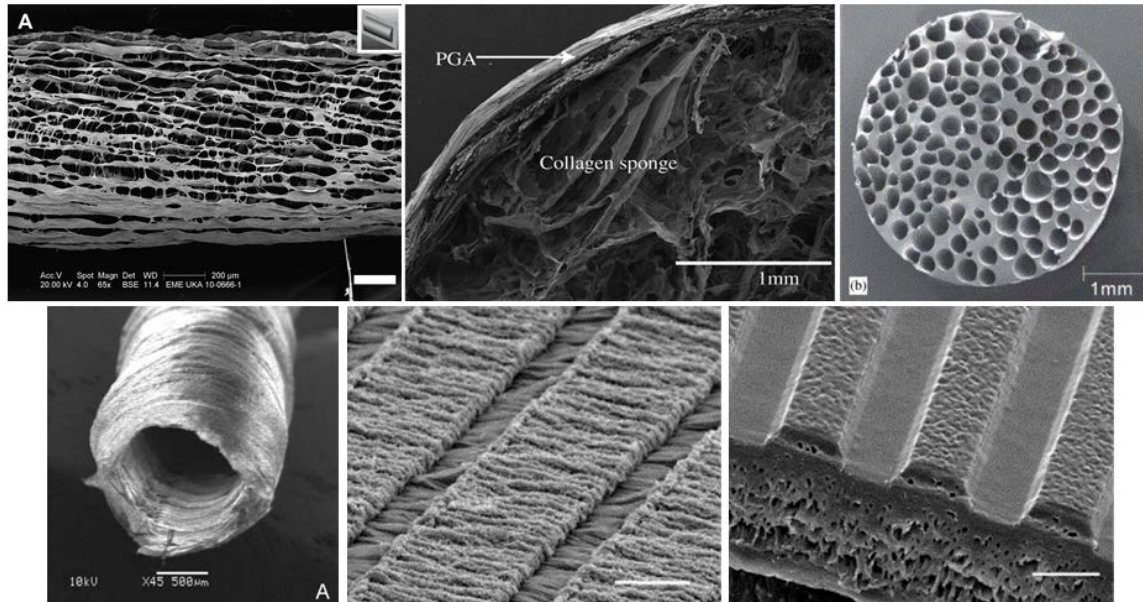
Figure 5.2: Images of various guidance features incorporated into NGC, adapted from references: [265], [266], [267], [268], [269], [269] from left to right, top to bottom, respectively, with permissions from Elsevier, John Wiley & Sons, Inc., and under CC 4.0. Scale bars are 200μm, 1mm, 1mm, 500μm, 10μm and 10μm from left to right.

Of these approved NGC, one feature they are notably lacking is intraluminal guidance, which many nerve repair products in development make use of. These guidance strategies include both chemical and physical structures that serve to preferentially induce directional growth. Physical features include incorporation of structures such as intraluminal channels[265], grooves[269], sponges[266], fibers[270], and electrospun mats[271] in order to provide nanotopographical cues which guide directional growth along their length[272]. Alignment along such structures has been demonstrated

along features from 200nm up to a few hundred microns[272]. Several examples of conduits containing these features are shown in Figure 5.2.

Chemical cue addition has included the use of neurotrophic growth factors like: nerve growth factor[273,274], ciliary neurotrophic factor[275,276], glial cell line-derived neurotrophic factor[277,278], as well as vascular endothelial growth factor[279] in various spatial (e.g. gradients) and temporal (e.g. controlled release) arrangements. One interesting alternative to the use of native growth factors that is being developed are biomimetic small molecules that bind the endogenous receptors and elicit the same result[252,280–282].

Overall, these conduits along with the various physical and chemical modifications have served to increase options for promoting nerve regeneration, however none have been able to surpass autografts and achieve widespread adoption. Using the Bioskiving process, tubular conduits for use in such applications, comprised of tendon-derived collagen can be created with the potential to improve these options. The collagen in the tendon sections within these conduits will retain the highly aligned native collagen fiber structure[4,144]. The goal of the work was to evaluate the suitability of collagen sections created through our fabrication process for neuronal applications such as NGCs. As such we assay the growth of nerves, or nerve-related cell types at increasing complexities, verifying the growth.

5.2 *IN VITRO* GROWTH OF NEURONAL CELLS ON THE TENDON SECTIONS

The growth of Schwann cells, along with their adhesion and proliferation is important as they are an integral part of the peripheral nerve repair process[272]. In a healthy nerve they primarily serve to ensheath and myelinate nerves, however when the nerve is damaged they undergo a phenotypic switch to a regenerative state, acting in a neurotrophic role[283]. Once the nerve is damaged, and following fluid infiltration, Schwann cells will migrate from the proximal and distal stumps, proliferating and

forming glial Bands of Büngner[252]. It is this process that the nanotopography of the tendon sections should align, and ideally, promote proliferation; therefore the growth of Schwann cells on the material was assessed.

5.2.1 Schwann cell growth and alignment

Initially, Schwann cells were cultured on tendon sections, collagen gel, and standard tissue culture polystyrene (TCPS). Cells were seeded onto tendon sections, collagen and TCPS wells, along with each substrate coated with PDL. The adhesion was measured after cells had incubated on the substrate for 0.5 hours, 1 hour and 2 hours (Figure 5.3A). At all time points, Schwann cells displayed the greatest adhesion on the PDL-coated TCPS while uncoated tendon and collagen displayed the least cell adhesion at 0.5 hours. The addition of PDL served to restore the adhesion at both time points when compared to both TCPS and PDL TCPS. After 2h hours of incubation, collagen showed greater adhesion compared to tendon, however at no time point was there any statistically significant difference between PDL-coated tendon and PDL-coated collagen. In the proliferation assays (Figure 5.3B), a 1 hour incubation time was used prior to washing non-adherent cells and adding media to prevent non-adherent cells from being washed off of the tendon substrates. One day following cell seeding, no significant difference was seen between any conditions, however for the rest of the days the PDL coated tendon and TCPS had a greater number of cells, indicating increased proliferation. On day 10, PDL tendon and PDL TCPS had a greater number of cells than all other substrates, while the tendon and TCPS had a greater number of cells than the PDL and the PDL-coated collagen.

The growth of Schwann cells, along with their adhesion and proliferation are important as they are an integral part of the peripheral nerve repair process [272]. At several of the time periods observed, collagen and tendon substrates had reduced adhesion

compared to the synthetic TCPS. The addition of positively charged PDL was able to increase adhesion of all substrates at each of the time points, including increasing the adhesion of Schwann cells on tendon and collagen to comparable levels with TCPS (Figure 5.3A). This is most likely a result of the positively charged PDL increasing the adhesion of the Schwann cells through a charge interaction [284,285].

Schwann cells cultured on each substrate were then stained using rhodamine-phalloidin to show actin, elucidating cellular structure. Differing morphologies were seen on each of these substrates. Cells on TCPS and Collagen displayed more spreading with no particular orientation of the actin cytoskeleton (Figure 5.4A,B), while cells cultured on tendon displayed a more condensed and elongated morphology with a distinct orientation following the direction of the tendon's collagen fibers (Figure 5.4C). No obvious differences in morphology were seen between each substrate and the equivalent substrate coated with PDL (Figure 5.4D-F). Any differences in perceived cell density in images in Figure 5.4 are a result of attempting to obtain clear, representative images of the cytoskeleton rather than a reflection of actual cell density. Alignment of Schwann cells has been shown to upregulate markers of myelination and down regulate neurotrophin and neurotrophic receptors associated with an immature Schwann cell phenotype [286]. Aligned Schwann cells, in the form of bands of Bünger, are also a crucial step during regrowth of axons in nerve repair following Wallerian degeneration[286,287].
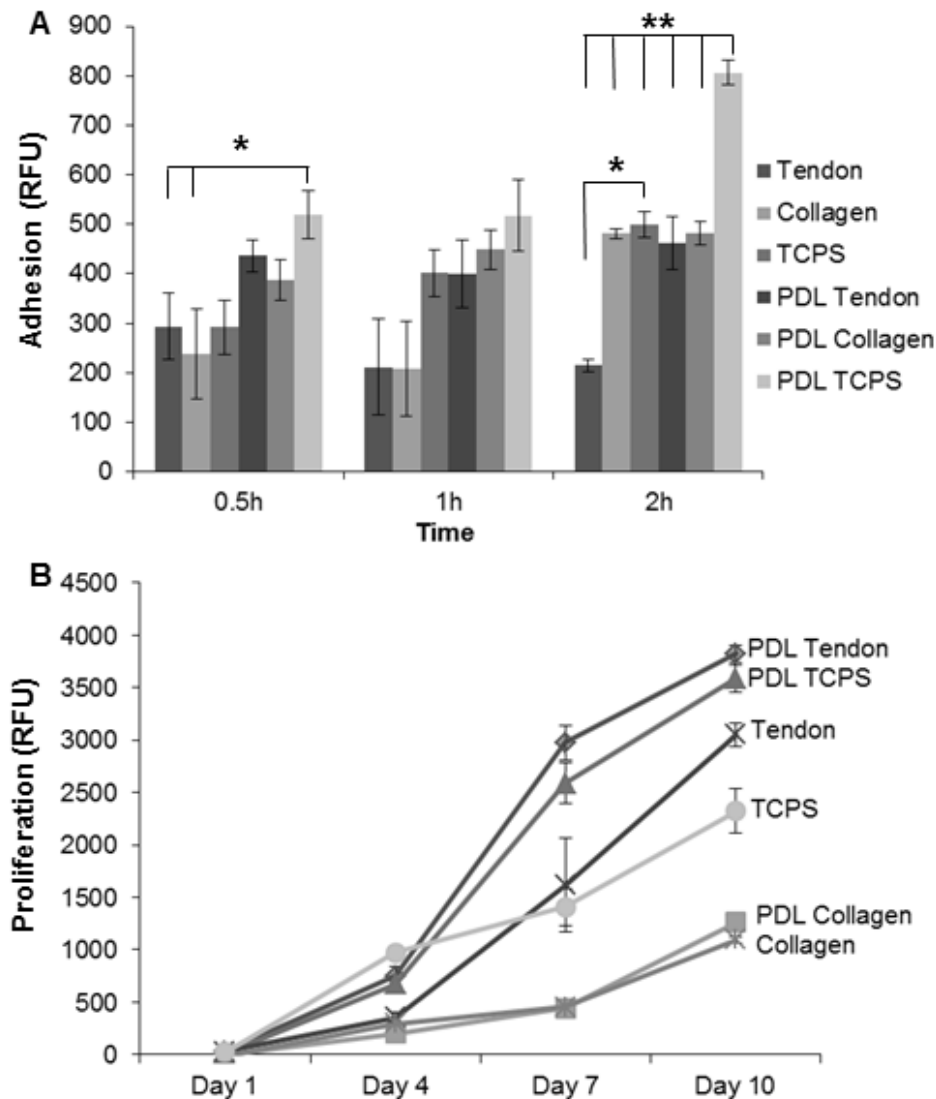
Figure 5.3: A) Adhesion of Schwann cells on tendon, collagen or TCPS, along with each substrate coated with PDL; Measured via AlamarBlue assay after cells are incubated on the surface for 0.5h, 1h and 2h before having non-adherent cells washed off. No difference is seen in adhesion after 1h of incubation. Statistical significant of $p<0.05$ indicated by * and $p<0.005$ by **. **B)** Proliferation rate (via AlamarBlue assay) of Schwann cells on the same culture surfaces measured at 1, 4, 7 and 10 days. An initial incubation period of 1h was used. Detailed statistical differences can be found in [69]; PDL tendon and PDL TCPS are statistically greater than other substrates at days 7 and 10.
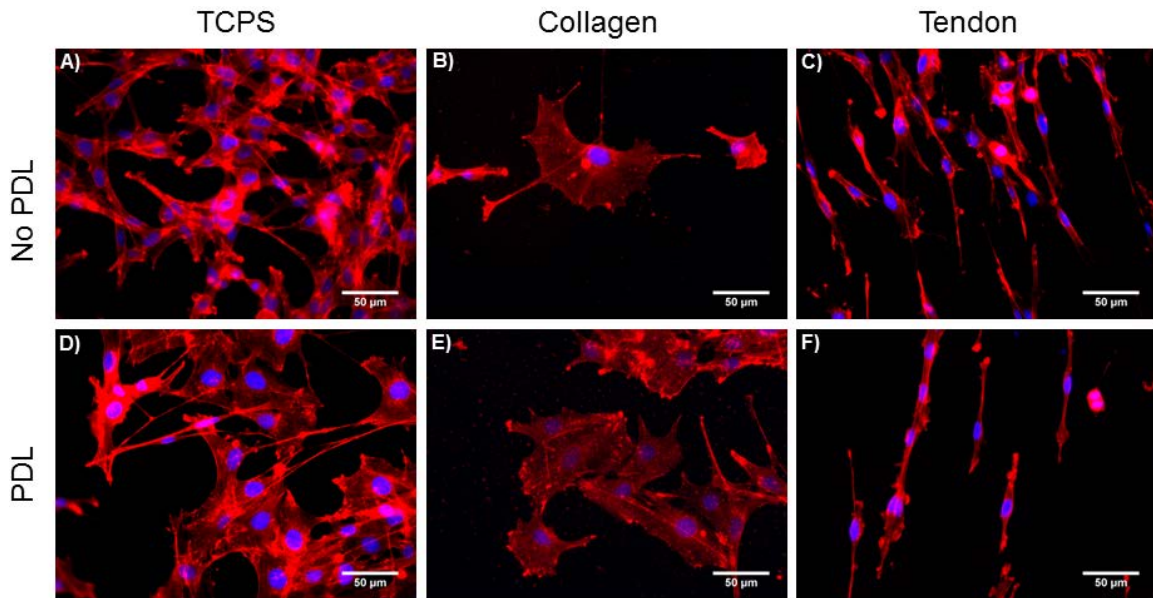
Figure 5.4: Fluorescence images of Schwann cells cultured for 1 day on: **A)** TCPS, **B)** collagen gel, **C)** tendon, **D**) PDL-coated TCPS, **E)** PDL-coated collagen, **F)** PDL-coated tendon. Cells orient along collagen fibers with and without the PDL coating. No difference is seen in morphology with the PDL coating. Red is F-actin staining with rhodamine-phalloidin and blue is nuclei staining with DAPI. Scale bars are 50μm.

5.2.2 Chick dorsal root ganglia growth and alignment

More complex, multicellular systems such as chick dorsal root ganglia (DRG) can also provide insight into how a material will influence peripheral nerve regeneration. Therefore, DRG were explanted from embryonic day 8 chicken eggs and cultured on the tendon surface as well as collagen gels and TCPS. Chick DRG at from day 8 embryos adhere to TCPS, collagen and tendon coated with PDL. By day 3, neurite extensions can be seen on all substrates, with DRG on TCPS and collagen displaying round extension of neurites (Figure 5.5 A,B), while DRG on tendon appear to have extension in the direction of the tendon fibers (Figure 5.5 C). This pattern continues for DRG cultured for 5 days (Figure 5.5 D-F) as well as 7 days (Figure 5.5 G-I). As DRG neurite extensions grow

denser after being cultured for longer time periods on the tendon substrate, neurites appear to extend radially directly surrounding the main DRG body. Once these neurites reach past the direct branching they begin following the tendon fibers. This organization of the neurite outgrowth as demonstrated by the DRG is important in regards to peripheral nerve regeneration as maintenance of functional organization in the repairing nerve is key to prevent wrong connections at the distal end of the damaged nerve [128,288].
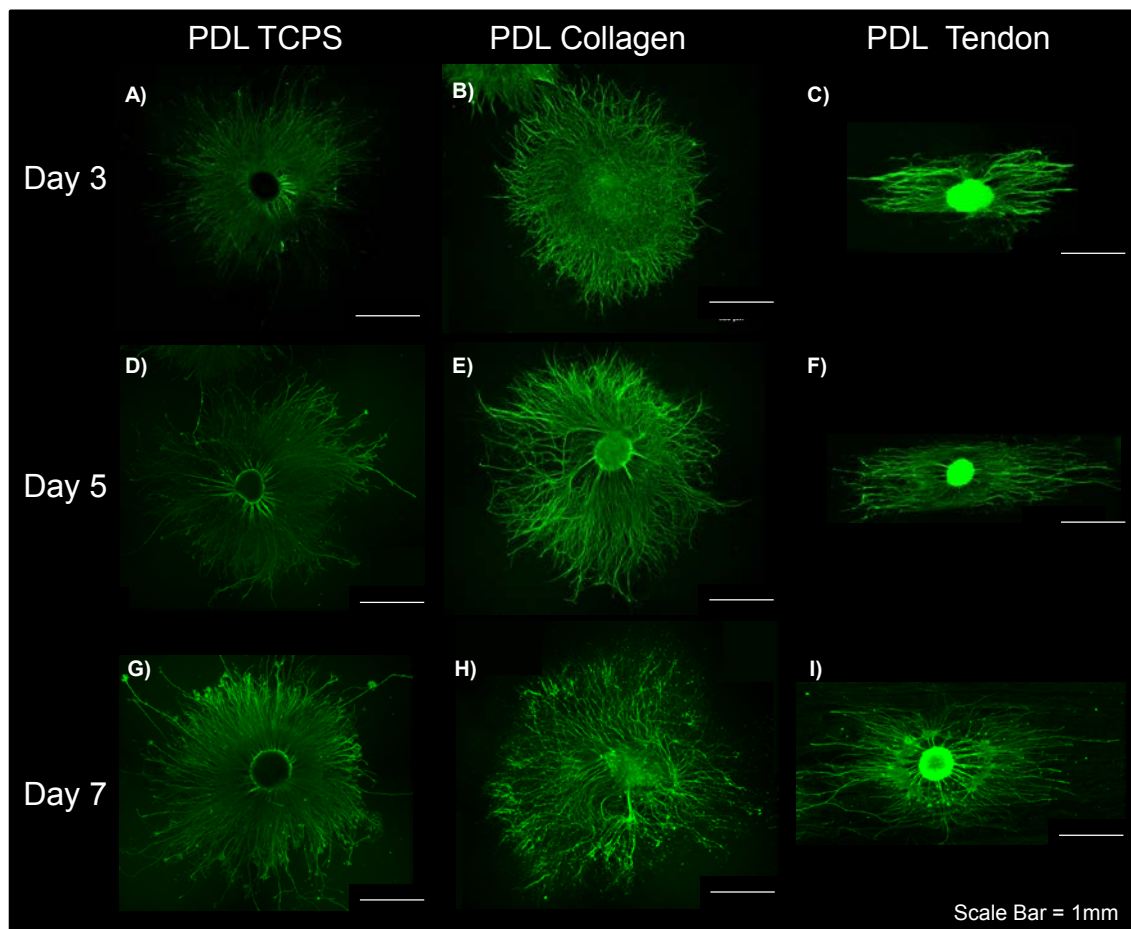
Figure 5.5: Representative fluorescence images of chick DRG isolated at E8 and cultured for 3, 5 or 7 days. DRG were cultured on PDL-coated TCPS **(A,D,G)**, PDL-coated collagen gel **(B,E,H)**, and PDL-coated tendon sections **(C,F,I)**. DRG cultured on tendon sections extend neurites along the orientation of the collagen fibers in the tendon, while DRG cultured on TCPS and the collagen gel extend neurites radially. Green is anti-β-III tubulin staining. All scale bars are 1mm.
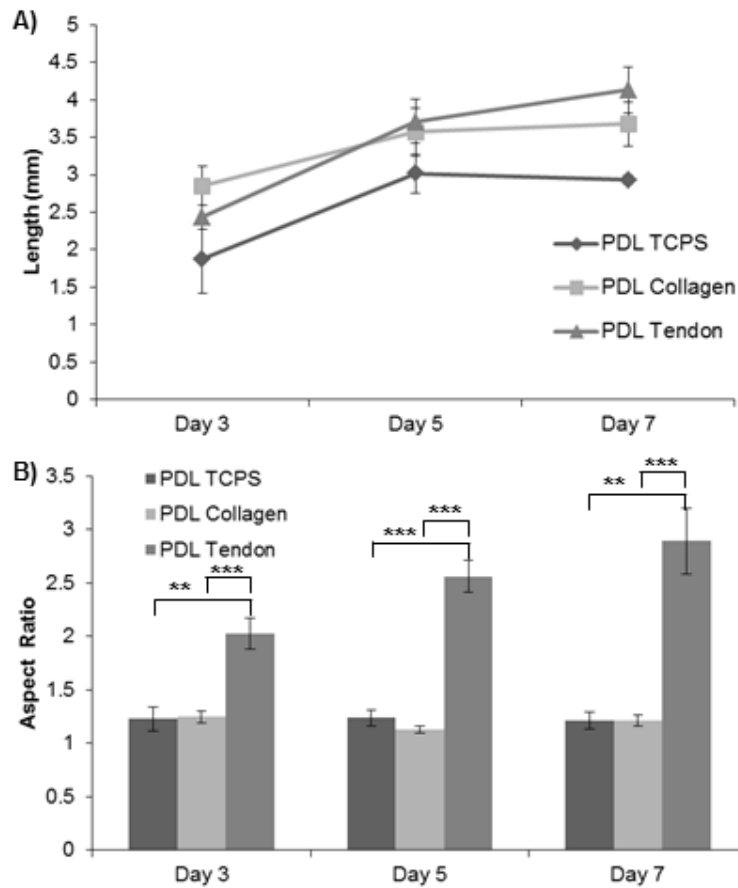
Figure 5.6: Growth of DRG after culture for 3, 5 or 7 days on TCPS, collagen and tendon, each with PDL. **A)** Length in mm of the longest direction of neurite growth, in a straight line through the DRG body. No significant difference between substrates at 3, 5 or 7 days. **B)** Aspect ratio of DRG growth indicating directional growth, where the aspect ratio is the length of the major axis divided by the length of the minor axis. DRG cultured on tendon shows much greater directional growth at all time points. Statistical significance of $p<0.005$ indicated by ** and $p<0.0005$ by ***.

On all substrates DRG extend at similar rates (Figure 5.6A), reaching total lengths of 2.93 ± 0.06mm, 3.67 ± 0.29mm and 4.13 ± 0.31mm by day 7 for TCPS, collagen, and tendon substrates, respectively. Measurement of the aspect ratio (Figure 5.6B) of DRG growth on the substrates shows that DRG grow in one direction preferentially on the tendon substrate compared to the other substrates, at all of the time points observed. The total area of DRG growth (Figure 5.6) was less on the tendon substrate compared to the

collagen gel, however this does not reflect density of the neurites, which was not quantified in these experiments. N=4, 7, 8 for TCPS, collagen, and tendon, respectively, at each time point.

No significant difference was seen in the length of growth (Figure 5.6 A), between the tendon substrate, collagen substrate, or TCPS. However the greatly increased degree of alignment (Figure 5.6 B) observed on the tendon may be beneficial for *in vivo* nerve repair and proper connection formation.
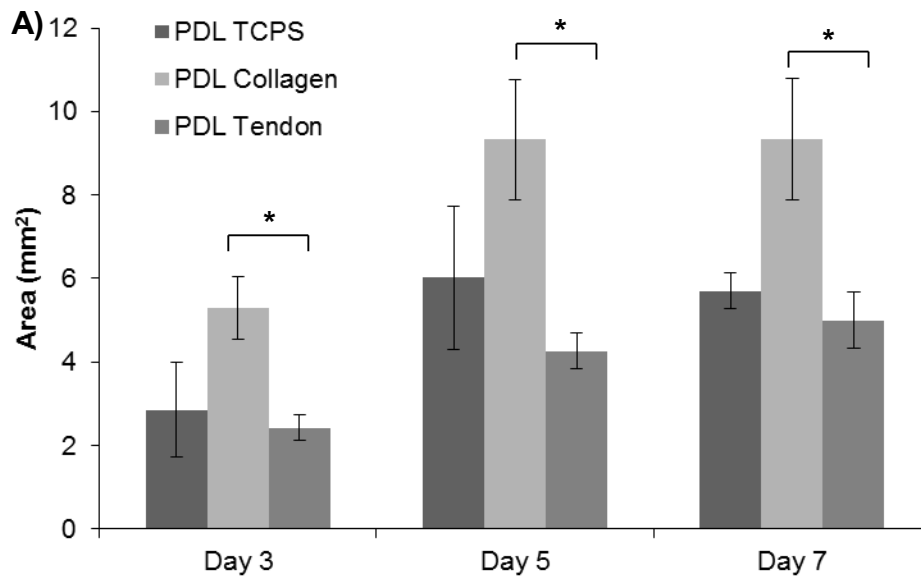
Figure 5.7: Measurement showing the total area of chick DRG grown for 3, 5 or 7 days. Neurite density was not taken into consideration. Collagen shows a greater total area of growth than both TCPS and tendon. Statistical significance of $p<0.05$ indicated by *.

The radial growth, followed by the directional growth that can be seen in day 7 DRG may be explained by the complex nature of neurite outgrowth and nerve growth cone extension. As discussed by Maskery[289], this may be a result of differing adhesion or chemotactic cues. We hypothesize that neurites are initially growing on top of one another close to the DRG body and extend radially. Once they reach a sufficient distance

from the DRG body, they come into contact with the tendon substrate and their direction of growth is influenced. The directional change caused by the tendon should also be noted, as growth cones have a tendency to grow in a uniformly straight path on flat surfaces[289,290].

DRG isolated from several species, such as chicken and rat embryos have been used to model nerve growth for various purposes, including guiding or directing oriented neurite growth [291,292]. Different methods of directing the growth of chick DRG have been used including micropatterning growth factors[293], and proteins[294] onto surfaces. Other experiments have utilized physical cues such as magnetically aligned collagen fibers[292], Schwann-cell-mimicking topography in poly(dimethylsiloxane) [295] or electrospun fibers [296,297]. The Schwann cell-patterned conduits and electrospun poly-l-lysine conduits were able to achieve oriented DRG growth on the synthetic polymers, indicating that the orientation observed on the tendon substrates can be a result strictly from physical cues rather than a result of the inherent property of the collagen. However, the growth of DRG on electrospun poly-ε-caprolactone fibers compared to a blend of collagen and poly-ε-caprolactone resulted in greater alignment but decreased neurite length on the collagen-containing substrate[297]. This indicates that the alignment may also be influenced by some adhesion molecule or other binding site found on collagen.

5.3 *IN VIVO* NERVE GROWTH IN A RAT SCIATIC NERVE DEFECT

In vitro analysis of nerve growth may give some indicators as to whether a material will function as a substrate for nerve regeneration; however, the injured nerve environment is a complex milieu of cell, inflammatory, and neurotrophic signaling responses that cannot recapitulated *ex vivo*. As such, animal models have been developed that allow evaluation of a material or design's regenerative capability. Sciatic nerve

injury models have been used for over a century in various forms, and have shown to be a relevant estimator of nerve repair[298].

The objective of this study was to determine whether tendon-derived NGC created using Bioskiving will promote nerve regeneration *in vivo*, in a rat sciatic nerve defect model, and how promoted regeneration will compare to the "gold standard", which in the case of syngeneic animals can be an isograft rather than an allograft. This experiment was designed to measure several key factors: functional recovery, morphological analysis, and a quantitative assessment of cellular composition. As such, cryosectioning was chosen in order to maximize the integrity of the antigenic markers, with the limitation that tissue quality is not as well maintained as with standard paraffin-embedded microtomy. Additionally, multiple sections along the length of the implant were analyzed in order to reduce any bias from selection along the length of the nerve.

5.3.1 Conduit design

A number of nerve guidance conduits have been developed and received FDA approval, including several comprised of collagen. However, none of the clinically available conduits intentionally contain physical cues to guide and improve the nerve regeneration. Our decellularized tendon-derived material contains a hierarchical structure of bundled collagen fibers and fibrils, and we have shown these to guide and orient neuronal growth[299]. Furthermore, maintenance of the native collagen structure may affect peripheral nerve regeneration as collagen has been shown to influence cell behavior through intracellular signal triggering[300]. In order to increase the contact area that regenerating nerves will have with the material, multiple smaller tubes were included in the lumen of the conduit (Figure 5.8), an idea that has been discussed and demonstrated a number of time previously[150,252,257]. Additionally, the particular conduits used here were constructed to match the anatomy of the rat nerve in both diameter and the choice of three

inner lumen for the three main bundles of the rat sciatic nerve that the distal end terminate in; the common peroneal, tibial, and sural nerves[301]. The conduits were crosslinked with glutaraldehyde, as results work in Chapter 3 indicated that non-crosslinked samples degrade rapidly. We reasoned that samples which degraded rapidly following implantation would not provide adequate physical cell guidance cues for an adequate lifetime of the conduit.
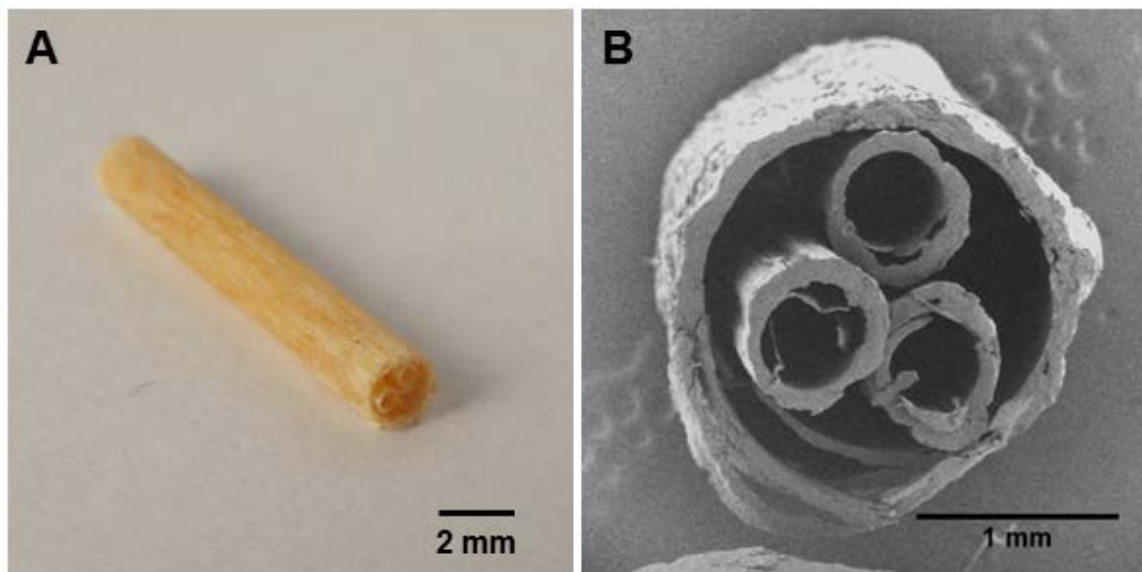
Figure 5.8: A) Photograph of NGC showing general structure and luminal fillers. **B)** Cross-section electron micrograph showing conduit and luminal fillers.

5.3.2 Sciatic nerve defect model

The *in vivo* work involved repairing a defect created in the rat sciatic nerve with either an isograft from a syngeneic rat, or with a tendon-derived NGC. The surgical procedure (illustrated in Figure 5.9) was as follows: Briefly, rats were anesthetized and an incision made parallel to the femur. Muscle splitting and blunt dissection were used to expose the sciatic nerve at the exit from the pelvis to the distal trifurcation. A 5mm

segment was excised and the nerves allowed to retract, after which the isograft or conduit were implanted and secured to both ends of the nerve using two epineurial mattress sutures. The conduits were 17mm long and had 1mm of nerve overlap at each end, creating a critical-sized defect[302] of 15mm gap. The muscle and skin were then closed and the animals allowed to recover.

At the initiation of the experiment 25 male Lewis rats each weighing 250-300g were obtained and 10 animals allocated for conduit implantation, and 10 isograft implantation, while 5 rats were used to provide the 10 donor nerves. During the course of surgery one rat expired, while three rats were found to have dehiscent wounds in the immediate days following surgery. From thereon, there were groups of 8 each in the isograft and conduit groups. Four rats from each group were sacrificed at 6 weeks and the remainder at 14 weeks. No additional complications were noted during the procedure, and no autophagy was noted throughout the course of study. Lewis rats in particular were chosen as they have shown to have a much lower rate of autophagy[303,304].
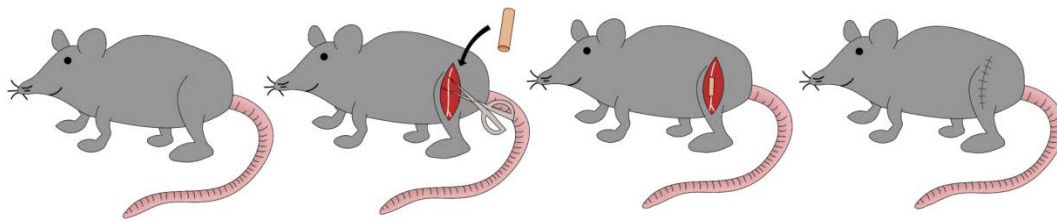
Figure 5.9: Schematic illustrating the implant location and basic procedure of a sciatic nerve injury repair.

5.3.3 Functional assessment

As a means of quantifying functional recovery at non-terminal time points, we conducted a weekly walking track assessment and calculated the Sciatic Functional Index from the injured and healthy rear paw prints (Figure 5.10). A detailed description of the test and analysis method can be found in the methods and materials section (Section

5.4.2.3). This test has appeared in several variations[305,306] since it's development by de Medinaceli[307]. No significant difference was observed between the two experimental groups in terms of SFI. The animals recovered at similar rates, with isograft rats starting with a SFI of -103.73 ± 5.35 (n=8) at week 2, progressing to 84.86 ± 7.13 (n=8) at week 6 and finally a SFI of -44.14 ± 10.27 (n=4) at week 14. Conduit-treated rats progressed from -96.06 ± 11.03 (n=8), to -81.04 ± 10.25 (n=8), to -53.62 ± 6.81 (n=4) at 2, 6 and 14 weeks respectively. These results taken on their own suggest that both groups are achieving similar functional recovery rates.
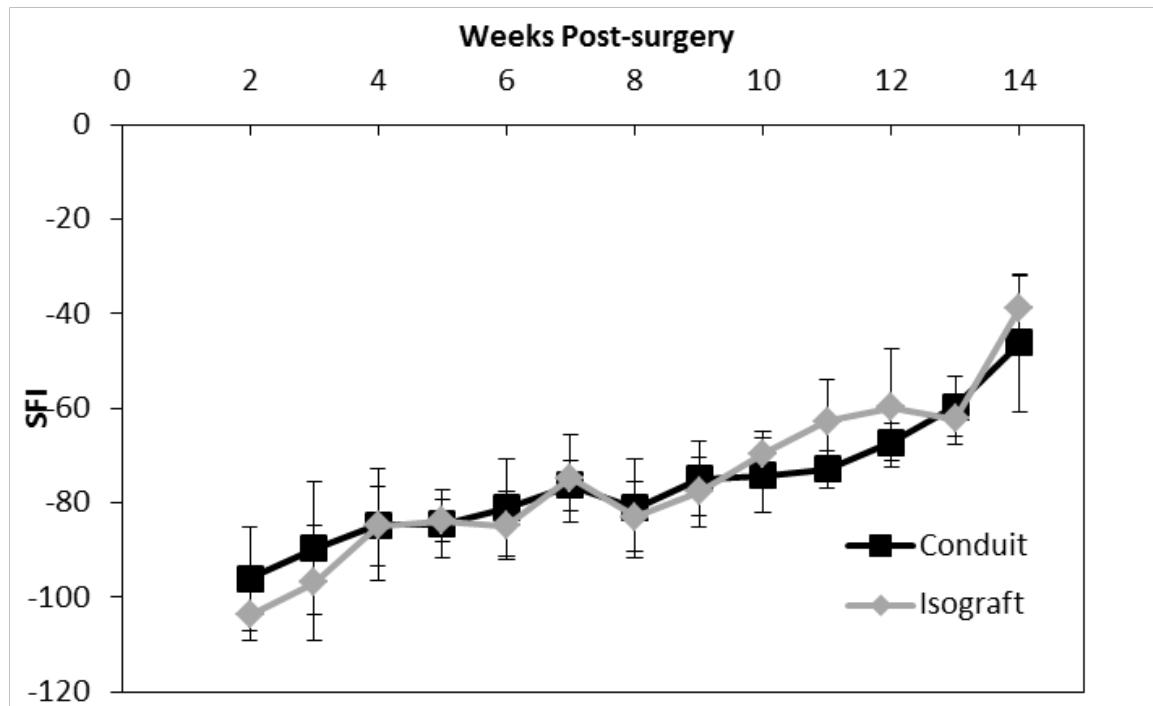
Figure 5.10: Sciatic functional index (SFI) showing progression of recovery from weeks 2 through fourteen post-surgery, for conduit and isograft treated animals (n=8 for weeks 2-6, n=4 for weeks 7-14).

5.3.4 Conduit explantation

Rats sacrificed at both 6 and 14 week time points displayed no overt signs of infection or inflammation at the wound site or surrounding the surgical implant. For the

isograft-treated animals, the nerves appear to be growing well at week 6 (Figure 5.11A), however at week 14 there appears to be some aberrant nerve sprouting in some animals at the interface between the isograft and distal and proximal nerve stumps (Figure 5.11 B). This neuroma may indicate that there is dislocation of the nerve and potential scarring which may result in fewer axonal connections.

The conduit-treated animals however show no such additional nerve outgrowth or neuroma formation (Figure 5.11 C,D). As discussed by others, the conduit may function to contain the nerve outgrowth preventing fibrosis and neuroma[308]. The overall structure of the conduit appears to be degrading between the 6 and 14 week time points as evidenced by the rounding over of the ends of the conduits and evidence of blood vessel regeneration can be seen. Despite being glutaraldehyde crosslinked, these results here again demonstrate that the conduit remains biodegradable.
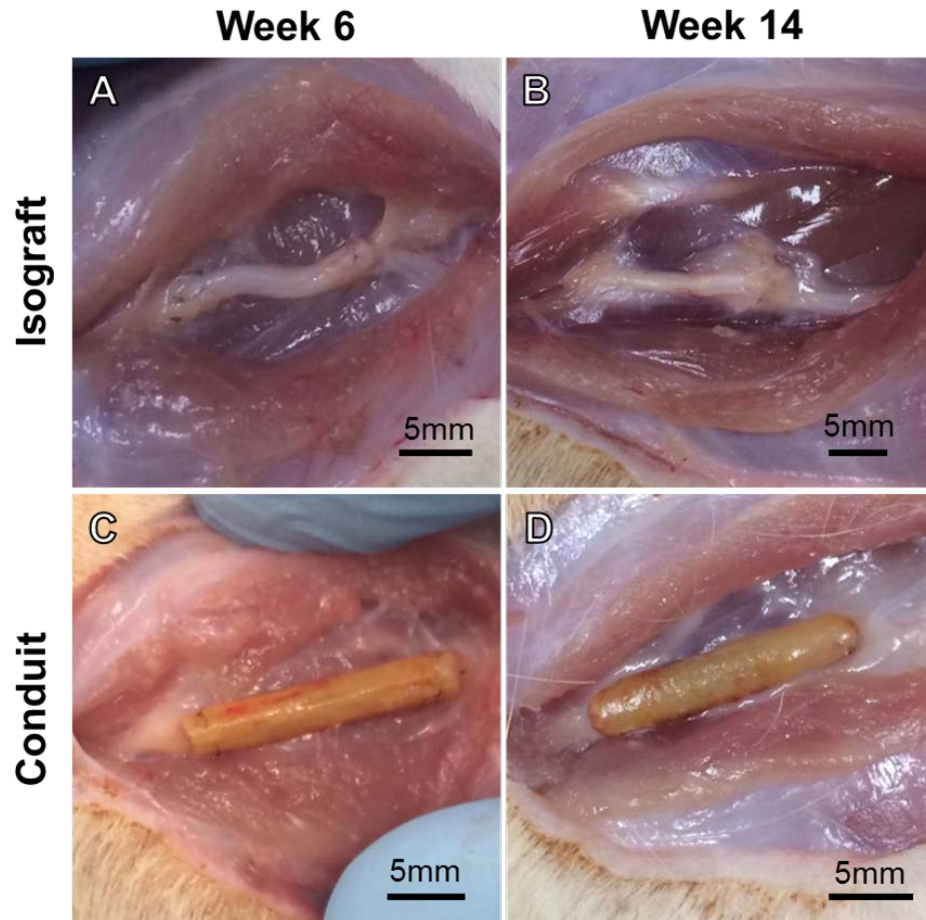
Figure 5.11: Representative photographs showing conduits at time of explant, following sacrifice. **A,B)** Isograft at week 6 and 14; **C,D)** Conduit at week 6 and 14.

5.3.5 Gastrocnemius weight

One of the muscles innervated by the sciatic nerve is the gastrocnemius muscle, and as such reinnervation should prevent muscle degeneration and subsequent muscle weight loss. Gastrocnemii were carefully excised from the experimental side and contralateral side of the animals (Figure 5.12 A-E). At week 6 the average healthy isograft gastrocnemius muscle weighed 2.55g, compared to the treated side of 0.55g, a reduction to 21.6% of the healthy weight, while the conduit group had weights of 2.65g and 0.65g, a reduction of 23.8%. At week 14, the isograft group had muscle weights of 2.85g (healthy) and 1.325g (experimental), a reduction to 46.9%. The conduit group had

weights of 2.625g and 0.45g, a reduction to 17.1% of the original weight. The isografts likely had earlier innervation, and thus had less muscle loss, or compounding factors prevented muscle restoration despite function. There is no significant difference between the muscle mass of the conduit at week 6 and week 14 which can may be due to the fact that there are a number of bifurcations in the sciatic nerve, of which only two enervate the gastrocnemius muscle. Multiple other nerves enervate other muscles, such as the flexor digitorum longus and flexor hallucis longus, involved in toe position, which may account for the restoration of function as measured with SFI, yet a lack of gastrocnemius recovery.
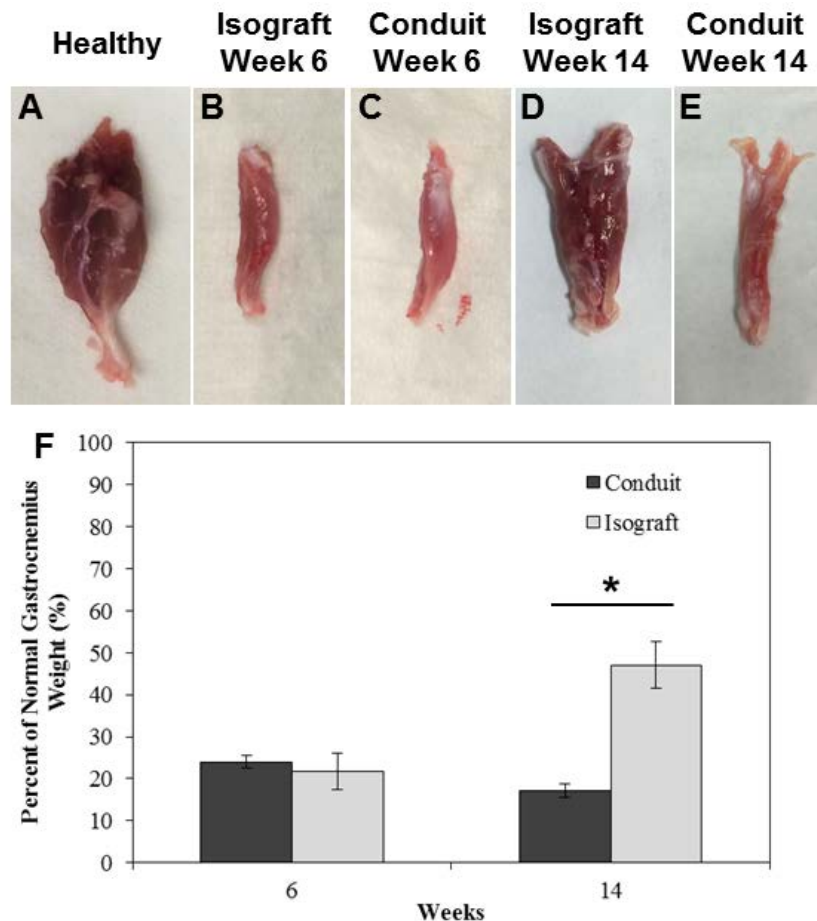
Figure 5.12: Photographs showing representative gastrocnemius muscles excised from **A)** healthy rats; **B,C)** Isograft and conduit treated rats at week 6; **D,E)** Isograft and conduit treated rats at week 14. **F)** Graph showing gastrocnemius weight of treated side, calculated as a percent of healthy side weight. $*$ = $p < 0.05$

5.3.6 Histological assessment

The regeneration of the nerve at 6 and 14 weeks was evaluated using a Masson's trichrome stain. Figure 5.13 shows representative images of the nerves seen at the proximal, middle, and distal sections. Compared to healthy, control nerve sections (Figure 5.14), both isograft and conduit samples show a differing morphology, with no defined axons visible at week 6 of the isograft. At week 14 however, defined structures appear to have morphology consistent to healthy nerves, including an epineurium. The conduit sections at both 6 and 14 weeks show staining representative of nerve tissue; however well-defined bundled nerves are not observable, as they are in the isograft. The tissue at week 6 is relatively sparsely packed with some collagen generated in the repair process in areas (Figure 5.13 D) which does not appear to be a part of the collagen conduit. The collagen of the conduit and the collagen regenerated during the healing process can be identified via differences in depth of staining, as the collagen used in the conduit is much more densely packed, resulting in a deep blue color, while regenerated collagen is pale blue. It is possible that this collagen may be regenerating perineurium-like structure or some other collagen integrated in the nerve structure. In addition to nerve tissue, some areas of the conduit also appear to show large blood vessels regenerating (Figure 5.13 D, E). At week 14 the nervous tissue in the conduit samples appears much more densely packed, with tissue throughout the conduit walls, and along the outside of the conduit. A fibrous collagen layer is also visible in multiple of the explanted samples, which may be regeneration of the epineurium-like structures (Figure 5.13 K, 5.15 B).
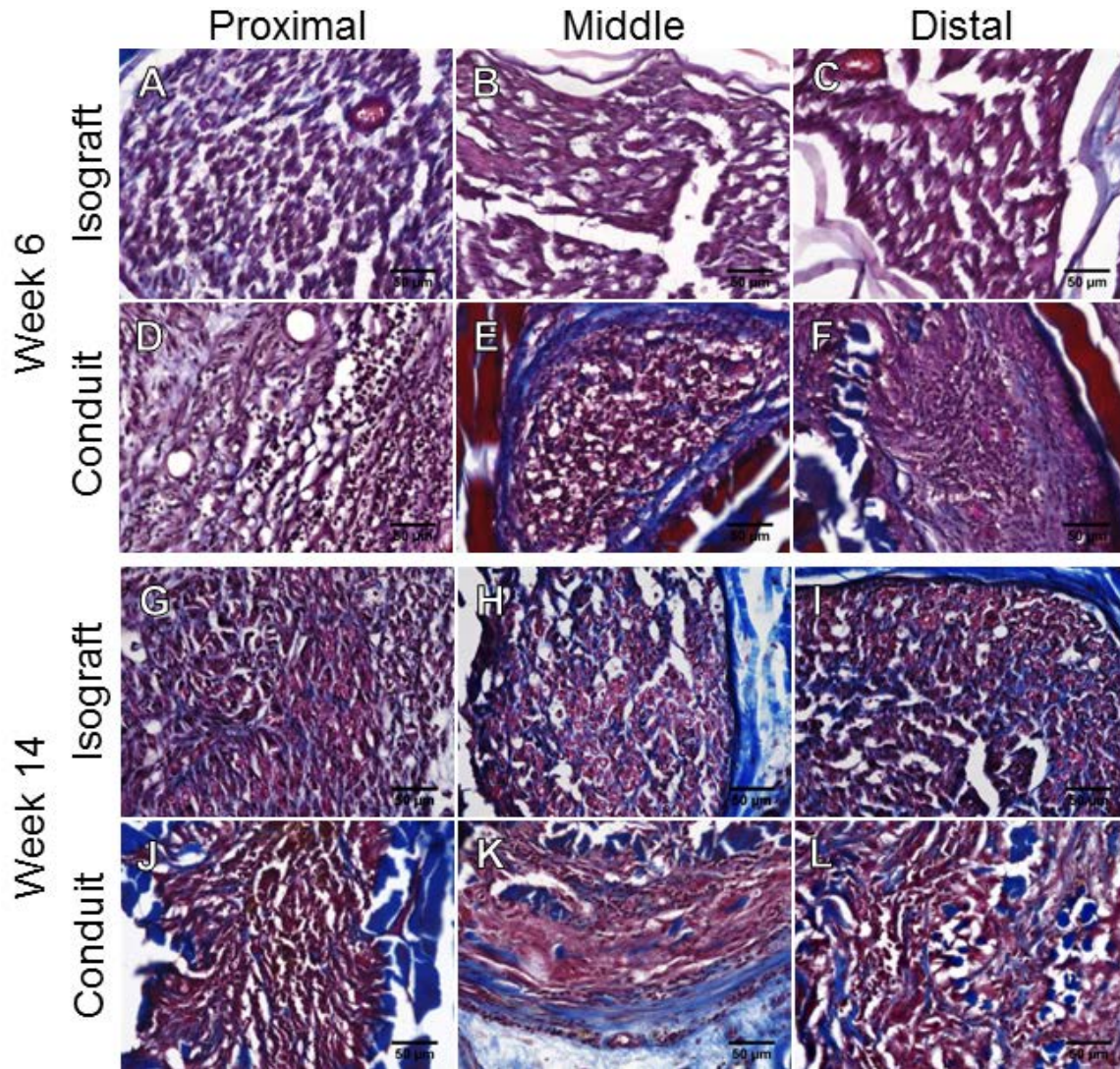
Figure 5.13: Representative histological sections of proximal, middle and distal isograft **(A,B,C)**, and conduit **(D,E,F)** as week 6. Week 14 isograft **(G,H,I)** and conduit **(J,K,L)**.

Overall, the trichrome stain of the isograft shows an increase in density, and restoration of original morphology between weeks 6 and 14. The conduit sections show a generation of physiological support, such as epineurium and perineurium-like structures, blood vessels; however, identification of myelin is not possible with this stain[309]. An increase in tissue density throughout the conduit can be observed in both Figures 5.13 and 5.15, while Figure 5.15 also shows that the lumen of the conduit, along with the

luminal inserts appear to remain patent, with some deformation in structure of the luminal inserts.

The size difference between the conduits should also be noted. Figure 5.15 shows two images of representative sections at week 14, where the conduit is roughly 2.5 times greater in area than the isograft (conduit average size: 7.36mm^2 vs isograft average size: 2.89mm^2) (Figure 5.15). The original design of the conduit matched the inner lumen of the conduit to the size of the healthy nerve; however, there appears to be a significant amount of neural tissue growth occurring on the exterior of the conduit in several animals. Again these figures show encasement of this outer nerve tissue with a fibrous collagen layer containing blood vessels (Figure 5.15 B).
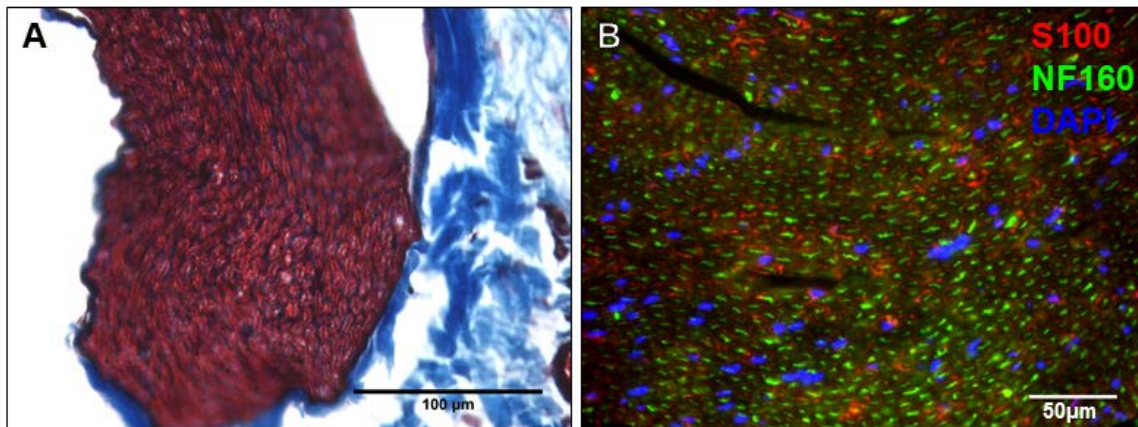
Figure 5.14: A) Masson's trichrome staining and **B)** double immunofluorescence of control healthy nerve sections. Red fluorescence indicates S100, representative of Schwann cells, green indicates neurofilamen-160, representative of neurons and blue indicates cell nuclei.
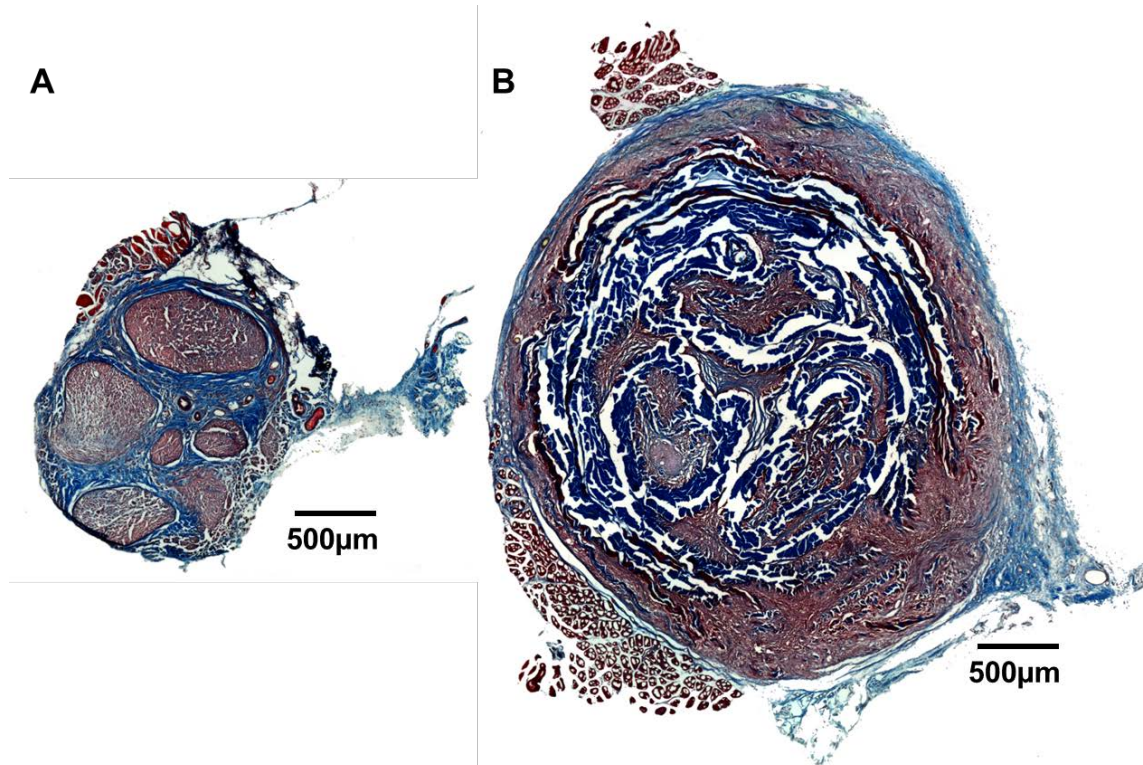
Figure 5.15: Representative composite micrographs of a **A)** whole proximal isograft section and **B)** whole proximal conduit section, stained with Masson's trichrome. The dense tendon-derived conduit collagen stains dark blue while the loose regenerated collagen stains light blue.

5.3.7 Immunohistochemical analysis

Two specific markers of regeneration were used: the middle weight protein of neurofilament (NF160), found in neurons, and the protein S100, indicative of Schwann cells[310]. The results of the IHC staining were similar to those of the Masson's trichrome. The isograft at 6 weeks shows loosely packed structures, staining for some NF160 and S100 while the conduit shows some NF160, little to no S100 in the proximal and middle conduit. In the distal portion of the conduit however, a greater amount of staining for S100 can be seen. We believe this to be Schwann cells remodeling the distal portion of the nerve stump to create a local microenvironment that promotes axonal regeneration[311]. The isograft at week 14 shows a much greater density in nerves, and much more S100

with an expected healthy morphology. The conduits at week 14 however show some S100 starting, and a greater degree of NF160 staining.

One major limitation preventing any quantitative analysis from this procedure is autofluorescence from collagen. In particular, the glutaraldehyde-crosslinked collagen in the conduits has high levels of autofluorescence, overlapping with the spectra of both Texas Red and fluorescein isothiocyanate, used here, as can be seen in Figure 5.16E,L. Similar autofluorescence was also observed in unstained control conduits.

As an alternative to double immunostaining with fluorescently conjugated antibodies, we switched to single immunostaining with horse radish peroxidase (HRP) conjugated antibodies. This allowed us to get a quantifiable measure of NF160 and S100 present in each section of the conduit and isograft. Similar analytical techniques have been demonstrated previously using immunofluorescence for neurofilament, S100 and laminin[312,313]. Figure 5.17 shows the subsequent analysis of this, where NF160 appears to be higher throughout the length of the conduit, declining slightly as you progress from proximal to distal end. However, it must also be noted that neurofilament intensity has been shown to be significantly higher in healthy nerves compared to newly regenerated nerves[309], and this analysis does not reflect intensity of staining.

Figure 5.17B shows higher S100 in all sections of the conduit, but the distal nerve, compared to the isograft. There is however a significant drop off in S100 content following the proximal nerve, showing that many of the nerves in the conduit may not be myelinated, or may still be in the process of regenerating. The difference in cross-sectional size here should also be accounted for, as there is higher NF160 and S100 content in conduit sections which are significantly larger than the isografts, as shown in Figure 5.17. This means greater nerve regeneration area, and could account for the higher amount of staining, but doesn't necessarily mean all that excess nerve is necessary to properly innervate the normal targets or reconnect with the distal stump. This is a common occurrence with nerve regeneration, known as compartmentation, where

daughter axons will sprout from the damaged nerves and grow as many small units. Some of these axons will reach their target and mature into larger axons, which will in turn cause the retraction of axons that have not reached their targets[264].
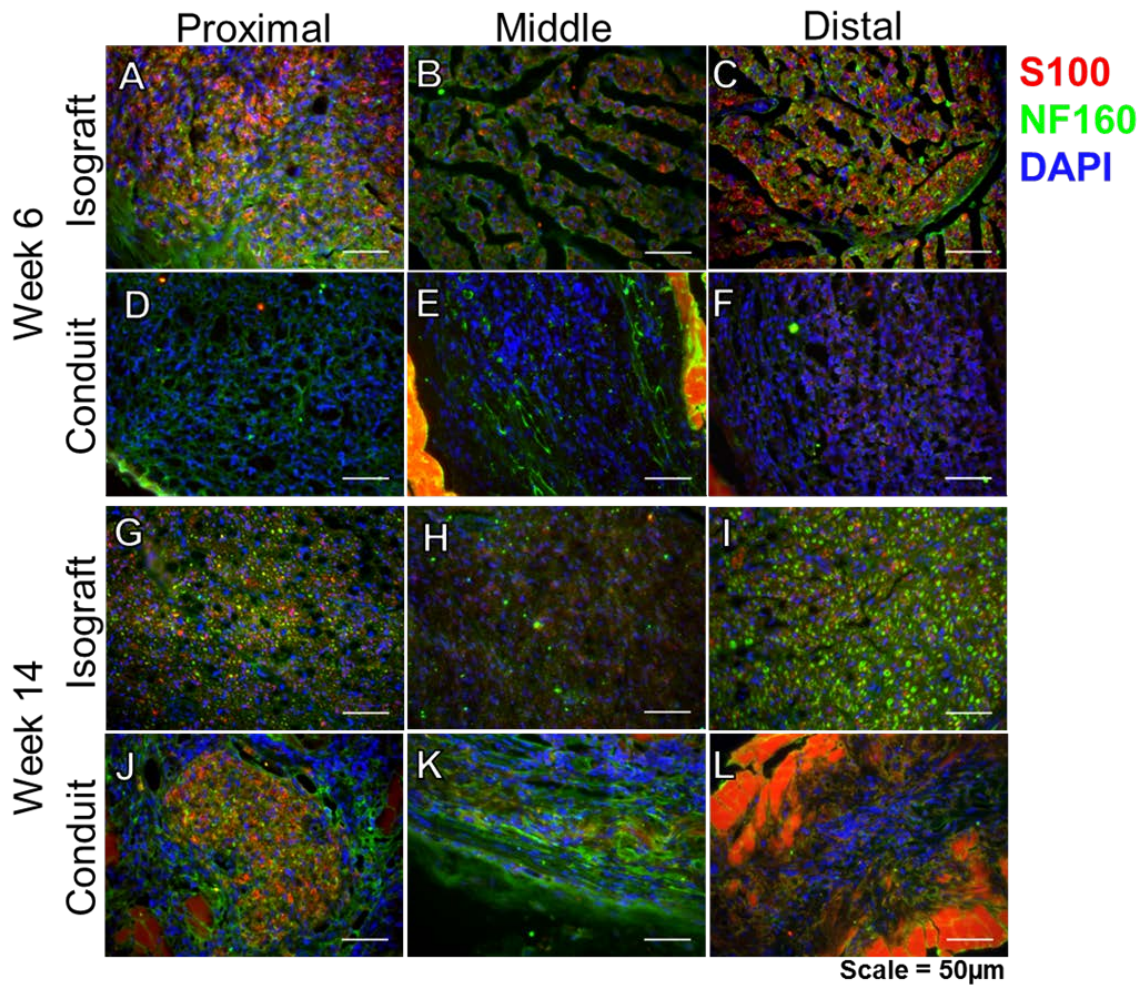
Figure 5.16: Representative immunofluorescent micrographs of proximal, middle and distal isograft **(A,B,C)**, and conduit **(D,E,F)** at week 6. Week 14 isograft **(G,H,I)** and conduit **(J,K,L)**. Red = S100 (Schwann cells), Green = NF-160 (neurons) Blue = DAPI (nuclei).
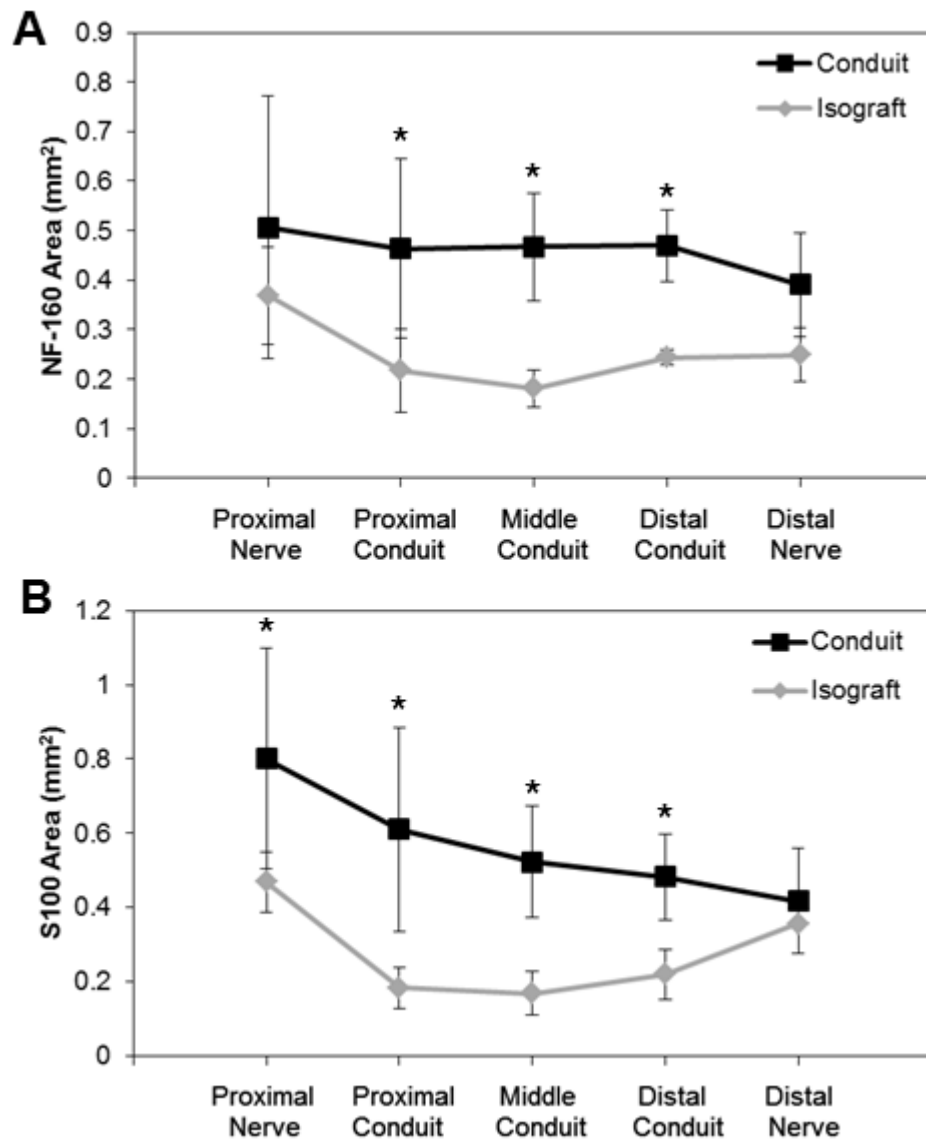
Figure 5.17: Averaged total **A)** NF-160 and **B)** S100 content present in entire sections of proximal through distal nerve and conduit sections (n=4). (* = P-value < 0.05)

Additionally, the presence of S100 indicates that there are glial cells such as Schwann cells present, but doesn't necessarily mean they are myelinating the nerves, as Schwann cells are also a crucial player in the repair process and may also wrap around nerves without myelinating them[309].

To account for differences in cross-sectional area, the volume of total stained area for both NF160 and S100 can be converted to a percent, or area fraction of the total conduit/isograft (Figure 5.18). If that is done, the isograft samples have higher percent areas of NF160, but not S100. Similar studies calculating area fraction of S100 and neurofilament staining have been conducted for Neuragen nerve guidance conduits by Carriel et al.[312] and found 14.24% S100 and 5.43% neurofilament (compared to 12.44% S100 and 7.44% NF found here), however differences in rat strain, staining technique (fluorescence vs. HRP), and analysis technique, make direct comparisons difficult.
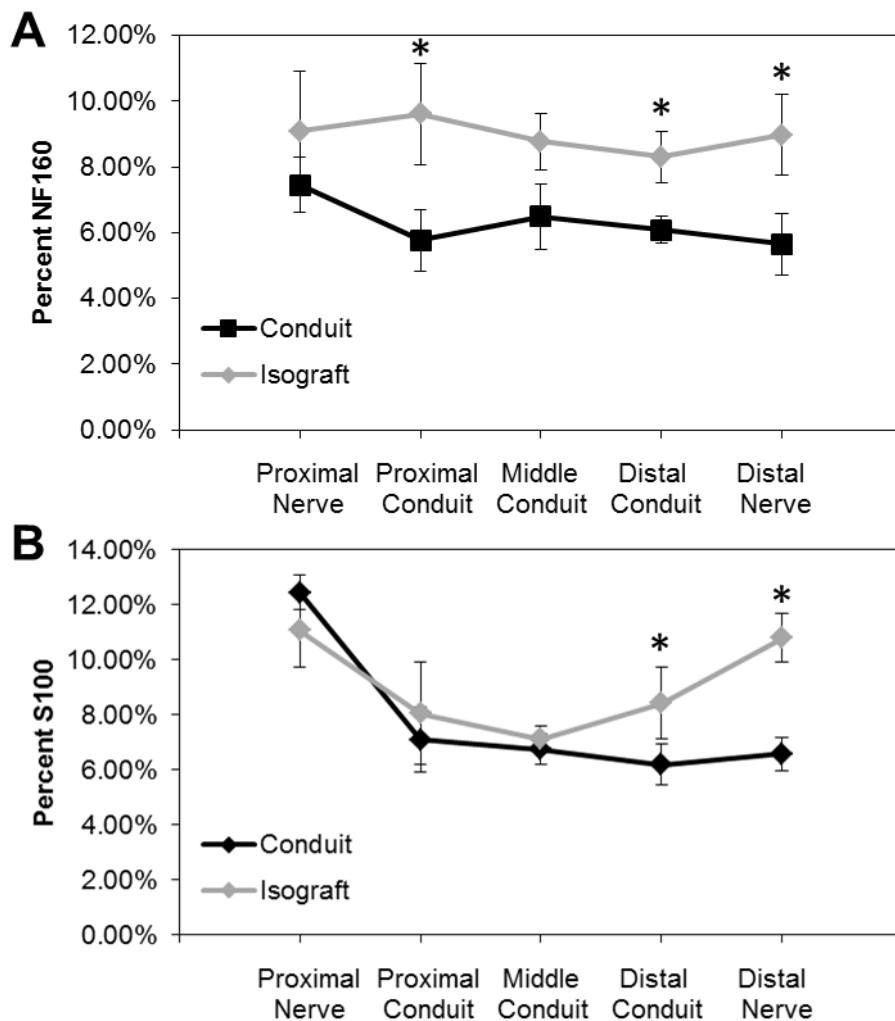
Figure 5.18: A) NF-160 and **B)** S100 content normalized as a percent of the cross-sectional area for proximal through distal nerve and conduit sections (n=4), * = p<0.05.

5.3 SUMMARY

The results presented here suggest that nerve guidance conduits constructed from decellularized tendon sections can function to repair damaged peripheral nerves. This is demonstrated through neuronal-related growth *in vitro* and *in vivo* with systems of increasing complexity. Schwann cells are able to grow and align on the material in the orientation of the collagen fibers, and proliferate more rapidly than on collagen gels. Chick dorsal root ganglia are also able to grow on the tendon and extend neurites out along the fibers in a highly oriented manner.

Lastly, a multi-lumen nerve guidance conduit constructed from decellularized tendon via Bioskiving was able to induce nerve regeneration over a critical-size defect. At week 6 post-implantation, the tissue regenerated in the nerve guidance conduit is not as dense, nor as morphologically similar to healthy nerves when compared to isografts; however, functional recovery can still be observed. At week 14 post-implantation, the regenerated tissue is more densely packed and representative of healthy nerve tissue. Tissue is generated throughout the luminal fillers of the conduits along with the exterior of the conduits. Additionally, supporting structures like blood vessels, and epineurium and perineurium-like structures are observed to regenerate. Lastly, the tissues stain positive for NF160 and S100, at total levels greater than isografts.

Taken together, these results indicate that tendon-derived nerve guidance conduits are able to support peripheral nerve repair. Future work should consider potential improvements such as the addition of other neurotrophic factors to the conduits and analysis of the conduits over longer gaps, and comparing them directly to commercially available nerve guides.

5.4 MATERIALS AND METHODS

5.4.1 *In vitro* growth of neuronal cells on tendon sections

5.4.1.1 Sample preparation

Tendon sections were decellularized and sectioned as previously described. For Schwann cell adhesion and proliferation assays 50μm tendon sections were placed on 22mm diameter glass coverslips (Electron Microscopy Sciences, Hattsfield, PA). For DRG and alignment experiments 50μm sections were placed on Superfrost Plus slides. All samples were sterilized by soaking in 70% ethanol, rinsing 3x with PBS, followed by 1h of UV irradiation. Then, for specified experiments tendon samples, collagen gel-coated wells, or tissue culture poly styrene (TCPS) wells were coated in poly-D-lysine (PDL) (MW 70,000-150,000, Sigma) by filling the well with a 0.01mg/ml solution overnight and rinsing with phosphate buffered saline (PBS).

For adhesion, proliferation and DRG experiments collagen gel samples were prepared using Culturex 3-D Culture Matrix ™ Rat Collagen I (Trevigen, Gaithersburg, MD). The gel was prepared in a 12-well tissue culture plate following the manufacturer's directions. For each plate, 250μl of a 1mg/ml neutralized collagen gel was pipetted into each well, and the plate placed in a 37°C humidified incubator for 1 hour. Each well was then rinsed three times with PBS and either used as-is or coated with PDL as described above.

5.4.1.2 Schwann cell culture

Rat Schwann cells (CRL-2768, ATCC, Manassas, VA) were maintained in Dulbecco's Modified Eagles Medium (Life Technologies, Grand Island, NY) supplemented with 10% heat-inactivated fetal bovine serum and Penicillin-Streptomycin (10,000 units Penicillin, 10,000μg Streptomycin/mL) (Life Technologies) in a 37°C

humidified incubator at 5% CO2. Cell morphology and alignment were observed via immunofluorescence by fixing the cells in 10% neutral buffered fomalin (Sigma) for 10 minutes and then permeabilized with 0.1% (v/v) Triton X-100 (Sigma) for 5 minutes. After blocking with 1% (w/v) bovine serum albumin solution for 30min, the cells were stained with rhodamine-phalloidin (Sigma) for 30min, counterstained the cell nuclei with 4',6-diamidino-2-phenylindole (DAPI) and observed via fluorescence microscopy.

5.4.1.3 Schwann cell adhesion measurement

For adhesion determination, Schwann cells were plated onto the samples (tendon, PDL-tendon, collagen, collagen-PDL, TCPS and PDL TCPS) in 12 well plates at a concentration of 100,000 cells in 50μl per well. Each substrate and time point was assayed in quadruplicate using cells of the same passage number. At a given time (0.5h, 1h or 2h) the wells were rinsed gently with PBS and aspirated to remove any non-adherent cells. To each well, 1ml of media was added with 100μL alamarBlue stock solution (Life Technologies). We then incubated the cells for 5 hour at 37°C. Following incubation, aliquots of the media were transferred to a black 96 well plated and the fluorescence determined using a microplate reader (excitation: $\lambda=550nm$, emission: $\lambda=590nm$). The results are presented as relative fluorescence units (RFU) normalized to background fluorescence.

5.4.1.4 Schwann cell proliferation measurement

For proliferative determination, Schwann cells were plated onto the samples (tendon, PDL-tendon, collagen, collagen-PDL, TCPS and PDL TCPS) in 12 well plates at a concentration of 100,000 cells in 50μL per well. After one hour the wells were rinsed with PBS to remove any non-adherent cells that may have otherwise adhered to the tissue culture plate, rather than the tendon substrates as desired. Media was then added and the

remaining cells were monitored at time points of 1, 4, 7 and 10 days following seeding, via an alamarBlue assay as described above, with a 3 hour incubation period. Between assays the alamarBlue solution was removed and cells cultured in media. Each substrate was assayed in quadruplicate, with the same samples being used for each time point measurement.

5.4.1.5 Chick dorsal root ganglia harvest and culture

Chick dorsal root ganglia (DRG) were isolated from chicken eggs at development day E8. Immediately following isolation we seeded the chick DRG onto PDL-coated tendon samples, PDL-coated collagen gel and PDL-coated TCPS, and incubated them in DMEM supplemented with 2% FBS and 10ng/ml neurotrophin-3 (NT-3, Sigma). The DRG were cultured for 3, 5 or 7 days and then fixed and immunostained to determine morphology. The chick DRG were fixed in 4% (w/v) paraformaldehyde (Sigma) for 15 minutes and then permeabilized them with 0.1% (v/v) Triton X-100 (Sigma) for 5 minutes. After blocking with 2% (v/v) goat serum solution for 45 minutes, we incubated the cells were with primary antibodies at 4°C overnight. The following antibodies were used for the staining: primary anti-β-tubulin-III (T2200, Sigma) (1:250) and secondary antibodies Alexa Flour 488 Goat Anti-Rabbit IgG (Life Technologies) (1:500). After washing with PBS, we added secondary antibodies and then incubated for 45min covered, followed by 3 washes with PBS for 15min each.

5.4.1.6 Chick dorsal root ganglia growth and aspect ratio measurement

DRG outgrowth and orientation were analyzed with modification of the technique described by Richardson et al. [201,314,315]. Briefly, the perimeter of the DRG neurites was traced, and an ellipse fit to the perimeter using ImageJ. The dimensions of the major and

minor axes were recorded and the value of the major axes reported as the length, while the aspect ratio =length major-axis/length minor-axis

5.4.1.7 Statistics

Data were analyzed for significance with IBM SPSS software, using a one-way ANOVA with post hoc Tukey's testing for each time point in the above assays. The α-value was set to 0.05 and results determined to be significant when $p \leq 0.05$.

5.4.2 *In vivo* peripheral nerve repair in a rat sciatic nerve defect model

5.4.2.1 Sample preparation

Tendon sections were decellularized and sectioned as previously described. Tubular conduits were fabricated by wrapping either 5 layers of section around a PTFE rod, 1.6mm in diameter, or one layer around a 500µm PTFE-coated wire (McMaster-Carr). Layers 1,2 and 4 were wrapped with the fibers oriented parallel to the direction of the tube, while layers 3 and 5 were oriented circumferentially to provide both guidance cues and mechanical integrity for suturing. The tubes were left on the rods, and rinsed three times in diH2O and then crosslinked using a 1% glutaraldehyde solution for 20min. Afterwards, tubes were rinsed five times in diH2O, allowed to dry O/N and then removed from the rods. Three 500µm rods were cut to 15mm in length, and inserted into the larger 1.6mm rod that had been cut to 17mm in length. The conduits were then immersed in 70% ethanol for 1h, then placed under UV light for 1h, before being implanted.

5.4.2.2 Surgical procedure

The surgical research protocol was approved and in compliance with Tufts University's Institutional Animal Care and Use Committee (IACUC, protocol # M2013-

53) in accordance with the Office of Laboratory Animal Welfare (OLAW) at the National Institutes of Health (NIH). Tendon-derived conduits or isografts were implanted into a 15mm sciatic nerve defect as follows: Each animal was weighed and anesthetized via isoflurane inhalation. The surgical area was shaved and cleaned using alternating povidone-iodine and ethanol scrubs. A longitudinal gluteal skin incision was made parallel to the femur, and muscle splitting and blunt dissection used to expose the whole length of the right sciatic nerve from the exit at the pelvis to distal trifurcation, under a dissecting microscope. The exposed sciatic nerve was then sharply transected 0.5 cm from the proximal bifurcation, 0.5cm of nerve tissue is then excised and the nerve stumps are allowed to retract. The 1.7cm nerve guidance conduit is then inserted and sutured with two 9-0 prolene epineurial mattress stitches at each end, with 1mm of nerve/conduit overlap, creating a nerve defect 15mm in total length. The gluteal muscle and the skin were closed with 4-0 vicryl sutures in a simple interrupted manner and disinfected with a povodine-iodine solution. For isograft animals, a similar procedure was followed. One animal was sacrificed, and the sciatic nerve removed from both sides, producing two isografts. These isografts were trimmed, and placed in sterile phosphate buffered saline (PBS) following removal, and immediately implanted into the recipient animals. Baytril (0.1mL of 2.27% enrofloxacin solution) was injected subcutaneously after each surgery to prevent infection. Buprenex was provided once prior to surgery, and twice daily for three days. All animals were provided with drinking water containing Sulfatrim, (240 mg sulfamethoxazole/48 mg trimethoprim per 500 ml water bottle) and acetaminophen (2.5 mg/ml), along with food, ad libitum throughout the treatment period. Wound healing was monitored daily for dehiscence or infection until completely healed.

5.4.2.3 Sciatic functional index assessment

Starting two weeks after surgery, and weekly thereafter, functional recovery was monitored via assessment of the sciatic functional index. To do this, toe spread and paw

length were monitored by having the rats walk down a wooden walking path. Briefly, the rats are placed on a wooden walking pathway ending in a cage, and allowed two or three conditioning trials to become acclimated to the track. White paper was cut to the appropriate dimensions and placed on the bottom of the track. The rat's hind feet are dipped in water soluble paint, and the animal allowed to walk down the track, leaving its hind footprints on the paper. The paper was then scanned and analyzed digitally using ImageJ software (NIH) using previously described methods[316]. Briefly, the paw length (PL), toe spread (TS) between the 1st and 5th toes, and intermediate toe spread (IT)between the 2nd and 4th toes was measured (as illustrated in Figure 5.19), and the SFI calculated using the following formula, for three sets of footprints per trial run, and averaged:

$$SFI = -38.3 \times \frac{EPL-NPL}{NPL} + 109.5 \times \frac{ETS-NTS}{NTS} + 13.3 \times \frac{EIT-NIT}{NIT} - 8.8$$
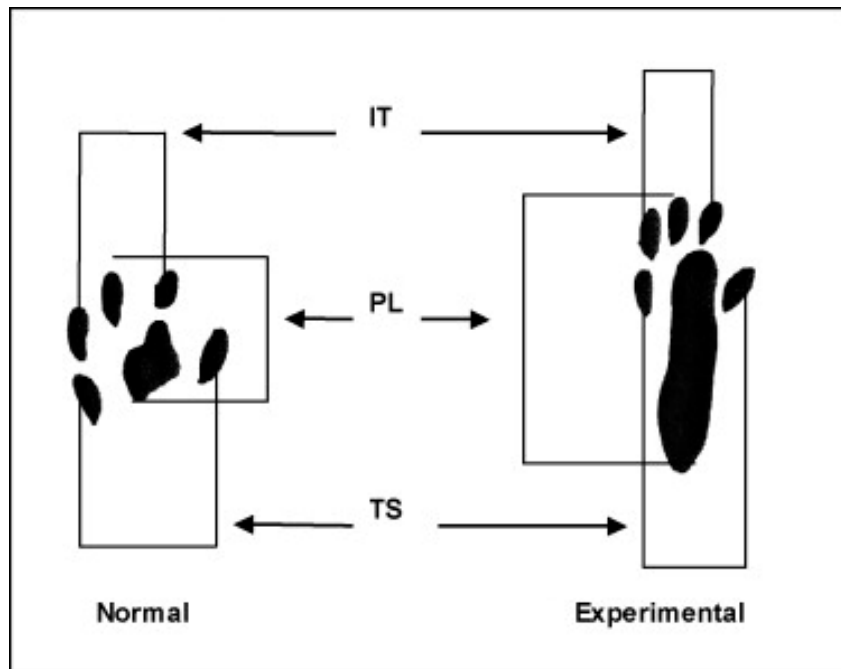
Figure 5.19: Schematic illustrating the measurement parameters used for the SFI test, on healthy and experimental paws. Reprinted from [316] with permission from Elsevier Limited.

5.4.2.4 Gastrocnemius weight assessment

Following sacrifice and removal of the implanted nerve, the gastrocnemius muscle from the operated side, and the healthy contralateral side were carefully dissected and weighed. The total weight loss of the muscle on the operated side was then calculated as a percent of the healthy side.

5.4.2.5 Nerve histology

Animals were sacrificed at 6 and 14 weeks via CO_2 asphyxiation followed by thoracotomy. The implantation site was then exposed following the original incision, along with muscle splitting and blunt dissection. The conduit or isograft were then removed, along with 5mm of nerve on each side of the suture site, and secured to a wooden stick with the physiological orientation marked, using sutures to prevent shrinkage of the nerve during fixation. The nerve was then placed into a freshly prepared 4% formaldehyde solution overnight at 4°C. The samples were then removed from the formaldehyde, rinsed three times with PBS and transferred to a 30% sucrose solution overnight. Each sample was then cut into 5 sections: proximal nerve (PN), proximal conduit (PC), middle conduit (MC), distal conduit (DC) and distal nerve (DN), and immersed in optimal cutting temperature (OCT) compound for 1h at room temperature. Samples were then quickly frozen on dry ice and sectioned on a cryomicrotome. Each sample was sectioned at 6μm thick and placed on a SuperFrost Plus slide (Fisherbrand) and allowed to dry overnight before being placed at -20°C until staining. Sections from each animal were then brought to room temperature, and stained with Masson's Trichrome Stain (Sigma), following the manufacturers protocol (Accustain Trichrome Stain Procedure #HT15).

5.4.2.6 Immunohistochemistry

All reagents were purchased from Sigma Aldrich unless otherwise noted. Cryosections prepared as described above were allowed to come to room temperature and rinsed twice in PBS to remove residual OCT. The sections were then permeabilized in 0.25% Triton X-100 in PBS for 10min, rinsed three times in PBS, and incubated in 1% bovine serum albumin (BSA) in PBS with 0.1% Tween 20 (PBST) for 30min to block nonspecific binding. Following this, the sections were incubated in primary antibodies. For immunofluorescent studies the sections were double stained with mouse anti-neurofilament-160 (NF-160) (Sigma N5246) diluted 1:80 and rabbit anti-S100 (Sigma S2644) diluted 1:200 in PBST containing 1% BSA, overnight at 4°C. The samples were then washed three times with PBST, and FITC-conjugated goat anti-mouse IgG (and Texas red-conjugated goat anti-rabbit secondary antibodies diluted 1:100 were then applied to the sections for 1h at room temperature. The samples were rinsed three times with PBS, and mounted using Fluoroshield mounting media with DAPI.

For horseradish peroxidase (HRP) studies, the samples were incubated in only one of the primary antibodies listed above, followed by rinsing, and treated with freshly prepared 0.3% hydrogen peroxide in PBS for 15min to reduce any endogenous peroxidase activity. Following this, the hydrogen peroxide was decanted and the appropriate secondary antibody (HRP-conjugated goat anti-rabbit or goat anti mouse) applied at a dilution of 1:100 for 1h at room temperature. The samples were then rinsed 3x with PBS and the HRP developed using Sigmafast DAB with metal for 10min, followed by 3 rinses with tap water. These sections were dehydrated in graded ethanol, followed by xylene and mounted using DPX mountant.

5.4.2.7 Histomorphometric analysis

All HRP-stained and developed sections were imaged using a 20x objective, and individual images combined using Microsoft Image Composite Editor using only planar translation. These images were then automatically processed using ImageJ to remove uneven background illumination and converted into a binary image using the automated threshold function. From here the total area for NF160 or S100 was able to be measured for total pixels stained, as well as by percent of the total conduit or isograft area.

5.4.2.8 Statistics

Statistical significance was calculated by performing a two-way Student's t-test assuming an equal variance with an α-value of 0.05. A p-value <0.05 was determined to be statistically significant.

Chapter 6.

Conclusions and Future Work

6.1 CONCLUSIONS

The biomedical field is ever expanding as innovative materials are constantly developed for new applications. Often these new materials comprise well defined micro and nanostructures designed to improve or impart some function, from diagnostics[317], to drug delivery[318,319], to producing a biomimetic surface for cell growth[320]. Many of these materials take inspiration from nature of seek to replicate those structures. Bioskiving, as demonstrated here, directly utilizes the collagen found in tendon in its native form. This process maintains the nano and microtopography of the tendon — the collagen fibrils and fibers. Maintenance of these features serves two primary benefits: one is that they have the ability to provide cell growth guidance cues, and the second is that they impart greater mechanical strength. One of the major benefits of this process is its ease. Many other techniques for fabricating collagen-based scaffolds involve breaking down the native collagen structure which then requires subsequent reconstruction for use, a challenging process.

The fabrication procedure and mechanical characterization are covered in Chapter 2. Bioskiving allows a user to create both two- and three-dimensional constructs directly from tendon sections. These constructs can be of varying isotropy and have tunable mechanical properties, based on the fiber orientations and crosslinking density. Non-

crosslinked tendon-derived samples have an ultimate tensile strength an order of magnitude greater than reconstituted collagen (0.63MPa vs <0.7MPa) and crosslinking again can increase that another 20-fold (0.63MPa vs 13.59MPa).

The biological characteristics are also quantified, namely the degradation, both *in vitro* and *in vivo,* and the thrombogenicity. In addition to increasing the mechanical strength of the material, crosslinking also serves to tune the degradation process. The crosslinking slows collagenase degradation *in vitro*, and macrophage and fibroblast degradation *in vivo* in a rat. The collagen's tendency to activate and induce platelet adhesion can also be attenuated through covalent conjugation of an anticoagulant such as heparin.

Lastly, the material's ability to influence cellular growth is demonstrated with neuronal applications in mind. Schwann cells are shown to adhere, grow and proliferate on the material, as are chick dorsal root ganglia which extend neurites out along then tendon fibers. And, as a final test, the material is used to successfully regenerate peripheral nerves in a rat sciatic nerve defect model. This was confirmed via functional recover as well as histological analysis (H&E and Masson's trichrome) and immunohistochemical staining for neurofilament-160 and S100, representative of neurons and Schwann cells, respectively.

Of great importance to applying a material to solve an engineering problem is to know how the material will behave under given circumstances. This allows for correct material selection and remediation of any potential challenges. The work completed here characterizes multiple properties of the tendon-derived Bioskiving material, and puts this information together to demonstrate its application in solving a biomedical engineering problem. This work demonstrates the utility of tendon-derived sections as a material, and Bioskiving as a platform fabrication technique.

6.2 FUTURE WORK

6.2.1 Extending Bioskiving to other materials

The Bioskiving technique was developed with the idea that it was a platform fabrication technique that could be expanded to a number of different materials. The work presented here demonstrates the utility of technique for creating a scaffold directly from native materials through sectioning. Tendon was used for proof-of-concept work as it comprises highly aligned collagen fibers that can be directly exploited. However, many other common natural materials have micro and nanostructures that could be utilized as well.

Muscular tissues are comprised of many linear protein components, actin and myosin filaments, bundled into hierarchical structures, and is a logical step to expand Bioskiving into, as both materials comprise fibrous elements. Similar constructs could be fabricated, yet would have differing mechanical properties as well as ECM composition in protein and glycosaminoglycans that could greatly alter the material's mechanical properties and cellular interaction.

Vastly different tissue, like bone could also be explored. The combination of longitudinal, circumferential and disordered micro and macro structures produce an intricate array when take as a cross section[321], not to mention the hardness compared to tendon. Cutting hard materials such as bone may be a challenge, but can be done through modifications to the procedure, like using a sledge microtome[322].

One can imagine expanding this technique to any type of tissue with a well-defined ECM architecture to capitalize on those features. Beyond the structure, the biological composition of the ECM could be utilized. Decellularized brain[323] and liver[324] ECM have both shown to retain unique protein and growth factor compositions, and Bioskiving could be used to make coatings from this material. In particular, these types of

decellularized tissues which may not possess robust mechanical properties could be used in conjunction with other tissues like decellularized tendon, to create a hybrid material that contains both chemical and physical bioinstructive cues. The layers of tendon would act as the structural framework while layers of brain or liver throughout could act as a biochemical depot. In a similar manner, two materials with different mechanical properties, like tendon and more elastic ligaments or some blood vessels could be sectioned and stacked together to more finely tune the properties, even within specific orientations. This would further the potential to use these ECM-based scaffolds for repair of non-homologous anatomical sites.

Advantages to using these native materials over synthetic materials replicating these structures could come in several forms; one would be ease of fabrication. Bioskiving does not require a clean room or other equipment that requires a significant investment in order to make a material with these well-defined nanostructures as nature has already accomplished that. A second is that these natural polymer scaffolds contain many biological cues to influence cells, and yet their intricate structure may imbue interesting mechanical properties, a common hindrance of using natural polymers vs synthetic.

6.2.2 Modifying tendon-derived sections

The potential modifications that can be done to further improve the tendon-derived scaffolds are nearly endless, and most processes done to alter traditional collagen scaffolds could be expanded to the tendon-derived material, and there are several that could be of great interest for the tendon-derived material in particular.

One is to explore additional methods of crosslinking, beyond the crosslinkers used in Chapter 2. Riboflavin/ultraviolet mediated crosslinking would be a simple, biologically compatible crosslinker[157], with the possibility to crosslink *in situ*. *In situ* crosslinking

could be used to wrap and adhere individual sections or stacked sections around a nerve or tendon/ligament. Alternatively, a riboflavin-impregnated scaffold could be directly crosslinked to existing collagenous ECM in the body to provide a patch and supportive matrix. Preliminary mechanical testing data for several additional crosslinkers, including Riboflavin is shown in Table 6.1. Parallel tendon scaffolds were treated with 1mM riboflavin in diH2O for 1h under UV light while EDC/NHS scaffolds with 16mM EDC 6.4mM NHS in 2-(N-morpholino)ethanesulfonic acid (MES) buffer for 2h at room temperature

Crosslinker	Ultimate Tensile Strength (MPa)	Modulus (MPa)
Non-crosslinked	0.63 ± 0.07	3.11 ± 1.35
2.5% GA-crosslinked	13.59 ± 1.35	145.54 ± 18.72
EDC/NHS-crosslinked	3.69 ± 0.15	48.47 ± 3.79
Riboflavin/UV-crosslinked	2.64 ± 0.26	23.84 ± 1.37

Table 6.1: Ultimate tensile strength and moduli for several preliminary tests for alternative crosslinkers.

Dimethyl 3,3'-dithiobispropionimidate (DTBP) has also been shown to be a successful crosslinker of collagen that is more biocompatible than GA[158]. This particular crosslinker contains a central disulfide bond than can be cleaved by reducing agents such as dithiothreitol, or glutathione. Were DTBP to be used as a crosslinker, degradation of a scaffold could be selectively triggered, or degraded following specific events *in vivo*, such as the physiological niche of a regenerating nerve where glutathione and thioredoxin are upregulated[325].

In addition to crosslinking the collagen itself, functional molecules could be crosslinked to the scaffold, such as was demonstrated here with heparin. Neuronal-related growth factors that could be of interest, like neurotrophin-3[326] or nerve growth factor[327]. If crosslinking the functional molecule to the scaffold is not possible or not desired, additional delivery methods could be utilized. A drug-containing collagen gel or

microparticles could be incorporated into the scaffold that would release over time, or with degradation. This could be accomplished through either direct impregnation into voids into the tendon material, or by casting a block of the gel and sectioning it in a similar manner to the tendon.

6.2.3 Additional applications for tendon-derived sections

The wide array of potential applications is one of the benefits of the fabrication technique, in that it allows for the construction of diverse structures that recapitulate the structure in non-homologous anatomical sites. Several tissues contain features that lend themselves to repair or regeneration with the tendon material. For example, the bulk of corneal stroma tissue is comprised of ~200 lamellae of highly organized collagen fibers that are oriented perpendicular to each other in adjacent layers[328]. This is quite similar to some of the structures possible through Bioskiving, although the collagen fibers in cornea are smaller than those found here in the tendon (30nm[329] vs 200nm). Reconstruction of the natural stroma structure in particular is one of the challenges of corneal repair, and such material could serve as a template for repair or tissue engineering[330].

The annulus fibrosus in intervertebral discs is another structure consisting of lamellae of highly-glycated collagen fibers, oriented at 60° in opposing directions[331]. Degenerative disk disease is currently a problem with few treatment options[332], that could benefit from a tissue engineered or biomaterial solution. With the techniques discussed here it may be possible to create a scaffold with suitable mechanical properties to repair a damaged annulus fibrosus.

And of course, a repair patch for tendon or ligaments is logical application that tendon-derived scaffolds could be expanded towards. Reconstruction and repair of commonly injured connective tissue such as the Achilles tendon or anterior cruciate ligament have high success rates (>90%)[333], however more complex anatomical locations

like a rotator cuff have high rates of failure (20-70%) with limited clinical options for augmentation[171].

Another structure that could be created using the material is a replacement for esophageal or intestinal structures. Separated segments of tendon sections could be aligned and joined with perpendicularly oriented tendon sections to create a structure capable of peristaltic contraction. This could find use as a direct tissue engineered replacement, as an in vitro model, or with some modification, as a contractile soft robot capable of motion.
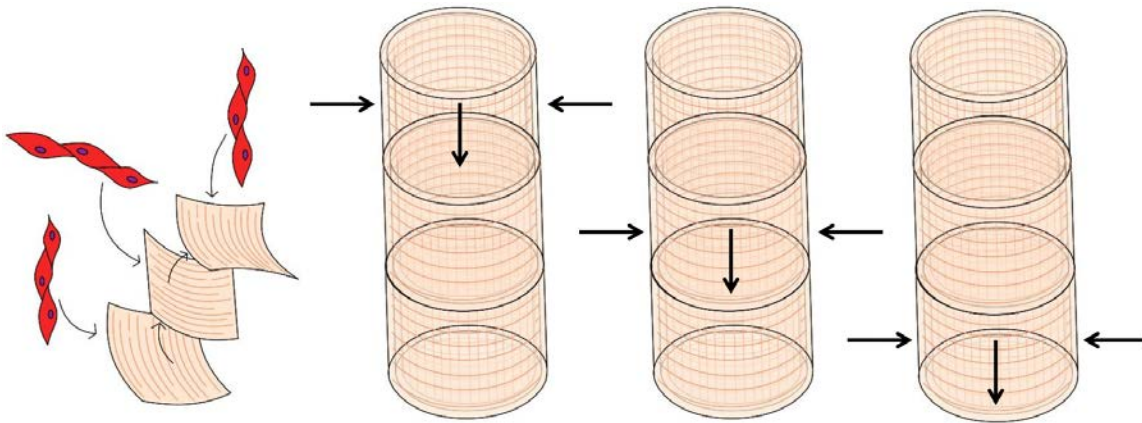
Figure 6.1: Schematic illustrating tendon sections being used to create peristaltic contractile scaffold.

Lastly, as briefly mentioned in the previous chapters, the tubular conduits would make an ideal substrate for the construction of tissue engineered blood vessels (TEBV). The ability for multiple cell types to grow and orient along the collagen fibrils and fibers has already been demonstrated. Growth of endothelial cells on sections would allow for construction of an intimal layer, smooth muscle cells a medial layer and multiple properly oriented layers an adventitial layer[334]. These layers could then be assembled layer by layer around a template (Figure 6.2) and cultured in a bioreactor[335]. Refinement of a TEBV scaffold or vascular graft could also involve greater turning of the elasticity to

prevent compliance mismatch, and modifications to further improve the hemocompatibility and thrombogenicity.
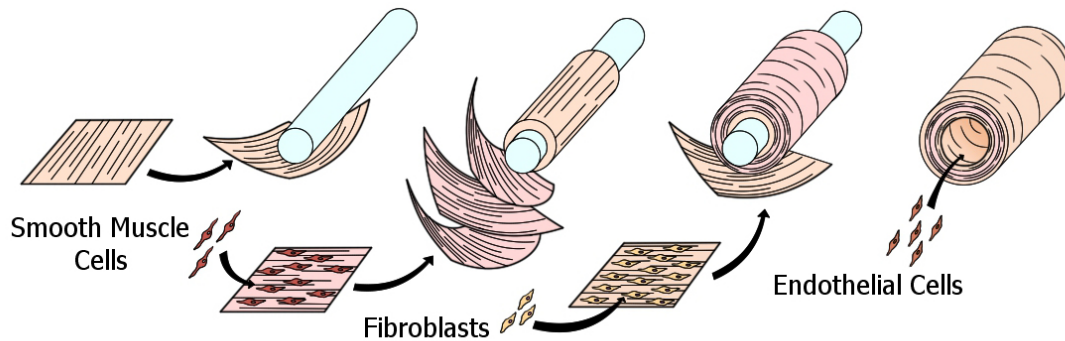
Figure 6.2: Schematic illustrating one possible method to fabricate tissue engineered blood vessels from tendon-derived sections produced via Bioskiving.

6.2.4 Additional characterization

Despite the numerous methods of characterization here, there remains just as many tests that could still be conducted. In particular there are several relevant to the biocompatibility of the material that would be conducted. These include cytotoxicity tests (e.g. ISO 10993-5) sensitization and irritation tests (e.g. ISO 10993-10), and possibly quantification of breakdown products depending on the type of crosslinking used (e.g. ISO 10993-9). Finally, effects of sterilization methods like ethylene oxide or gamma irradiation on the material should also be determined, as ethanol and ultraviolet treatment are not considered terminal sterilization techniques.

Lastly, further characterization of the collagen as prepared from the bovine Achilles tendon should be conducted. This includes evaluation of adventitious agents (endotoxins, microorganisms, impurities etc.), storage stability, and issues arising from the use of xenogeneic collagen (ASTM F2212-11). As collagen is highly conserved between species, particularly fibrillar collagen in vertebrates[336,337], it is not likely that the

material itself will elicit a much of an immune response, and if so, will resolve itself[236].

However, animal-derived collagen runs the risk of transmitting transmissible spongiform encephalopathies (TSE). Relevant methods to test samples should be established as per ISO 22442-1, 2, 3. Safe sourcing and handling practices should be ensured in order to prevent this as per industry standards (21 CFR Part 820 or ISO 13408-1).

One alternative to the use of animal-derived collagen would be the use of allogeneic cadaver collagen. This method would still run the risk (albeit lower) of TSE transmission however it would reduce the potential of immunological response. One major limiting factor of using human tendon as a raw material for expanded applications would be sourcing the material to construct many devices. Tendons available in good condition from healthy cadavers would be severely limited. A second would be size limitations; bovine Achilles tendon is 1-2cm thick vs 0.55cm in human Achilles tendon[338].

Once established the additional characterization of the material and manufacturing process will further strengthen the material's potential for greater use, and may make it an attractive option for further industrial development.

Appendix

Additional Coauthored Publications

Pericellular Hydrogel/Nanonets Inhibit Cancer Cells**

Yi Kuang, Junfeng Shi, Jie Li, Dan Yuan, Kyle A. Alberti, Qiaobing Xu, and Bing Xu

Dedicated to Professor George M. Whitesides on the occasion of his 75th birthday

Abstract: *Fibrils formed by proteins are vital components for cells. However, selective formation of xenogenous nanofibrils of small molecules on mammalian cells has yet to be observed. Here we report an unexpected observation of hydrogel/nanonets of a small D-peptide derivative in pericellular space. Surface and secretory phosphatases dephosphorylate a precursor of a hydrogelator to trigger the self-assembly of the hydrogelator and to result in pericellular hydrogel/nanonets selectively around the cancer cells that overexpress phosphatases. Cell-based assays confirm that the pericellular hydrogel/nanonets block cellular mass exchange to induce apoptosis of cancer cells, including multidrug-resistance (MDR) cancer cells, MES-SA/Dx5. Pericellular hydrogel/nanonets of small molecules to exhibit distinct functions illustrates a fundamentally new way to engineer molecular assemblies spatiotemporally in cellular microenvironment for inhibiting cancer cell growth and even metastasis.*

Besides serving as important internal components (e.g., cytoskeletons) of cells, fibrils outside the cells also bear significant functions. For example, fibrils formed by polysaccharides and fibrous proteins, such as fibronectin, collagens, and laminins,[1] afford networks that withhold extracellular fluid, and the resulting extracellular matrix maintains multicellular structures and mediates cell–cell communication.[2] A recent study demonstrated that human α-defensin 6 (HD6) self-assembles in contact with bacteria surface protein to form nanonets that entrap the bacteria and block their translocation.[3] The various functionalities of extracellular fibrils and networks formed by biomolecules suggest that it is feasible to build xenogenous fibrils extracellularly (e.g., in the pericellular space) as a new approach for regulating the interaction of cell with its microenvironment,[4] thus controlling the fate of cells.

Like self-assembling peptides and proteins, certain small organic molecules self-assemble[5] in water to afford nano-

fibrils as matrices of hydrogels[6] (e.g., in response to biostimuli such as enzymes[7]). Interestingly, a vancomycin–pyrene conjugate, which self-assembles in water to form nanofibrils,[8] exhibits two orders of magnitude enhanced antibacterial activity against vancomycin resistant enterococci (VRE), plausibly through self-assembled multivalent vancomycin binding the receptors on bacterial cell wall.[9] However, the observation of xenogenous nanofibrils on mammalian cells has yet to be reported. During our research of enzyme-catalyzed self-assembly of D-peptide derivatives,[10] the self-assembly of a small D-peptide derivative, surprisingly, forms pericellular hydrogel/nanonets. Here, we report the observation, the origin of formation, and a potential application (i.e., inhibiting cancer cells) of the pericellular hydrogel/nanonets.

As illustrated in Figure 1 a, our results show that 1) surface and secretory phosphatases[11] from cells catalytically dephosphorylate a small D-peptide derivative (e.g., D-**1**) to form a hydrogelator (e.g., D-**2**); 2) the accumulation of the hydrogelator results in a network of nanofibrils as the scaffold of a hydrogel in the pericellular space; 3) the pericellular hydrogel/nanonets entrap secretory proteins, block cellular uptake, thus decreasing cell migration, preventing cell adhesion, and induce cell apoptosis; 4) most importantly, due to the overexpression of surface and secretory phosphatases by cancer cells,[12] the pericellular nanonets selectively form on the cancer cells (e.g., HeLa, MES-SA, and MES-SA/Dx5). As an unexpected example of enzyme-instructed self-assembly[7c] in pericellular space, this work illustrates a new way that controls the fate of different types of cells according to the expression and location of enzymes that regulate the

[*] Dr. Y. Kuang, J. Shi, J. Li, D. Yuan, Prof. Dr. B. Xu
     Department of Chemistry, Brandeis University
     415 South St, Waltham, MA 02454 (USA)
     E-mail: bxu@brandeis.edu
     Homepage: http://people.brandeis.edu/~bxu
     K. A. Alberti, Prof. Q. Xu
     Department of Biomedical Engineering, Tufts University
     419 Boston Ave, Medford, MA 02155 (USA)

      Supporting information for this article is available on the WWW under http://dx.doi.org/10.1002/anie.201402216.
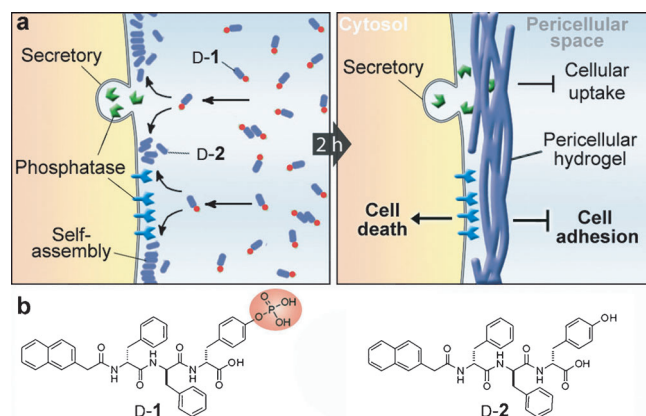

Figure 1. a) Enzyme-catalyzed formation of pericellular hydrogel/nanonets to induce cell death. b) Molecular structures of the precursor (D-**1**) and the hydrogelator (D-**2**).

spatiotemporal profiles of molecular nanofibrils for controlling cellular processes.

Being synthesized according to the reported procedure[13] and consisting of a naphthalene-capped tripeptide, D-Phe-D-Phe-D-Tyr, molecule D-**1** differs with D-**2** only in that the D-Tyr is phosphorylated (Figure 1 b). Like a previous work on enzyme-instructed self-assembly of D-peptides,[10b] alkaline phosphatase (ALP) catalyzes the dephosphorylation of the precursor (D-**1**; 0.20 wt %/2.77 mM) to form the hydrogelator (D-**2**; 0.18 wt %/2.77 mM), which self-assembles in water to form nanofibrils and to result in a hydrogel in PBS buffer. However, an unexpected phenomenon occurred when incubating HeLa cells with D-**1**. As shown in Figure 2 a, the incubation of a confluent layer of HeLa cells (in a 35 mm Petri dish) in complete culture medium (1 mL) containing D-**1** (560 μM) results in a layer of hydrogel-like soft materials on the cells after 2 h of incubation at 37 °C. While reducing the concentration of D-**1** to 280 μM still causes hydrogelation on cells (Figure 2 b), little such hydrogel occurs on the HeLa cells treated by D-**1** at 140 μM (Figure 2 c). LC-MS analysis reveals that the hydrogel contains D-**2** at about 2.05 mM (Table S1 in the Supporting Information), much higher than the concentration used for incubation. This result suggests that the conversion of D-**1** to D-**2** leads to the pericellular accumulation of D-**2** for the hydrogelation on the HeLa cells. In contrast, the incubation of HeLa cells with D-**2** at even 560 μM hardly results in hydrogelation (Figure 2 d), further suggesting that phosphatase-catalyzed dephosphorylation of D-**1** results in localized self-assembly of D-**2** in the pericellular space for hydrogelation. This notion agrees with the observation that the phosphatase inhibitors ("Pierce") prevent forming the pericellular hydrogel around the HeLa cells (Figure S2a).

HeLa cell conditioned medium also dephosphorylates D-**1** to result in hydrogelation. After 48 h of incubation, the medium treated by D-**1** at 560 μM completely transforms from a solution to a hydrogel (Figure S1a,b), and the medium treated by D-**1** at 280 μM also contains clots of hydrogels in the solution. Being similar to the case of HeLa cells, the medium containing D-**1** at 140 μM or D-**2** at 560 μM fails to form a hydrogel (Figure S1c,d). These results confirm that the secretory phosphatases from the HeLa cells convert D-**1** to D-**2** and contribute to the transition from the solution to the hydrogel. Because of the presence of surface and secretory phosphatases on/near cell membrane, the concentration of phosphatases is high in pericellular space, thus, more D-**2** accumulates and localizes in the pericellular space to self-assemble for hydrogelation. Being directly incubated with the cells at 560 μM (Figure 2 d), D-**2** distributes homogenously in the culture medium (like the case of Figure S1d), thus it is unable to accumulate on cells to form pericellular hydrogels. Moreover, the incubation of HeLa cells with D-**1** (at 560 μM) and ALP (0.1 U mL^{-1}) for 2 h hardly results in pericellular hydrogelation (Figure S2b), suggesting that the gradient of phosphatases is critical for the dynamics of the pericellular accumulation of the hydrogelators (i.e., D-**2**). Although it remains difficult to distinct the contributions from surface and secreted phosphatases, the much faster gelation in the presence of the cells than the cell conditioned medium implies more contribution from the surface phosphatases. We speculate that the major phosphatases for the dephosphorylation of D-**1** are placental alkaline phosphatases (PLAP), which exist in both membrane-bound and secretory forms and exhibit elevated expression in cervical adenocarcinoma cells (HeLa)[14] and uterine sarcoma cells (MES-SA; MES-SA/Dx5).[15]

Scanning electron microscopy (SEM) reveals that the surface of the HeLa cells incubated with D-**1** differs from that of the untreated HeLa cells. Because the organic solvent (e.g., alcohol or acetone) used in cell fixation and the repeated washing destroy the supramolecular hydrogels, we had to freeze-dry the cells grown on a glass slide for preserving the structure of the nanofibrils in the hydrogels. As shown in Figure 2 e, while the untreated HeLa cells exhibit a smooth surface, the cells treated with D-**1** at 560 μM show a completely different morphology of porous structures cover the surfaces of the cells (i.e., nanonets). Additionally, the cells treated with D-**1** at 280 μM display fiber-like structures attached closely to the cell surface (Figure S3). These results coincide with the pericellular hydrogelation on HeLa cells treated with D-**1** at 280 and 560 μM. The transmission electron microscope (TEM) image of the pericellular hydrogel on HeLa cells treated by D-
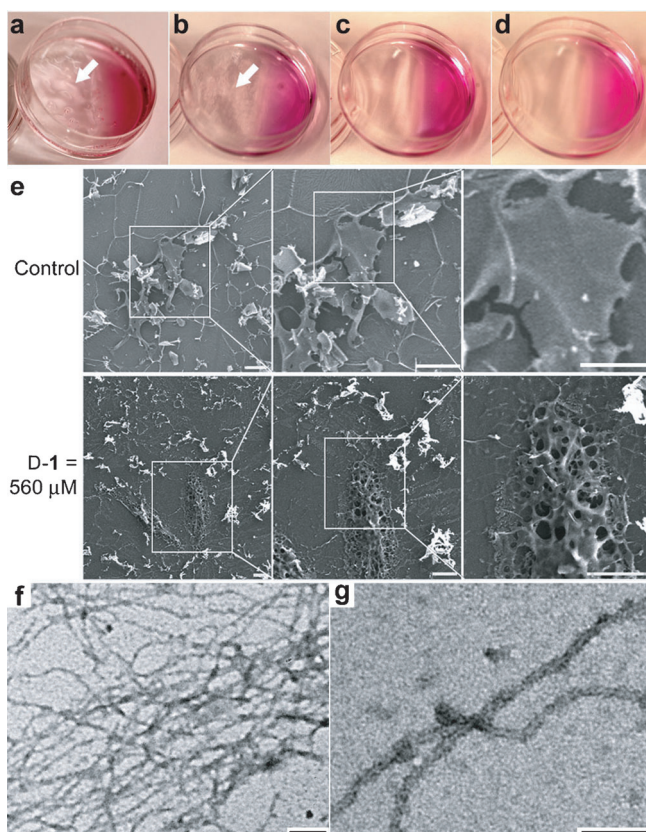
Figure 2. Enzymatic formation of the hydrogel/nanonets on the cells. Optical images of the HeLa cells incubated with D-**1** at a) 560, b) 280, and c) 140 μM, or with D-**2** at d) 560 μM for 2 h. White arrows point at the hydrogel/nanonets. e) SEM images of freeze-dried HeLa cells treated with D-**1** at 0 μM (control) or 560 μM for 2 h. Scale bar = 10 μm. f) Negative stained TEM images of the pericellular hydrogels on the HeLa cells treated by D-**1** at 280 μM. g) High magnification image of the nanofibrils in Figure 2 f. Scale bar in (f) and (g) is 100 nm.

1 at 280 μM reveals that the hydrogel consists of networks of nanofibrils (Figure 2 f) that have diameters about 20 nm (Figure 2 g). That is, the nanofibrils form nanonets. Similar to the nanofibrils of D-**2** formed by the addition of ALP into the solution of D-**1** in PBS buffer (Figure S4), these nanofibrils on the cell surface entangle with each other to form the matrices of the hydrogel. Moreover, TEM shows the rough dark edges on the pericellular nanofibrils (Figure 2 g), indicating that other biomacromolecules likely attach to the nanofibrils.

Congo red and DAPI,[16] a stain for nanofibrils formed by self-assembly[17] and a nucleus dye, respectively, help further visualize the pericellular hydrogel/nanonets on single cells. As shown in Figure 3 a, after incubation with D-**1** at 280 μM for 12 h and the addition of Congo red and DAPI, HeLa cells show obvious red fluorescence that outlines the cell shape, while untreated HeLa cells (i.e., the control) show little red fluorescence. Moreover, DAPI is unable to enter the HeLa cells treated with D-**1** at 280 μM and co-localizes with Congo red, as shown in both the 2-D image and the 3-D stacked image (see video in the Supporting Information). This result differs drastically from the staining of the untreated HeLa cells (i.e., DAPI stains the nuclei) and confirms that 1) the hydrogel/nanonets form exclusively in pericellular space and 2) the pericellular hydrogels/nanonets prevent the diffusion of DAPI into the cells. Since DAPI is a small molecule (M.W. = 277 Da), the block of the cell entry of DAPI suggests that the pericellular hydrogel/nanonets are able to block other molecules (e.g., biomacromolecules) entering cells. The uneven distribution of the Congo red on the surface of the D-**1** treated HeLa cells agrees with the result from SEM, suggesting the inhomogeneous distribution of the hydrogel on the surface of the HeLa cells.

We treated Ect1/E6E7 cells (immortalized normal human cervical epithelial cells, which have same tissue and organ origins as HeLa cells) with the same procedure as that on the HeLa cells. The Ect1/E6E7 cells, after being incubated with D-**1** even at 560 μM for 12 h, hardly display any red fluorescence, which is similar to that of the untreated Ect1/E6E7 cells, and DAPI stains the nuclei of both the treated and the untreated Ect1/E6E7 cells (Figure 3 a). These results agree with that hydrogels hardly form on Ect1/E6E7 cells even for a prolonged incubation time of 48 h (Figure S5). The difference of hydrogel/nanonets formation by D-**1** on HeLa cells and Ect1/E6E7 cells agrees with that HeLa cells have higher levels phosphatase activities than Ect1/E6E7 cells do (Figure S6).

To verify whether the pericellular hydrogel/nanonets block secretory proteins/enzymes into the culture medium, we evaluated the amount of phosphatases in the four samples: the blank medium (Blank), medium incubated with untreated HeLa cells (Control), pericellular hydrogel on HeLa cells treated by D-**1** at 560 μM for 12 h (Gel), and the suspension of the medium of HeLa cells treated by D-**1** after removing the hydrogel (Suspension). According to the result shown in Figure 3 b, the amount of phosphatases accumulated in the Gel is about 27 times higher than that in the Control. Consequently, the amount of phosphatases in the Suspension is significantly lower than that in the Control. These results indicate that the pericellular hydrogel/nanonets capture the
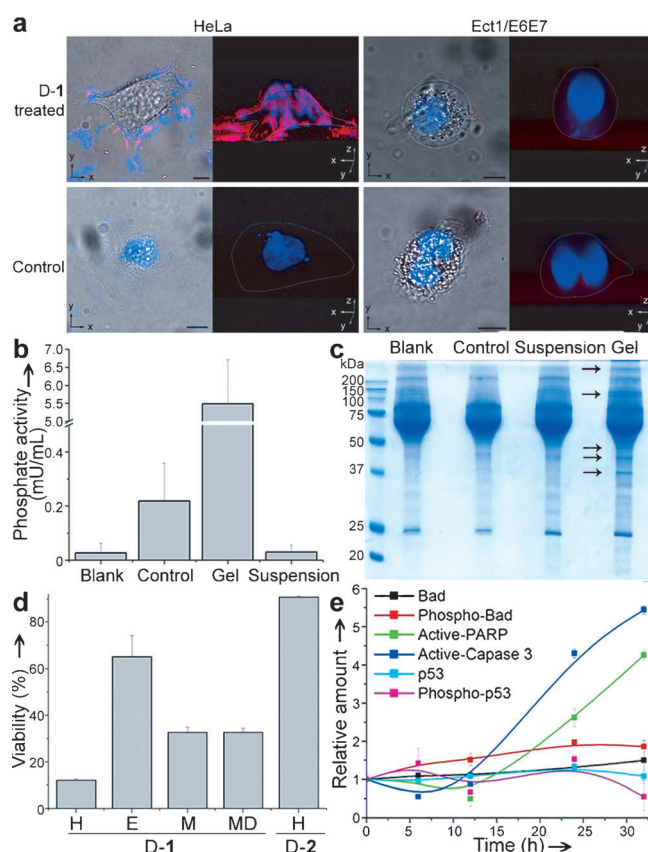
Figure 3. The pericellular hydrogel/nanonets inhibit cancer cells. a) Overlaid images and 3D stacked z-scan images of Congo red and DAPI stained HeLa and Ect1/E6E7 cell treated by D-**1** or just culture medium as control for 12 h. HeLa cells treated by D-**1** at 280 μM; Ect1/E6E7 cells treated by D-**1** at 560 μM. Scale bar = 10 μm. White dots outline the cells. b) Comparison of phosphate activity in blank medium (Blank), medium incubated with HeLa cells (Control), pericellular hydrogels on HeLa cells treated by D-**1** at 560 μM (Gel), and the suspension medium of HeLa cells treated by D-**1** at 560 μM (Suspension). c) SDS-PAGE showing the protein composition in the Blank, Control, Gel, and Suspension. Arrows point at protein bands that appear only in the lane of the Gel. d) Cell viabilities of HeLa (H), Ect1/E6E7 (E), MES-SA (M) and MES-SA/Dx5 (MD) cells treated by 280 μM of D-**1** or HeLa cells treated by 280 μM of D-**2** for 48 h. e) Change of relative amount of apoptosis signal molecules over time in HeLa cells treated by D-**1** at 280 μM.

secretory proteins/enzymes from the cells, thus blocking them to enter the culture medium. Moreover, we analyzed the protein composition in the four samples by SDS-PAGE and Coomassie staining (Figure 3 c) and found that the Gel lane contains more bands than in the lanes of the Control and the Suspension, suggesting that the pericellular hydrogel/nanonets block diffusion to enrich secretory proteins. In other words, the pericellular hydrogel/nanonets largely block cellular mass exchange between the cells with their environment.

Blocking cellular mass exchange has profound effects on critical cellular activities (e.g., migration, adhesion, and proliferation) of the cancer cells. According to migration assay[18] shown in Figure S7 a, the HeLa cells treated by D-**1** at 280 and 560 μM have gaps larger than that of the untreated HeLa cells (i.e., the control) and those of the HeLa cells

treated by D-**1** at 140 μM or D-**2** at 560 μM, confirming that the pericellular hydrogel/nanonets decrease the migration of the HeLa cells. Moreover, as shown by the time progression curve of the cell adhesion (Figure S7b) of trypsinized HeLa cells,[19] the addition of D-**1** at 560 μM significantly delays the adhesion of HeLa cells (i.e., less than 5% cells reattach to surface after at 4 h). The addition of D-**2** at 560 μM, though exhibiting a slight delay of adhesion at the beginning of incubation, hardly hampers cell adhesion (e.g., being similar to that of control, more 80% of cells reattach at 4 h). Most importantly, as shown in Figure 3d, at 280 μM, D-**1** significantly decreases the viability of the HeLa cells to about 10% after 48 h incubation. Moreover, 280 μM of D-**1** also forms pericellular hydrogel/nanonets (Figure S8) and inhibits the growth of MES-SA and MES-SA/dx5 cells, regardless of the multi-drug resistance of the latter. In contrast, over 60% of the Ect1/E6E7 cells treated with D-**1** at 280 μM for 48 h remain viable. The direct addition of D-**2** at 280 μM hardly inhibits the growth of HeLa cells. These results confirm that the pericellular dephosphorylation of D-**1** leads to the self-assembly of D-**2** on the surface of cancer cells, thus the network of nanofibrils on the cancer cells inhibit the entrapped cells (Figure S9). We used ELISA to quantify the amount of several key apoptosis signal molecules over time in the HeLa cells incubated with D-**1** at 280 μM (Figure 3e), and we found that the amount of active Caspase 3 and active PARP increase at 24 and 32 h of incubation, suggesting that the cells undergo caspases dependent apoptosis. The apoptosis of the HeLa cells also implies that the toxicity of pericellular hydrogel/nanonets unlikely originates from the perturbation of plasma membrane, which primarily results in necrosis of the cells.[20] Moreover, the removal of the media containing D-**1** (at gradient concentration) after 4 hour incubation restores cell viability (Figure S12), suggesting little tight ligand-receptor type interaction between D-**2** (or the nanofibrils of D-**2**) with plasma membrane to disrupt the plasma membrane of cells.

One key prerequisite for pericellular hydrogelation is the proteolytic stability of the small molecular precursors and hydrogelators. The incubation of HeLa cells with L-**1** (the L-peptide counterpart of D-**1**; Figure S10) at 560 μM at 37°C fails to form pericellular hydrogel/nanofibrils due to the proteolysis of L-**1** in cellular environment (Figure S11).

In summary, this work demonstrates that molecular nanofibers, formed by enzyme-instructed self-assembly of innocuous monomers, selectively inhibit cancer cells. The rapid formation of the pericellular D-peptide hydrogels contributes to the entrapment of secretory phosphatases in the hydrogel, suggesting a fundamentally new way, which relies on the localization of enzymes, to form supramolecular hydrogels/nanofibrils in a specific cellular location for controlling the fate of cells.[21] In addition, the pericellular hydrogelation also promises a new method that enriches and regulates secretome of cells for understanding and modulating cellular microenvironment.

[1] A. V. Persikov, B. Brodsky, *Proc. Natl. Acad. Sci. USA* **2002**, *99*, 1101.

[2] S. Mann, *Angew. Chem.* **2008**, *120*, 5386; *Angew. Chem. Int. Ed.* **2008**, *47*, 5306.

[3] H. T. Chu, M. Pazgier, G. Jung, S. P. Nuccio, P. A. Castillo, M. F. de Jong, M. G. Winter, S. E. Winter, J. Wehkamp, B. Shen, N. H. Salzman, M. A. Underwood, R. M. Tsolis, G. M. Young, W. Y. Lu, R. I. Lehrer, A. J. Baumler, C. L. Bevins, *Science* **2012**, *337*, 477.

[4] N. Iida, A. Dzutsev, C. A. Stewart, L. Smith, N. Bouladoux, R. A. Weingarten, D. A. Molina, R. Salcedo, T. Back, S. Cramer, R. M. Dai, H. Kiu, M. Cardone, S. Naik, A. K. Patri, E. Wang, F. M. Marincola, K. M. Frank, Y. Belkaid, G. Trinchieri, R. S. Goldszmid, *Science* **2013**, *342*, 967.

[5] a) J. M. Lehn, *Science* **2002**, *295*, 2400; b) G. M. Whitesides, B. Grzybowski, *Science* **2002**, *295*, 2418.

[6] a) L. A. Estroff, A. D. Hamilton, *Chem. Rev.* **2004**, *104*, 1201; b) M. M. Zhang, D. H. Xu, X. Z. Yan, J. Z. Chen, S. Y. Dong, B. Zheng, F. H. Huang, *Angew. Chem.* **2012**, *124*, 7117; *Angew. Chem. Int. Ed.* **2012**, *51*, 7011; c) D. Kiriya, M. Ikeda, H. Onoe, M. Takinoue, H. Komatsu, Y. Shimoyama, I. Hamachi, S. Takeuchi, *Angew. Chem.* **2012**, *124*, 1585; *Angew. Chem. Int. Ed.* **2012**, *51*, 1553; d) S. Tamesue, Y. Takashima, H. Yamaguchi, S. Shinkai, A. Harada, *Angew. Chem.* **2010**, *122*, 7623; *Angew. Chem. Int. Ed.* **2010**, *49*, 7461.

[7] a) Z. M. Yang, H. W. Gu, D. G. Fu, P. Gao, J. K. Lam, B. Xu, *Adv. Mater.* **2004**, *16*, 1440; b) S. Toledano, R. J. Williams, V. Jayawarna, R. V. Ulijn, *J. Am. Chem. Soc.* **2006**, *128*, 1070; c) Z. Yang, G. Liang, B. Xu, *Acc. Chem. Res.* **2008**, *41*, 315; d) J. P. Yuan, D. Wen, N. Gaponik, A. Eychmuller, *Angew. Chem.* **2013**, *125*, 1010; *Angew. Chem. Int. Ed.* **2013**, *52*, 976; e) R. Krishna Kumar, X. X. Yu, A. Patil, M. Li, S. Mann, *Angew. Chem.* **2011**, *123*, 9515; *Angew. Chem. Int. Ed.* **2011**, *50*, 9343; f) R. J. Williams, A. M. Smith, R. Collins, N. Hodson, A. K. Das, R. V. Ulijn, *Nat. Nanotechnol.* **2009**, *4*, 19.

[8] B. G. Xing, C. W. Yu, K. H. Chow, P. L. Ho, D. G. Fu, B. Xu, *J. Am. Chem. Soc.* **2002**, *124*, 14846.

[9] B. G. Xing, P. L. Ho, C. W. Yu, K. H. Chow, H. W. Gu, B. Xu, *Chem. Commun.* **2003**, 2224.

[10] a) J. Y. Li, Y. Kuang, Y. Gao, X. W. Du, J. F. Shi, B. Xu, *J. Am. Chem. Soc.* **2013**, *135*, 542; b) J. Y. Li, Y. Gao, Y. Kuang, J. F. Shi, X. W. Du, J. Zhou, H. M. Wang, Z. M. Yang, B. Xu, *J. Am. Chem. Soc.* **2013**, *135*, 9907.

[11] C. C. Wu, C. W. Hsu, C. D. Chen, C. J. Yu, K. P. Chang, D. I. Tai, H. P. Liu, W. H. Su, Y. S. Chang, J. S. Yu, *Mol. Cell. Proteomics* **2010**, *9*, 1100.

[12] W. H. Fishman, N. R. Inglis, S. Green, C. L. Anstiss, N. K. Gosh, A. E. Reif, R. Rustigia, M. J. Krant, L. L. Stolbach, *Nature* **1968**, *219*, 697.

[13] Z. Yang, G. Liang, M. Ma, Y. Gao, B. Xu, *Small* **2007**, *3*, 558.

[14] N. A. Elson, R. P. Cox, *Biochem. Genet.* **1969**, *3*, 549.

[15] K. G. Nelson, J. S. Haskill, S. Sloan, J. M. Siegfried, G. P. Siegal, L. Walton, D. G. Kaufman, *Cancer Res.* **1987**, *47*, 2814.

[16] J. Kapuscinski, *Biotech. Histochem.* **1995**, *70*, 220.

[17] W. H. Binder, O. W. Smrzka, *Angew. Chem.* **2006**, *118*, 7482; *Angew. Chem. Int. Ed.* **2006**, *45*, 7324.

[18] D. A. Lauffenburger, A. F. Horwitz, *Cell* **1996**, *84*, 359.

[19] M. J. Humphries in *Extracellular Matrix Protocols, Vol. 522* (Eds.: S. Even-Ram, V. Artym), Humana Press, New York, **2009**, p. 203.

[20] S. M. Ogbourne, A. Suhrbier, B. Jones, S. J. Cozzi, G. M. Boyle, M. Morris, D. McAlpine, J. Johns, T. M. Scott, K. P. Sutherland, J. M. Gardner, T. T. T. Le, A. Lenarczyk, J. H. Aylward, P. G. Parsons, *Cancer Res.* **2004**, *64*, 2833.

[21] Y. Kuang, B. Xu, *Angew. Chem.* **2013**, *125*, 7082; *Angew. Chem. Int. Ed.* **2013**, *52*, 6944.

Protein Delivery

Combinatorially Designed Lipid-like Nanoparticles for Intracellular Delivery of Cytotoxic Protein for Cancer Therapy**

Ming Wang, Kyle Alberti, Shuo Sun, Carlos Luis Arellano, and Qiaobing Xu*

Abstract: *An efficient and safe method to deliver active proteins into the cytosol of targeted cells is highly desirable to advance protein-based therapeutics. A novel protein delivery platform has been created by combinatorial design of cationic lipid-like materials (termed "lipidoids"), coupled with a reversible chemical protein engineering approach. Using ribonuclease A (RNase A) and saporin as two representative cytotoxic proteins, the combinatorial lipidoids efficiently deliver proteins into cancer cells and inhibit cell proliferation. A study of the structure–function relationship reveals that the electrostatic and hydrophobic interactions between the lipidoids and the protein play a vital role in the formation of protein–lipidoid nanocomplexes and intracellular delivery. A representative lipidoid (EC16-1) protein nanoparticle formulation inhibits cell proliferation in vitro and suppresses tumor growth in a murine breast cancer model.*

Protein therapy has been considered as the safest and most direct approach to manipulate cell function and treat human disease since the early 1980s, when insulin began to be used as the first human recombinant protein therapeutic.[1] A majority of protein pharmaceuticals (for example, cytokines, growth factors, and monoclonal antibodies) elicit their biological activity by targeting cell surface ligands or extracellular domains.[2] Nevertheless, advancements in molecular biology have suggested that proteins that target intracellular biological activity could be potent therapeutics.[3] The delivery of proteins safely and efficiently through the cell membrane to reach their intracellular targets remains a challenge for the success of protein therapy.[3b] As such, the development of methods for intracellular protein delivery is needed. Over the past few decades, the most thoroughly studied protein delivery approach has been fusing target protein cargos with protein transduction domains (PTD) or membrane transport signals. The delivery efficiency of PTD-protein fusions vary with protein type[4] and lack the capability to target a specific tissue or organ. More recently,

nanoparticle drug delivery systems have offered alternative approaches for spatially and temporally controlled protein delivery. A number of synthetic nanomaterials, including liposomes,[5] polymers,[6] and inorganic nanoparticles,[7] have been designed for this purpose. These nanoparticules, however, are still of limited utility for protein therapy owing to the low delivery efficiency and/or complicated nanoparticle fabrication processes. Thus, a facile and convenient approach to develop novel nanomaterials for efficient intracellular protein delivery has yet to be developed.

We report herein a novel and efficient protein delivery platform that uses combinatorially designed cationic lipid-based nanoparticles combined with a reversible protein modification approach. Pioneered by Anderson, Langer, et al.,[8] the combinatorial library strategy has recently been used to generate cationic lipid-like materials (termed "lipidoids") for siRNA delivery. We have further extended this class of materials for use in DNA and mRNA delivery.[9] We hypothesize that lipidoids can be used as a novel protein delivery platform, as the charge–charge and hydrophobic interactions between lipidoids and proteins can load proteins into lipidoid nanoparticles. In turn, the hydrophobic nature of lipidoid nanoparticles allows easy protein transport through the cell membrane. In an attempt to strengthen the charge–charge binding of proteins and lipidoids, we modified the lysine residues of proteins with *cis*-aconitic anhydride in this investigation. The conjugation reaction between the amine groups of lysine and *cis*-aconitic anhydride converts the positively charged lysines into negatively charged carboxylate groups, thus increasing the negative charge density of protein and its binding with cationic lipidoids. Moreover, the *cis*-aconitic anhydride modification is reversible in the slightly acidic intracellular environment (for example, the pH of endosome and lysosome is in the range of 5–6),[10] leading to the restoration of the biological activity of the modified proteins.

As a proof-of-concept for developing cationic lipid-based nanoparticles for protein delivery, we designed and synthesized a library of lipidoids through the ring-opening reaction of 1, 2-epoxyhexadecane and aliphatic amines with diversified chemical structures (Figure 1). Using RNase A and saporin, two representative cytotoxic proteins, along with the *cis*-aconitic anhydride modified versions (RNase A-Aco and saporin-Aco), we demonstrate that the lipidoid nanoparticles can deliver protein into cancer cells and inhibit cell proliferation, for potential applications such as cancer therapy. RNase A can cleave intracellular RNA and induce cytotoxic effects when taken up by cells,[11] while saporin irreversibly inhibits protein synthesis in eukaryotic cells by rending the 28S subunit of ribosomes.[12] RNase A and saporin have both

[*] Dr. M. Wang, K. Alberti, S. Sun, C. L. Arellano, Prof. Dr. Q. B. Xu
    Department of Biomedical Engineering, Tufts University
    4 Colby Street, Medford, MA (USA)
    E-mail: qiaobing.xu@tufts.edu

Figure 1. a) Route of synthesis for lipidoids. b) The chemical structures of the library of amines used for lipidoid synthesis (The lipidoids are named EC16, for 1, 2-epoxyhexadecane, followed by the amine number).

Figure 2. Evaluation of lipidoid-facilitated protein delivery on B16F10 cell line via a cytotoxicity assay. Black: lipidoid controls (4 µg mL^{-1}); green: RNase A (3.3 µg mL^{-1}); yellow: RNase A-Aco (3.3 µg mL^{-1}); blue: saporin (0.17 µg mL^{-1}); red: Saporin-Aco (0.17 µg mL^{-1}). Cytotoxicity was determined by MTT assay. Data are presented as mean ± SD ($n = 4$).

been used in clinical trials in cancer patients that are refractory to traditional chemotherapy.[13] In an in vivo study, we demonstrate that the administration of a representative lipidoid/saporin nanoparticle formulation suppresses tumor growth in a 4T1 murine breast cancer model by accumulating saporin at tumor sites.

The library of lipidoids was synthesized through the ring-opening reaction between 1,2-epoxyhexadecane and amine under mild conditions according to the methods of previous reports.[9a,b] The crude products were used directly for initial identification of protein delivery materials, and subsequently purified for detailed formulation studies. The lipidoids are named EC16 followed by the amine number in the library (Figure 1), where EC16 indicates 1,2-epoxyhexadecane. The reversible chemical modifications of RNase A or saporin were achieved by reacting proteins with excessive amounts of cis-aconitic anhydride, followed by a dialysis purification process. RNase A-Aco was selected for detailed study to confirm the acid-labile nature and chemical reversibility of the cis-aconitic anhydride modification of the proteins. The treatment of RNase A-Aco with an acidic buffer solution (NaOAc, pH 5.2) restored the protein back to RNase A, as confirmed by SDS-PAGE analysis (Supporting Information, Figure S1 A). Moreover, the acid-treated RNase A-Aco significantly enhances ribonuclease activity compared to that of neutral PBS treated RNase A-Aco (Figure S1 B). These results suggest that protein modification using cis-aconitic anhydride is acid-labile and chemically reversible. Such a reversible protein modification approach has the potential to boost electrostatic binding of protein with cationic lipidoids while having minor effect on their intracellular function.

The capability of lipidoids to deliver protein was evaluated by co-culturing murine melanoma cancer cells (B16F10) with lipidoid–protein complexes of RNase A, saporin, RNase A-Aco, or saporin-Aco. As the successful transduction of RNase A or saporin into cell induces cyto-

toxicity and inhibits cell proliferation,[11,13b] the protein delivery efficiency by various lipidoid-based nanoparticles was compared by measuring the viability of differently treated cells. As shown in Figure 2, all lipidoids displayed low carrier cytotoxicity, with cell viabilities greater than 90% following exposure to each of the lipidoids at a concentration of 4 µg mL^{-1}. Similarly, we observed no detectable toxicity to B16F10 cells following exposure to the four proteins (3.3 µg mL^{-1} for RNase A and RNase A-Aco, 0.17 µg mL^{-1} for saporin and saporin-Aco). This can be attributed to the naked protein lacking an efficient mode of entry to cells. Lipidoid–protein complex treated cells, however, showed distinct changes in cell viability, depending on the lipidoid and protein type. No appreciable viability decrease was observed for lipidoid/RNase A treated cells, indicating a low RNase A delivery efficiency by all lipidoids in the library. This is most likely because of the high intrinsic positive charge, and hydrophilic nature of RNase A, which prevented the formation of stable nanocomplexes for membrane penetration. In contrast, RNase A-Aco, saporin, and saporin-Aco can be delivered using seven of the lipidoids in the library (EC16-1, EC16-3, EC16-4, EC16-5, EC16-6, EC16-12, and EC16-14). A notable example of a lipidoid with high protein delivery efficiency is EC16-1, which facilitates the delivery of RNase A-Aco, saporin, and saporin-Aco, and reduces B16F10 cell viability down to 30%. It is also noteworthy that EC16-1 delivered both chemically modified and non-modified saporin with comparable efficiency. This indicates that the charge–charge interaction is not the only driving force facilitating lipidoid and protein binding, and that hydrophobic interactions may also contribute to the complexation between protein (saporin) and lipidoid. The significance of hydrophobic interaction between lipidoid and protein in facilitating protein delivery was further demonstrated by delivering RNase A-Aco and saporin with lipidoids of varied tail length.

Two lipidoids with shorter hydrophobic tails, EC14-1 and EC14-12, delivered RNase A-Aco and saporin and subse-

quently inhibited cell proliferation less efficiently than EC16-1 and EC16-12 (Figure S2). This suggests that lipidoids with longer hydrophobic tails have higher protein delivery efficiency. Moreover, these findings demonstrate the advantage of a combinatorial approach for the discovery of novel nanocarriers for protein delivery and the investigation of structure–function relationships. The complexation between EC16-1 and proteins was characterized by dynamic light scattering (DLS) analysis. The complexation between negatively charged RNase A-Aco or saporin-Aco and EC16-1 increased the size and decreased the zeta-potential of the EC16-1 particles, while the addition of unmodified RNase A or saporin into the EC16-1 solution had only minor effect on the size and surface charge of EC16-1 (Table S1). The representative nanoparticle structures of EC16-1 and EC16-1/RNase A-Aco complexes were further characterized by TEM imaging (Figure S3). The dispersed EC16-1 solution formed nanoparticles with a size of about 200 nm, while typical lipsome-like structures were observed for the EC16-1/RNase A-Aco complexes.

To investigate lipidoid facilitated protein delivery in detail, RNase A-Aco, and saporin were selected along with the lipidoid EC16-1 as representative proteins and lipidoid for the remainder of the studies. Protein delivery conditions were initially optimized by treating B16F10 cells with lipidoid–protein complexes mixed at varied EC16-1 to protein ratio, while the concentrations of RNase A-Aco and saporin that the cells were exposed to was fixed at 3.3 µg mL^{-1} and 0.17 µg mL^{-1}, respectively (Figure S4). Optimal results were achieved at mass ratio of 2:5 for EC16-1/RNase A-Aco, and 20:1 for EC16-1/saporin complex, and further increases in lipidoid to protein ratio did not improve the delivery efficiency. Furthermore, the cytotoxicity of EC16-1/RNase A-Aco and EC16-1/saporin complexes against B16F10 cells is dependent on protein dose. As shown in Figure 3, when used as stand-alone agents, RNase A-Aco and

mined to be 64 nM and 5.3 nM respectively, which was greatly improved compared to RNase A-Aco and saporin alone.

Whether lipidoids such as EC16-1 are able to deliver proteins to a panel of cancer cell lines was also investigated. An efficient protein delivery platform for cancer therapy must be able to transfect various cell lines, as each consists of different cell surface environments which may affect the internalization of nanoparticles and the protein delivery. We selected human breast cancer cells (MCF-7 and MDA-MB-231), human liver hepatocellular carcinoma cells (HepG 2), human prostate cancer cell lines (PC-3 and LNCaP), human cervical carcinoma cells (HeLa), and murine breast cancer cells (4T1) as target cell lines. These cells were treated with EC16-1/RNase A-Aco or EC16-1/saporin complexes at previously optimized delivery conditions. Table 1 summarizes the IC$_{50}$ values that were determined following the treatments of EC16-1/RNase A-Aco or EC16-1/saporin complexes to all of the cancer cell lines. The delivery of EC16-1/RNase A-Aco or EC16-1/saporin complexes resulted in significant cytotoxicity in all cell lines, suggesting the general applicability of lipidoid EC16-1 for protein delivery.

Table 1: IC$_{50}$ values of RNase A-Aco and saporin delivered by EC16-1 against various cancerous cell lines.

Cell line	Cancer type	RNaseA-Aco [nM]	Saporin [nM]
MCF-7	breast	40.6	2.9
MDA-MB-231	breast	57	2.5
B16F10	melanoma	64	5.3
HepG 2	liver	28	3.9
PC-3	prostate	125	2.3
LNCaP	prostate	243	1.4
HeLa	cervix	48	3.2
4T1	breast	412	0.9

Having demonstrated the high efficiency and generality of EC16-1 for protein delivery, we next developed a general protein delivery formulation that comprises protein (RNase A-Aco or saporin), lipidoid EC16-1, 1,2-dioleoyl-sn-glycero-3-phosphoethanolamine (DOPE), cholesterol, and *N*-(palmitoyl)sphingosine[succinyl{methoxy(polyethylene glycol)2000}] (C16-mPEG-ceramide) for in vivo protein delivery. We further post-modified the lipidoid/protein formulations with DSPE-PEG2000-biotin to target tumor cells and tissues. Biotinylated polymers or nanoparticles can be selectively taken up by cancer cells and accumulate in the tumor tissue, improving therapeutic efficacy.[14] The EC16-1/RNase A-Aco and EC16-1/saporin nanoparticle formulation and also empty EC16-1 formulated nanoparticles are about 120 nm in size, as determined by dynamic light scattering (DLS) analysis (Figure 4a). The typical nanoparticular structure of EC16-1/saporin formulation was visualized by TEM (Figure 4b). Subsequent zeta-potential analysis of the nanoparticles revealed the positively charged nature of EC16-1 (7.6 ± 0.3 mV) and EC16-1/saporin formulations (5.6 ± 0.2 mV), while EC16-1/RNase A-Aco formulation had a reduced zeta-potential of −13.5 ± 1.4 mV (Figure 4a). The surface charge measurements of EC16-1/protein nanoformu-

Figure 3. Protein concentration-dependent cytotoxicity of EC16-1 mediated RNase A-Aco (a) and saporin (b) delivery on B16F10 cells (Protein only: △; Lipidoid/protein nanoparticle: ■). Data are presented as mean ± SD (*n* = 4).

saporin show low cytotoxicities at all of the studied concentrations. EC16-1/RNase A-Aco and EC16-1/saporin complexes prepared at optimized delivery conditions, however, had significantly enhanced protein cytotoxicity and displayed protein-concentration dependence. The half-maximal growth inhibitory concentration (IC$_{50}$) of EC16-1/RNase A-Aco and EC16-1/saporin complexes against B16F10 cells was deter-

a)

	Size (nm)	Zeta potential (mV)
EC16-1	129.4 ± 5.4	7.65 ± 0.25
EC16-1/RNase A-Aco	126.0 ± 8.7	-13.5 ± 1.45
EC16-1/saporin	131.5 ± 9.7	5.64 ± 0.23

b)

Figure 4. Characterization of EC16-1/protein nanoformulations: a) size and zeta-potential measurements; b) TEM images of EC16-1/saporin nanoformulation.

lations further confirmed the different complexation modes of lipidoids with RNase A-Aco and saporin. The charge–charge interaction between RNase A-Aco and EC16-1 neutralizes the positive charge of the lipidoid nanoparticles, while saporin is encapsulated into the lipidoid primarily by hydrophobic interactions and thus has a minor effect on the surface charge of EC16-1 nanoparticles.

The cellular uptake and intracellular trafficking of EC16-1/protein nanoparticles were studied by formulating FITC-labeled RNase A-Aco (FITC-RNase A-Aco) with EC16-1 and exposing to B16F10 cells. A confocal laser fluorescence microscopy (CLSM) imaging study (Figure 5a) reveals that
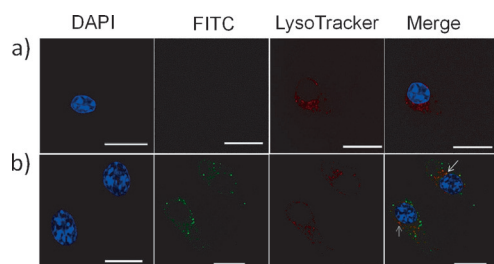
Figure 5. Confocal laser scanning microscopy (CLSM) images of B16F10 cells incubated for 4 h with free FITC-RNase A-Aco (a) and EC16-1/FITC-RNase A-Aco nanoformulations (b). Cells were counterstained with DAPI (for nuclei) and LysoTracker Red (for endosome/lysosomes). Scale bar: 20 μm.

free FITC-RNase A-Aco had a low efficiency of entry of protein. In contrast, significant cellular uptake and intracellular accumulation of EC16-1/protein nanoparticles were observed as green fluorescent pinpoints in the CLSM images of cells treated with the EC16-1/FITC-RNase A-Aco nanoformulation (Figure 5b). The different uptake of free protein and EC16-1/FITC-RNase A-Aco nanoparticles was further confirmed by a flow cytometry analysis (Figure S5). FITC-RNase A-Aco treated cells had comparable mean fluorescence intensity to that of untreated cells, while the cells exposed to EC16-1/FITC-RNase A-Aco nanoformulation had significantly enhanced fluorescence intensities, suggesting that the EC16-1 formulation is capable of delivering proteins. Moreover, B16F10 cells incubated with EC16-1/

FITC-RNase A-Aco nanoparticles at a lower temperature (4°C) have a significantly reduced nanoparticle uptake compared to that at 37°C (Figure S5). This is an indicative of endocytosis process of EC16-1/FITC-RNase A-Aco nanoparticles, as endocytosis of nanoparticles is known as an energy-dependent process. The endocytosized EC16-1/FITC-RNase A-Aco nanoparticles efficiently escape from endosome/lysosome after entering cells. The CLSM imaging studies by counterstaining endosome/lysosome reveals the co-localization of EC16-1/FITC-RNase A-Aco nanoparticles within endosome/lysosome after 4 h of incubation (white arrows in Figure 5b). However, significant amounts of protein had already escaped from the endosomal compartment, as indicated by the green fluorescence throughout the cell.

The efficiency of EC16-1/protein formulations to inhibit cell proliferation was further determined using B16F10 cells. The treatment of cells with RNase A-Aco or saporin nanoformulation inhibited cell proliferation in a protein-dose-dependent manner (Figure S6). The potential cytotoxicity of empty EC16-1 nanoparicles was excluded in Figure S7. Meanwhile, B16F10 cells treated with varying concentrations 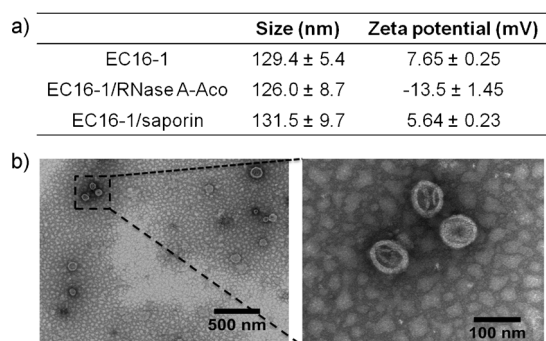of RNase A-Aco or saporin formulations, without EC16-1 caused only a minor decrease in cell viability, compared to that of similar formulations containing EC16-1 (Figure S8). This indicates the vital role that lipidoids play in the formulation of protein nanoparticles for intracellular delivery. The IC_{50} of RNase A-Aco and saporin nanoformulation against B16F10 cells was determined to be 36.5 nM and 4.2 nM, respectively, with an improvement compared to that of EC16-1/protein complexes without formulation processes (Table 1).

Finally, in vivo protein delivery using EC16-1/saporin nanoparticles as a representative protein formulation was conducted to assess the potential of intracellular delivery of EC16-1/protein nanoparticles for cancer therapy. First, the accumulation of EC16-1/saporin nanoformulation at tumor sites was investigated in a murine breast cancer model. Balb/c mice brearing 4T1 tumors were intravenously injected with EC16-1/saporin nanoparticles or free saporin (310 μg kg^{-1} of saporin). The tumors were harvested 4 h post-injectection for saporin analysis. Immunohistochemical studies (Figure 6a) showed significant amounts of saporin accumulation at tumor sites with EC16-1/saporin nanoformulation injection (as indicated by the dark regions), while no protein accumulation was observed for mice treated with free saporin. The in vivo protein delivery ability of EC16-1/saporin nanoparticles and saporin accumulation at tumor sites were also observed in a B16F10 murine melanoma cancer model. As shown in Figure S9, the intravenous injection of EC16-1/saporin nanoparticles into C57BL/6J mice bearing B16F10 melanoma tumors resulted in similar accumulation of saporin at the tumor site.

The accumulation of EC16-1/saporin nanoformulations at the tumor sites could be ascribed to the enhanced permeability and retention (EPR) effect of the leaky vascular structure of the tumor tissue.[15] Having confirmed the successful and efficient delivery of saporin into tumors, a comparative tumor growth suppression study was performed in the 4T1 murine breast cancer model. 4T1-tumor-
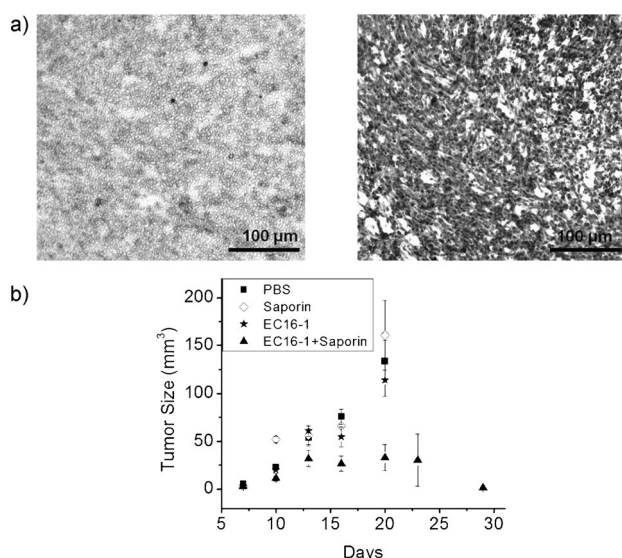
Figure 6. In vivo delivery of EC16-1/saporin nanoformulations into 4T1 breast tumor bearing mice: (a) immunohistochemistry (IHC) studies of saporin accumulation at tumor sites. Saporin in an uncomplexed form (left) and in EC16-1/saporin nanoparticles (right), administrated by tail-vein injection. (b) EC16-1/saporin nanoparticle delivery suppresses tumor growth on a 4T1 breast cancer model. Tumor sizes reported as mean ± SEM.

bearing mice were divided into four groups, and each group of mice received a different treatment (PBS, EC16-1, saporin, or EC16-1/saporin) by intravenous tail vein injection every three days for a total of three injections per mouse. Following each treatment, the tumor growth was monitored by direct caliper measurement. As shown in Figure 6b, EC16-1 and free saporin treated groups had similar tumor volumes to that of PBS control mice. EC16-1/saporin nanoparticle-treated mice, however, had significantly reduced tumor volumes (by 80%) compared to the control groups. Mouse body weight were also monitored during the treatments (Figure S10) to verify that administration did not result in significant toxicity. No significant body weight changes during the treatments were observed nor were a decrease in body condition. Furthermore, the immune response to EC16-1/saporin nanoparticle injections was monitored by measuring the TNF-α and IFN-γ level in the blood samples of mice (Figure S11) to confirm that reduction in tumor volume was not a result of immune stimulation. No significant increase in TNF-α or IFN-γ level were observed in EC16-1/saporin-nanoparticle treated mice compared to the levels in PBS or free saporin-treated mice. The above results demonstrate that EC16-1/saporin nanoparticles can deliver protein in vivo and suppress tumor growth. This suggests that lipidoids are a safe and efficient protein delivery platform for the delivery of cytotoxic proteins for cancer therapy.

In summary, we have reported that our combinatorially designed cationic lipidoid nanoparticles function as a novel protein delivery platform. We synthesized a library of lipidoids through the mild ring-opening reactions of 1,2-epoxyhexadecane with primary or secondary aliphatic amines. Using two representative cytotoxic proteins (RNase A and saporin), we have found that the intrinsic physical properties of the proteins (net negative charge and hydrophobicity) determine the protein–lipidoid interactions and affect the intracellular delivery efficiency. The lipidoid that we selected for primary study, EC16-1, is able to deliver cytotoxic RNase A-Aco and saporin to a panel of cancer cell lines and inhibit cell proliferation. Furthermore, we developed several lipidoid/protein formulations that are efficient for in vitro and in vivo protein delivery. EC16-1/saporin nanoparticles were shown to accumulate at the tumor site and they suppressed tumor growth in a murine breast cancer model. Taken together, these results suggest that combinatorially developed lipidoids can be a highly efficient and effective delivery platform for protein therapeutics. We believe the results disclosed herein will help advance and accelerate the clinical translation of protein pharmaceuticals for cancer therapy.

[1] D. V. Goeddel, D. G. Kleid, F. Bolivar, H. L. Heyneker, D. G. Yansura, R. Crea, T. Hirose, A. Kraszewski, K. Itakura, A. D. Riggs, *Proc. Natl. Acad. Sci. USA* **1979**, *76*, 106–110.

[2] B. Leader, Q. J. Baca, D. E. Golan, *Nat. Rev. Drug. Discovery* **2008**, *7*, 21–39.

[3] a) G. Walsh, *Nat. Biotechnol.* **2010**, *28*, 917–924; b) Z. Gu, A. Biswas, M. X. Zhao, Y. Tang, *Chem. Soc. Rev.* **2011**, *40*, 3638–3655.

[4] Z. B. Mi, J. Mai, X. L. Lu, P. D. Robbins, *Mol. Ther.* **2000**, *2*, 339–347.

[5] a) S. K. Kim, M. B. Foote, L. Huang, *Biomaterials* **2012**, *33*, 3959–3966; b) O. Zelphati, Y. Wang, S. Kitada, J. C. Reed, P. L. Felgner, J. Corbeil, *J. Biol. Chem.* **2001**, *276*, 35103–35110.

[6] J. S. Lee, J. Feijen, *J. Controlled Release* **2012**, *161*, 473–483.

[7] P. Ghosh, X. Yang, R. Arvizo, Z.-J. Zhu, S. S. Agasti, Z. Mo, V. M. Rotello, *J. Am. Chem. Soc.* **2010**, *132*, 2642–2645.

[8] a) A. Akinc, A. Zumbuehl, M. Goldberg, E. S. Leshchiner, V. Busini, N. Hossain, S. A. Bacallado, D. N. Nguyen, J. Fuller, R. Alvarez, A. Borodovsky, T. Borland, R. Constien, A. de Fougerolles, J. R. Dorkin, K. N. Jayaprakash, M. Jayaraman, M. John, V. Koteliansky, M. Manoharan, L. Nechev, J. Qin, T. Racie, D. Raitcheva, K. G. Rajeev, D. W. Y. Sah, J. Soutschek, I. Toudjarska, H. P. Vornlocher, T. S. Zimmermann, R. Langer, D. G. Anderson, *Nat. Biotechnol.* **2008**, *26*, 561–569; b) Y.-H. Huang, Y. Bao, W. Peng, M. Goldberg, K. Love, D. A. Bumcrot, G. Cole, R. Langer, D. G. Anderson, J. A. Sawicki, *Proc. Natl. Acad. Sci. USA* **2009**, *106*, 3426–3430; c) K. T. Love, K. P. Mahon, C. G. Levins, K. A. Whitehead, W. Querbes, J. R. Dorkin, J. Qin, W. Cantley, L. L. Qin, T. Racie, M. Frank-Kamenetsky, K. N. Yip, R. Alvarez, D. W. Sah, A. de Fougerolles, K. Fitzgerald, V. Koteliansky, A. Akinc, R. Langer, D. G. Anderson, *Proc. Natl. Acad. Sci. USA* **2010**, *107*, 1864–1869; d) D. N. Nguyen, K. P. Mahon, G. Chikh, P. Kim, H. Chung, A. P. Vicari, K. T. Love, M. Goldberg, S. Chen, A. M. Krieg, J. Chen, R. Langer, D. G. Anderson, *Proc. Natl. Acad. Sci. USA* **2012**, *109*, E797–E803; e) C. A. Alabi, K. T. Love, G. Sahay, H. Yin, K. M. Luly, R. Langer, D. G. Anderson, *Proc. Natl. Acad. Sci. USA* **2013**, *110*, 12881–12886.

[9] a) M. Wang, S. Sun, K. A. Alberti, Q. Xu, *ACS Synth. Biol.* **2012**, *1*, 403 – 407; b) S. Sun, M. Wang, S. A. Knupp, Y. Soto-Feliciano, X. Hu, D. L. Kaplan, R. Langer, D. G. Anderson, Q. B. Xu, *Bioconjugate Chem.* **2012**, *23*, 135 – 140; c) S. Sun, M. Wang, K. A. Alberti, A. Choy, Q. B. Xu, *Nanomed-Nanotechnol.* **2013**, *9*, 849 – 854.

[10] a) Y. Lee, T. Ishii, H. Cabral, H. J. Kim, J. H. Seo, N. Nishiyama, H. Oshima, K. Osada, K. Kataoka, *Angew. Chem.* **2009**, *121*, 5413 – 5416; *Angew. Chem. Int. Ed.* **2009**, *48*, 5309 – 5312; b) Y. Lee, T. Ishii, H. J. Kim, N. Nishiyama, Y. Hayakawa, K. Itaka, K. Kataoka, *Angew. Chem.* **2010**, *122*, 2606 – 2609; *Angew. Chem. Int. Ed.* **2010**, *49*, 2552 – 2555; c) K. Maier, E. Wagner, *J. Am. Chem. Soc.* **2012**, *134*, 10169 – 10173.

[11] R. T. Raines, *Chem. Rev.* **1998**, *98*, 1045 – 1065.

[12] J. G. Beitz, P. Davol, J. W. Clark, J. Kato, M. Medina, A. R. Frackelton, D. A. Lappi, A. Baird, P. Calabresi, *Cancer Res.* **1992**, *52*, 227 – 230.

[13] a) M. S. Iordanov, O. P. Ryabinina, J. Wong, T. H. Dinh, D. L. Newton, S. M. Rybak, B. E. Magun, *Cancer Res.* **2000**, *60*, 1983 – 1994; b) J. G. Beitz, P. Davol, J. W. Clark, J. Kato, M. Medina, A. R. Frackelton, D. A. Lappi, A. Baird, P. Calabresi, *Cancer Res.* **1992**, *52*, 227 – 230; c) L. Polito, M. Bortolotti, M. Pedrazzi, A. Bolognesi, *Toxins* **2011**, *3*, 697 – 720.

[14] a) A. Taheri, R. Dinarvand, F. S. Nouri, M. R. Khorramizadeh, A. T. Borougeni, P. Mansoori, F. Atyabi, *Int. J. Nanomed.* **2011**, *6*, 1863 – 1874; b) J. Su, F. Chen, V. L. Cryns, P. B. Messersmith, *J. Am. Chem. Soc.* **2011**, *133*, 11850 – 11853.

[15] Y. Matsumura, H. Maeda, *Cancer Res.* **1986**, *46*, 6387 – 6392.

Enhanced Intracellular siRNA Delivery using Bioreducible Lipid-Like Nanoparticles

Ming Wang, Kyle Alberti, Antonio Varone, Dimitria Pouli, Irene Georgakoudi, and Qiaobing Xu*

The discovery of RNA interference (RNAi) has had a transformative impact on the study of gene regulation for disease treatment. RNAi can knock down genes by targeting and cleaving complementary mRNA with a high efficiency using sequence-specific siRNA. It has the potential to silence any target gene, and to treat a variety of diseases, including cancers, viral infections, and hereditary disorders.[1] The therapeutic application of siRNA, however, is hindered by the lack of safe and efficient tools capable of delivering siRNA into the target cells. The past decade has witnessed substantive efforts in developing cationic lipids,[2] polymers,[3] and multifunctional inorganic nanoparticles[4,5] for siRNA delivery. A majority of these siRNA carriers encapsulate and escort siRNA into the cytosol in the form of nanoparticles and through an endocytotic pathway. These siRNA nanocomplexes, however, usually encounter a variety of biological barriers on their journey to their sites of action after entering cells, which could further affect their delivery efficiency. Notably, weak intracellular release of the siRNA from the nanocarriers limits the available siRNA that can initiate RNAi, and thus compromises gene silencing efficiency.[6] In general, siRNA is encapsulated into delivery vehicles in the form of nanoparticles, which can penetrate the cell membrane. However, binding between the siRNA and carrier that is too strong can retard the release of the siRNA, once the complex enters the cell. Therefore, designing smart siRNA delivery vehicles that can readily release siRNA in response to distinct intracellular environments has emerged as an effective approach to advance siRNA delivery.[7] Pioneering examples integrate components such as acid responsive units,[4,8] or reducible disulfide bonds[9] into cationic polymers. These complexes act as biodegradable siRNA nanocarriers by taking advantage of the acidic or strongly reductive environment that can be found within cells.

In this study, we report the design of bioreducible lipid-like materials (termed "lipidoid") integrating disulfide bonds, which are degradable in the presence of thiol-containing biomolecules, and can be used as a highly efficient siRNA delivery platform. It is generally known that glutathione (GSH) and/or other strongly reductive species are up-regulated inside cells, compared with levels found in blood plasma.[10] We believe that

a reductive intracellular environment such as this could trigger the degradation of bioreducible siRNA nanocomplexes via a route of thiol exchange reactions with the lipidoid, releasing the siRNA inside the cells efficiently, and boosting the gene knock down efficiency. Recently, Anderson and co-workers[11] have developed a combinatorial strategy that has been used to synthesize a library of lipidoids for siRNA delivery, which has also aided in the study of the structure–function relationship in lipidoid-facilitated siRNA delivery. We have further expanded this class of materials for use as delivery agents of DNA, mRNA, and proteins.[12,13]

Although there are a few reports that indicate that biodegradable lipids can improve DNA plasmid delivery,[14] a thorough investigation on the use of bioreducible lipid, or lipid-like materials for siRNA delivery has not been reported yet. This is mostly due to the laborious synthesis normally required, and inefficiencies associated with integrating biodegradable units into conventional lipids. In this paper, we synthesized six bioreducible lipidoids via Michael addition of aliphatic amines and acrylate, incorporating disulfide bonds (**Scheme 1**). To evaluate the effect of disulfide bond integration on the capability of lipidoid-facilitated delivery, six nonbioreducible lipidoids were synthesized using a similar strategy by replacing the disulfide bond in the acrylates with carbon–carbon bonds. All of the lipidoids were able to encapsulate siRNA via electrostatic interaction, forming nanoparticles, and efficiently entering cells. However, the lipoplexes composed of the bioreducible lipidoids released siRNA more efficiently than nonbioreducible lipidoid under a reductive environment, as revealed by gel electrophoresis assay and intracellular siRNA trafficking studies. Using siRNA targeting green fluorescence protein (GFP) as a model, it was observed that the bioreducible lipidoids/siRNA complexes suppressed the GFP expression of GFP-expressing MDA-MB-231 cells, with a significantly enhanced efficiency when compared with nonbioreducible lipidoids. A representative bioreducible lipidoid, **1**-O16B, was able to deliver siRNA-targeting polo-like kinase 1 (Plk-1) into cancer cells, depleting Plk-1 and inhibiting tumor cell proliferation, demonstrating the lipidoid's potential for cancer therapy.

The lipidoids, featuring bioreducible components were synthesized by reacting aliphatic amines with appropriate acrylates in a similar strategy to previous reports (Scheme 1).[13] Briefly, amines and acrylates were heated at molar ratios of 1:2.4 without any solvent, at 80 °C for 48 h. They were then cooled, and the crude products used directly for preliminary siRNA delivery studies. N,N-Dimethyl-1,3-propanediamine (**1**) and 2,2′-(3-aminopropyl-azanediyl) diethanol (**2**) were selected as representative amines based on our knowledge that they have the potential to form lipidoids with efficient gene delivery

Dr. M. Wang, K. Alberti, A. Varone, D. Pouli,
Prof. I. Georgakoudi, Prof. Q. Xu
Department of Biomedical Engineering
Tufts University
4 Colby Street, Medford MA, 02155, USA
E-mail: Qiaobing.Xu@tufts.edu

Materials
Views
www.MaterialsViews.com

ADVANCED
HEALTHCARE
MATERIALS
www.advhealthmat.de

COMMUNICATION
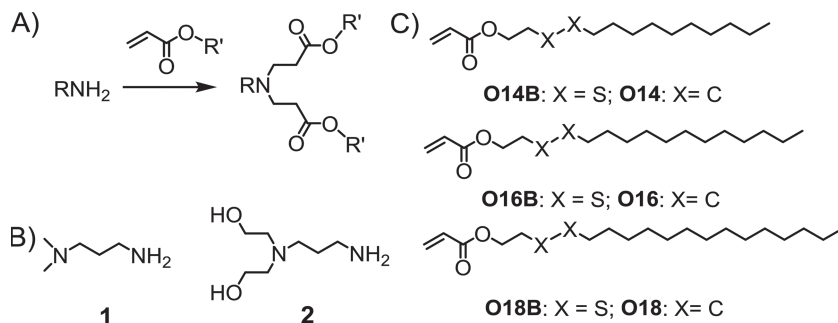
Scheme 1. A) Synthesis of lipidoids via Michael addition conjugation of an amine and an acrylate, B) Chemical structures of amines, and C) acrylates used for lipidoid synthesis. The lipidoids are named by the amine number, followed by the acrylate number.

ability.[13] Meanwhile, the incorporation of disulfide or carbon–carbon bonds into the acrylates allows us to evaluate the effect of bioreducible bond incorporation on the efficacy of lipidoid-facilitated siRNA delivery (Scheme 1). For simplicity, lipidoids were named using the following method: the first number indicates the amine number, followed by "O" indicating "acrylate," and the number of carbon atoms that comprises each hydrophobic tail of the acrylate. A "B" was added to the end of the name when referring to a bioreducible lipidoid. For example, **1-O16** represents the lipidoid synthesized from amine **1** and O16, while **1-O16B** indicates the lipidoid prepared by reacting amine **1** and acrylate O16B, which features two disulfide bonds in its hydrophobic tail.

We first evaluated the capability of lipidoids to deliver siRNA by transfecting a breast cancer cell line that stably expresses GFP (GFP-MDA-MB-231) with siRNA targeting the GFP gene (siGFP). Cells were exposed to siGFP complexes (24×10^{-9} M of siRNA) formulated with one of the 12 lipidoids in the library (Scheme 1), and the cellular GFP expression profile following each lipidoid/siGFP treatment was measured 48 h post-transfection using flow cytometry analysis. The GFP expression was calculated by dividing the mean fluorescence intensity of treated cells to that of untreated controls. As shown in **Figure 1**, naked siGFP treatment has no effect on suppressing GFP expression, suggesting that naked siRNA has inefficient cellular uptake or instability in serum. The lipidoid/siGFP-treated cells, however, display varying levels of GFP expression depending on the specific lipidoid used in the lipidoid/siRNA lipoplexes. All nonbioreducible lipoplex treatments suppressed GFP expression slightly; the most efficient nonbioreducible lipidoid, **2-O14**, reduced GFP expression to 80% of controls. In contrast, the bioreducible lipidoid/siRNA complexes silenced GFP expression with much higher efficiency than the nonbioreducible lipidoids that contained the same amine head and hydrophobic tail length. For example, **1-O16B**/siGFP suppressed GFP expression down to 28% compared with 90% expression by **1-O16**/siGFP. Similarly, the exposure of cells to the other five bioreducible lipidoids/siGFP complexes suppressed GFP expression by greater percentages than their nonbioreducible counterparts. More noteworthy, four of the six bioreducible lipidoids, **2-O14B**, **1-O16B**, **2-O16B**, and **1-O18B**, suppressed GFP expression with an efficiency outperforming the commercial gene transfection reagent, Lipofectamine 2000 (Figure 1). The preliminary siRNA delivery screening results indicate that the integration

of bioreducible disulfide bonds into lipidoids enhanced their capability as siRNA delivery vehicles.

To understand the mechanism of enhanced siRNA delivery using bioreducible lipidoids, **1-O16B** and **1-O16** were selected and purified as representative bioreducible and nonbioreducilbe lipidoids, respectively. The chemical structures of **1-O16B** and **1-O16** were confirmed by ^{1}H NMR (Figure S1, Supporting Information) and electrospray ionization-mass spectrometry (ESI-MS). Both **1-O16B** and **1-O16** can effectively bind siRNA, as revealed by an agarose gel retardation assay (**Figure 2**a). The complexation of siRNA with **1-O16B** or **1-O16** at an N/P ratio of 24 completely retarded the migration of siRNA (10 pmol), though the nonbioreducible lipidoid (**1-O16**) has a slightly higher binding affinity toward siRNA. The encapsulaion of siRNA by **1-O16B** and **1-O16** efficiently protects siRNA from nuclease degradation. As shown in Figure 2b, naked siRNA (10 pmol) was completely degraded within 2 h upon exposure to RNase A (4 µg mL^{-1}). However, when the same amount of siRNA was complexed with **1-O16B** or **1-O16** (at an N/P ratio of 24), the siRNA remained intact for more than 2 h of RNase A treatment showing that both bioreducible and nonbioreducible lipidoid can protect siRNA from enzymatic degradation at comparable efficiencies.

To understand whether the bioreducible lipidoid/siRNA complexes can release siRNA more efficiently than nonbioreducible lipidoids under a reductive intracellular environment, a gel retardation assay (Figure 2c) was used. It is generally known that glutathione (GSH) is up-regulated over 1000-fold in the cytoplasm compared with blood plasma.[10] This high concentration of intracellular GSH can degrade the bioreducible lipidoids
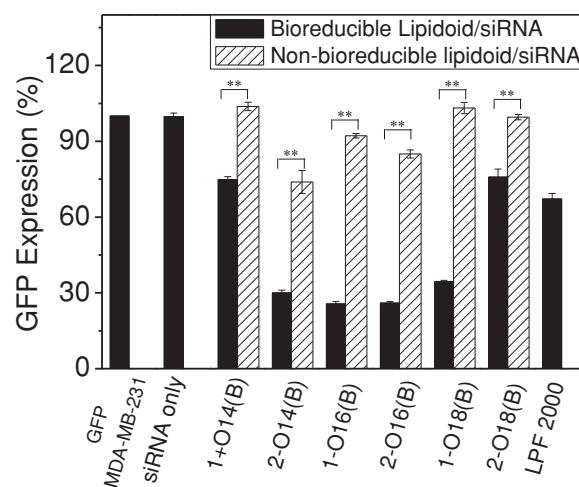
Figure 1. GFP expression of GFP-MDA-MB-231 cells treated with naked siGFP, lipidoid/siGFP nanocomplexes, and Lipofectamine 2000 (LPF 2000)/siGFP complexes. The siRNA complexes were prepared by mixing siGFP (24×10^{-9} M) with lipidoids at N/P ratios of 5:1 or LPF2000 at weight/weight ratio of 6:1. Data are presented as mean ± SD ($n = 3$, the two asterisks refer to statistical significance between bioreducible and nonbioreducible lipidoid facilitated siRNA delivery, $P < 0.05$, Student's t-test).

**ADVANCED
HEALTHCARE
MATERIALS**

www.advhealthmat.de

Materials Views

www.MaterialsViews.com

Figure 2. A) Gel electrophoresis assay of siRNA/lipidoid complexes at varying N/P ratios. 1) siRNA only; 2–4: **1**-O16B/siRNA complexes mixed at N/P ratios of 6 (lane 2); 12 (lane 3), 24 (lane 4); 5–7: **1**-O16/siRNA complexes mixed at N/P ratios of 6 (lane 5); 12 (lane 6), 24 (lane 7); B) Lipidoid **1**-O16B and **1**-O16 protected siRNA from nuclease degradation; C) GSH-triggered siRNA release from lipidoid/siRNA complexes. Lane 1: siRNA; 2–3: siRNA/**1**-O16B complex in the absence (lane 2) and presence of 5×10^{-3} M GSH (lane 3); 4–5: siRNA/**1**-O16 complex in the absence (lane 4) and presence of 5×10^{-3} M GSH (lane 5).

through a route of disulfide bond exchange with GSH, and such a degradation process can facilitate the release of siRNA from the lipoplexes, potentially improving the siRNA delivery. As shown in Figure 2c, the treatment of **1**-O16B/siRNA or **1**-O16/siRNA complexes with GSH (5×10^{-3} M) results in differences in siRNA release. The **1**-O16B/siRNA lipoplex releases a significant amount of siRNA (lane 3) upon GSH treatment, while in contrast, this siRNA release is not observed from **1**-O16/siRNA complexes in the presence of the same concentration of GSH (lane 5).

The nanoparticle structures of the lipidoid/siRNA complexes as well as the GSH-treated bioreducible lipoplexes after degradation were further characterized by dynamic light scattering (DLS) analysis and transmission electron microscopy (TEM) studies. The complexation of **1**-O16B and **1**-O16 with siRNA formed nanoparticles with mean sizes of 160 nm and 106 nm, respectively. The treatment of **1**-O16B/siRNA nanoparticles with 5×10^{-3} M GSH degraded the lipoplexes and broadened the particle size distribution, as measured by DLS analysis (**Table 1**). However, no significant nanoparticle size variation was observed for the **1**-O16/siRNA complexes in the absence or presence of GSH. The degradation of the lipidoid/siRNA complexes in the presence of GSH was further confirmed by TEM imaging. **1**-O16B/siRNA and **1**-O16/siRNA complexes form nanoparticles with diameters of ≈100 nm (**Figure 3** and Figure S2, Supporting Information). However, following the addition of GSH to the above lipoplexes, no discrete nanoparticles were observed for **1**-O16B/siRNA complexes (Figure 3), while nanoparticles that retained their original diameter were observed for the **1**-O16/siRNA complexes (Figure S2, Supporting Information). Taken together, the gel electrophoresis assay and nanoparticle characterization reveal that the intracellular reductive environment can trigger bioreducible lipidoid degradation and facilitate intracellular siRNA release. We hypothesize that this

accounts for the enhanced gene silencing efficiency observed in the bioreducible lipidoid-facilitated siRNA delivery.

To further study whether the increased siRNA delivery efficiency of the bioreducible lipidoids was a result of the triggered release of siRNA intracellularly, the cellular uptake and intracellular siRNA trafficking of **1**-O16B/siRNA and **1**-O16/siRNA nanoparticles were monitored by delivering fluorescently labeled siRNA (FAM-siRNA) into MDA-MB-231 cells, coupled with confocal laser scanning microscopy (CLSM) imaging. As shown in **Figure 4**, MDA-MB-231 cells treated with fluorescent lipoplexes have a significant amount of green fluorescence, arising from FAM-siRNA, indicating the efficient cellular uptake of **1**-O16B/siRNA or **1**-O16/siRNA complexes. The endosome/lysosome were then stained using LysoTracker@Red, which showed that **1**-O16B/siRNA lipoplex escaped from the endosome/lysosome after 6 h of incubation (Figure 4A), as the green fluorescence (FAM-siRNA) was no longer co-localized with the red endosome/lysosome fluorescence. However, when the cells were treated with **1**-O16/siRNA complexes, the green fluorescence remained co-localized with the endosome/lysosome (yellow spots in Figure 4b), suggesting the entrapment of siRNA within
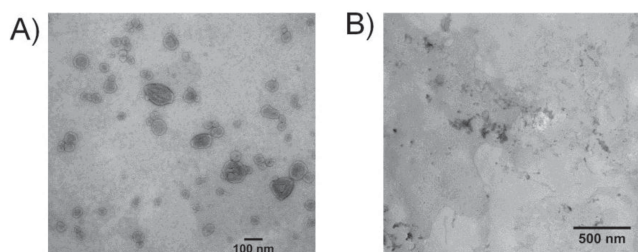
Figure 3. TEM images of siRNA and **1**-O16B complexes at N/P = 5 A) before and B) after GSH treatment.
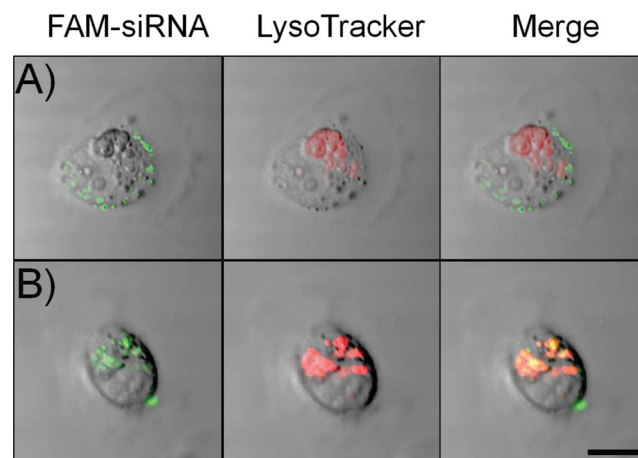
Figure 4. CLSM studies of MDA-MB-231 cells treated with A) **1**-O16B/FAM-siRNA complexes and B) **1**-O16/FAM-siRNA complexes for 6 h. The endosome/lysosome of cells were counter-stained using LysoTracker@Red. Scale bar: 12 µm.

Table 1. Hydrodynamic mean diameters of lipidoid-siGFP nanoparticles in the absence and presence of glutathione.

	1-O16B	1-O16
Lipidoid	74.7 ± 7.4 nm	117.2 ± 3.1 nm
Lipidoid+siGFP	160.8 ± 1.4 nm	106.7 ± 3.7 nm
Lipidoid+siGFP+GSH	Broad distribution	114.6 ± 16.4 nm

Figure 5. The GFP expression of MDA-MB-231-GFP cells treated with **1**-O16B/siGFP complexes with different N/P ratios. The siRNA complexes were prepared by mixing siGFP (15 pmol) and varying amounts of **1**-O16B. Data are presented as mean ± SD ($n = 3$).

Figure 6. siGFP dose-dependent gene silencing of MDA-MB-231-GFP cells after transfection with **1**-O16B/siGFP complexes. **1**-O16B and siRNA were mixed at N/P ratios of 5:1. For control experiments, 8×10^{-9} M of siGFP or scrambled siRNA was used. Data are presented as mean ± SD ($n = 3$). The asterisks refer to statistical significance between **1**-O16B-facilitated siGFP and scrambled siRNA delivery ($P < 0.05$).

the subcellular compartments, which leads to less efficient gene silencing by the nonbioreducible lipidoid.

Next, the conditions for siRNA delivery were optimized using the bioreducible lipidoid **1**-O16B. GFP-MDA-MB-231 cells were treated with **1**-O16B/siGFP lipoplexes with N/P ratios in the range of 1.25 to 16. As shown in **Figure 5**, an increase in the N/P ratios of **1**-O16B/siRNA complexes from 1.25 to 5 enhances the efficiency of GFP gene silencing, from 60% to 25%, while a further increase of the N/P ratio above 5 does not improve siRNA delivery efficacy. Therefore, the N/P ratio of **1**-O16B and siRNA complexes was fixed at 5 for the remainder of the study. Similarly, the GFP expression of GFP-MDA-MB-231 cells following **1**-O16B/siGFP treatment was found to be siRNA-dose dependent. As the cells were exposed to increased concentrations of siGFP from 0.25×10^{-9} to 8×10^{-9} M, cellular GFP expression decreased from 78% down to 28% (**Figure 6**). However, the treatment of cells with **1**-O16B/scrambled siRNA complexes only had a minor effect on suppressing GFP expression, suggesting that siRNA sequence-specific gene knock down is involved in the RNAi.

The biocompatibility and cytotoxicity of delivery vehicles has also posed a challenge for the safe delivery of siRNA, along with the success of RNAi therapeutics. In order to evaluate the cytotoxicity of the bioreducible lipidoids as a siRNA delivery platform, MDA-MB-231 cells were incubated with varying concentrations of **1**-O16B/siGFP nanocomplexes. Cell viability measurements via AlamarBlue assay indicated that viability remained at 90% or above following treatment with **1**-O16B/siGFP nanocomplexes (Figure S3, Supporting Information). This result was observed for siGFP as concentrations increased from 1 to 32×10^{-9} M (lipidoid concentration increased from 0.16 to 5.3 µg mL^{-1}), suggesting that bioreducible lipidoids are highly biocompatible for siRNA delivery.

Having identified the bioreducible lipidoid **1**-O16B as a safe and highly efficient siRNA delivery nanocarrier, the ability of **1**-O16B to deliver therapeutic siRNA into cancer cells, and its
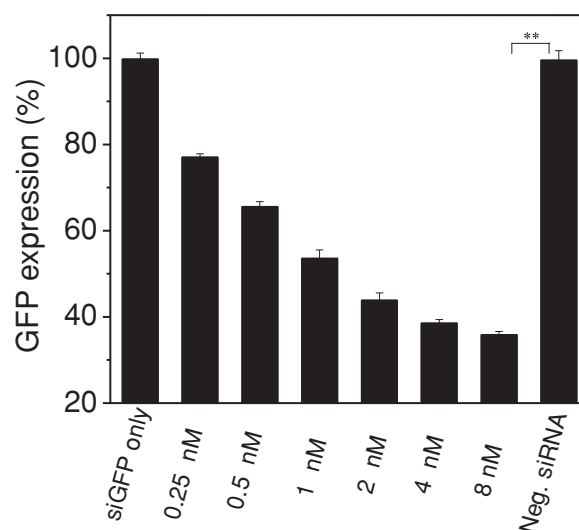
ability to interfere with cell-cycle progression as a potential cancer therapy strategy was investigated. To this end, polo-like kinase 1 (Plk1), a protein kinase that plays a crucial role in cell proliferation and cancer progression, was selected as a target. Plk1 is overexpressed in a broad spectrum of cancer cells, and previous investigations have suggested Plk1 as a highly potent target for cancer therapy.[15] Additionally, RNAi[16] and chemical inhibitors[17] interfering with Plk1 function have been shown to induce cell apoptosis in vitro, and suppress tumor growth in vivo. In this study, MDA-MB-231 cells were treated with a **1**-O16B/siPlk-1 complex formulated at the optimized siRNA delivery conditions (N/P ratio of 5). The viability of the cells was determined 48 h post-transfection and compared with that of the cells treated with **1**-O16B only, **1**-O16B/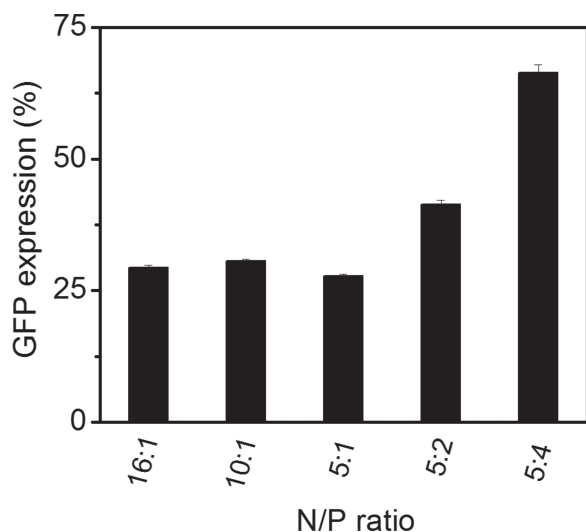scrambled siRNA complex, or Lipofectamine 2000/siPlk-1. As shown in **Figure 7**, treatment of MDA-MB-231 cells with **1**-O16B/siPlk-1 complexes (siRNA concentration: 50×10^{-9} M) reduced cell viability down to 25%, outperforming Lipofectamine 2000 facilitated siPlk-1 delivery under the same conditions (50% cell viability). Control experiments conducted by exposing cells to **1**-O16B or **1**-O16B/scrambled siRNA complex had a negligible effect on cell viability. Moreover, the proliferation of cells treated with the **1**-O16B/siPlk-1 complexes was dependent on the dose of siRNA that the cells were exposed to. Cells treated with 32×10^{-9} M had a reduced viability of 45%, while 16×10^{-9} M siPlk-1-treated cells had a viability of 75% (Figure 7A). To examine whether Plk-1 depletion accompanied **1**-O16B/siPlk-1 treatment and subsequent cell proliferation inhibition, Plk-1 protein expression of MDA-MB-231 cells was detected by Western blot analysis. As shown in Figure 7B, **1**-O16B/siPlk-1 treatment significantly reduced Plk-1 expression in MDA-MB-231 cells, while no similar reduction in Plk-1 expression was observed for cells treated with **1**-O16B or **1**-O16B/scrambled siRNA complexes.

ADVANCED
HEALTHCARE
MATERIALS
www.advhealthmat.de

Materials
Views
www.MaterialsViews.com

Figure 7. A) The viability assay of MDA-MB-231 cells after transfection with varying concentrations of siPlk-1/**1-O16B** complexes. For controls, the cells were dosed with scrambled siRNA/**1-O16B**, siPlk-1/LPF2000, or **1-O16B**. The cell viability was measured by AlamarBlue assay. Data are presented as mean $\pm$ SD ($n = 3$), the asterisks refer to statistical significance between **1-O16B** facilitated siPlk-1 and scrambled siRNA delivery ($P < 0.05$); B) Plk-1 protein expression in MDA-MB-231 cells after transfection with siPlk-1 or scrambled siRNA complexes of **1-O16B**. 50×10^{-9} M of siRNA was mixed with 1-O16B at N/P ratios of 5:1 prior to the cells being exposed.

An efficient siRNA delivery tool should be able to transfect different cell lines, as variations in cell surface and extracellular environments may affect the siRNA nanoparticle internalization and gene-silencing efficiency. To further demonstrate bioreducible lipidoids as an efficient siRNA delivery platform, siPlk-1 delivery facilitated by **1-O16B** was investigated on several different cell lines. Human cervical carcinoma cells (HeLa) and murine breast cancer cells (4T1) were selected as another two representative cancer cell lines. As shown in **Figure 8**, the treatment of HeLa and 4T1 cells with **1-O16B**/siPlk-1 complexes inhibited the proliferation of tumor cells, similar to MDA-MB-231 cells, while also being siRNA dose dependen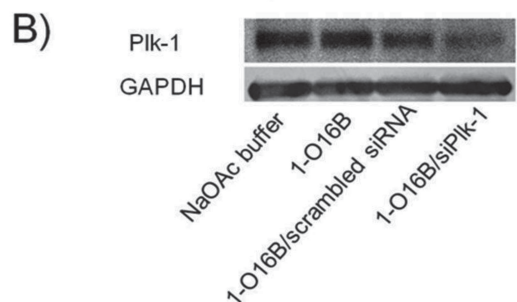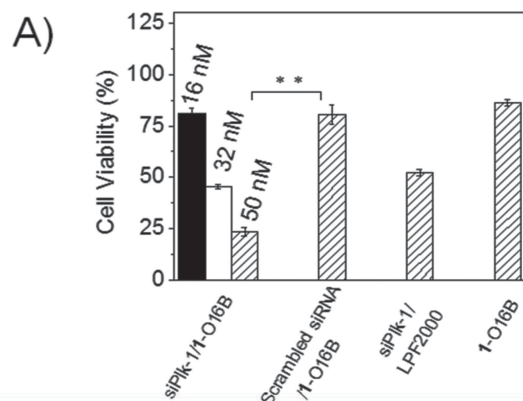t. No obvious cell proliferation inhibition was observed for **1-O16B** or **1-O16B**/scrambled siRNA complex-treated cells. Moreover, **1-O16B** is more efficient at delivering siPlk-1 and inhibiting cell proliferation than Lipofectamine 2000 on all cell lines investigated.

In summary, we report the development of combinatorially designed bioreducible lipid-like nanoparticles as a novel siRNA delivery platform. The integration of bioreducible disulfide bonds into lipidoids, facilitated lipidoid degradation and siRNA release in response to intracellular GSH, which enhanced the siRNA delivery efficiency. A representative bioreducible lipidoid selected in this study, **1-O16B** can deliver siRNA-targeting GFP to suppress GFP expression of MDA-MB-231 cells, and siRNA
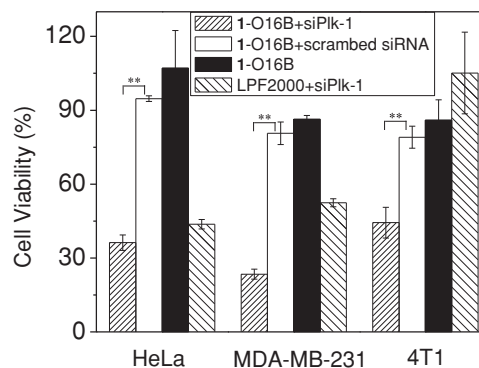
Figure 8. Bioreducible lipidoid **1-O16B** facilitated siPlk-1 delivery reduced the viability of different cancer cells. siRNA (50×10^{-9} M) was mixed with **1-O16B** at a N/P ratio of 5:1, or LPF2000 at a weight/weight ratio of 3:1. The cell viability was measured by AlamarBlue assay. Data are presented as mean $\pm$ SD ($n = 3$, $P < 0.05$).

targeting Plk-1 into cancer cells to interfere with cell progression and prohibit rapid tumor cell proliferation. These findings provide an efficient approach towards developing biodegradable nanocarriers for siRNA delivery for clinical translation as well as a novel approach in studying the structure–functionality relationships of lipid-based siRNA delivery system.

Supporting Information

Supporting Information is available from the Wiley Online Library or from the author.

Acknowledgements

[1] a) K. A. Whitehead, R. Langer, D. G. Anderson, *Nat. Rev. Drug Discovery* **2009**, *8*, 129; b) J. Kurreck , *Angew. Chem. Int. Ed.* **2009**, *48*, 1378.

[2] L. C. Gomes-da-Silva, N. A. Fonseca, V. Moura, M. C. P. de Lima, S. Simoes, J. N. Moreira, *Acc. Chem. Res.* **2012**, *45*, 1163.

[3] E. Wagner, *Acc. Chem. Res.* **2012**, *45*, 1005.

[4] L. Han, J. Zhao, X. Zhang, W. Cao, X. Hu, G. Zou, X. Duan, X. J. Liang, *ACS Nano* **2012**, *6*, 7340.

[5] J. J. Jung, A. Solanki, K. A. Memoli, K. Kamei, H. Kim, M. A. Drahl, L. J. Williams, H. R. Tseng, K. Lee, *Angew. Chem. Int. Ed.* **2010**, *49*, 103.

[6] A. Mescalchin, A. Detzer, M. Wecke, M. Overhoff, W. Wunsche, G. Sczakiel, *Expert Opin. Biol. Ther.* **2007**, *7*, 1531.

[7] T. Suma, K. Miyata, Y. Anraku, S. Watanabe, R. J. Christie, H. Takemoto, M. Shioyama, N. Gouda, T. Ishii, N. Nishiyama, K. Kataoka, *ACS Nano* **2012**, *6*, 6693.

[8] L. N. Cui, J. L. Cohen, C. K. Chu, P. R. Wich, P. H. Kierstead, J. M. J. Frechet, *J. Am. Chem. Soc.* **2012**, *134*, 15840.

[9] a) M. S. Shim, S. H. Bhang, K. Yoon, K. Choi, Y. Xia, *Angew. Chem. Int. Ed.* **2012**, *51*, 11899; b) S. S. Dunn, S. Tian, S. Blake,

Materials
Views
www.MaterialsViews.com

ADVANCED
HEALTHCARE
MATERIALS
www.advhealthmat.de

COMMUNICATION

J. Wang, A. L. Galloway, A. Murphy, P. D. Pohlhaus, J. P. Rolland, M. E. Napier, J. M. DeSimone, *J. Am. Chem. Soc.* **2012**, *134*, 7423; c) H. Liu, H. Wang, W. Yang, Y. Cheng, *J. Am. Chem. Soc.* **2012**, *134*, 17680.

[10] C. Hwang, A. J. Sinskey, H. F. Lodish, *Science* **1992**, *257*, 1496.

[11] A. Akinc, A. Zumbuehl, M. Goldberg, E. S. Leshchiner, V. Busini, N. Hossain, S. A. Bacallado, D. N. Nguyen, J. Fuller, R. Alvarez, A. Borodovsky, T. Borland, R. Constien, A. de Fougerolles, J. R. Dorkin, K. N. Jayaprakash, M. Jayaraman, M. John, V. Koteliansky, M. Manoharan, L. Nechev, J. Qin, T. Racie, D. Raitcheva, K. G. Rajeev, D. W. Y. Sah, J. Soutschek, I. Toudjarska, H. P. Vornlocher, T. S. Zimmermann, R. Langer, D. G. Anderson, *Nat. Biotechnol.* **2008**, *26*, 561.

[12] S. Sun, M. Wang, K. A. Alberti, A. Choy, Q. Xu, *Nanomed. Nanotechnol.* **2013**, *9*, 849.

[13] a) M. Wang, S. Sun, K. A. Alberti, Q. Xu, *ACS Synth. Biol.* **2012**, *1*, 403; b) S. Sun, M. Wang, S. A. Knupp, Y. Soto-Feliciano, X. Hu,

D. L. Kaplan, R. Langer, D. G. Anderson, Q. B. Xu, *Bioconjugate Chem.* **2012**, *23*, 135.

[14] a) C. Gehin, J. Montenegro, E.-K. Bang, A. Cajaraville, S. Takayama, H. Hirose, S. Futaki, S. Matile, H. Riezman, *J. Am. Chem. Soc.* **2013**, *135*, 9295; b) G. Candiani, D. Pezzoli, L. Ciani, R. Chiesa, S. Ristori, *PLoS One* **2010**, *5*, e13430; c) F. X. Tang, J. A. Hughes, *Biochem. Biophy. Res. Commun.* **1998**, *242*, 141; d) F. X. Tang, J. A. Hughes, *Bioconjugate Chem.* **1999**, *10*, 791.

[15] a) Y. Degenhardt, T. Lampkin, *Clin. Cancer Res.* **2010**, *16*, 384; b) K. Strebhardt, A. Ullrich, *Nat. Rev. Cancer* **2006**, *6*, 321.

[16] a) X. Z. Yang , J. Z. Du, S. Dou, C. Q. Mao, H. Y. Long, J. Wang, *ACS Nano* **2012**, *6*, 771; b) J. O. McNamara, E. R. Andrechek, Y. Wang, K. D. Viles, R. E. Rempel, E. Gilboa, B. A. Sullenger, P. H. Giangrande, *Nat. Biotechnol.* **2006**, *24*, 1005.

[17] S. M. Kim, S. Yoon, N. Choi, K. S. Hong, R. N. Murugan, G. Cho, E. K. Ryu, *Biomaterials* **2012**, *33*, 6915.

Research Article

DOPE facilitates quaternized lipidoids (QLDs) for in vitro DNA delivery

Shuo Sun, MSc[a,1], Ming Wang, PhD[b,1], Kyle A. Alberti, BSc[b], Alex Choy, BSc[b],
Qiaobing Xu, PhD[a,b,*]

[a]*Department of Chemical and Biological Engineering, Tufts University, Medford, MA*
[b]*Department of Biomedical Engineering, Tufts University, Medford, MA*

Received 12 July 2012; accepted 24 January 2013

Abstract

This paper describes the synthesis of a combinatorial library of quaternized lipidoids (QLDs) and an evaluation of their abilities to facilitate in vitro DNA delivery. The QLDs alone showed low efficiency for DNA delivery. By formulating liposomes with a neutral helper lipid, such as 1,2-dioleoyl-*sn*-glycero-3-phosphoethanolamine (DOPE), the capability of QLDs for gene transfection is significantly enhanced due to the fusogenic properties of DOPE which facilitate endosomal escape and cargo delivery. We further optimized the liposome composition and DNA dose for gene transfection and investigated the structure–activity relationships of the lipidoid library in DNA delivery.

From the Clinical Editor: This paper describes the synthesis and evaluation of a combinatorial library of quaternized lipidoids to facilitate in vitro DNA delivery, which occurs at a low level but can be enhanced with DOPE. The authors also further optimized the liposome composition and DNA dose for delivery and investigated the structure-activity relationships of the lipidoid library.
© 2013 Elsevier Inc. All rights reserved.

Key words: Quaternized lipidoids; Non-viral gene delivery; Helper lipid

Recently, a combinatorial library of lipid-like materials termed "lipidoids" was developed and screened for their abilities to facilitate DNA and siRNA delivery.[1–6] A variety of amines, acrylamides, acrylates, and epoxides have been used as reactants, allowing the chemical synthesis of structurally diverse lipidoids.[1,2] From the large data sets accumulated from screening the library of lipidoids, a correlation between structure and function of delivery systems is evolving.[3,7] Their easy and economic combinatorial synthesis, as well as their high delivery efficiencies makes these lipidoids attractive as a new class of non-viral delivery vectors.[1–3,8]

So far, it has been found that the lipidoids with high cargo delivery efficiency usually comprise secondary or tertiary amines.[1–3,6] The synthesis of lipidoids with quaternized amine was reported previously by Akinc et al[1] for siRNA delivery, but with low efficiency. No further studies of using this class of materials for nucleic acid delivery were reported afterwards. Considering the quaternized lipidoids (QLDs) having similar chemical structures to many cationic lipids, such as DOTMA,

DOTAP etc. which are commonly used for non-viral nucleic acid delivery,[9–14] we hypothesize that the QLDs would be also capable of mediating the nucleic acid delivery, if not as stand-alone reagent, with the addition of "helpers". In order to evaluate this hypothesis, we herein synthesized a combinatorial library of QLDs through reaction of a variety of amines with 1, 2-epoxyhexadecane, followed by the quaternization of ternary amines (Figure 1). These QLDs are formulated with or without a neutral helper lipid, DOPE, and used for DNA delivery. The DOPE has well-known fusogenic properties, and could facilitate endosomal escape and gene delivery.[11,12] We found that the QLDs alone are not effective for DNA delivery. However, some of the QLDs formulated with DOPE showed high DNA transfection efficiency, even higher than the commercial transfection agent, Lipofectamine 2000.

Methods

Synthesis of QLDs

The synthesis of lipidoids was performed and characterized as previously described.[1,3] Briefly, amine and 1, 2-epoxyhexadecane in a molar ratio of 1:2.4 were added to a 5-mL Teflon-lined glass screw-top vial followed by a further 3 days of stirring at 90 °C. After cooling, the reaction mixtures were purified unless otherwise specified. The purified lipidoids were dissolved in THF and quaternized by reaction with excessive amount of methyl iodide
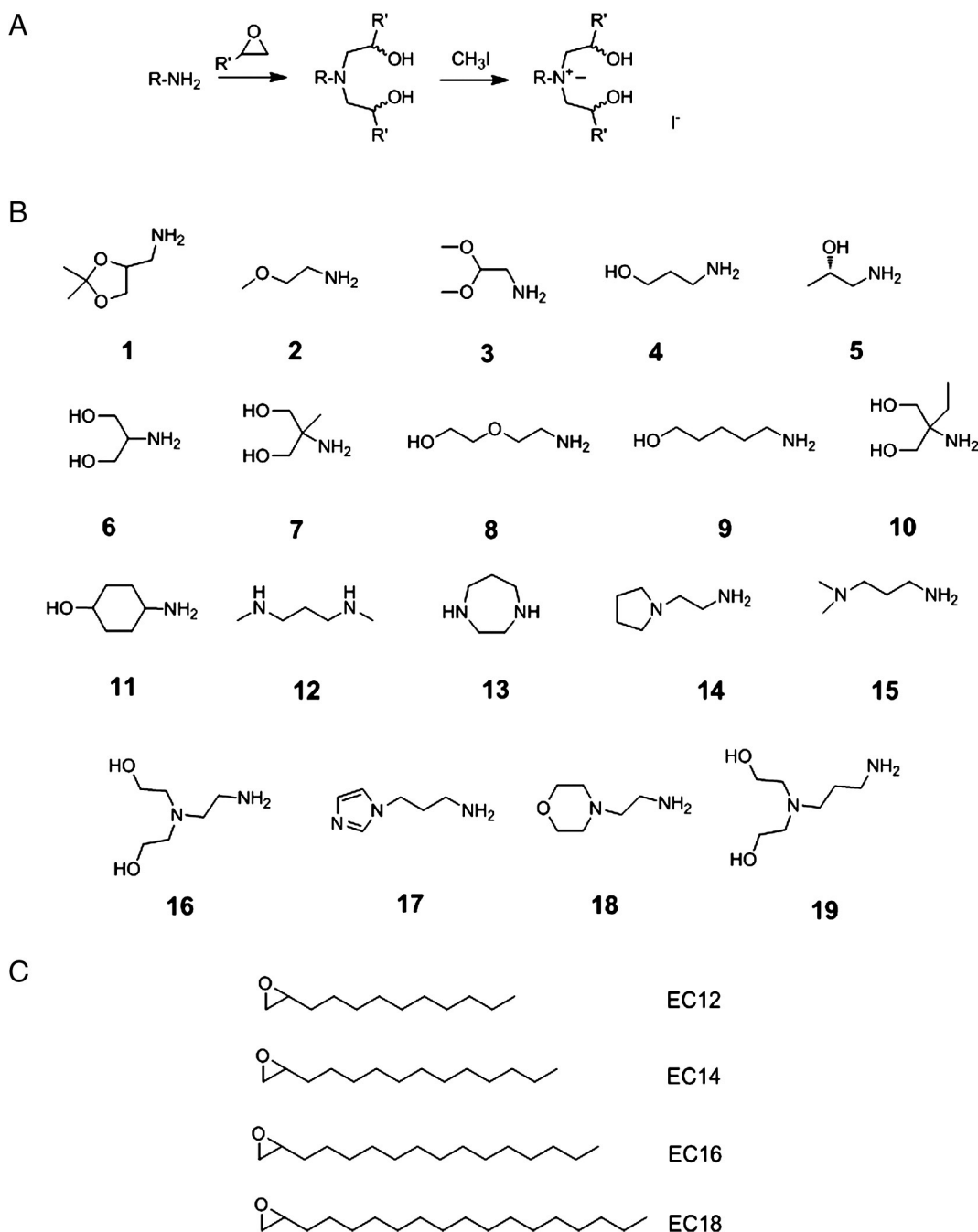
Figure 1. **(A)** Combinatorial synthesis of quaternized lipidoids (QLDs) for DNA delivery; **(B)** Amine molecules used for the library synthesis; **(C)** Alkyl-epoxide used for the library synthesis. QLDs are named as follows: (Quaternized Lipidoids (QLD)) (carbon numbers of tail)-(amine number).

overnight at room temperature, in the dark. The precipitations obtained were filtered, washed with diethyl ether and dried in vacuum for further use. Representative QLDs were characterized by thin layer chromatography, IR, ^{1}H NMR, and mass spectroscopy.

Liposome formulation

QLDs and DOPE liposomes were formulated using a procedure described by Huang et al with slight modification.[15] Briefly, the desired amounts of QLDs and DOPE were dissolved with chloroform in a glass vial; the organic solvent was then evaporated under reduced pressure to form a thin film on the bottom of the vial. A sodium acetate buffer solution (25 mM, pH = 5.5) was added to the vial and the suspension was sonicated for 15 min until a clear, uniform suspension was obtained. The suspension was kept in the fridge overnight to allow for complete hydration prior to use.

Cell culture

All cell culture reagents were purchased from Invitrogen (Carlsbad, CA) unless otherwise noted. HeLa cells were obtained
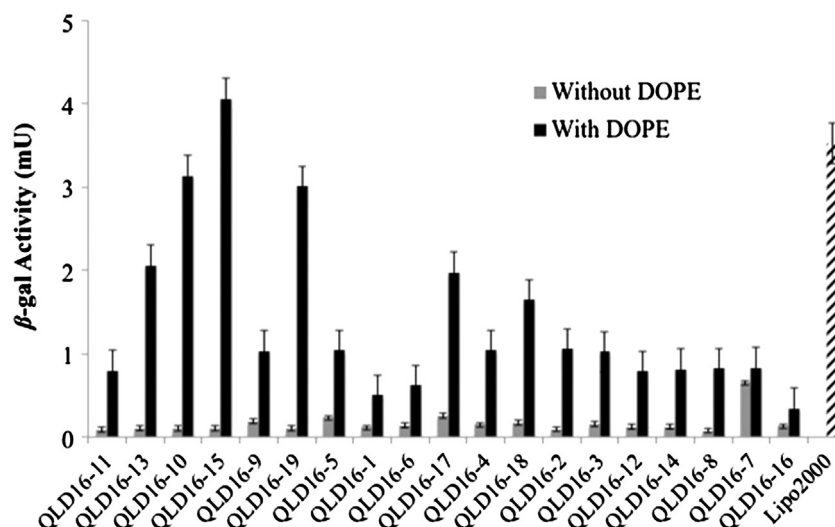
Figure 2. Initial in vitro screening of quaternized lipidoids formulated with (QLD/DOPE molar ratio of 1:1) and without DOPE for DNA delivery. QLDs were screened by delivering β-gal encoding plasmid DNA into HeLa cells. Relative β-gal expression level was determined by assaying the enzyme activity according to reported methods, for details see experimental section.

from ATCC (Manassas, VA) and cultured in high glucose DMEM supplemented with 10% fetal bovine serum and 100 U/mL of penicillin/streptomycin at 37 °C in the presence of 5% CO_2. Cells were seeded into 96-well plates at a density of 10,000 cells per well one day prior to transfection experiments.

In vitro DNA transfection

To facilitate the high-throughput screening of QLDs for DNA delivery, the QLDs alone or formulated with DOPE liposomes were mixed with DNA in sodium acetate buffer solutions (25 mM, pH = 5.5) at a fixed P/N ratio of 2:1(QLD:DNA), followed by 15 min of incubation at room temperature to allow for complete lipoplex formation. For transfection experiments: in 96-well plates, cells were transfected with lipoplexes containing 200 ng of DNA (per well) at fixed liposome/DNA ratio. After a further 48 h of incubation at 37 °C, cells were lysed and assayed for β-gal activity. Control experiments were performed by using Lipofectamine 2000 as per the manufacturer's instructions. All transfection experiments were performed in quadruplicate.

β-gal activity assay

The β-gal activity was assayed following previously reported methods with slight modification.[3] Briefly, 48 h following cell transfection experiments, all growth medium was removed by vacuum aspiration, cells were washed with PBS two times, and cells were lysed with 0.5% triton (50 μL/well in PBS). Then 50 μL of *o*-nitrophenyl-β-D-galactoside (ONPG) solution (4 mg/mL in z-buffer) was added, followed by a 15 min incubation at 37 °C to allow the enzymatic hydrolysis of ONPG. At the end of the incubation, the concentration of β-gal was determined by measuring the absorbance at 409 nm.

DNA encapsulation assay

The DNA encapsulation efficiency of liposomes was determined by PicoGreen assay as previously described.[3,16]

Briefly, 50 μL/well of liposome solution (1 mg/mL in NaOAc buffer solution, 25 mM, pH = 5.5) and 50 μL/well of DNA (60 μg/mL in NaOAc buffer solution, 25 mM, pH = 5.5) were mixed in a 96-well plate, followed by a 15 min incubation at 37 °C to allow for lipoplex formation. Then, 100 μL/well of PicoGreen working solution (diluted 190 times from the Picogreen assay kit with NaOAc buffer solution, 25 mM, pH = 5.5) was added. After incubating for 5 min, 30 μL of lipoplex/PicoGreen solution was diluted by 200 μL DMEM in a black 96-well polystyrene plate. The fluorescence intensity of the solution was monitored at 535 nm with excitation at 485 nm on a SpectraMax® M2 Multi-Mode Microplate Reader (Molecular Devices, Inc. California, USA). The relative fluorescence (*RF*) was calculated by the following formula: $RF = (F_1-F_0)/(F_2-F_0)$, where: F_1 and F_2 are the fluorescence intensities of the DNA-PicoGreen complexes with and without liposomes, F_0 is the fluorescence intensity of PicoGreen solution. The DNA encapsulation ratio was calculated as $(1-RF) \times 100\%$.

Transmission electron microscopy (TEM)

QLDs and QLDs/DOPE complexed with DNA were prepared using the same procedure as the in vitro experiments. Droplets of the sample (5 μL) were applied to carbon-covered copper grids (300 meshes) for 30 min. The sample was subsequently rinsed with contrasting material (1% uranyl acetate at pH 4.5). The remaining stain solution was removed with a filter paper and air-dried. TEM microstructure was determined using a Tecnai FEG TEM (FEI Tecnai 12 Spirit Bio-twin, FEI Company, Hillsboro, OR) operating at 80 kV.

In vitro cytotoxicity assay

The in vitro cytotoxicity of the QLDs/DNA was evaluated by MTT assay. Briefly, 3-(4, 5-Dimethylthiazol-2-yl)-2, 5-diphe-nyltetrazolium bromide (MTT) was dissolved in phenol red free DMEM at a concentration of 0.5 mg/mL. Cells transfected with
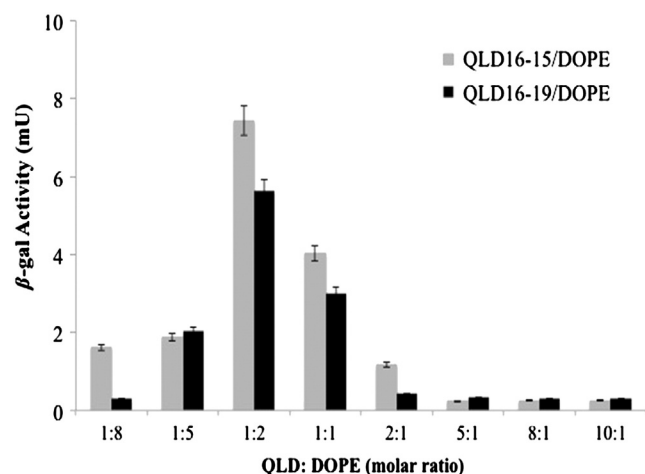
Figure 3. The effect of QLD/DOPE molar ratios on DNA delivery efficiency (Liposome/DNA ratio was fixed at the P/N ratio of 2:1). The efficiency was monitored as β-gal expression level.

Figure 4. The effect of QLD/DOPE liposome to DNA ratios on gene transfection efficiency (QLDs and DOPE were formulated at a fixed molar ratio of 1:2).The transfection efficiency was monitored as β-gal expression level.

various lipoplexes were washed with warm DMEM, and MTT solution was added (125 μL per well in a 96 well plate), followed by 3 h of incubation at 37 °C. At the end of the incubation, the DMEM solution was removed and 125 μL DMSO was added per well. The solutions were pipetted up and down several times to ensure the converted dye was completely dissolved. Absorbance of solutions was measured at 570 nm with background subtraction at 650 nm.

Results

Screening of quaternized lipidoids (QLDs) formulated with and without DOPE for DNA delivery

In order to facilitate the initial screening, we used a 3/1 charge ratio (+/−), which according to previous studies[12,17] was a condition in which a majority of DNA molecules were complexed. The β-gal encoding DNA and HeLa cells was used as a model system to test the QLD mediated gene delivery efficiency. We found that none of the QLDs were effective in mediating efficient DNA delivery as a stand-alone reagent (Figure 2). We then evaluated the influence of the transfection efficiency by adding helper lipid DOPE. In the initial screening, we produced QLD/DOPE liposomes with a fixed QLD to DOPE molar ratio (1:1) and a fixed charge (P/N) ratio (3:1) for the lipoplex of QLD/DOPE liposome and DNA. The β-gal activity assay indicated that QLDs formulated with DOPE all showed some level of effectiveness in DNA delivery (Figure 2). Several QLDs (such as QLD16-10, QLD16-17, and QLD16-19, the quaternized lipidoids were named in the sequence of QLD-tail length of the epoxide-amine number in the library) formulated with DOPE showed DNA transduction level in HeLa cells with efficiency comparable to the commercial reagent, Lipofectamine 2000.

DOPE promotes the transfection efficiency of QLDs

The preliminary screening results showed that the formulations containing DOPE can enhance the transfection abilities of QLDs. We then investigated the effect of the ratio of QLD to DOPE on the transfection efficiency. Quaternized lipidoids QLD16-15, and QLD16-19 both derived from diamines were selected for detailed study due to their high transfection performance in the library screening (see Figure 2). Liposomes formulated from QLDs and DOPE with molar ratios varying from 1:8 to 10:1 (QLD:DOPE) were prepared and tested for their capability to facilitate DNA delivery. As shown in Figure 3, the QLD liposome formulations showed increased transfection efficiency with the increased percentage of the DOPE in the liposomes with highest transfection efficiency achieved at a QLD: DOPE molar ratio of 1:2. Any further increase of the DOPE percentage in the QLD/DOPE liposomes lowered their transfection efficiency significantly. The enhanced transfection abilities of the QLDs formulated with DOPE compared to the QLDs alone may result from the hexagonal-phase-forming propensity of liposomes when interacting with cell membrane.[18–20]
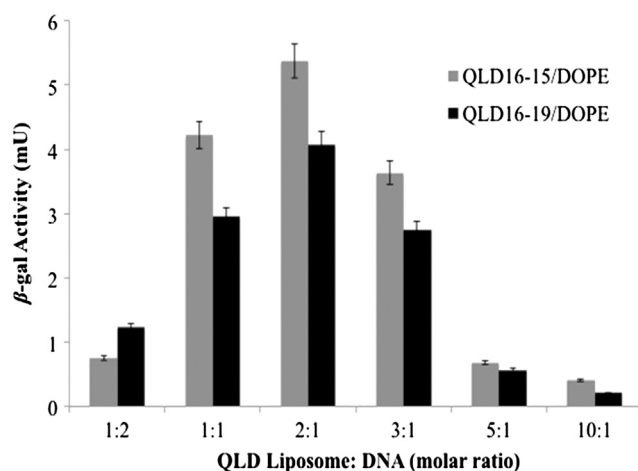
By fixing the molar ratio of quaternized lipidoid and DOPE at 1:2, we varied the QLD/DOPE to DNA molar ratio and further investigated the effect of charge ratios (P/N) on the transfection abilities of the liposomes. As indicated in Figure 4, we increased the QLD/DOPE to DNA ratio from 1:2 to 10:1. Both QD16-19/DOPE and QD16-15/DOPE liposome had increasing transfection efficiency with a peak of β-gal activity at the QLDs/DOPE to DNA of 2:1. The higher transfection efficiency at increased QLDs/DOPE to DNA ratios may be ascribed to the higher DNA encapsulation and cellular uptake, which was confirmed by Picogreen assay.

Effect of QLDs tail length on DNA transfection efficiency

To further investigate the structure–activity relationship of QLDs in facilitating DNA delivery, the QLDs with head amines of 15 and 19 provide high transfection efficiencies from initial screening results (Figure 2). Here we synthesized structurally similar QLDs by reacting these amines with epoxides of different tail lengths. The purified QLDs were quaternized, formulated with DOPE at the optimized ratio (1:2 molar ratio), and tested for

Figure 5. The effect of QLD tail length on the DNA transfection efficiency. QLDs were formulated with DOPE at molar ratios of 1:2. Lipoplexes were prepared by using a fixed QLD:DNA molar ratio of 2:1. The efficiency was expressed as β-gal activity.
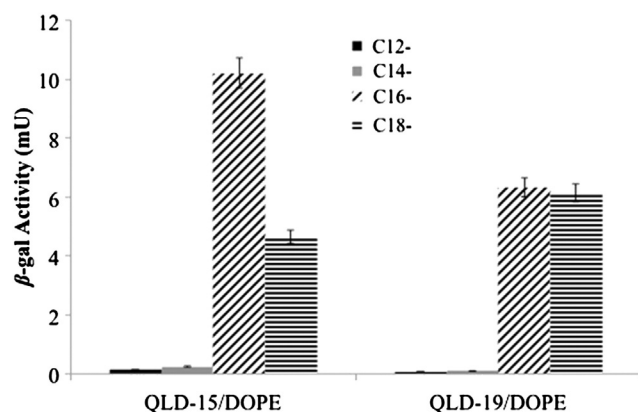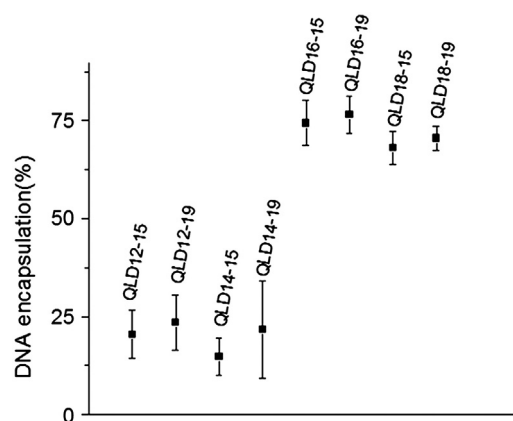

Figure 6. The effect of QLDs tail length on the DNA encapsulation efficiency. QLDs were formulated with DOPE at molar ratios of 1:2. Lipoplexes were prepared by a fixed QLD to DNA molar ratio of 2:1(molar/molar). The DNA encapsulation efficiency was determined by Picogreen assay.

DNA delivery in HeLa cells. As shown in Figure 5, all QLDs comprising two hydrophobic tails of 12- or 14-carbon showed relatively low transfection efficiencies; while QLDs with longer hydrophobic chains (C16 and C18) showed high transfection efficiency. This is probably because the long hydrophobic tail provides some degree of rigidity enabling the formation of stable liposomes and lipoplexes.[21,22] The DNA encapsulation efficiency of liposomes comprising QLDs of different tail lengths was determined by PicoGreen assay as a way to better illustrate the effect of the tail length of QLD on the transfection efficiency. As shown in Figure 6, the liposomes derived from QLD with C12 and C14 tails encapsulated DNA with low efficiency, while QLDs with C16 and C18 tails increased the DNA encapsulation efficiency greatly. The increased DNA encapsulation efficiency of QLDs with long tail lengths correlated well with the high transfection efficiency (Figure 5).

Discussions

The easy and economic combinatorial synthesis, as well as their high delivery efficiencies makes the lipidoids attractive as a new class of non-viral delivery vectors.[1–7] However, using the quaternized lipidoids (QLDs) alone for nucleic acids delivery is not successfully demonstrated. Here, we synthesized a combinatorial library of quaternized lipidoid (QLDs) and evaluated their potential application as efficient non-viral gene delivery vectors. We found that QLDs are not effective for gene delivery as stand-alone reagents, while the QLDs formulated with DOPE showed significant enhancement in DNA delivery in vitro. The transfection ability of a given lipid or liposome is dependent on the lipoplex structures and physicochemical properties.[23] We used negative-staining transmission electron microscopy (TEM) to characterize the size and morphology of the DNA and QLD complexes formulated with and without DOPE (Supporting Information Figure S1). The QD16-15/DOPE liposomes were able to self-assemble with DNA, forming condensed multi-lamellar structure with sizes around 100 nm, in which DNA was

intercalated between the lipid bilayers. However, QD16-15 itself can only form large aggregation clusters (2 ~ 3 micrometers) with DNA binding, though multilamellar structured nanocomplexes were also observed. The different lipoplex structures induced cellular uptake and gene transfection with different efficiencies, and it has been recognized that the nanoscale particles usually have a higher cellular uptake than the particles in micrometer size range.

An increase of the QLD/DOPE to DNA ratio can enhance the DNA encapsulation efficiency to a maximum at a 5:1 (Supporting Information Figure S2), at which liposomes QLD16-15 and QLD16-19 can encapsulate DNA at nearly 100%. The higher DNA encapsulation enables the increased cellular uptake and gene transfection. However, maximal β-gal activity was observed at the QLD/DOPE to DNA molar ratio of 2:1 (~80% DNA encapsulation rate) rather than at a higher ratio, even with the latter having a higher DNA encapsulation rate (nearly 100%). This is because when the QLD/DOPE to DNA ratio increases, the QLD/DOPE amount also increases which leads to increased cytotoxicity at high dose (Supporting Information Figure S3). The influence of hydrophobic tail length on the gene transfection ability of QLD was also studied. The QLDs with high transfection efficiency usually have long hydrophobic chains (C16 and C18) rather than short ones (C12 and C14), which is because the long hydrophobic tail of QLDs enables the formation of stable liposomes. The importance of anchor chain length of lipids in gene delivery efficiency has been studied by Felgner et al previously.[24] They observed that the alkyl chain length can affect the transfection efficiency in the following sequence: C14, C16 > C18, C12, C10, while we observed in this paper the sequence of C16, C18 > C14, C12 for QLDs. This is because most of the conventional cationic lipids have a single quaternized amine head, while the QLDs (such as those derived from amine 15 and 19) mostly comprise two quaternized amine heads. The long hydrophobic tail (e. g. C16 and C18) of QLDs having two quaternized amine heads may provide an optimal solubility (or some degree of rigidity) and enable the formation of stable DNA/lipid complexes. Even though we only demonstrated the QLD/DOPE formulation for efficient DNA

delivery in this paper, we believe these materials and formulations are also useful for delivery of other nucleic acid-based cargos, including mRNA and siRNA. The design rationales demonstrated in this paper could provide new principles for developing new materials for gene delivery and therapy with high efficiency.

Appendix A. Supplementary data

Supplementary data to this article can be found online at http://dx.doi.org/10.1016/j.nano.2013.01.006.

References

1. Akinc A, Zumbuehl A, Goldberg M, Leshchiner ES, Busini V, Hossain N, et al. A combinatorial library of lipid-like materials for delivery of RNAi therapeutics. *Nat Biotechnol* 2008;**26**:561-9.
2. Love KT, Mahon KP, Levins CG, Whitehead KA, Querbes W, Dorkin JR, et al. Lipid-like materials for low-dose, in vivo gene silencing. *Proc Natl Acad Sci USA* 2010;**107**:1864-9.
3. Sun S, Wang M, Knupp SA, Soto-Feliciano Y, Hu X, Kaplan DL, et al. Combinatorial library of lipidoids for in vitro DNA delivery. *Bioconjug Chem* 2011;**23**:135-40.
4. Whitehead KA, Langer R, Anderson DG. Knocking down barriers: advances in siRNA delivery. *Nat Rev Drug Discov* 2009;**8**:129-38.
5. Frank-Kamenetsky M, Grefhorst A, Anderson NN, Racie TS, Bramlage B, Akinc A, et al. Therapeutic RNAi targeting PCSK9 acutely lowers plasma cholesterol in rodents and LDL cholesterol in nonhuman primates. *Proc Natl Acad Sci USA* 2008;**105**:11915-20.
6. Akinc A, Goldberg M, Qin J, Dorkin JR, Gamba-Vitalo C, Maier M, et al. Development of lipidoid-siRNA formulations for systemic delivery to the liver. *Mol Ther* 2009;**17**:872-9.
7. Wang M, Sun S, Alberti KA, Xu Q. A combinatorial library of unsaturated lipidoids for efficient intracellular gene delivery. *ACS Synth Biol* 2012;**1**:403-7.
8. Nguyen DN, Mahon KP, Chikh G, Kim P, Chung H, Vicari AP, et al. Lipid-derived nanoparticles for immunostimulatory RNA adjuvant delivery. *Proc Natl Acad Sci USA* 2012;**109**:E797-803.
9. Zhang XX, McIntosh TJ, Grinstaff MW. Functional lipids and lipoplexes for improved gene delivery. *Biochimie* 2012;**94**:42-58.
10. Torchilin VP. Recent advances with liposomes as pharmaceutical carriers. *Nat Rev Drug Discov* 2005;**4**:145-60.
11. Kim TW, Chung H, Kwon IC, Sung HC, Jeong SY. Optimization of lipid composition in cationic emulsion as in vitro and in vivo transfection agents. *Pharm Res* 2001;**18**:54-60.
12. Xu YH, Szoka FC. Mechanism of DNA release from cationic liposome/DNA complexes used in cell transfection. *Biochemistry* 1996;**35**:5616-23.
13. Gao X, Huang L. A novel cationic liposome reagent for efficient transfection of mammalian cells. *Biochem Biophys Res Commun* 1991;**179**:280-5.
14. Bailey AL, Cullis PR. Modulation of membrane-fusion by asymmetric transbilayer distributions of amino lipids. *Biochemistry* 1994;**33**:12573-80.
15. Tan Y, Whitmore M, Li S, Frederik P, Huang L. LPD nanoparticles—novel nonviral vector for efficient gene delivery. *Methods Mol Med* 2002;**69**:73-81.
16. Green JJ, Zugates GT, Tedford NC, Huang YH, Griffith LG, Lauffenburger DA, et al. Combinatorial modification of degradable polymers enables transfection of human cells comparable to adenovirus. *Adv Mater* 2007;**19**:2836-42.
17. Gershon H, Ghirlando R, Guttman SB, Minsky A. Mode of formation and structural features of DNA cationic liposome complexes used for transfection. *Biochemistry* 1993;**32**:7143-51.
18. Smisterova J, Wagenaar A, Stuart MC, Polushkin E, ten Brinke G, Hulst R, et al. Molecular shape of the cationic lipid controls the structure of cationic lipid/dioleylphosphatidylethanolamine-DNA complexes and the efficiency of gene delivery. *J Biol Chem* 2001;**276**:47615-47622.
19. Hulst R, Muizebelt I, Oosting P, van der Pol C, Wagenaar A, Šmisterová J, et al. Sunfish amphiphiles: conceptually new carriers for DNA delivery. *Eur J Org Chem* 2004;**2004**:835-49.
20. Koltover I, Salditt T, Rädler JO, Safinya CR. An inverted hexagonal phase of cationic liposome–DNA complexes related to DNA release and delivery. *Science* 1998;**281**:78-81.
21. Srilakshmi GV, Sen J, Chaudhuri A, Ramadas Y, Rao NM. Anchor-dependent lipofection with non-glycerol based cytofectins containing single 2-hydroxyethyl head groups. *Biochim Biophys Acta* 2002;**1559**:87-95.
22. Balasubramaniam RP, Bennett MJ, Aberle AM, Malone JG, Nantz MH, Malone RW. Structural and functional analysis of cationic transfection lipids: the hydrophobic domain. *Gene Ther* 1996;**3**:163-72.
23. Chesnoy S, Huang L. Structure and function of lipid–DNA complexes for gene delivery. *Annu Rev Biophys Biomol Struct* 2000;**29**:27-47.
24. Felgner JH, Kumar R, Sridhar CN, Wheeler CJ, Tsai YJ, Border R, et al. Enhanced gene delivery and mechanism studies with a novel series of cationic lipid formulations. *J Biol Chem* 1994;**269**:2550-61.

A Combinatorial Library of Unsaturated Lipidoids for Efficient Intracellular Gene Delivery

Ming Wang,[†] Shuo Sun,[‡] Kyle A. Alberti,[†] and Qiaobing Xu*,[†,‡]

[†]Department of Biomedical Engineering and [‡]Department of Chemical and Biological Engineering, Tufts University, 4 Colby Street, Medford, Massachusetts 02155, United States

S *Supporting Information*

ABSTRACT: A combinatorial library of unsaturated lipidoids was synthesized through the Michael addition of amines to oleyl acrylamide. Their capability in facilitating in vitro gene delivery was evaluated by transfecting HeLa cells with EGFP-encoding plasmid DNA and mRNA. The preliminary screening results indicated that lipidoids with unsaturated oleyl tails are superior transfection agents compared to saturated lipidoids with *n*-octadecyl tails under the same conditions. The different transfection abilities of the unsaturated and saturated lipidioids were ascribed to the large, tightly packed lipoplexes of saturated lipidoids. The potential applications of the library of lipidoids were further expanded by looking at their ability to transfect fibroblasts as well as different cancerous cell lines.

KEYWORDS: *lipidoid, gene delivery, combinatorial library*
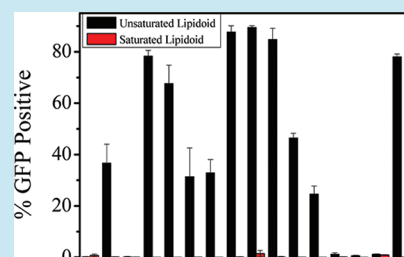
The lack of a safe and efficient gene delivery vehicle remains a bottleneck in the genetic treatment of inherited and acquired diseases.[1−8] A combinatorial strategy of constructing libraries of lipid-like materials termed "lipidoids" has been developed for efficient in vitro and in vivo gene delivery.[9−15] These lipidoids can be synthesized via solvent- and catalyst-free conjugation reactions of amines and α,β-unsaturated carbonyl compounds (e.g., acylates, acrylamides) or epoxides. These simple and mild reactions have enabled us to refine the structure of the lipidoids and improve their transfection capability. This was accomplished by reacting structurally diverse amines, α,β-unsaturated carbonyl compounds, or epoxides. It has been demonstrated that the tail length and head amine group of the lipidoid play significant roles in identifying the efficient carriers for gene delivery. For example, lipidoids incorporating tails in the range of 8−12 carbons as well as a secondary amine were reported to have high efficiency for siRNA delivery,[9] whereas lipidoids containing two tails of 14 carbons each were superior at delivering DNA.[14]

To further explore the structure−activity relationship of lipidoids in gene delivery, we have designed a new library of lipidoids with unsaturated hydrophobic tails. We compared this new group to saturated lipidoids containing the same amine group and tail length and evaluated their ability to facilitate in vitro gene delivery. Lipids with lower saturation levels usually have higher gene transfection efficiencies due to increased membrane fluidity;[16−19] however, the effect tail saturation levels of lipidoids plays on gene delivery has not been investigated. As shown in Figure 1, a library of unsaturated and saturated lipidoids was prepared through the reaction of amines with oleyl acrylamide (Figure 1B, I) and *n*-octadecyl acrylamide (Figure 1B, II), respectively. This was completed in the absence of any solvents or catalysts, and the simple and

mild reactions allowed us to generate a structurally diverse library of 32 lipidoids. Their capability to facilitate intracellular gene delivery was first evaluated by delivering enhanced green fluorescent protein (EGFP)-encoding DNA and mRNA (mRNA) into human cervical carcinoma cells (HeLa). The preliminary screening results indicated that unsaturated lipidoids are the superior gene transfection agent compared to saturated lipidoids under the same conditions. Such differences can be ascribed to the large, tightly packed lipoplexes of the saturated lipidoids, which prohibit efficient cellular uptake of lipidoid/gene complexes and intracellular gene releases. The potential applications of the unsaturated lipidoids for gene therapy were further determined by looking at their ability to transfect fibroblasts as well as different cancerous cell lines.

The capability of the lipidoids in transfecting HeLa cells was evaluated by counting GFP-positive cells after DNA or mRNA delivery. As summarized in Figure 2, unsaturated lipidoids 8-I, 9-I, 10-I, and 16-I (the Arabic numeral indicates the amine number in Figure 1C, the Roman numeral indicates unsaturated (I) or saturated tails (II)) were effective in facilitating DNA delivery (Figure 2A). More than 40% cells were positive for GFP expression, whereas less than 10% GFP expression was observed for cells transfected with the saturated lipidoid/DNA complexes. Additionally, the unsaturated lipidoids were more efficient in facilitating mRNA delivery, as shown in Figure 2B. A majority of the unsaturated lipidoids facilitated intracellular mRNA delivery; 4-I, 5-I, 8-I, 9-I, 10-I, and 16-I can transfect the cells with efficiency greater than 50%, which was even higher than that obtained with the commercial
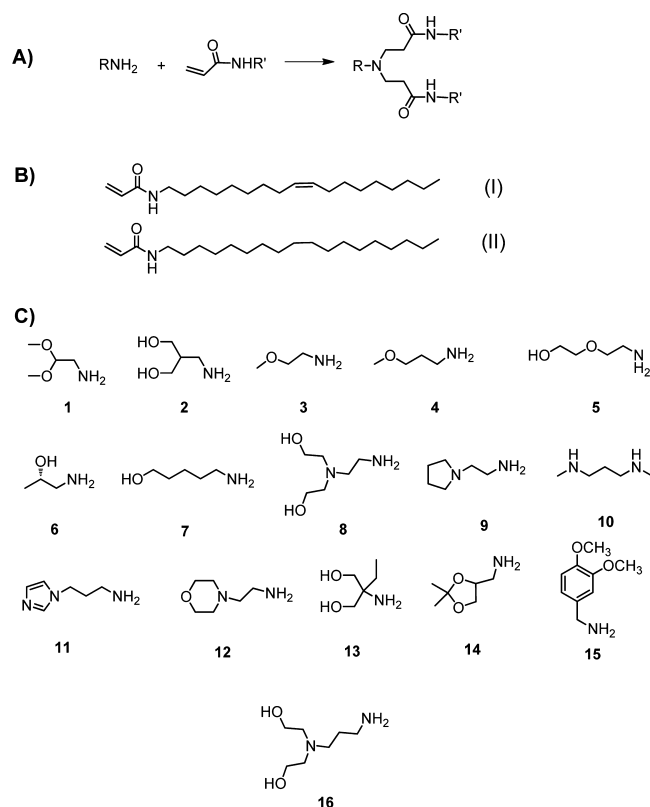
Figure 1. (A) Synthesis route of lipidoids. (B) Chemical structures of acrylamides used. (C) Amines used for lipidoids synthesis.

Figure 2. Initial *in vitro* screening results of lipidoid efficiency at delivering EGFP encoding (A) DNA and (B) mRNA into HeLa. (1−16: DNA or mRNA was delivered by lipidoids with different amine headgroups as indicated in Figure 1C; 17: DNA or mRNA was delivered using Lipofectamine 2000; 18: DNA or mRNA only). The transfection efficiency was determined by counting GFP-positive cells.

transfection agent Lipofectamine 2000. However, none of the saturated lipidoids displayed any significant ability to deliver mRNA. The screening results clearly demonstrated that for lipidoids with 18 carbon tails, the introduction of unsaturated bonds can effectively improve their performance in gene delivery. Furthermore, we observed a higher GFP expression level for the HeLa cells transfected with mRNA compared with those dosed with DNA combined with unsaturated lipidoids. This difference is understandable when the different protein transcription mechanisms of intracellular mRNA and DNA delivery are considered. For DNA-based gene delivery and therapy, DNA released into the cytoplasm has to enter the nucleus, be translated into mRNA, and then be released back into the cytoplasm. The mRNA must then be transcribed as the GFP that is then expressed in the cell. In contrast, mRNA is released intracellularly and can initiate the transcription process directly, omitting entering the nucleus. This shorter process leads to the higher transient GFP expression levels observed with lipidoid/mRNA transfection.[20,21] These results agree with previous reports for mRNA delivery using cationic lipids and polymers as carriers.[22]

To probe the mechanism that leads to the different transfection capabilities of unsaturated and saturated lipidoids, lipidoids 16-I and 16-II were selected and purified for further investigation. The DNA condensation abilities of 16-I and 16-II were evaluated first by Picogreen assay. By fixing a lipidoid/DNA ratio (5:1 w/w), the DNA condensation efficiency of 16-I was determined to be 68.4%, whereas only 38.2% DNA was condensed by 16-II. The different DNA condensation abilities of unsaturated and saturated lipidoids may result from the rigid and long hydrophobic chains of the saturated lipidoids, which comprise the water solubility of lipoplexes and thus affect DNA

condensation efficiency.[19,23] Negative-staining transmission electron microscopy (TEM) was then used to characterize the self-assembled structures of lipidoids and genes. As shown in Figure 3, multilamellar nanostructures (∼ 50 nm) with genes intercalated between the lipidoid bilayers formed when 16-I was bound to either DNA or mRNA at a 5:1 (w/w) ratio. For lipidoid 16-II however, shapeless and large aggregation complexes formed upon DNA or mRNA binding (Supplementary Figure S1). The hydrodynamic sizes of lipidoid/DNA and lipidoid/mRNA complexes were also analyzed by dynamic light scattering (DLS). Unsaturated lipidoid 16-I/DNA and 16-I/mRNA formed narrow distributed nanoparticles of 131.9 ± 10.8 and 84.6 ± 3.8 nm, respectively. However, saturated lipidoid 16-II formed particles in the size range of 100−600 nm following DNA or mRNA binding. In addition, the large, tightly packed saturated lipidoid/genes complexes may prohibit efficient intracellular gene release and result in low transfection efficiency. The intracellular gene release from the lipidoid/gene complexes was then simulated by a heparin competition assay. Heparin is a biopolymer with a high negative charge and can compete with DNA or mRNA in binding to the lipidoids. These competitive interactions can be assayed by gel electrophoresis and ethidium bromide (EB) exclusion assay. By using a fixed ratio of lipidoid to genes (5:1 w/w), the amount of heparin required to displace genes from the lipidoid/gene complexes is a good indicator of the degree of intracellular
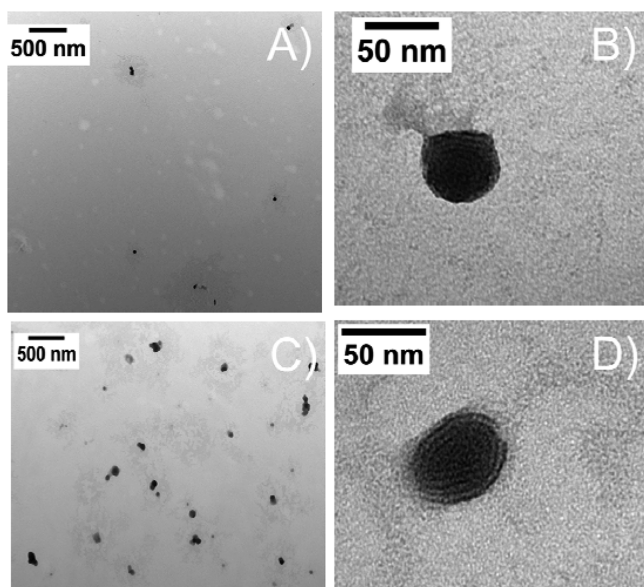
Figure 3. TEM images of (A,B) lipidoid 16-I/DNA complex and (C,D) 16-II/mRNA complex.

gene release.[24,25] As shown in Figure 4, both 16-I and 16-II can bind with DNA or mRNA effectively. By increasing
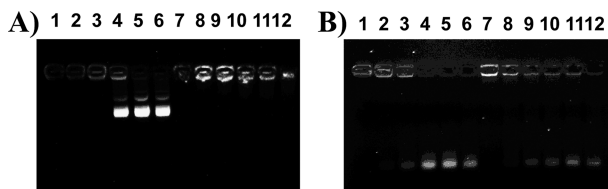
Figure 4. Heparin competition assay of lipidoid/gene complexes. (A) 16-I/DNA(1−6) and 16-II/DNA (7−12) in the absence (1, 7) and presence of heparin (2−6, 8−12). (B) 16-I/mRNA(1−6) and 16-II/mRNA (7−12) in the absence (1, 7) and presence of heparin (2−6, 8−12). The lipidoid/gene ratios were fixed at 5:1 (w/w); the concentration of heparin in lane 2 and 8 was 4 mg/mL; in 3 and 8, 8 mg/mL; in 4 and 9, 16 mg/mL; in 5 and 10, 32 mg/mL; in 6 and 11, 50 mg/mL.

concentration of heparin from 4 to 50 mg/mL, DNA is released gradually from the lipidoids. It was observed that the DNA was completely released from the 16-I/DNA complex in the presence of 16 mg/mL heparin. For 16-II with DNA, no DNA release was observed in the presence of same amount of heparin. The EB exclusion assay also demonstrated the different DNA release behavior of 16-I/DNA and 16-II/DNA complexes in the presence of heparin. As shown in Supplementary Figure S2, the relative fluorescence intensity of DNA/EB complex without any lipidoid was set to be 100%, and the binding of DNA with 16-I or 16-II quenched the emission. However, with the addition of heparin, the EB fluorescence restored gradually. The addition of 16 μg/mL heparin restored 85% of emission for 16-I/DNA, whereas only 55% was restored for 16-II/DNA complex. The gel retardation and EB exclusion assay demonstrated that the genes could be easily released from the lipoplexes of unsaturated lipidoids. The lipidoid/mRNA complexes displayed a mRNA release behavior similar to that of the lipidoid/DNA complexes, in which mRNA is released easier from 16-I/mRNA complex than from the 16-II/mRNA complexes. The heparin competition assay results correlate

very well with the cellular transfection experiments. They showed that poor transfection ability of the saturated lipidoids is likely due to the large, tightly packed aggregation complexes formed, resulting in the ineffective intracellular gene release.

The potential of the library of lipidoids for gene therapy was further expanded by optimizing the lipidoid/gene ratio and transfecting different cell lines. As shown in Figure 5, GFP
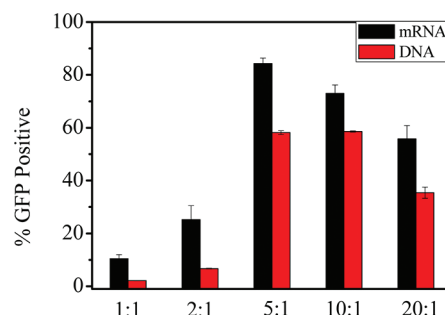
Figure 5. Relationships of lipidoid 16-I to DNA or mRNA ratios and delivery efficiency. The delivery efficiency was monitored by counting GFP-positive cells.

expression was enhanced by increasing the ratio of 16-I to DNA or mRNA. This increase in expression was seen with ratios from 1:1 to 5:1 (lipidoid:DNA/mRNA), while any further increase led to a lower transfection efficiency. Furthermore, different cell lines including the cancerous NIH3T3, MCF-7, HepG2, and MDA-MB-231 cell lines and non-cancerous fibroblasts (BJ cells) were dosed with 16-I/DNA or 16-I/mRNA to test the versatility of the lipidoids. As shown in Figure 6, lipidoid 16-I facilitates both DNA and mRNA delivery
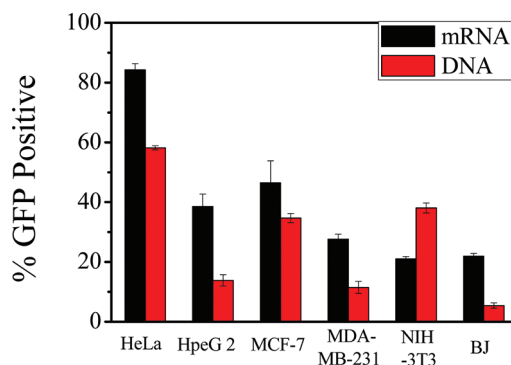
Figure 6. Gene delivery efficiency of lipidoid 16-I in different cancerous and non-cancerous cell lines.

in all of the tested cell lines. It was observed that HeLa cell can be transfected at the highest efficiency (greater than 50%) of the tested cells. For MCF-7, HepG2, MDA-MB-231, and BJ cells, mRNA transfection led to higher GFP expression compared to DNA transfection. For NIH-3T3 cells, DNA delivery was more efficient than mRNA delivery.

In conclusion, we have used a combinatorial approach to design and construct a lipidoid library consisting of lipidoids with different saturation levels to facilitate intracellular gene delivery. The investigation of the structure−activity relationships indicates that the introduction of unsaturated bonds can improve the transfection ability of the lipidoids. This is most likely due to the increased cellular uptake and enhanced intracellular gene release of the unsaturated complexes.

Meanwhile, the amine groups in the lipidoids play critical roles in determining the transfection efficiency, and a secondary amine and a hydrophilic group incorporated in a lipidoid can facilitate the gene delivery. The potential applications of these unsaturated lipidoids for gene therapies were expanded by evaluating their ability to transfect different cells lines. Furthermore, we have reported the first application of lipidoids for in vitro mRNA delivery. This application has the potential to be beneficial for cancer vaccines[26] and cellular reprogramming[27] due to the advantages of using mRNA rather than DNA. These advantages include pharmaceutical safety as well as the ability to transiently transfect cells.

■ METHODS

Materials. Compounds in the library were synthesized and characterized as previously described by our group as well as several others.[9,14] All chemicals were purchased from Sigma-Aldrich or Alfa-Aesar and used directly. EGFP encoding Plasmid DNA was purchased from Elim Biopharmaceuticals, Inc. (Hayward, CA). Messenger RNA encoding EGFP was purchased from Stemgent Inc. (Cambridge, MA). Picogreen assay kit was purchased from Invitrogen (Carlsbad, CA), and the DNA condensation efficiency was determined according to the manufacturer's instruction.

Synthesis of Lipidoids. Oleyl acrylamide and n-octadecyl acrylamide were synthesized according to the published methods.[28] In a 5-mL Telfon-lined glass screw-top vial, oleyl acrylamide or n-octadecyl acrylamide was added to amine at a molar ratio of 1:2.4 (amine:acrylamide). The mixture was then stirred at 90 °C for 2 days. After cooling, the lipidoid mixtures were used without purification unless otherwise noted. Representative lipidoids 16-I and 16-II were purified through flash chromatography on silica gel and characterized by ^{1}H NMR.

Cell Culture. All cell lines used in this paper (HeLa, MCF-7, HepG2, MDA-MB-231, NIH-3T3, BJ) were purchased from ATCC (Manassas, VA) and cultured in DMEM supplemented with 10% FBS and 1% penicillin/streptomycin at 37 °C in the presence of 5% CO_2. For gene transfection experiments, cells were seeded in 96-well plates at a density of 10,000 cells per well 1 day prior to transfection.

In Vitro Gene Transfection. To facilitate high-throughput screening, the lipidoid/DNA or lipidoid/mRNA complexes were prepared simply by adding lipidoid to the sodium acetate buffer solutions (25 mM, pH = 5.5) of DNA or mRNA at ratios of 5:1 (w/w), followed by 15 min of incubation at room temperature. After the addition of the lipidoid/gene complexes to the cells (200 ng DNA or 100 ng mRNA complexed with lipidoids per well), HeLa cells were incubated at 37 °C for an additional 48 h. Control experiments were performed by complexing DNA or mRNA with Lipofectamine 2000 (Invitrogen, Carlsbad, CA) in OPTI-MEM as per the manufacturer's instructions. The percentage of GFP expressing cells was evaluated by a flow cytometer (BD FACS LSRII) attached with a high-throughput system. All transfection experiments were performed in quadruplicate.

Cytotoxicity of Unsaturated Lipidoids (MTT Assay). Cytotoxicity of unsaturated lipidoids was assessed by incubating lipidoid (7 μg/μL) with cells seeded on 96-well plate at a density of 10,000 cells per well. Lipidoids were incubated with cells for 24 h, and the cell viability was evaluated through MTT assay according to previous reports.[29]

Transmission Electron Microscopy (TEM). Lipidoid/DNA or lipidoid/mRNA complexes were prepared with the same protocol as in vitro transfection experiment. One drop of the samples (10 μL) was applied to hydrophilic carbon-covered copper grids (300 meshes) for 10 min. The grids were subsequently rinsed with contrasting materials (1% uranyl acetate solution at pH 4.5). Any remaining staining solution was removed with filter paper and air-dried. TEM micro-structure was determined using a Tecnai FEG TEM (FEI tecnai 12 spirit Biotwin, FET company, Hillsboro, OR) operating at 80 kV.

Gel Retardation and Heparin Competition Assay. Lipidoid/DNA and Lipidoid/mRNA complexes were prepared by mixing 0.5 μg of DNA or 0.25 μg of mRNA with lipidoids at a ratio of 1:5 (w/w), respectively. For the heparin competition assay, heparin solutions with concentrations increasing from 0 to 50 mg/mL were added to the lipidoid/DNA or lipidoid/mRNA complexes, followed by 15 min of incubation before loading into gels. The electrophoresis gels were prepared by dissolving 0.4 g of agarose in 50 mL of TBE with 0.1 μg/mL ethidium bromide.

Ethidium Bromide (EB) Exclusion Assay. Briefly, 2 μg of DNA and 2 μL of EB solution (0.01%) were mixed in 500 μL of sodium acetate buffer solution (25 mM, pH = 5.5) and incubated for 10 min, and the fluorescence intensity at 605 nm was recorded and set as 100%. For the heparin competition assay, the lipidoid 16-I or 16-II (10 μg), 2 μg of DNA, and 2 μL of EB solution (0.01%) were incubated in 500 μL of sodium acetate buffer solution (25 mM, pH = 5.5) for 10 min, followed by the addition of different amount of heparin and 10 min of incubation. The emission intensity was monitored and compared with that of the lipidoid/DNA mixtures.

■ ASSOCIATED CONTENT

Ⓢ Supporting Information

Cytotoxicity assay of unsaturated lipidoid; TEM images of 16II/DNA and 16II/mRNA complexes; ethidium bromide exclusion assay for heparin competition binding of lipidoid/DNA complexes. This material is available free of charge via the Internet at http://pubs.acs.org.

■ AUTHOR INFORMATION

Corresponding Author
*E-mail: qiaobing.xu@tufts.edu.

Notes
The authors declare no competing financial interest.

■ REFERENCES

(1) Mintzer, M. A., and Simanek, E. E. (2008) Nonviral vectors for gene delivery. Chem. Rev. 109, 259−302.

(2) Whitehead, K. A., Langer, R., and Anderson, D. G. (2009) Knocking down barriers: advances in siRNA delivery. Nat. Rev. Drug Discovery 8, 129−138.

(3) Bhattacharya, S., and Bajaj, A. (2009) Advances in gene delivery through molecular design of cationic lipids. Chem. Commun., 4642−4656.

(4) Gaynor, J. W., Campbell, B. J., and Cosstick, R. (2010) RNA interference: a chemist's perspective. Chem. Soc. Rev. 39, 4169−4184.

(5) Zhou, J., Liu, J., Cheng, C. J., Patel, T. R., Weller, C. E., Piepmeier, J. M., Jiang, Z., and Saltzman, W. M. (2011) Biodegradable poly(amine-co-ester) terpolymers for targeted gene delivery. Nat. Mater. 11, 82−90.

(6) Yuan, X., Naguib, S., and Wu, Z. (2011) Recent advances of siRNA delivery by nanoparticles. *Expert Opin. Drug Delivery 8*, 521–536.

(7) Sigwalt, D., Holler, M., Iehl, J., Nierengarten, J.-F., Nothisen, M., Morin, E., and Remy, J.-S. (2011) Gene delivery with polycationic fullerene hexakis-adducts. *Chem. Commun. 47*, 4640–4642.

(8) Mellet, C. O., Fernandez, J. M. G., and Benito, J. M. (2011) Cyclodextrin-based gene delivery systems. *Chem. Soc. Rev. 40*, 1586–1608.

(9) Akinc, A., Zumbuehl, A., Goldberg, M., Leshchiner, E. S., Busini, V., Hossain, N., Bacallado, S. A., Nguyen, D. N., Fuller, J., Alvarez, R., Borodovsky, A., Borland, T., Constien, R., de Fougerolles, A., Dorkin, J. R., Narayanannair Jayaprakash, K., Jayaraman, M., John, M., Koteliansky, V., Manoharan, M., Nechev, L., Qin, J., Racie, T., Raitcheva, D., Rajeev, K. G., Sah, D. W. Y., Soutschek, J., Toudjarska, I., Vornlocher, H.-P., Zimmermann, T. S., Langer, R., and Anderson, D. G. (2008) A combinatorial library of lipid-like materials for delivery of RNAi therapeutics. *Nat. Biotechnol. 26*, 561–569.

(10) Akinc, A., Goldberg, M., Qin, J., Dorkin, J. R., Gamba-Vitalo, C., Maier, M., Jayaprakash, K. N., Jayaraman, M., Rajeev, K. G., Manoharan, M., Koteliansky, V., Rohl, I., Leshchiner, E. S., Langer, R., and Anderson, D. G. (2009) Development of lipidoid-siRNA formulations for systemic delivery to the liver. *Mol. Ther. 17*, 872–879.

(11) Mahon, K. P., Love, K. T., Whitehead, K. A., Qin, J., Akinc, A., Leshchiner, E., Leshchiner, I., Langer, R., and Anderson, D. G. (2010) Combinatorial approach to determine functional group effects on lipidoid-mediated siRNA delivery. *Bioconjugate Chem. 21*, 1448–1454.

(12) Goldberg, M. S., Xing, D., Ren, Y., Orsulic, S., Bhatia, S. N., and Sharp, P. A. (2011) Nanoparticle-mediated delivery of siRNA targeting Parp1 extends survival of mice bearing tumors derived from Brca1-deficient ovarian cancer cells. *Proc. Natl. Acad. Sci. U.S.A. 108*, 745–750.

(13) Leuschner, F., Dutta, P., Gorbatov, R., Novobrantseva, T. I., Donahoe, J. S., Courties, G., Lee, K. M., Kim, J. I., Markmann, J. F., Marinelli, B., Panizzi, P., Lee, W. W., Iwamoto, Y., Milstein, S., Epstein-Barash, H., Cantley, W., Wong, J., Cortez-Retamozo, V., Newton, A., Love, K., Libby, P., Pittet, M. J., Swirski, F. K., Koteliansky, V., Langer, R., Weissleder, R., Anderson, D. G., and Nahrendorf, M. (2011) Therapeutic siRNA silencing in inflammatory monocytes in mice. *Nat. Biotechnol. 29*, 1005–1010.

(14) Sun, S., Wang, M., Knupp, S. A., Soto-Feliciano, Y., Hu, X., Kaplan, D. L., Langer, R., Anderson, D. G., and Xu, Q. (2012) Combinatorial library of lipidoids for in vitro DNA delivery. *Bioconjugate Chem. 23*, 135–140.

(15) Love, K. T., Mahon, K. P., Levins, C. G., Whitehead, K. A., Querbes, W., Dorkin, J. R., Qin, J., Cantley, W., Qin, L. L., Racie, T., Frank-Kamenetsky, M., Yip, K. N., Alvarez, R., Sah, D. W. Y., de Fougerolles, A., Fitzgerald, K., Koteliansky, V., Akinc, A., Langer, R., and Anderson, D. G. (2010) Lipid-like materials for low-dose, in vivo gene silencing. *Proc. Natl. Acad. Sci. U.S.A. 107*, 1864–1869.

(16) Felgner, J., Kumar, R., Sridhar, C., Wheeler, C., Tsai, Y., Border, R., Ramsey, P., Martin, M., and Felgner, P. (1994) Enhanced gene delivery and mechanism studies with a novel series of cationic lipid formulations. *J. Biol. Chem. 269*, 2550–2561.

(17) Byk, G., Dubertret, C., Escriou, V., Frederic, M., Jaslin, G., Rangara, R., Pitard, B., Crouzet, J., Wils, P., Schwartz, B., and Scherman, D. (1998) Synthesis, activity, and structure–activity relationship studies of novel cationic lipids for DNA transfer. *J. Med. Chem. 41*, 224–235.

(18) Bell, P. C., Bergsma, M., Dolbnya, I. P., Bras, W., Stuart, M. C. A., Rowan, A. E., Feiters, M. C., and Engberts, J. B. F. N. (2003) Transfection mediated by gemini surfactants: Engineered escape from the endosomal compartment. *J. Am. Chem. Soc. 125*, 1551–1558.

(19) Zhang, S. B., Zhi, D. F., Wang, B., Zhao, Y. N., Yang, B. L., and Yu, S. J. (2010) Transfection efficiency of cationic lipids with different hydrophobic domains in gene delivery. *Bioconjugate Chem. 21*, 563–577.

(20) Yamamoto, A., Kormann, M., Rosenecker, J., and Rudolph, C. (2009) Current prospects for mRNA gene delivery. *Eur. J. Pharm. Biopharm. 71*, 484–489.

(21) Tavernier, G., Andries, O., Demeester, J., Sanders, N. N., De Smedt, S. C., and Rejman, J. (2011) mRNA as gene therapeutic: How to control protein expression. *J. Controlled Release 150*, 238–247.

(22) Rejman, J., Tavernier, G., Bavarsad, N., Demeester, J., and De Smedt, S. C. (2010) mRNA transfection of cervical carcinoma and mesenchymal stem cells mediated by cationic carriers. *J. Controlled Release 147*, 385–391.

(23) Zuhorn, I. S., Oberle, V., Visser, W. H., Engberts, J. B. F. N., Bakowsky, U., Polushkin, E., and Hoekstra, D. (2002) Phase behavior of cationic amphiphiles and their mixtures with helper lipid influences lipoplex shape, DNA translocation, and transfection efficiency. *Biophy. J. 83*, 2096–2108.

(24) Barnard, A., Posocco, P., Pricl, S., Calderon, M., Haag, R., Hwang, M. E., Shum, V. W. T., Pack, D. W., and Smith, D. K. (2011) Degradable self-assembling dendrons for gene delivery: Experimental and theoretical insights into the barriers to cellular uptake. *J. Am. Chem. Soc. 133*, 20288–20300.

(25) Glodde, M., Sirsi, S. R., and Lutz, G. J. (2005) Physiochemical properties of low and high molecular weight poly(ethylene glycol)-grafted poly(ethylene imine) copolymers and their complexes with oligonucleotides. *Biomacromolecules 7*, 347–356.

(26) Mitchell, D. A., and Nair, S. K. (2000) RNA transfected dendritic cells as cancer vaccines. *Curr. Opin. Mol. Ther. 2*, 176–181.

(27) Warren, L., Manos, P. D., Ahfeldt, T., Loh, Y. H., Li, H., Lau, F., Ebina, W., Mandal, P. K., Smith, Z. D., Meissner, A., Daley, G. Q., Brack, A. S., Collins, J. J., Cowan, C., Schlaeger, T. M., and Rossi, D. J. (2010) Highly efficient reprogramming to pluripotency and directed differentiation of human cells with synthetic modified mRNA. *Cell Stem Cell 7*, 618–630.

(28) Wang, Y. F., Chen, T. M., Okada, K., Sakurai, I., and Nakaya, T. (1999) Structure in the condensed state and amphiphilic properties of novel copolymers having alkyl chains and phosphatidylcholine analogous groups. *J. Polym. Sci. Part A: Polym. Chem. 37*, 1293–1302.

(29) Liu, C.-L., Wu, H.-T., Hsiao, Y.-H., Lai, C.-W., Shih, C.-W., Peng, Y.-K., Tang, K.-C., Chang, H.-W., Chien, Y.-C., Hsiao, J.-K., Cheng, J.-T., and Chou, P.-T. (2011) Insulin-directed synthesis of fluorescent gold nanoclusters: Preservation of insulin bioactivity and versatility in cell imaging. *Angew. Chem., Int. Ed. 50*, 7056–7060.

Bibliography

1. Sanchez, C., Arribart, H. & Guille, M. M. G. Biomimetism and bioinspiration as tools for the design of innovative materials and systems. *Nat. Mater.* **4,** 277–88 (2005).

2. Geim, A. K. *et al.* Microfabricated adhesive mimicking gecko foot-hair. *Nat. Mater.* **2,** 461–463 (2003).

3. Dreyfus, R. *et al.* Microscopic artificial swimmers. *Nature* **437,** 862–865 (2005).

4. Dai, X., Schalek, R. & Xu, Q. Staining and Etching: A Simple Method to Fabricate Inorganic Nanostructures from Tissue Slices. *Adv. Mater.* **24** 370–374 (2011).

5. Van Bommel, K. J. C., Friggeri, A. & Shinkai, S. Organic templates for the generation of inorganic materials. *Angew. Chemie - Int. Ed.* **42,** 980–999 (2003).

6. Shin, H., Jo, S. & Mikos, A. Biomimetic materials for tissue engineering. *Adv. Drug Deliv. Rev.* **24,** 4353–4364 (2003).

7. Lutolf, M. P. & Hubbell, J. A. Synthetic biomaterials as instructive extracellular microenvironments for morphogenesis in tissue engineering. *Nat. Biotechnol.* **23,** 47–55 (2005).

8. Macchiarini, P. *et al.* Clinical transplantation of a tissue-engineered airway. *Lancet* **372,** 2023–2030 (2008).

9. Atala, A., Bauer, S. B., Soker, S., Yoo, J. J. & Retik, A. B. Tissue-engineered autologous bladders for patients needing cystoplasty. *Lancet* **367,** 1241–1246 (2006).

10. Ruoslahti, E. RGD and other recognition sequences for integrins. *Annu. Rev. Cell Dev. Biol.* **12,** 697–715 (1996).

11. Hersel, U., Dahmen, C. & Kessler, H. RGD modified polymers: Biomaterials for stimulated cell adhesion and beyond. *Biomaterials* **24,** 4385–4415 (2003).

12. Jackson, D. & Fessler, J. Isolation and Properties of a Collagen soluble in Salt Solution at Neutral pH. *Nature* **176,** 69–70 (1955).

13. Aberoumand, A. Comparative study between different methods of collagen extraction from fish and its properties. *World Appl. Sci. J.* **16,** 316–319 (2012).

14. Altman, G. H. *et al.* Silk-based biomaterials. *Biomaterials* **24,** 401–16 (2003).

15. Vepari, C. & Kaplan, D. L. Silk as a Biomaterial. *Prog. Polym. Sci.* **32,** 991–1007 (2007).

16. Rinaudo, M. Chitin and chitosan: Properties and applications. *Prog. Polym. Sci.* **31,** 603–632 (2006).

17. Ramshaw, J. A. M., Peng, Y. Y., Glattauer, V. & Werkmeister, J. A. Collagens as biomaterials. *J. Mater. Sci. Mater. Med.* **20 Suppl 1,** S3–8 (2009).

18. Daamen, W. F., Veerkamp, J. H., van Hest, J. C. M. & van Kuppevelt, T. H. Elastin as a biomaterial for tissue engineering. *Biomaterials* **28,** 4378–98 (2007).

19. Lazaris, A. *et al.* Spider silk fibers spun from soluble recombinant silk produced in mammalian cells. *Science* **295,** 472–476 (2002).

20. Bosman, F. T. & Stamenkovic, I. Functional structure and composition of the extracellular matrix. *J. Pathol.* **200,** 423–8 (2003).

21. Fu, R. H. *et al.* Decellularization and recellularization technologies in tissue engineering. *Cell Transplant.* **23,** 621–630 (2014).

22. Screen, H. R. C. *et al.* The influence of noncollagenous matrix components on the micromechanical environment of tendon fascicles. *Ann. Biomed. Eng.* **33,** 1090–9 (2005).

23. Birch, H. L., Thorpe, C. T. & Rumian, A. P. Specialisation of extracellular matrix for function in tendons and ligaments. *J. Muscles Ligaments Tendons* **3,** 12–22 (2013).

24. Clarke, B. Normal bone anatomy and physiology. *Clin. J. Am. Soc. Nephrol.* **3 Suppl 3,** S131–9 (2008).

25. Kleinman, H. K., Philp, D. & Hoffman, M. P. Role of the extracellular matrix in morphogenesis. *Curr. Opin. Biotechnol.* **14,** 526–532 (2003).

26. Hoganson, D. M. *et al.* The retention of extracellular matrix proteins and angiogenic and mitogenic cytokines in a decellularized porcine dermis. *Biomaterials* **31,** 6730–7 (2010).

27. Ning, L. J. *et al.* Preparation and characterization of decellularized tendon slices for tendon tissue engineering. *J. Biomed. Mater. Res. A* **100,** 1448–56 (2012).

28. Crapo, P. M., Gilbert, T. W. & Badylak, S. F. An overview of tissue and whole organ decellularization processes. *Biomaterials* **32,** 3233–43 (2011).

29. Gilbert, T. W., Sellaro, T. L. & Badylak, S. F. Decellularization of tissues and organs. *Biomaterials* **27,** 3675–83 (2006).

30. Jackson, D. W. *et al.* The effects of processing techniques on the mechanical properties of bone-anterior cruciate ligament-bone allografts. An experimental study in goats. *Am. J. Sports Med.* **16,** 101–105

31. Gulati, a K. Evaluation of acellular and cellular nerve grafts in repair of rat peripheral nerve. *J. Neurosurg.* **68,** 117–123 (1988).

32. Flynn, L. E. The use of decellularized adipose tissue to provide an inductive microenvironment for the adipogenic differentiation of human adipose-derived stem cells. *Biomaterials* **31,** 4715–4724 (2010).

33. Dahl, S., Koh, J., Prabhakar, V. & Niklason, L. Decellularized native and engineered arterial scaffolds for transplantation. *Cell Transplant.* **12,** 659–666 (2003).

34. Dahl, S. L. M., Rhim, C., Song, Y. C. & Niklason, L. E. Mechanical properties and compositions of tissue engineered and native arteries. *Ann. Biomed. Eng.* **35,** 348–55 (2007).

35. Brown, B. N. *et al.* Comparison of three methods for the derivation of a biologic scaffold composed of adipose tissue extracellular matrix. *Tissue Eng. Part C. Methods* **17,** 411–421 (2011).

36. Hodde, J. & Hiles, M. Virus safety of a porcine-derived medical device: Evaluation of a viral inactivation method. *Biotechnol. Bioeng.* **79,** 211–216 (2002).

37. Chen, R. N., Ho, H. O., Tsai, Y. T. & Sheu, M. T. Process development of an acellular dermal matrix (ADM) for biomedical applications. *Biomaterials* **25,** 2679–2686 (2004).

38. Cartmell, J. S. & Dunn, M. G. Development of cell-seeded patellar tendon allografts for anterior cruciate ligament reconstruction. *Tissue Eng.* **10,** 1065–75 (2004).

39. Reing, J. E. *et al.* The effects of processing methods upon mechanical and biologic properties of porcine dermal extracellular matrix scaffolds. *Biomaterials* **31,** 8626–8633 (2010).

40. Lumpkins, S. B., Pierre, N. & McFetridge, P. S. A mechanical evaluation of three decellularization methods in the design of a xenogeneic scaffold for tissue engineering the temporomandibular joint disc. *Acta Biomater.* **4,** 808–816 (2008).

41. Cui, X., Zhang, Y. & Xue, J. Trypsin versus Triton X-100 for decellularization of porcine articular cartilage. *J. Clin. Rehabil. Tissue Eng. Res.* **13,** 9080–9083 (2009).

42. Xu, H. *et al.* Comparison of decellularization protocols for preparing a decellularized porcine annulus fibrosus scaffold. *PLoS One* **9,** 1–13 (2014).

43. Oh, J. Y. *et al.* Processing porcine cornea for biomedical applications. *Tissue Eng. Part C. Methods* **15,** 635–645 (2009).

44. Uygun, B. E. *et al.* Organ reengineering through development of a transplantable recellularized liver graft using decellularized liver matrix. *Nat. Med.* **16,** 814–820 (2010).

45. Rieder, E. *et al.* Decellularization protocols of porcine heart valves differ importantly in efficiency of cell removal and susceptibility of the matrix to recellularization with human vascular cells. *J. Thorac. Cardiovasc. Surg.* **127,** 399–405 (2004).

46. Elkins, R. C., Dawson, P. E., Goldstein, S., Walsh, S. P. & Black, K. S. Decellularized human valve allografts. *Ann. Thorac. Surg.* **71,** (2001).

47. Woods, T. & Gratzer, P. F. Effectiveness of three extraction techniques in the development of a decellularized bone-anterior cruciate ligament-bone graft. *Biomaterials* **26,** 7339–7349 (2005).

48. Schenke-Layland, K. *et al.* Impact of decellularization of xenogeneic tissue on extracellular matrix integrity for tissue engineering of heart valves. *J. Struct. Biol.* **143,** 201–208 (2003).

49. Grauss, R. W. *et al.* Histological evaluation of decellularised porcine aortic valves: Matrix changes due to different decellularisation methods. *Eur. J. Cardiothoracic Surg.* **27,** 566–571 (2005).

50. Ott, H. C. *et al.* Regeneration and orthotopic transplantation of a bioartificial lung. *Nat. Med.* **16,** 927–933 (2010).

51. Petersen, T. H. *et al.* Tissue-engineered lungs for in vivo implantation. *Science* **329,** 538–541 (2010).

52. Ott, H. C. *et al.* Perfusion-decellularized matrix: using nature's platform to engineer a bioartificial heart. *Nat. Med.* **14,** 213–221 (2008).

53. Uygun, B. E. *et al.* Organ reengineering through development of a transplantable recellularized liver graft using decellularized liver matrix. *Nat. Med.* **16,** 814–820 (2010).

54. Ott, H. C. *et al.* Regeneration and orthotopic transplantation of a bioartificial lung. *Nat. Med.* **16,** 927–933 (2010).

55. Shin'oka, T., Imai, Y. & Ikada, Y. Transplantation of a Tissue-Engineered Pulmonary Artery. *N. Engl. J. Med.* **344,** 532–533 (2001).

56. L'Heureux, N. *et al.* Human tissue-engineered blood vessels for adult arterial revascularization. *Nat. Med.* **12,** 361–5 (2006).

57. L'Heureux, N., McAllister, T. N. & de la Fuente, L. M. Tissue-engineered blood vessel for adult arterial revascularization. *N. Engl. J. Med.* **357,** 1451–1453 (2007).

58. Wang, X. *et al.* Generation of three-dimensional hepatocyte/gelatin structures with rapid prototyping system. *Tissue Eng.* **12,** 83–90 (2006).

59. Inzana, J. A. *et al.* 3D printing of composite calcium phosphate and collagen scaffolds for bone regeneration. *Biomaterials* **35,** 4026–4034 (2014).

60. Skardal, A., Zhang, J. & Prestwich, G. D. Bioprinting vessel-like constructs using hyaluronan hydrogels crosslinked with tetrahedral polyethylene glycol tetracrylates. *Biomaterials* **31,** 6173–6181 (2010).

61. Derby, B. Printing and prototyping of tissues and scaffolds. *Science* **338,** 921–6 (2012).

62. Elia, R. *et al.* Silk-hyaluronan-based composite hydrogels: A novel, securable vehicle for drug delivery. *J. Biomater. Appl.* **27,** 749–762 (2011).

63. Melchels, F. P. W. *et al.* Additive manufacturing of tissues and organs. *Prog. Polym. Sci.* **37,** 1079–1104 (2012).

64. Norotte, C., Marga, F. S., Niklason, L. E. & Forgacs, G. Scaffold-free vascular tissue engineering using bioprinting. *Biomaterials* **30,** 5910–5917 (2009).

65. Derby, B. Bioprinting: inkjet printing proteins and hybrid cell-containing materials and structures. *J. Mater. Chem.* **18,** 5717 (2008).

66. Faulk, D. M. *et al.* ECM hydrogel coating mitigates the chronic inflammatory response to polypropylene mesh. *Biomaterials* **35,** 8585–8595 (2014).

67. Wolf, M. T. *et al.* Polypropylene surgical mesh coated with extracellular matrix mitigates the host foreign body response. *J. Biomed. Mater. Res. - Part A* **102,** 234–246 (2014).

68. Van't Riet, M., Burger, J. W. A, Bonthuis, F., Jeekel, J. & Bonjer, H. J. Prevention of adhesion formation to polypropylene mesh by collagen coating: A randomized controlled study in a rat model of ventral hernia repair. *Surg. Endosc. Other Interv. Tech.* **18,** 681–685 (2004).

69. Patterson, J., Martino, M. M. & Hubbell, J. A. Biomimetic materials in tissue engineering. *Mater. Today* **13,** 14–22 (2010).

70. Shengjie Li *et al.* Direct Fabrication of a Hybrid Cell/Hydrogel Construct by a Double-nozzle Assembling Technology. *J. Bioact. Compat. Polym.* **24,** 249–265 (2009).

71. Eberli, D., Filho, L. F., Atala, A. & Yoo, J. J. Composite scaffolds for the engineering of hollow organs and tissues. *Methods* **47,** 109–115 (2009).

72. Badylak, S. F. *et al.* Esophageal reconstruction with ECM and muscle tissue in a dog model. *J. Surg. Res.* **128,** 87–97 (2005).

73. Sadr, N. *et al.* Enhancing the biological performance of synthetic polymeric materials by decoration with engineered, decellularized extracellular matrix. *Biomaterials* **33,** 5085–5093 (2012).

74. Pati, F. *et al.* Ornamenting 3D printed scaffolds with cell-laid extracellular matrix for bone tissue regeneration. *Biomaterials* **37,** 230–241 (2015).

75. Coombes, A. G. *et al.* Biocomposites of non-crosslinked natural and synthetic polymers. *Biomaterials* **23,** 2113–2118 (2002).

76. Lun, S. *et al.* A functional extracellular matrix biomaterial derived from ovine forestomach. *Biomaterials* **31,** 4517–4529 (2010).

77. Floden, E. W. *et al.* Biophysical characterization of ovine forestomach extracellular matrix biomaterials. *J. Biomed. Mater. Res. - Part B Appl. Biomater.* **96 B,** 67–75 (2011).

78. Lim, P. S. *et al.* Repair of left ventricular aneurysm with acellular dermis graft: A case report. *J. Cardiol. Cases* **6,** e42–e44 (2012).

79. Bellows, C. F., Albo, D., Berger, D. H. & Awad, S. S. Abdominal wall repair using human acellular dermis. *Am. J. Surg.* **194,** 192–198 (2007).

80. Eberli, D., Atala, A. & Yoo, J. J. One and four layer acellular bladder matrix for fascial tissue reconstruction. *J. Mater. Sci. Mater. Med.* **22,** 741–751 (2011).

81. Choi, J. W. *et al.* Small intestine submucosa and mesenchymal stem cells composite gel for scarless vocal fold regeneration. *Biomaterials* **35,** 4911–4918 (2014).

82. Perry, S. M. *et al.* Use of small intestine submucosa in a rat model of acute and chronic rotator cuff tear. *J. Shoulder Elb. Surg.* **16,** 179–183 (2007).

83. Roeder, R. *et al.* Compliance, elastic modulus, and burst pressure of small-intestine submucosa (SIS), small-diameter vascular grafts. *J. Biomed. Mater. Res.* **47**, 65-70 (1999).

84. Shim, S. W. *et al.* Evaluation of Small Intestine Submucosa and Poly(caprolactone-co-lactide) Conduits for Peripheral Nerve Regeneration. *Tissue Eng. Part A* **21,** 1142–1151 (2015).

85. Du, X. F., Kwon, S. K., Song, J. J., Cho, C. G. & Park, S. W. Tracheal reconstruction by mesenchymal stem cells with small intestine submucosa in rabbits. *Int. J. Pediatr. Otorhinolaryngol.* **76,** 345–351 (2012).

86. Moore, D. C., Pedrozo, H. A, Crisco, J. J. & Ehrlich, M. G. Preformed grafts of porcine small intestine submucosa (SIS) for bridging segmental bone defects. *J. Biomed. Mater. Res. A* **69,** 259–266 (2004).

87. Hodde, J. Naturally Occuring Scaffolds for Soft Tissue Repair and Regeneration. *Tissue Eng.* **8,** 295–308 (2002).

88. Badylak, S. F. Xenogeneic extracellular matrix as a scaffold for tissue reconstruction. *Transpl. Immunol.* **12,** 367–377 (2004).

89. Lee, C. H., Singla, A. & Lee, Y. Biomedical applications of collagen. *Int. J. Pharm.* **221,** 1–22 (2001).

90. Schegg, B., Hülsmeier, A. J., Rutschmann, C., Maag, C. & Hennet, T. Core glycosylation of collagen is initiated by two beta(1-O)galactosyltransferases. *Mol. Cell. Biol.* **29,** 943–952 (2009).

91. Lodish, H., Berk, A., Zipursky, S. & Al., E. in *Mol. Cell Biol.* (WH Freeman, 2000).

92. Kalamajski, S. & Oldberg, A. The role of small leucine-rich proteoglycans in collagen fibrillogenesis. *Matrix Biol.* **29,** 248–253 (2010).

93. Kastelic, J., Galeski, A. & Baer, E. The multicomposite structure of tendon. *Connect. Tissue Res.* **6,** 11–23 (1978).

94. Silver, F. H., Freeman, J. W. & Seehra, G. P. Collagen self-assembly and the development of tendon mechanical properties. *J. Biomech.* **36,** 1529–1553 (2003).

95. Thorpe, C. T., Birch, H. L., Clegg, P. D. & Screen, H. R. C. The role of the non-collagenous matrix in tendon function. *Int. J. Exp. Pathol.* **94,** 248–59 (2013).

96. Rees, S. G. *et al.* Catabolism of aggrecan, decorin and biglycan in tendon. *Biochem. J.* **350 Pt 1,** 181–188 (2000).

97. Samiric, T., Ilic, M. Z. & Handley, C. J. Characterisation of proteoglycans and their catabolic products in tendon and explant cultures of tendon. *Matrix Biol.* **23,** 127–140 (2004).

98. Rees, S. G. *et al.* Immunolocalisation and expression of proteoglycan 4 (cartilage superficial zone proteoglycan) in tendon. *Matrix Biol.* **21,** 593–602 (2002).

99. Ryan, C. *et al.* Glycosaminoglycans in tendon physiology, pathophysiology and therapy. *Bioconjug. Chem.* 150513115403002 (2015).

100. Franchi, M. *et al.* Contribution of glycosaminoglycans to the microstructural integrity of fibrillar and fiber crimps in tendons and ligaments. *ScientificWorldJournal.* **10,** 1932–1940 (2010).

101. Gosline, J. *et al.* Elastic proteins: biological roles and mechanical properties. *Philos. Trans. R. Soc. Lond. B. Biol. Sci.* **357,** 121–132 (2002).

102. Swatschek, D., Schatton, W., Kellermann, J., MullerMüller, W. E. G. & Kreuter, J. Marine sponge collagen: isolation, characterization and effects on the skin parameters surface-pH, moisture and sebum. *Eur. J. Pharm. Biopharm.* **53,** 107–113 (2002).

103. Zeugolis, D. I., Paul, R. G. & Attenburrow, G. Factors influencing the properties of reconstituted collagen fibers prior to self-assembly: animal species and collagen extraction method. *J. Biomed. Mater. Res. A* **86,** 892–904 (2008).

104. Danielsen, C. C. Mechanical properties of reconstituted collagen fibrils. A study on reconstitution methodology and influence of in vitro maturation. *Connect. Tissue Res.* **9,** 51–7 (1981).

105. Techatanawat, S., Surarit, R., Suddhasthira, T. & Khovidhunkit, S. O. P. Type I collagen extracted from rat-tail and bovine Achilles tendon for dental application: A comparative study. *Asian Biomed.* **5,** 787–798 (2011).

106. Kosen, Y., Miyaji, H., Kato, A., Sugaya, T. & Kawanami, M. Application of collagen hydrogel/sponge scaffold facilitates periodontal wound healing in class II furcation defects in beagle dogs. *J. Periodontal Res.* **47,** 626–634 (2012).

107. Sumita, Y. *et al.* Performance of collagen sponge as a 3-D scaffold for tooth-tissue engineering. *Biomaterials* **27,** 3238–3248 (2006).

108. Yang, X. B., Bhatnagar, R. S., Li, S. & Oreffo, R. O. C. Biomimetic collagen scaffolds for human bone cell growth and differentiation. **10,** 1148–1159 (2004).

109. Qi, Y., Zhao, T., Xu, K., Dai, T. & Yan, W. The restoration of full-thickness cartilage defects with mesenchymal stem cells (MSCs) loaded and cross-linked bilayer collagen scaffolds on rabbit model. *Mol. Biol. Rep.* **39,** 1231–1237 (2012).

110. Yuan, T. *et al.* Collagen hydrogel as an immunomodulatory scaffold in cartilage tissue engineering. *J. Biomed. Mater. Res. - Part B Appl. Biomater.* **102,** 337–344 (2014).

111. Duan, X. & Sheardown, H. Dendrimer crosslinked collagen as a corneal tissue engineering scaffold: Mechanical properties and corneal epithelial cell interactions. *Biomaterials* **27,** 4608–4617 (2006).

112. Malafaya, P. B., Silva, G. A. & Reis, R. L. Natural-origin polymers as carriers and scaffolds for biomolecules and cell delivery in tissue engineering applications. *Adv. Drug Deliv. Rev.* **59,** 207–233 (2007).

113. Sehgal, P. K. & Srinivasan, A. Collagen-coated microparticles in drug delivery. *Expert Opin. Drug Deliv.* **6,** 687–95 (2009).

114. Ruszczak, Z. & Friess, W. Collagen as a carrier for on-site delivery of antibacterial drugs. *Adv. Drug Deliv. Rev.* **55,** 1679–1698 (2003).

115. Gopinath, D. *et al.* Dermal wound healing processes with curcumin incorporated collagen films. *Biomaterials* **25,** 1911–1917 (2004).

116. Sano, A., Hojo, T., Maeda, M. & Fujioka, K. Protein release from collagen matrices. *Adv. Drug Deliv. Rev.* **31,** 247–266 (1998).

117. Capito, R. M. & Spector, M. Collagen scaffolds for nonviral IGF-1 gene delivery in articular cartilage tissue engineering. *Gene Ther.* **14,** 721–732 (2007).

118. Zhao, B. *et al.* DNA-collagen complex as a carrier for Ag+ delivery. *Int. J. Biol. Macromol.* **37,** 143–147 (2005).

119. Kojima, C. *et al.* Doxorubicin-conjugated dendrimer/collagen hybrid gels for metastasis-associated drug delivery systems. *Acta Biomater.* **9,** 5673–5680 (2013).

120. Wolinsky, J. B. *et al.* Prevention of in vivo lung tumor growth by prolonged local delivery of hydroxycamptothecin using poly(ester-carbonate)-collagen composites. *J. Control. Release* **144,** 280–287 (2010).

121. Matthews, J. a, Wnek, G. E., Simpson, D. G. & Bowlin, G. L. Electrospinning of collagen nanofibers. *Biomacromolecules* **3,** 232–8 (2002).

122. Bürck, J. *et al.* Resemblance of electrospun collagen nanofibers to their native structure. *Langmuir* **29,** 1562–1572 (2013).

123. Karageorgiou, V. & Kaplan, D. Porosity of 3D biomaterial scaffolds and osteogenesis. *Biomaterials* **26,** 5474–91 (2005).

124. Yang, L. *et al.* Mechanical properties of single electrospun collagen type I fibers. *Biomaterials* **29,** 955–62 (2008).

125. Torbet, J. *et al.* Orthogonal scaffold of magnetically aligned collagen lamellae for corneal stroma reconstruction. *Biomaterials* **28,** 4268–4276 (2007).

126. Torbet, J. & Ronzière, M. C. Magnetic alignment of collagen during self-assembly. *Biochem. J.* **219,** 1057–1059 (1984).

127. Guo, C. & Kaufman, L. J. Flow and magnetic field induced collagen alignment. *Biomaterials* **28,** 1105–1114 (2007).

128. Dubey, N., Letourneau, P. C. & Tranquillo, R. T. Guided neurite elongation and schwann cell invasion into magnetically aligned collagen in simulated peripheral nerve regeneration. *Exp. Neurol.* **158,** 338–50 (1999).

129. Hoogenkamp, H. R. *et al.* Directing collagen fibers using counter-rotating cone extrusion. *Acta Biomater.* **12,** 113–121 (2015).

130. Dietch, S., Kunkle, C., Cui, X., Boland, T. & Dean, D. Collagen Matrix Alignment Using Inkjet Printer Technology. *MRS Proc.* **1094,** (2008).

131. Paten, J. a. *et al.* Utility of an optically-based, micromechanical system for printing collagen fibers. *Biomaterials* **34,** 2577–2587 (2013).

132. Recknor, J. B., Sakaguchi, D. S. & Mallapragada, S. K. Directed growth and selective differentiation of neural progenitor cells on micropatterned polymer substrates. *Biomaterials* **27,** 4098–108 (2006).

133. Mahoney, M. J., Chen, R. R., Tan, J. & Saltzman, W. M. The influence of microchannels on neurite growth and architecture. *Biomaterials* **26,** 771–8 (2005).

134. Stokols, S. & Tuszynski, M. H. The fabrication and characterization of linearly oriented nerve guidance scaffolds for spinal cord injury. *Biomaterials* **25,** 5839–46 (2004).

135. Vader, D., Kabla, A., Weitz, D. & Mahadevan, L. Strain-induced alignment in collagen gels. *PLoS One* **4,** e5902 (2009).

136. Girton, T. S., Barocas, V. H. & Tranquillo, R. T. Confined compression of a tissue-equivalent: collagen fibril and cell alignment in response to anisotropic strain. *J. Biomech. Eng.* **124,** 568–575 (2002).

137. Quekett John. *A practical treatise on the use of the microscope, including the different methods of preparing and examining animal, vegetable, and mineral structures.* 600 (H. Bailliere, 1852).

138. Xu, Q., Rioux, R. M., Dickey, M. D. & Whitesides, G. M. Nanoskiving: a new method to produce arrays of nanostructures. *Acc. Chem. Res.* **41,** 1566–77 (2008).

139. Lipomi, D. J., Martinez, R. V & Whitesides, G. M. Use of thin sectioning (nanoskiving) to fabricate nanostructures for electronic and optical applications. *Angew. Chem. Int. Ed. Engl.* **50,** 8566–83 (2011).

140. Rho, J. Y., Kuhn-Spearing, L. & Zioupos, P. Mechanical properties and the hierarchical structure of bone. *Med. Eng. Phys.* **20,** 92–102 (1998).

141. Zhang, K., Si, F. W., Duan, H. L. & Wang, J. Microstructures and mechanical properties of silks of silkworm and honeybee. *Acta Biomater.* **6,** 2165–2171 (2010).

142. Hale, M. S. & Mitchell, J. G. Functional morphology of diatom frustule microstructures: Hydrodynamic control of brownian particle diffusion and advection. *Aquat. Microb. Ecol.* **24,** 287–295 (2001).

143. Orgel, J. P. R. O., Irving, T. C., Miller, A. & Wess, T. J. Microfibrillar structure of type I collagen in situ. *Proc. Natl. Acad. Sci. U. S. A.* **103,** 9001–5 (2006).

144. Alberti, K. A. & Xu, Q. Slicing, Stacking and Rolling: Fabrication of Nanostructured Collagen Constructs from Tendon Sections. *Adv. Healthc. Mater.* **2,** 817–21 (2013).

145. Cartmell, J. & Dunn, M. Effect of chemical treatments on tendon cellularity and mechanical properties. *J. Biomed. Mater. Res.* **49,** 134–140 (2000).

146. Damink, L. & Dijkstra, P. Glutaraldehyde as a crosslinking agent for collagen-based biomaterials. *J. Mater. Sci. Mater. Med.* **4530,** (1995).

147. Cheung, D. T., Perelman, N., Ko, E. C. & Nimni, M. E. Mechanism of crosslinking of proteins by glutaraldehyde III. Reaction with collagen in tissues. *Connect. Tissue Res.* **13,** 109–15 (1985).

148. Jayakrishnan, A. & Jameela, S. R. Glutaraldehyde as a fixative in bioprostheses and drug delivery matrices. *Biomaterials* **17,** 471–84 (1996).

149. Dahl, S. L. M. *et al.* Readily available tissue-engineered vascular grafts. *Sci. Transl. Med.* **3,** 68ra9 (2011).

150. Kehoe, S., Zhang, X. F. & Boyd, D. FDA approved guidance conduits and wraps for peripheral nerve injury: A review of materials and efficacy. *Injury* **43,** 553–572 (2011).

151. Sung, H. W., Huang, R. N., Huang, L. L. & Tsai, C. C. In vitro evaluation of cytotoxicity of a naturally occurring cross-linking reagent for biological tissue fixation. *J. Biomater. Sci. Polym. Ed.* **10,** 63–78 (1999).

152. Gough, J. E., Scotchford, C. A. & Downes, S. Cytotoxicity of glutaraldehyde crosslinked collagen/poly(vinyl alcohol) films is by the mechanism of apoptosis. *J. Biomed. Mater. Res.* **61,** 121–30 (2002).

153. Barnes, C. P., Pemble, C. W., Brand, D. D., Simpson, D. G. & Bowlin, G. L. Cross-linking electrospun type II collagen tissue engineering scaffolds with carbodiimide in ethanol. *Tissue Eng.* **13,** 1593–605 (2007).

154. Zeeman, R. Cross-Linking of Collagen Based Materials. Thesis: University of Twente (1998).

155. Kato, Y. P. *et al.* Mechanical properties of collagen fibres: a comparison of reconstituted and rat tail tendon fibres. *Biomaterials* **10,** 38–42 (1989).

156. Wollensak, G., Spoerl, E. & Seiler, T. Riboflavin/ultraviolet-A-induced collagen crosslinking for the treatment of keratoconus. *Am. J. Ophthalmol.* **135,** 620–627 (2003).

157. Gkika, M., Labiris, G. & Kozobolis, V. Corneal collagen cross-linking using riboflavin and ultraviolet-A irradiation: A review of clinical and experimental studies. *Int. Ophthalmol.* **31,** 309–319 (2011).

158. Charulatha, V. & Rajaram, A. Dimethyl 3,3'-dithiobispropionimidate: a novel crosslinking reagent for collagen. *J. Biomed. Mater. Res.* **54,** 122–8 (2001).

159. Charulatha, V. & Rajaram, a. Influence of different crosslinking treatments on the physical properties of collagen membranes. *Biomaterials* **24,** 759–67 (2003).

160. Sionkowska, A., Skopinska-Wisniewska, J., Gawron, M., Kozlowska, J. & Planecka, a. Chemical and thermal cross-linking of collagen and elastin hydrolysates. *Int. J. Biol. Macromol.* **47,** 570–7 (2010).

161. Weadock, K. S., Miller, E. J., Keuffel, E. L. & Dunn, M. G. Effect of physical crosslinking methods on collagen-fiber durability in proteolytic solutions. *J. Biomed. Mater. Res.* **32,** 221–226 (1996).

162. Fujimori, E. Ultraviolet light-induced change in collagen macromolecules. *Biopolymers* **3,** 115–119 (1965).

163. Wess, T. J. & Orgel, J. P. Changes in collagen structure: Drying, dehydrothermal treatment and relation to long term deterioration. *Thermochim. Acta* **365,** 119–128 (2000).

164. Chen, R. N., Ho, H. O. & Sheu, M. T. Characterization of collagen matrices crosslinked using microbial transglutaminase. *Biomaterials* **26,** 4229–4235 (2005).

165. Collighan, R. J. & Griffin, M. Transglutaminase 2 cross-linking of matrix proteins: Biological significance and medical applications. *Amino Acids* **36,** 659–670 (2009).

166. Alberti, K. A., Sun, J. Y., Illeperuma, W., Z., S. & Xu, Q. Laminar Tendon Composites with Enhanced Mechanical Properties. *J. Mater. Sci.* (2014).

167. Vidal, B. D. C. & Mello, M. L. S. Collagen type I amide I band infrared spectroscopy. *Micron* **42,** 283–9 (2011).

168. Wang, X., Zhang, J. & Wang, Q. Surface Modification of GTA Crosslinked Collagen-based Composite Scaffolds with Low Temperature Plasma Technology. *J. Macromol. Sci. Part A* **45,** 585–589 (2008).

169. Ocak, B. Complex coacervation of collagen hydrolysate extracted from leather solid wastes and chitosan for controlled release of lavender oil. *J. Environ. Manage.* **100,** 22–8 (2012).

170. Derwin, K. A, Badylak, S. F., Steinmann, S. P. & Iannotti, J. P. Extracellular matrix scaffold devices for rotator cuff repair. *J. Shoulder Elbow Surg.* **19,** 467–76 (2010).

171. Aurora, A., McCarron, J., Iannotti, J. P. & Derwin, K. Commercially available extracellular matrix materials for rotator cuff repairs: state of the art and future trends. *J. Shoulder Elbow Surg.* **16,** S171–8

172. Coons, D. A. & Alan Barber, F. Tendon graft substitutes-rotator cuff patches. *Sports Med. Arthrosc.* **14,** 185–90 (2006).

173. Altman, G. H. *et al.* Silk matrix for tissue engineered anterior cruciate ligaments. *Biomaterials* **23,** 4131–41 (2002).

174. Xu, W. *et al.* Mechanical properties of small-diameter polyurethane vascular grafts reinforced by weft-knitted tubular fabric. *J. Biomed. Mater. Res. A* **92,** 1–8 (2010).

175. Qin, T. W. *et al.* Mechanical characteristics of native tendon slices for tissue engineering scaffold. *J. Biomed. Mater. Res. B. Appl. Biomater.* **100,** 752–8 (2012).

176. Legerlotz, K., Riley, G. P. & Screen, H. R. C. Specimen dimensions influence the measurement of material properties in tendon fascicles. *J. Biomech.* **43,** 2274–80 (2010).

177. Buehler, M. J. Multiscale mechanics of biological and biologically inspired materials and structures. *Acta Mech. Solida Sin.* **23,** 471-483 (2010).

178. Cox, H. The elasticity and strength of paper and other fibrous materials. *Br. J. Appl. Phys.* **72,** (1952).

179. Amis, A. A., Basso, O. & Johnson, D. P. The anatomy of the patellar tendon. *Knee Surgery, Sport. Traumatol. Arthrosc.* **9,** 2–5 (2001).

180. Provenzano, P. P. & Vanderby, R. Collagen fibril morphology and organization: implications for force transmission in ligament and tendon. *Matrix Biol.* **25,** 71–84 (2006).

181. Vinson, J. R. & Sierakowski, R. L. *The Behavior of Structures Composed of Composite Materials*. (Springer, 2006).

182. Zimmermann, E. a. *et al.* Mechanical adaptability of the Bouligand-type structure in natural dermal armour. *Nat. Commun.* **4,** 1–7 (2013).

183. Staab, G. *Laminar Composites*. (Butterworth-Heinemann, 1999).

184. Holzapfel, G. A, Gasser, T. C. & Ogden, R. W. A new constitutive framework for arterial wall mechanics and a comperative study of material models. *J. Elast.* **61,** 1–48 (2000).

185. Isenberg, B. C., Williams, C. & Tranquillo, R. T. Small-diameter artificial arteries engineered in vitro. *Circ. Res.* **98,** 25–35 (2006).

186. Bassiouny, H. *et al.* Anastomotic intimal hyperplasia: mechanical injury or flow induced. *J. Vasc. Surg.* **15,** 708–717 (1992).

187. Tai, N. R., Salacinski, H. J., Edwards, A., Hamilton, G. & Seifalian, A. M. Compliance properties of conduits used in vascular reconstruction. *Br. J. Surg.* **87,** 1516–1524 (2000).

188. L'Heureux, N., Pâquet, S., Labbé, R., Germain, L. & Auger, F. A. A completely biological tissue-engineered human blood vessel. *FASEB J.* **12,** 47–56 (1998).

189. Valentin, J. E. *et al.* Oxygen diffusivity of biologic and synthetic scaffold materials for tissue engineering. *J. Biomed. Mater. Res. A* **91,** 1010–7 (2009).

190. Gray, C., Oliva, T., Christakis, A., Rolle, M. & Billiar, K. Design of a versatile, inexpensive vessel burst pressure measurement device. *2009 IEEE 35th Annu. Northeast Bioeng. Conf.* 1–2 (2009).

191. Pabinger, C., Berghold, A., Boehler, N. & Labek, G. Revision rates after knee replacement: Cumulative results from worldwide clinical studies versus joint registers. *Osteoarthr. Cartil.* **21,** 263–268 (2013).

192. Woessner, J. F. Matrix metalloproteinases and their inhibitors in connective tissue remodeling. *FASEB J.* **5,** 2145–54 (1991).

193. Record, R. D. *et al.* In vivo degradation of 14C-labeled small intestinal submucosa (SIS) when used for urinary bladder repair. *Biomaterials* **22,** 2653–2659 (2001).

194. Harriger, M. D., Supp, A. P., Warden, G. D. & Boyce, S. T. Glutaraldehyde crosslinking of collagen substrates inhibits degradation in skin substitutes grafted to athymic mice. *J. Biomed. Mater. Res.* **35,** 137–45 (1997).

195. Olde Damink, L. H. *et al.* In vitro degradation of dermal sheep collagen cross-linked using a water-soluble carbodiimide. *Biomaterials* **17,** 679–84 (1996).

196. Badylak, S. F. & Gilbert, T. W. Immune response to biologic scaffold materials. *Semin. Immunol.* **20,** 109–116 (2008).

197. Harper, E., Berger, A. & Katchalski, E. The hydrolysis of poly (L-Prolyl-Glycyl-L-Prolyl) by bacterial collagenase. *Biopolymers* **11,** 1607–1612 (1972).

198. Stenzel, K., Miyata, T. & Rubin, A. Collagen as a biomaterial. *Annu. Rev. Biophys. Bioeng.* **3,** 231–253 (1974).

199. Yannas, I. V., Burke, J. F., Huang, C. & Gordon, P. L. Correlation of in vivo collagen degradation rate with in vivo measurements. *J. Biomed. Mater. Res.* **9,** 623–628 (2004).

200. Sung, H. W., Hsu, C. S., Wang, S. P. & Hsu, H. L. Degradation potential of biological tissues fixed with various fixatives: an in vitro study. *J. Biomed. Mater. Res.* **35,** 147–155 (1997).

201. Thompson, D. M. & Buettner, H. M. Neurite outgrowth is directed by schwann cell alignment in the absence of other guidance cues. *Ann. Biomed. Eng.* **34,** 161–8 (2006).

202. Santoro, S. A., Walsh, J. J., Staatz, W. D. & Baranski, K. J. Distinct determinants on collagen support alpha 2 beta 1 integrin-mediated platelet adhesion and platelet activation. *Cell Regul.* **2,** 905–913 (1991).

203. Gibbins, J. M., Okuma, M., Farndale, R., Barnes, M. & Watson, S. P. Glycoprotein VI is the collagen receptor in platelets which underlies tyrosine phosphorylation of the Fc receptor. *FEBS Lett.* **413,** 255–259 (1997).

204. Moroi, M. & Jung, S. M. Platelet glycoprotein VI: Its structure and function. *Thromb. Res.* **114,** 221–233 (2004).

205. Nieswandt, B. & Watson, S. P. Platelet-collagen interaction: Is GPVI the central receptor? *Blood* **102,** 449–461 (2003).

206. Savage, B., Saldívar, E. & Ruggeri, Z. M. Initiation of platelet adhesion by arrest onto fibrinogen or translocation on von Willebrand factor. *Cell* **84,** 289–297 (1996).

207. Wissink, M. J. *et al.* Immobilization of heparin to EDC/NHS-crosslinked collagen. Characterization and in vitro evaluation. *Biomaterials* **22,** 151–63 (2001).

208. Keuren, J. F. W. *et al.* Covalently-bound heparin makes collagen thromboresistant. *Arterioscler. Thromb. Vasc. Biol.* **24,** 613–7 (2004).

208. Senatore, F. *et al.* In vitro and in vivo studies of heparinized-collageno-elastic tubes. *J. Biomed. Mater. Res.* **24,** 939–957 (1990).

210. Lindon, J. *et al.* Catalytic activity and platelet reactivity of heparin covalently bonded to surfaces. *J. Lab. Clin. Med.* **105,** 214–218 (1985).

211. Buckwalter, J., Einhorn, T. & Simon, S. in *Orthop. Basic Sci.* 582–616 (2000).

212. Smith, P. K. & Mallia, A. K. Colorimetric Method for the Assay of Heparin Immobilized Heparin Preparations Content in. *Anal. Biochem.* **109,** 466–473 (1980).

213. Sridharan, G. & Shankar, A. Toluidine blue: A review of its chemistry and clinical utility. *J. Oral Maxillofac. Pathol.* **16,** 251–255 (2012).

214. Hirsh, J., Anand, S. S., Halperin, J. L. & Fuster, V. Mechanism of action and pharmacology of unfractionated heparin. *Arterioscler. Thromb. Vasc. Biol.* **21,** 1094–1096 (2001).

215. Rastegar-Lari, G. *et al.* von Willebrand factor binding to heparin in various types of von Willebrand disease. *Heamtology* **1,** 190–198 (2000).

216. Sobel, M. *et al.* Heparin inhibition of von Willebrand factor-dependent platelet function in vitro and in vivo. *J. Clin. Invest.* **87,** 1787–1793 (1991).

217. Liu, R. *et al.* The in vivo blood compatibility of bio-inspired small diameter vascular graft: effect of submicron longitudinally aligned topography. *BMC Cardiovasc. Disord.* **13,** 79 (2013).

218. Ruggeri, Z. M. & Mendolicchio, G. L. Adhesion mechanisms in platelet function. *Circ. Res.* **100,** 1673–1685 (2007).

219. Kuwahara, M. *et al.* Platelet shape changes and adhesion under high shear flow. *Arterioscler. Thromb. Vasc. Biol.* **22,** 329–334 (2002).

220. Tsen, A. *et al.* The effect of anticoagulants and the role of thrombin on neutrophil-endothelial cell interactions in septic shock. *Shock* **31,** 120–124 (2009).

221. He, W., Ma, Z., Yong, T., Teo, W. E. & Ramakrishna, S. Fabrication of collagen-coated biodegradable polymer nanofiber mesh and its potential for endothelial cells growth. *Biomaterials* **26,** 7606–7615 (2005).

222. Inoguchi, H., Tanaka, T., Maehara, Y. & Matsuda, T. The effect of gradually graded shear stress on the morphological integrity of a huvec-seeded compliant small-diameter vascular graft. *Biomaterials* **28,** 486–495 (2007).

223. Anderson, J., Rodriguez, A. & Change, D. Foreign Body Reaction to Biomaterials. *Semin. Immunol.* **20,** 86–100 (2008).

224. Anderson, J. M. & Shive, M. S. Biodegradation and biocompatibility of PLA and PLGA microspheres. *Adv. Drug Deliv. Rev.* **64,** 72–82 (2012).

225. Baker, J. L., Chandler, M. L. & LeVier, R. R. Occurrence and activity of myofibroblasts in human capsular tissue surrounding mammary implants. *Plast. Reconstr. Surg.* **68,** 905–912 (1981).

226. Majd, H. *et al.* Novel micropatterns mechanically control fibrotic reactions at the surface of silicone implants. *Biomaterials* **54,** 136–147 (2015).

227. Oliver, R. F., Barker, H., Cooke, A. & Grant, R. A. Dermal collagen implants. *Biomaterials* **3,** 38–40 (1982).

228. Valentin, J. E., Stewart-Akers, A. M., Gilbert, T. W. & Badylak, S. F. Macrophage participation in the degradation and remodeling of extracellular matrix scaffolds. *Tissue Eng. Part A* **15,** 1687–1694 (2009).

229. Oliver, R., Hulme, M., Mudie, A. & Grant, R. Skin collagen allografts in the rat. *Nature* **258,** 537–539 (1975).

230. Oliver, R., Grant, R., Cox, R., Hulme, M. & Mudie, A. Histological studies of subcutaneous and intraperitoneal implants of trypsin prepared dermal collagen allografts in the rat. *Clin. Orthop. Relat. Res.* **115,** (1976).

231. Oliver, R. F., Grant, R. A. & Kent, C. M. The fate of cutaneously and subcutaneously implanted trypsin purified dermal collagen in the pig. *Br. J. Exp. Pathol.* **53,** 540–549 (1972).

232. Griffiths, R. W. & Shakespeare, P. G. Human dermal collagen allografts: a three year histological study. *Br. J. Plast. Surg.* **35,** 519–523 (1982).

233. Macleod, T. M., Williams, G., Sanders, R. & Green, C. J. Histological evaluation of Permacol as a subcutaneous implant over a 20-week period in the rat model. *Br. J. Plast. Surg.* **58,** 518–532 (2005).

234. Eppley, B. L. Experimental assessment of the revascularization of acellular human dermis for soft-tissue augmentation. *Plast. Reconstr. Surg.* **107,** 757–762 (2001).

235. Delustro, F., Smith, S. T., Sundsumo, J., Salem, G., Kincaid, S. & Ellingsworth, L. Reaction to injectable collagen: results in animal models and clinical use. *Plast. Reconstr. Surg.* **79,** 581-594 (1987).

236. DeLustro, F., Dasch, J., Keefe, J. & Ellingsworth, L. Immune responses to allogeneic and xenogeneic implants of collagen and collagen derivatives. *Clin. Orthop. Relat. Res.* **260,** 263–279 (1990).

237. Ciaramitaro, P. *et al.* Traumatic peripheral nerve injuries: epidemiological findings, neuropathic pain and quality of life in 158 patients. *J. Peripher. Nerv. Syst.* **15,** 120–7 (2010).

238. Ichihara, S., Inada, Y. & Nakamura, T. Artificial nerve tubes and their application for repair of peripheral nerve injury: an update of current concepts. *Injury* **39 Suppl 4,** 29–39 (2008).

239. Kincaid, J. C. & Stewart, J. D. Focal peripheral neuropathies. *J. Clin. Neuromuscul. Dis.* **1,** 113 (1999).

240. Elkwood, A. I. *et al.* Nerve allograft transplantation for functional restoration of the upper extremity: case series. *J. Spinal Cord Med.* **34,** 241–247 (2011).

241. Hall, J. *Guyton and Hall Textbook of Medical Physiology.* (2010).

242. Martini, R., Xin, Y., Schmitz, B. & Schachner, M. The L2/HNK-1 carbohydrate epitope is involved in the preferential outgrowth of motor neurons on ventral roots and motor nerves. *Eur. J. Neurosci.* **4,** 628–639 (1992).

243. Macias, M. Y., Lehman, C. T., Sanger, J. R. & Riley, D. A. Myelinated sensory and alpha motor axon regeneration in peripheral nerve neuromas. *Muscle and Nerve* **21,** 1748–1758 (1998).

244. Brushart, T., Tarlov, E. & Mesulam, M. Specificity of muscle reinnervation after epineurial and individual fascicular suture of the rat sciatic nerve. *J. Hand Surg. Am.* **8,** 248–253 (1983).

245. Brushart, T. M. Motor axons preferentially reinnervate motor pathways. *J. Neurosci.* **13,** 2730–2738 (1993).

246. Brushart, T. M. Preferential reinnervation of motor nerves by regenerating motor axons. *J. Neurosci.* **8,** 1026–1031 (1988).

247. Forman, D. S., Wood, D. K. & DeSilva, S. Rate of regeneration of sensory axons in transected rat sciatic nerve repaired with epineurial sutures. *J. Neurol. Sci.* **44,** 55–59 (1979).

248. Macias, M. Y., Lehman, C. T., Sanger, J. R. & Riley, D. A. Myelinated sensory and alpha motor axon regeneration in peripheral nerve neuromas. *Muscle and Nerve* **21,** 1748–1758 (1998).

249. Moldovan, M., Sørensen, J. & Krarup, C. Comparison of the fastest regenerating motor and sensory myelinated axons in the same peripheral nerve. *Brain* **129,** 2471–2483 (2006).

250. Lago, N., Rodriguez, F., Guzman, M., Jaramillo, J. & Navarro, X. Effects of Motor and Sensory Nerve Transplants on Amount and Specificity of Sciatic Nerve Regeneration. *J. Neurosci. Res.* **85,** 2800–2812 (2007).

251. Belkas, J. S., Shoichet, M. S. & Midha, R. Peripheral nerve regeneration through guidance tubes. *Neurol. Res.* **26,** 151–160 (2004).

252. Daly, W., Yao, L., Zeugolis, D., Windebank, a & Pandit, a. A biomaterials approach to peripheral nerve regeneration: bridging the peripheral nerve gap and enhancing functional recovery. *J. R. Soc. Interface* **9,** 202–21 (2012).

253. Deumens, R. *et al.* Repairing injured peripheral nerves: Bridging the gap. *Prog. Neurobiol.* **92,** 245–76 (2010).

254. Pabari, A., Yang, S. Y., Seifalian, A. M. & Mosahebi, A. Modern surgical management of peripheral nerve gap. *J. Plast. Reconstr. Aesthet. Surg.* **63,** 1941–8 (2010).

255. Weber, R. V & Mackinnon, S. E. Bridging the neural gap. *Clin. Plast. Surg.* **32,** 605–16 (2005).

256. Elkwood, A. I. *et al.* Nerve allograft transplantation for functional restoration of the upper extremity: case series. *J. Spinal Cord Med.* **34,** 241–247 (2011).

257. Nectow, A. R., Marra, K. G. & Kaplan, D. L. Biomaterials for the Development of Peripheral Nerve. *Tissue Eng. Part B* **18,** 40–50 (2012).

258. Yao, L., Billiar, K., Windebank, A. & Pandit, A. Multichanneled collagen conduits for peripheral nerve regeneration: design, fabrication, and characterization. *Tissue Eng. Part C.* **16,** 1585-1596 (2010).

259. Stang, F., Fansa, H., Wolf, G., Reppin, M. & Keilhoff, G. Structural parameters of collagen nerve grafts influence peripheral nerve regeneration. *Biomaterials* **26,** 3083–91 (2005).

260. Zhang, Q. *et al.* Preparation of uniaxial multichannel silk fibroin scaffolds for guiding primary neurons. *Acta Biomater.* **8,** 2628–38 (2012).

261. Ghaznavi, A. M., Kokai, L. E., Lovett, M. L., Kaplan, D. L. & Marra, K. G. Silk fibroin conduits: a cellular and functional assessment of peripheral nerve repair. *Ann. Plast. Surg.* **66,** 273–9 (2011).

262. Waitayawinyu, T. *et al.* A Comparison of Polyglycolic Acid Versus Type 1 Collagen Bioabsorbable Nerve Conduits in a Rat Model: An Alternative to Autografting. *J. Hand Surg. Am.* **32,** 1521–1529 (2007).

263. Whitlock, E. L. *et al.* Processed allografts and type I collagen conduits for repair of peripheral nerve gaps. *Muscle and Nerve* **39,** 787–799 (2009).

264. Belkas, J. S., Shoichet, M. S. & Midha, R. Peripheral nerve regeneration through guidance tubes. *Neurol. Res.* **26,** 151–160 (2004).

265. Bozkurt, A. *et al.* The role of microstructured and interconnected pore channels in a collagen-based nerve guide on axonal regeneration in peripheral nerves. *Biomaterials* **33,** 1363–1375 (2012).

266. Toba, T. *et al.* Regeneration of Canine Peroneal Nerve with the Use of a Polyglycolic Acid-Collagen Tube Filled with Laminin-Soaked Collagen Sponge: A Comparative Study of Collagen Sponge and Collagen Fibers as Filling Materials for Nerve Conduits. *J. Biomed. Mater. Res.* **58,** 622–630 (2001).

267. Yu, T. T. & Shoichet, M. S. Guided cell adhesion and outgrowth in peptide-modified channels for neural tissue engineering. *Biomaterials* **26,** 1507–1514 (2005).

268. Panseri, S. *et al.* Electrospun micro- and nanofiber tubes for functional nervous regeneration in sciatic nerve transections. *BMC Biotechnol.* **8,** 39 (2008).

269. Miller, C., Shanks, H., Witt, A., Rutkowski, G. & Mallapragada, S. Schwann cell interactions with polymer films are affected by groove geometry and film hydrophilicity. *Biomaterials* **22,** 1263–1269 (2001).

270. Matsumoto, K. *et al.* Peripheral nerve regeneration across an 80-mm gap bridged by a polyglycolic acid (PGA)-collagen tube filled with laminin-coated collagen fibers: A histological and electrophysiological evaluation of regenerated nerves. *Brain Res.* **868,** 315–328 (2000).

271. Kim, Y. T., Haftel, V. K., Kumar, S. & Bellamkonda, R. V. The role of aligned polymer fiber-based constructs in the bridging of long peripheral nerve gaps. *Biomaterials* **29,** 3117–3127 (2008).

272. Hoffman-Kim, D., Mitchel, J. a & Bellamkonda, R. V. Topography, cell response, and nerve regeneration. *Annu. Rev. Biomed. Eng.* **12,** 203–31 (2010).

273. Wang, Z. *et al.* Improved peripheral nerve regeneration with sustained release nerve growth factor microspheres in small gap tubulization. *Am. J. Transl. Res.* **6,** 413–21 (2014).

274. Chang, C. J. Effects of nerve growth factor from genipin-crosslinked gelatin in polycaprolactone conduit on peripheral nerve regeneration - In vitro and in vivo. *J. Biomed. Mater. Res. - Part A* **91,** 586–596 (2009).

275. Dinis, T. M. *et al.* Complementary Effects of Two Growth Factors in Multifunctionalized Silk Nanofibers for Nerve Reconstruction. *PLoS One* **9,** e109770 (2014).

276. Shen, H. *et al.* Ciliary neurotrophic factor-coated polylactic-polyglycolic acid chitosan nerve conduit promotes peripheral nerve regeneration in canine tibial nerve defect repair. *J. Biomed. Mater. Res. - Part B Appl. Biomater.* **95,** 161–170 (2010).

277. Kokai, L. E., Bourbeau, D. & Weber, D. Sustained Growth Factor Delivery Promotes Axonal Regeneration in Long Gap Peripheral Nerve Repair. *Tissue Eng. Pt. A.* **17,** 1263-1275 (2011).

278. Madduri, S., di Summa, P., Papaloïzos, M., Kalbermatten, D. & Gander, B. Effect of controlled co-delivery of synergistic neurotrophic factors on early nerve regeneration in rats. *Biomaterials* **31,** 8402–8409 (2010).

279. Hobson, M. I. Increased vascularisation enhances axonal regeneration within an acellular nerve conduit. *Ann. R. Coll. Surg. Engl.* **84,** 47–53 (2002).

280. Longo, F. M., Xie, Y. & Massa, S. M. Neurotrophin Small Molecule Mimetics: Candidate Therapeutic Agents for Neurological Disorders. *Curr. Med. Chem.* **5,** 29–41 (2005).

281. Peleshok, J. & Saragovi, H. U. Functional mimetics of neurotrophins and their receptors. *Biochem. Soc. Trans.* **34,** 612–617 (2006).

282. Colangelo, A. M. *et al.* A new nerve growth factor-mimetic peptide active on neuropathic pain in rats. *J. Neurosci.* **28,** 2698–2709 (2008).

283. Fu, S. Y. & Gordon, T. The cellular and molecular basis of peripheral nerve regeneration. *Mol. Neurobiol.* **14,** 67–116 (1997).

284. Vleggeert-Lankamp, C. L. M. *et al.* Adhesion and proliferation of human Schwann cells on adhesive coatings. *Biomaterials* **25,** 2741–51 (2004).

285. Hu, M., Sabelman, E. E., Tsai, C., Tan, J. & Hentz, V. R. Improvement of Schwann cell attachment and proliferation on modified hyaluronic acid strands by polylysine. *Tissue Eng.* **6,** 585–93 (2000).

286. Chew, S. Y., Mi, R., Hoke, A. & Leong, K. W. The effect of the alignment of electrospun fibrous scaffolds on Schwann cell maturation. *Biomaterials* **29,** 653–61 (2008).

287. Jiang, X., Lim, S. H., Mao, H. Q. & Chew, S. Y. Current applications and future perspectives of artificial nerve conduits. *Exp. Neurol.* **223,** 86–101 (2010).

288. Brushart, T. M., Mathur, V., Sood, R. & Koschorke, G.-M. Dispersion of regenerating axons across enclosed neural gaps. *J. Hand Surg. Am.* **20,** 557–564 (1995).

289. Maskery, S. & Shinbrot, T. Deterministic and stochastic elements of axonal guidance. *Annu. Rev. Biomed. Eng.* **7,** 187–221 (2005).

290. Brushart, T. M., Mathur, V., Sood, R. & Koschorke, G.-M. Dispersion of regenerating axons across enclosed neural gaps. *J. Hand Surg. Am.* **20,** 557–564 (1995).

291. Schnell, E. *et al.* Guidance of glial cell migration and axonal growth on electrospun nanofibers of poly-epsilon-caprolactone and a collagen/poly-epsilon-caprolactone blend. *Biomaterials* **28,** 3012–25 (2007).

292. Dubey, N., Letourneau, P. C. & Tranquillo, R. T. Guided neurite elongation and schwann cell invasion into magnetically aligned collagen in simulated peripheral nerve regeneration. *Exp. Neurol.* **158,** 338–50 (1999).

293. Heron, P. M., Sutton, B. M., Curinga, G. M., Smith, G. M. & Snow, D. M. Localized gene expression of axon guidance molecules in neuronal co-cultures. *J. Neurosci. Methods* **159,** 203–14 (2007).

294. Voyiadjis, A. G., Doumi, M., Curcio, E. & Shinbrot, T. Fasciculation and defasciculation of neurite bundles on micropatterned substrates. *Ann. Biomed. Eng.* **39,** 559–69 (2011).

295. Richardson, J. A., Rementer, C. W., Bruder, J. M. & Hoffman-Kim, D. Guidance of dorsal root ganglion neurites and Schwann cells by isolated Schwann cell topography on poly(dimethyl siloxane) conduits and films. *J. Neural Eng.* **8,** 046015 (2011).

296. Corey, J., Lin, D. & Mycek, K. Aligned electrospun nanofibers specify the direction of dorsal root ganglia neurite growth. *J. Biomed. Mater. Res. A* **83,** 10–15 (2007).

297. Schnell, E. *et al.* Guidance of glial cell migration and axonal growth on electrospun nanofibers of poly-epsilon-caprolactone and a collagen/poly-epsilon-caprolactone blend. *Biomaterials* **28,** 3012–25 (2007).

298. Savastano, L. E. *et al.* Sciatic nerve injury: A simple and subtle model for investigating many aspects of nervous system damage and recovery. *J. Neurosci. Methods* **227,** 166–180 (2014).

299. Alberti, K. A., Hopkins, A. M., Tang-Schomer, M. D., Kaplan, D. L. & Xu, Q. The behavior of neuronal cells on tendon-derived collagen sheets as potential substrates for nerve regeneration. *Biomaterials* **35,** 3551–7 (2014).

300. Chen, P., Cescon, M. & Bonaldo, P. The Role of Collagens in Peripheral Nerve Myelination and Function. *Mol. Neurobiol.* (2014).

301. Savastano, L. E. *et al.* Sciatic nerve injury: A simple and subtle model for investigating many aspects of nervous system damage and recovery. *J. Neurosci. Methods* **227,** 166–180 (2014).

302. Berrocal, Y. A., Almeida, V. W., Gupta, R. & Levi, A. D. Transplantation of Schwann cells in a collagen tube for the repair of large, segmental peripheral nerve defects in rats. *J. Neurosurg.* **119,** 720–32 (2013).

303. Carr, M., Best, T., Mackinnon, S. & Evans, P. Strain differences in autotomy in rats undergoing sciatic nerve transection or repair. *Ann. Plast. Surg.* **28,** 538–544 (1992).

304. Inbal, R., Devor, M., Tuchendler, O. & Lieblich, I. Autotomy following nerve injury: genetic factors in the development of chronic pain. *Pain* **9,** 327–337 (1980).

305. Baptista, A. F. *et al.* A new approach to assess function after sciatic nerve lesion in the mouse - adaptation of the sciatic static index. *J. Neurosci. Methods* **161,** 259–64 (2007).

306. Lowdon, I. M., Seaber, a V & Urbaniak, J. R. An improved method of recording rat tracks for measurement of the sciatic functional index of de Medinaceli. *J. Neurosci. Methods* **24,** 279–81 (1988).

307. De Medinaceli, L., Freed, W. J. & Wyatt, R. J. An index of the functional condition of rat sciatic nerve based on measurements made from walking tracks. *Exp. Neurol.* **77,** 634–643 (1982).

308. Geuna, S. The sciatic nerve injury model in pre-clinical research. *J. Neurosci. Methods* **243,** 39–46 (2015).

309. Carriel, V., Garzon, I., Alaminos, M. & Cornelissen, M. Histological assessment in peripheral nerve tissue engineering. *Neural Regen. Res.* **9,** 1657–1660 (2014).

310. Raimondo, S. *et al. Chapter 5 Methods and Protocols in Peripheral Nerve Regeneration Experimental Research. Part II-Morphological Techniques. Int. Rev. Neurobiol.* **87,** 81–103 (Elsevier Inc., 2009).

311. Fu, S. Y. & Gordon, T. The cellular and molecular basis of peripheral nerve regeneration. *Mol. Neurobiol.* **14,** 67–116 (1997).

312. Carriel, V. *et al.* Combination of fibrin-agarose hydrogels and adipose-derived mesenchymal stem cells for peripheral nerve regeneration. *J. Neural Eng.* **10,** 026022 (2013).

313. Carriel, V. S. *et al.* A novel histochemical method for a simultaneous staining of melanin and collagen fibers. *J. Histochem. Cytochem.* **59,** 270–277 (2011).

314. Bilsland, J., Rigby, M., Young, L. & Harper, S. A rapid method for semi-quantitative analysis of neurite outgrowth from chick DRG explants using image analysis. *J. Neurosci. Methods* **92,** 75–85 (1999).

315. Richardson, J. a, Rementer, C. W., Bruder, J. M. & Hoffman-Kim, D. Guidance of dorsal root ganglion neurites and Schwann cells by isolated Schwann cell topography on poly(dimethyl siloxane) conduits and films. *J. Neural Eng.* **8,** 046015 (2011).

316. Monte-Raso, V. V., Barbieri, C. H., Mazzer, N., Yamasita, A. C. & Barbieri, G. Is the Sciatic Functional Index always reliable and reproducible? *J. Neurosci. Methods* **170,** 255–61 (2008).

317. Rosi, N. L. & Mirkin, C. A. Nanostructures in biodiagnostics. *Chem. Rev.* **105**, 1547–1562 (2005).

318. Müller, R. H., Radtke, M. & Wissing, S. A. Nanostructured lipid matrices for improved microencapsulation of drugs. *Int. J. Pharm.* **242**, 121–128 (2002).

319. Hughes, G. A. Nanostructure-mediated drug delivery. *Nanomed.-Nanotechnol.* **1**, 22–30 (2005).

320. Lim, J. Y. & Donahue, H. J. Cell sensing and response to micro- and nanostructured surfaces produced by chemical and topographic patterning. *Tissue Eng.* **13**, 1879–1891 (2007).

321. De Boef, M. & Larsson, H. C. E. Bone microstructure: quantifying bone vascular orientation. *Can. J. Zoolog.* **85**, 63–70 (2007).

322. Goldschlager, T., Abdelkader, A., Kerr, J., Boundy, I. & Jenkin, G. Undecalcified bone preparation for histology, histomorphometry and fluorochrome analysis. *JoVE.* **8,** 13–15 (2010).

323. Crapo, P. M. *et al.* Biologic scaffolds composed of central nervous system extracellular matrix. *Biomaterials* **33**, 3539–47 (2012).

324. Lin, P., Chan, W., Badylak, S. & Bhatia, S. Assessing Porcine Liver-Derived Biomatrix for Hepatic Tissue Engineering. *Tissue Eng.* **10**, 1046–53 (2004).

325. Hama, I., Nakagomi, S., Konishi, H. & Kiyama, H. Simultaneous expression of glutathione, thioredoxin-1, and their reductases in nerve transected hypoglossal motor neurons of rat. *Brain Res.* **1306**, 1–7 (2010).

326. Yu, L. M. Y., Miller, F. D. & Shoichet, M. S. The use of immobilized neurotrophins to support neuron survival and guide nerve fiber growth in compartmentalized chambers. *Biomaterials* **31**, 6987–6999 (2010).

327. Tang, S. *et al.* The effects of gradients of nerve growth factor immobilized PCLA scaffolds on neurite outgrowth in vitro and peripheral nerve regeneration in rats. *Biomaterials* **34**, 7086–96 (2013).

328. Maurice, D. M. The structure and transparency of the cornea. *J. Physio.* **136**, 263–286.1 (1957).

329. Meek, K. M. & Leonard, D. W. Ultrastructure of the corneal stroma: a comparative study. *Biophys. J.* **64**, 273–280 (1993).

330. Ruberti, J. W. & Zieske, J. D. Prelude to corneal tissue engineering - gaining control of collagen organization. *Prog. Retin. Eye Res.* **27**, 549–77 (2008).

331. Horton, W. G. Further observations on the elastic mechanism of the intervertebral disc. *J. Bone Joint Surg.* **40-B**, 552–557 (1958).

332. Moazzaz, P. & Wang, J. C. Lumbar disk herniation and degenerative disk disease in athletes. *Sem. Spine Surg.* **22**, 206–209 (2010).

333. Toman, C. V *et al.* Success of meniscal repair at anterior cruciate ligament reconstruction. *Am. J. Sports Med.* **37**, 1111–1115 (2009).

334. Sarkar, S., Schmitz-Rixen, T., Hamilton, G. & Seifalian, A. M. Achieving the ideal properties for vascular bypass grafts using a tissue engineered approach: a review. *Med. Biol. Eng. Comput.* **45**, 327–36 (2007).

335. Yazdani, S. K. *et al.* Smooth muscle cell seeding of decellularized scaffolds: the importance of bioreactor preconditioning to development of a more native architecture for tissue-engineered blood vessels. *Tissue Eng. Pt. A* **15**, 827–40 (2009).

336. Boot-Handford, R. P. & Tuckwell, D. S. Fibrillar collagen: The key to vertebrate evolution? A tale of molecular incest. *BioEssays* **25**, 142–151 (2003).

337. Chus, M., Wetp, W. De, B., M. & Ramirezst, F. Fine Structural Analysis of the Human Pro-d(1) Collagen Gene. *Sem. Spine Surg.* **22,** 206-209 (1985)

338. Pang, B. & Ying, M. Sonographic measurement of Achilles tendons in asymptomatic subjects. *J. Ultras. Med.* **25**, 1291–1296 (2006).